Chemostratigraphy and Alteration Geochemistry of the Lundberg and Engine House Volcanogenic Massive Sulfide Mineralization, Buchans, Central Newfoundland

Gregory William Harry van Hees

Thesis submitted to the
Faculty of Graduate and Postdoctoral Studies
In partial fulfillment of the requirements
for the M.Sc degree in Earth Sciences

Department of Earth Sciences

Faculty of Science

University of Ottawa

Abstract

The world-class Buchans Mining Camp hosts a number of high-grade, low-tonnage volcanogenic massive sulfide (VMS) deposits. The Lundberg and Engine House zones form the lower-grade stockwork to the Lucky Strike deposit and have yet to be mined. A detailed study of the Lundberg and Engine House zones was conducted to establish the stratigraphic setting of the deposits, to determine the petrology of the host volcanic rocks and distribution of alteration facies, and to characterize the mineralization with the goal of improving exploration for polymetallic massive sulfide deposits in the Buchans camp.

The Buchans Group is historically divided into four formations from base to top: Lundberg Hill, Ski Hill, Buchans River, and Sandy Lake formations. Logging of new drill core within the Lundberg and Engine House zones requires a revision of this formational nomenclature. The Lundberg Hill Formation (LHF) is herein redefined as basaltic breccia with local multicoloured chert; felsic volcanic rocks are excluded. The Ski Hill Formation (SHF), as originally defined, consists of hyaloclastite, brecciated, and massive basalt flows. The Buchans River Formation (BRF) consists of a series of polymictic breccias and siltstone; however, a series of rhyolitic rocks, originally assigned to the BRF, were determined to be thrust-emplaced on the BRF and have been reclassified into a new informal unit, *the Lucky Strike hanging-wall succession*. The Sandy Lake Formation pillow basalt was not identified in this study area. Lithogeochemistry of each of the various Buchans formation is unique, allowing the identification of prospective (SHF and BRF) from barren (LSS) stratigraphy. All units were distinguished by their REE profiles.

Three footwall and two hanging-wall alteration facies were identified within the Lundberg and Engine House zones. The footwall alteration forms a pipe-like alteration zonation and consists of: siliceous core zone, strong to intense quartz-chlorite-sericite, and moderate quartz-chlorite-sericite. This alteration zonation provides an excellent framework for future exploration of VMS deposits in the Buchans camp.

I dedicate this work to my parents who taught

me that anything is possible. I love you both very much.

Table of Contents

List of Figures

List of Tables

List of Appendices

Foreword

This project is a component of the Geological Survey of Canada Targeted Geoscience Initiative 3 (TGI-3) program which aimed to enhance base metal exploration in existing mining camps. The TGI-3: Newfoundland Appalachians – Buchans-Robert's Arm belt component supported this project by funding the field work, chemical analyses, and stipend to GvH through the Research Affiliate Program. Additional funds from the Society of Economic Geologists in the form of a bursary were used for travel. Royal Roads Corporation provided in-kind support to the project by contributing extensive 3D diamond drill hole database of the Buchans Mining camp. The Geological Survey of Newfoundland and Labrador provided full access to the core storage facilities.

Acknowledgements

First and foremost I'll thank both Alex Zagorevski and Mark Hannington for their guidance and supervision. I'd like to thank Alex for finding such a small and beautiful town to do my research in, which has only one road in, and none out; and for finding such a nice, cost-effective home that had really, really nice neighbors. I'd also like to thank him for his various demotivational posters, as well as for his constant harassment and ridicule; and of course his relentless references to family guy (e.g., Peter, there's something off about that horse) which I very much enjoyed. I'd like to thank Mark for the litre of red ink that he poured onto this thesis, but also remind him that perhaps a warning sign 'sticky when wet' be attached to the top right hand corner as a common courtesy. I would also like to thank him for his constant reminder to get my samples out of the downstairs lab, and later on, his office, then eventually, my office. Last, I have to sincerely thank him for the various beers that we have drank together over the past few years, always a pleasure. Thank you very much to both Keiko Hattori and Brian Cousens for being on my defence committee and for their constructive comments. I'd also like to sincerely thank Alvin Harris and Stewart Cochrane of the Newfoundland Geological Survey. Both Alvin and Stewart catalogue and maintain the core storage facility in Buchans, Newfoundland, which made easy access and selection of the many drill holes studied in all but the winter months, which have the effect of turning back the clock 50 years to when the core barns were once hockey rinks. Sometimes, if you're lucky, you can still see the players skating in the night. Speaking of time machines, I'd like to thank shortwave infrared spectroscopy for teaching me what a time machine really is. Royal Roads Corp. also deserves special thanks for providing an extensive drill-hole and assay database and for the drill core that made up the majority of this study. I'd also like to take this opportunity to thank my professors during my graduate studies including Harold Gibson, Steve Piercey, Bruno Lefrance and Howard Poulsen, all of whom imparted knowledge of their respective subjects which provided key concepts in volcanology and stratigraphy, lithogeochemistry, and structural geology. I'd also like to thank Neil Rogers for his revision and comments on my second chapter. Special thanks to Helene de Gouffe for her kind staff support,

organizing TA-ships, reimbursements, and social events. I also have to thank my friends for the past, present, and ongoing shananagins which have severely delayed the submittal of this thesis. Trancing, 3 hour chess games, Perkins, Reed's cottages, pizza pockets, camping, and of course our reserved corner at Father and Sons will never be forgotten. Special thanks to green peppers, pineapple, and bacon; you make the world go around. I also want to thank Nike, the goddess of victory, for this big win. Last but not least, I have to thank my family for always being there for me, my fond childhood memories, their unending love, and for teaching me to work hard and have fun; principles which I try to live by every single day.

Chapter 1: Introduction

The Newfoundland Appalachians host over forty volcanogenic massive sulfide (VMS) deposits, each with greater than 200 000 tonnes of total past production and/or reserves (e.g., Swinden, 1991; Piercey, 2007). Since closure of the Buchans mining camp in 1984, exploration spending in Newfoundland has been highly variable. New discoveries (e.g., Duck Pond from 1985-1991 and Boomerang in 2004), the implementation of new government initiatives (e.g., Targeted Geoscience Initiative - 3 in 2001), and the economic downturn of late 2008 have all contributed to the variable spending (Figure 1.1). Before the economic downturn in 2008, Buchans River Ltd. obtained archived documents of Asarco (1974) which determined a resource estimate for stockwork mineralization surrounding the Lucky Strike deposit. This resource estimate included 11.9 million tonnes at an average grade of 1.83 % Zn, 0.67 % Pb, 0.38 % Cu, and 5.5 g/t Ag with traces of Au, but it was not compliant with National Instrument 43-101 (Webster and Barr, 2008). Buchans River Ltd. subsequently began an extensive drill program of 53 holes totalling 8 058 m to extend the previously known Lundberg and Engine House Zone mineralization. Buchans River Ltd. was subsequently taken over by Royal Roads Corporation who estimated the Lundberg and Engine House Zone mineralization to be > 20 Mt (Table 1.1; Webster and Barr, 2008). The extensive new drilling provided an excellent opportunity to study the stratigraphy, geochemistry, and alteration surrounding the largest in situ VMS deposit in the Buchans camp. Table 1.1 shows the grade and tonnage of all the deposits in the Buchans camp.

1.1 Regional Geology and Tectonic History

The Newfoundland Appalachians are divided into four tectonostratigraphic zones defined by rock type, faunal assemblage, and a variety of other characteristics: Humber, Dunnage, Gander, and Avalon zones (Figure 1.2; Williams, 1988; Zagorevski and Rogers, 2009). The Humber zone represents the Laurentian passive margin during the Cambrian and Ordovician, whereas Gander and Avalon represent microcontinents derived from Gondwana. The Dunnage zone reflects the opening

and closure of the early paleozoic Iapetus Ocean and consists of primitive arc and back-arc, with lesser mature arc rocks (Rogers et al., 2006; van Staal et al., 2007; Whalen et al., 1997; Zagorevski et al., 2006). It is subdivided into peri-Laurentian Notre Dame and Gondwanan Exploits subzones which are separated by the Red Indian Line; a major suture zone along which Iapetus was consumed (Figure 1.2; e.g., Williams, 1988).

To the west of the Red Indian line, the Annieopsquotch Accretionary Tract (van Staal et al., 1998) combines a collage of imbricated peri-Laurentian arc – backarc complexes that were accreted to Laurentia (Figure 1.3). From west to east it comprises Annieopsquotch Ophiolite Belt, Lloyds River Ophiolite Complex, Robert's Arm Group, Buchans Group, Red Indian Lake Group, and Crescent Lake Formation (Zagorevski et al., 2009). All of these rocks have suprasubduction zone geochemical signatures except for the Crescent Lake Formation which represents one of the only remnants of the Iapetus Ocean (within-plate alkali basalt; Zagorevski et al., 2009).

The Annieopsquotch Accretionary Tract (AAT) was formed during eastward subduction rollback, emplacement of the Dashwoods microcontinent, and closure of the Humber seaway (Waldron and van Staal, 2001; Zagorevski et al., 2009). Outboard of the newly developed composite margin, a west-dipping subduction zone was initiated leading to formation of the Annieopsquotch Ophiolite belt (485-480 Ma; Figure 1.3A; Dunning and Chorlton, 1985; Lissenberg et al., 2005). Continued west-dipping subduction zone led to formation of the Robert's Arm-Lloyd's River Arc-backarc complex on transitional crust (470 Ma). The Red Indian Lake volcanic Arc (upper Robert's Arm, parts of Crescent Lake formation, Buchans, and Red Indian Lake groups) formed at 468-465 Ma (Figure 1.3B). Simultaneously, a second west-dipping subduction zone formed underneath the composite margin in the back arc basin leading to assembly of the Annieopsquotch Accretionary Tract terranes (Zagorevski et al., 2009). At Buchans, the AAT comprise mature to rifted arc segments of a once continuous Red Indian Lake-Buchans arc (Zagorevski et al., 2009). The assembly of the AAT was terminated by closure of the main tract of Iapetus and arc-arc collision along the Red Indian Line (Zagorevski et al., 2008).

1.2 Distribution of Mineral Occurrences

The central Newfoundland portion of the AAT is in part represented by the Buchans Group which hosts the Buchans mining camp (Thurlow and Swanson, 1981). The Buchans mining camp produced a total of 16.2 Mt of ore at an average grade of 14.5% zinc, 7.6% lead, 1.3% copper, 126 g/t Ag, and 1.37 g/t Au rivalling many other VMS districts (Jambor, 1987). Deposits in the Buchans Camp are of three types: in situ, transported, and stockwork (e.g., Thurlow and Swanson, 1981; Thurlow and Swanson, 1987; Jambor, 1987). The deposits occur along two roughly linear 'channels' which extend outwards from the Lucky Strike in situ VMS deposit (Figure 1.4). The Lucky Strike deposit was a 5.5 Mt Zn-Pb-Cu massive sulfide deposit with important precious metal grades (Table 1.2). The NW-plunging Maclean trend was the largest producer of the two 'channels' and forms a ~3 km long zone of polymictic and transported ore breccias which includes the Two-level, North-orebody, Rothermere 1 and 2, Maclean, and Maclean Extension deposits northwest of Lucky Strike (e.g., Binney, 1987). The NE-trending 'channel' contains a more complicated assemblage of transported ore breccias and in situ VMS deposits. The in situ deposits include the large Oriental #1 and smaller Old Buchans East and West deposits; the transported ores include the Oriental # 2 and Old Buchans Conglomerate (e.g., Thurlow and Swanson, 1981). The Sandfill and Middle Branch prospects are located northeast of the Oriental orebodies.

The only significant stockwork mineralization in the Buchans Mining camp occurs in the Lundberg and Engine House zones adjacent to the Lucky Strike deposit (Figures 1.5 and 1.6). The Lundberg Zone is a sub-horizontal polymetallic stockwork which plunges to the northwest (Webster and Barr, 2008). It has an estimated resource of 20 700 000 tonnes at an average grade of 1.68 % Zn, 0.72% Pb, 0.38 % Cu, 5.92g/t Ag, and 0.07g/t Au (Webster and Barr, 2008). The Engine House stockwork is much smaller forming a resource of 1 120 000 tonnes at an average grade of 2.04% Zn, 0.85% Pb, 0.82% Cu, 9.79g/t Ag, and 0.12g/t Au and is modelled as a separate mineralized body (Webster and Barr, 2008). The proportion of Zn, Pb, and Cu in these stockwork zones is distinct from the massive and transported orebodies found throughout the camp (Figure 1.7).

1.3 Objectives and Presentation

The purpose of this study was to establish a predictable stratigraphy and to characterize the alteration and mineralization within the Lundberg and Engine House Zone polymetallic stockworks as guides to camp-scale exploration. The thesis is organized into five chapters. Chapter 1 introduces the thesis and provides the regional tectonic setting and mining history in Buchans, central Newfoundland. Chapter 2 describes the stratigraphy of the Lundberg and Engine House zones that was determined through logging and sampling of 28 vertical drill holes (5676 m of drill core) obtained from Royal Roads Corporation and archived core from BP Resources. The logging was accomplished during 25 days in November 2008. These drill holes have been previously examined by exploration companies who assigned the rocks to a number of Buchans formations. This study identified a number of additional units in the Lundberg Zone that require modification of the presently understood Buchans River Formation.

Chapter 3 uses lithogeochemistry to refine the stratigraphy of mineralized and barren felsic units. Mineralized felsic units were separated from barren felsic units on the basis of trace element characteristics that provide a useful tool for identifying favourable stratigraphy elsewhere in the camp.

Chapter 4 discusses the alteration in the Lundberg and Engine House zones. Four main alteration facies were identified using petrography, normative mineralogy and shortwave infrared spectroscopy. Application of shortwave infrared spectroscopy in the Lundberg and Engine House zones stratigraphy helped to identify previously unrecognized alteration zonation in the host stratigraphy. Mineralization in the Lundberg Zone was found to contain a number of vein types, including veins with bladed barite and calcite, which may be an indication of a transitional volcanogenic massive sulfide to epithermal environment for the Buchans ore deposits.

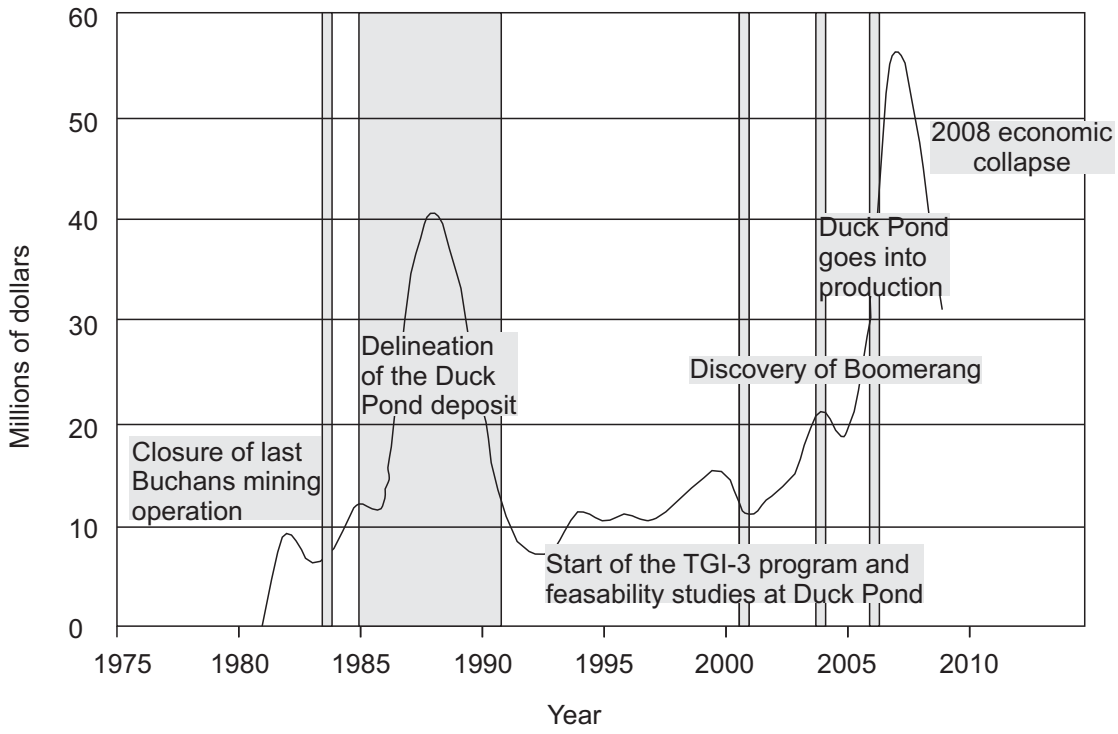

Figure 1.1: Exploration spending in Newfoundland and Labrador from 1981 to 2010 (Newfoundland Department of Natural Resources, 2010).

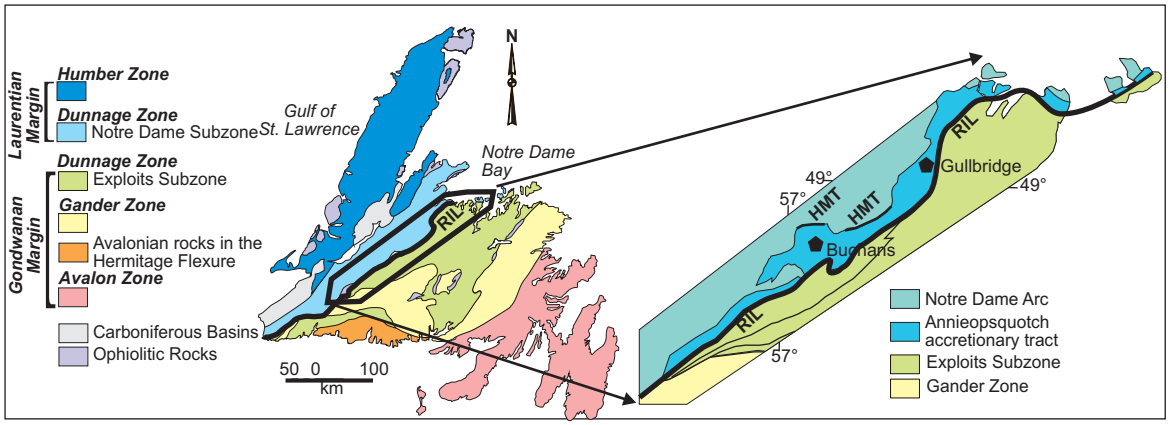

Figure 1.2: Position of the Annieopsquotch Accretionary Tract in central Newfoundland, west of the Red Indian Line (RIL), a major suture zone separating rocks of peri-Laurentian (west) and peri-Gondwanan (east) affinity (Zagorevski and Rogers, 2008).

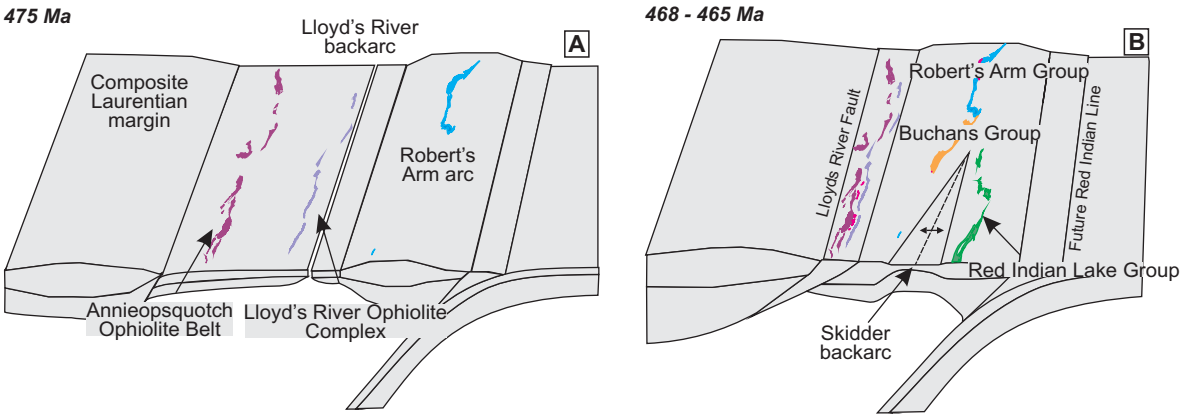

Figure 1.3: Tectonic setting and development of the Annieopsquotch Accretionary Tract (Zagorevski et al., 2008). A. Formation of the Roberts Arm arc associated with west-dipping subduction outboard of the composite Laurentian margin. B. Accretion of the Roberts Arm arc and formation of the Buchans Group within the Red Indian Lake/Buchans arc, followed by local extension forming the Skidder basalt and continued closure of the Iapetus Ocean.

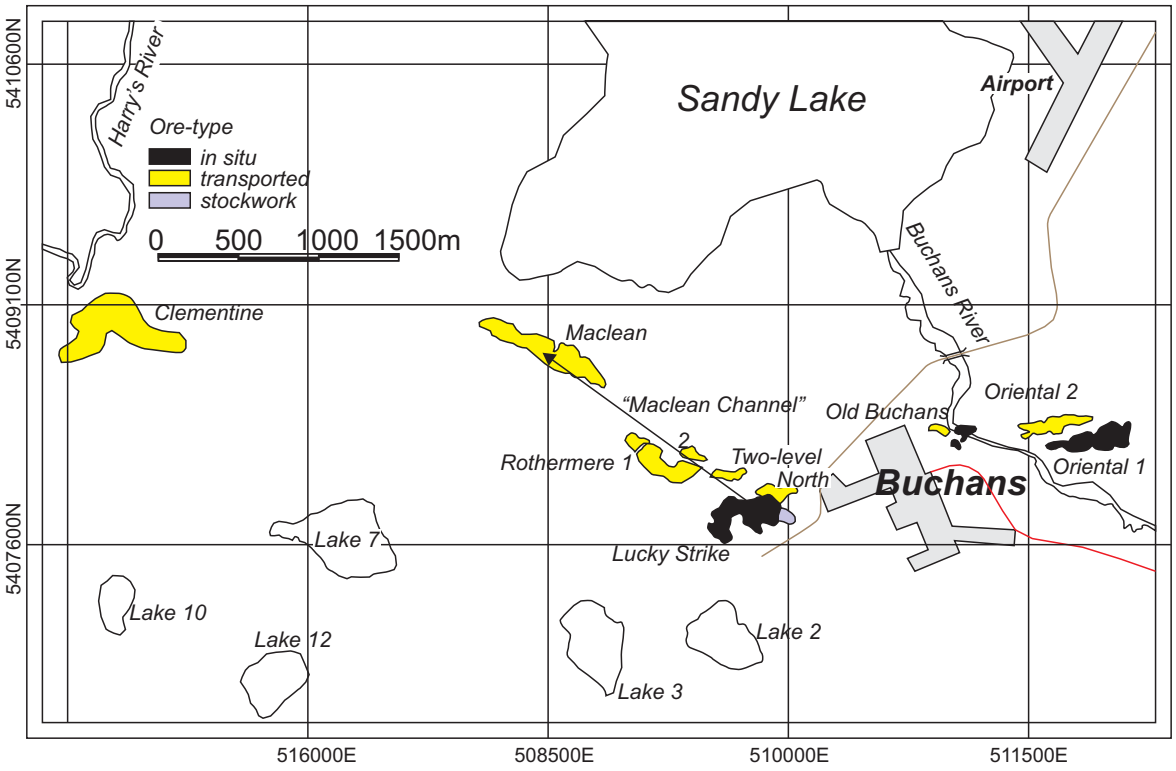

Figure 1.4: Distribution of mineral occurrences in the Buchans Mining Camp. The UTM datum is NAD 1927 (Calhoun and Hutchinson, 1981).

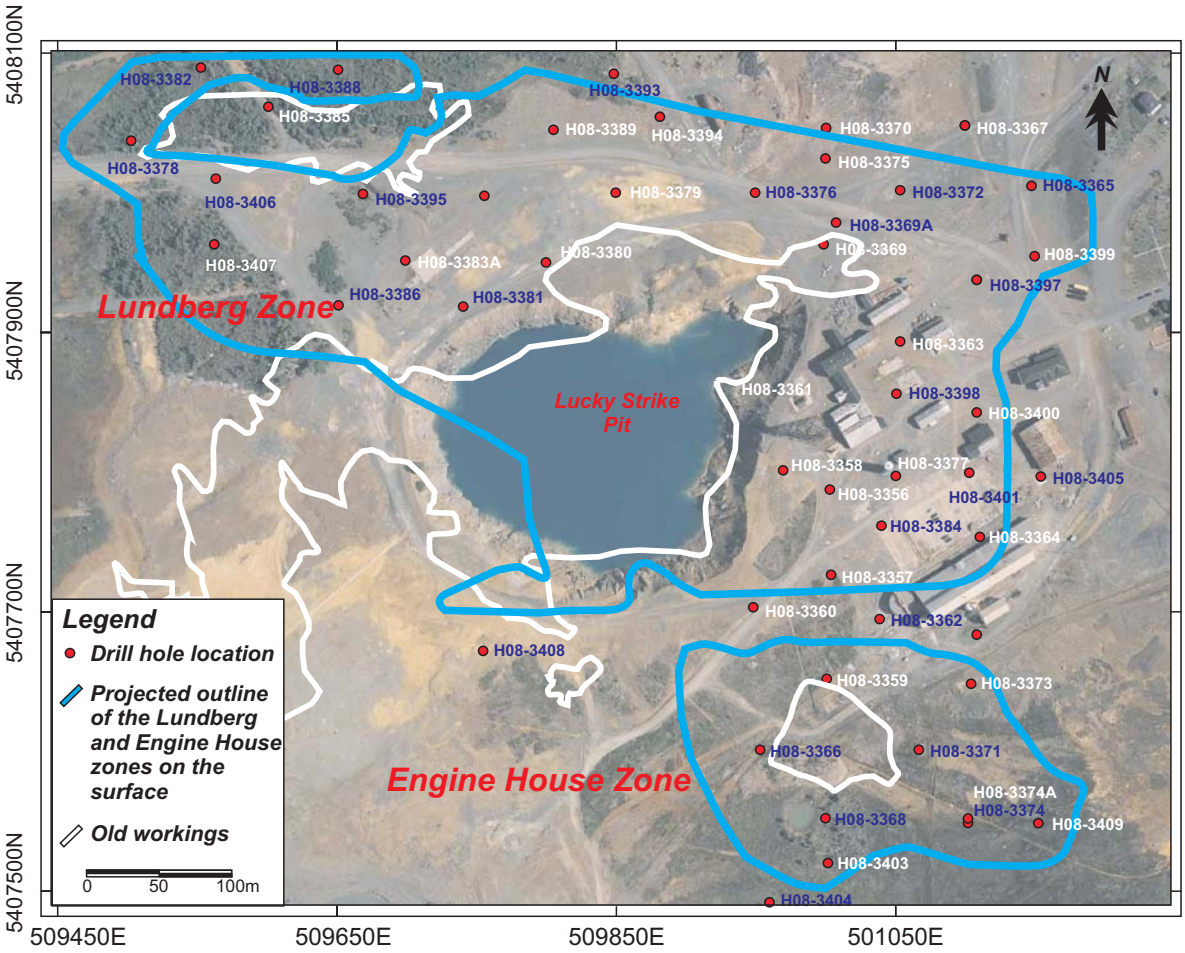

Figure 1.5: Aerial photograph of the Lundberg and Engine House zones projected to surface showing the Lucky Strike pit and the distribution of drilling (2008) by Royal Roads Corp. Drill holes labelled navy blue were logged in this study. The UTM datum is NAD 1983 (Modified from Webster and Barr, 2008).

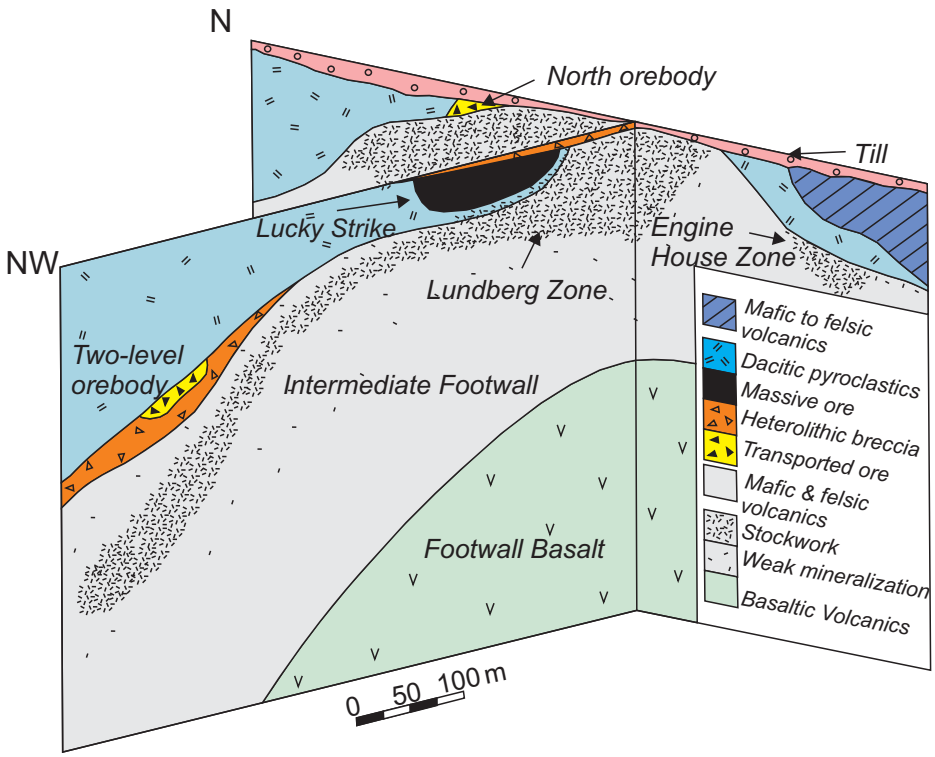

Figure 1.6: Cross sections illustrating the geology and mineralization of the Lucky Strike area as compiled by Kowalik et al. (1981). The Intermediate Footwall is defined as a very broad zone of intermediate pyroclastic rocks that is strongly altered and is locally mineralized. The 'Intermediate Footwall' as defined by Kowalik et al. (1981), however, is mostly basaltic andesite (Chapter 3) with local andesite.

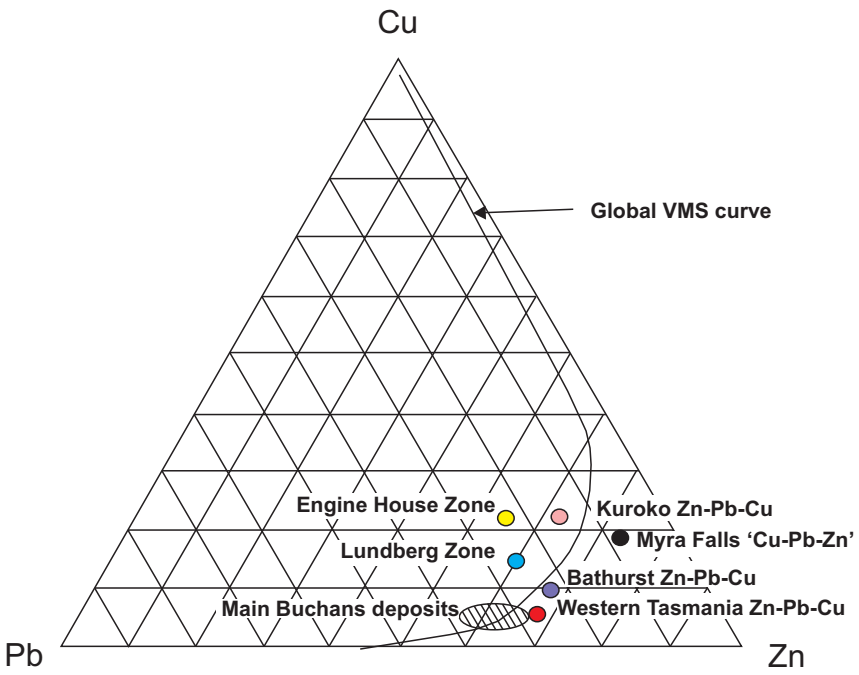

Figure 1.7: Zn-Pb-Cu ternary diagram illustrating the higher Cu/Pb ratio in the Buchans stockwork zones compared with in situ and transported orebodies of the Buchans Camp and VMS deposits of other districts. Data from Thurlow and Swanson (1987) and Large et al. (1992).

Table 1.1: Grade and Tonnage of Buchans VMS deposits (Thurlow and Swanson 1987; Webster and Barr, 2008)

Deposit	Type of ore	Tonnage*	Zn %	Pb %	Cu %	Ag* (g/t)	Au* (g/t)
Lundberg Zone	**stockwork**	**20 700 000**	**1.68**	**0.72**	**0.38**	**5.92**	**0.07**
Lucky Strike (main)	in situ	5 555 485	18.42	8.61	1.63	102.008	1.5239
Rothermere 1 & 2	transported	3 508 226	12.74	7.72	1.16	121.912	1.0263
Maclean	transported	3 268 556	13.5	7.46	1.13	119.424	0.8708
Oriental 1	in situ	2 891 924	15.73	8.44	1.7	122.845	1.8971
Engine House Zone	**stockwork**	**1 120 000**	**2.04**	**0.85**	**0.82**	**9.79**	**0.12**
Oriental 2	transported	928 863	9.41	6.2	0.76	191.265	1.4306
North orebody	transported	620 510	8.2	4.54	0.46	111.338	1.5239
Two-level orebody	transported	328 596	8.02	4.56	0.5	113.204	1.4617
Old Buchans East	in situ	133 353	14.27	7.57	1.65	141.505	2.0837
Old Buchans Conglomerate	transported	72 763	9.47	5.88	0.76	115.07	1.3995
Old Buchans West	in situ	19 907	16.8	10.4	1.7	93.3	1.3995

*Lundberg and Engine House Zone values are reported in metric tonnes. All other values are short tons.

Chapter 2: Volcanology and Stratigraphy of the Lundberg and Engine House Volcanogenic Massive Sulfide Zones, Buchans, Newfoundland

2.1 Abstract

Thrust repetition is characteristic of Buchans Group stratigraphy and hinders direct correlations of new drilling with previously proposed stratigraphy which groups both mafic and felsic volcanic rocks into single formations. Grouping of mafic and felsic volcanic rock into single formations is highly undesirable under the North American Stratigraphic Code; and for mineral exploration. This study was aimed at re-evaluating the nomenclature and correlations previously proposed within the Lundberg and Engine House VMS prospects taking into account a number of newly recognized mafic and felsic units in the deposit area. Twenty-eight drill holes were logged in detail resulting in the identification of seven units in the Lundberg Zone: basaltic pillow breccia, lower basaltic andesite, lower sedimentary sequence, upper basaltic andesite, rhyodacite, upper sedimentary sequence, and rhyolite. The pillow breccia consists of aphyric pillow cores and highly amygdaloidal chilled pillow margins and is locally overlain by finely bedded siltstone/mudstone. The pillow breccia is in structural contact with the overlying lower basaltic andesite. This unit consists of mafic breccia and massive and pillowed basalt with bedded chert, in turn structurally overlain by upper basaltic andesite above a heavily altered and weakly sheared contact. The upper basaltic andesite is moderately feldspar-phyric, massive to brecciated, with hyaloclastite and localized clinopyroxene-rich intervals. A conformable sedimentary lens within the upper basaltic andesite consists of mass flow breccias and siltstones collectively termed the lower sedimentary sequence. Conformably overlying the upper basaltic andesite is either the upper sedimentary sequence or rhyodacite. The upper sedimentary sequence consists of polymictic breccia overlain by siltstone/sandstone breccia with rhyodacitic tuff and polymictic breccia. The rhyodacite consists of massive and autobrecciated facies and is locally overlain by a barite-rich bed. At the top of the sequence is a thick succession of diabase sills that intrude rhyolite tuff and coherent and brecciated

QFP rhyolite. A similar sequence is observed within the Engine House Zone, however, a quartz-phyric rhyodacite occurs at the structural position of the uppermost QFP rhyolite and tuff observed in the Lundberg Zone. This new logging places the pillow breccia and lower basaltic andesite in the Lundberg Hill Formation, the upper basaltic andesite in the Ski Hill Formation, the upper sedimentary sequence and rhyodacite in the Buchans River Formation, and the rhyolite unit in a newly proposed 'Lucky Strike hanging-wall succession'. The Lucky Strike hanging-wall succession structurally overlies the Lucky Strike deposit. The entire sequence is continuous across the 800 x 500 m study area and is an excellent guide for mineral exploration in the Buchans area. In addition, identification of a conformable sedimentary lens with massive sulfide clasts within the upper basaltic andesite, opens up exploration in the entire Ski Hill Formation.

2.2 Introduction

This contribution examines the stratigraphic context of the stockwork (Lundberg Zone) peripheral to the largest VMS deposit in the Buchans mining camp (Lucky Strike, Table 1.1: Thurlow and Swanson, 1981, 1987; Thurlow et al., 1992). Extensive drilling of the Lundberg Zone in 2008 by Royal Roads Corp. has allowed the detailed study of previously undrilled areas surrounding the Lucky Strike deposit. The Lundberg Zone is herein shown to have laterally continuous stratigraphy that, in general, conforms to that originally proposed by Thurlow and Swanson (1987). The structural complications previously proposed by Barbour et al. (1989) are not seen. Furthermore, new features observed in the lower Lundberg Zone warrant deeper exploration beneath the level traditionally considered to be prospective.

The complex structure and stratigraphy of the area had not been appreciated prior to the recognition of thrust faults (e.g., Thurlow and Swanson, 1981) and antiformal thrust stacking (e.g., Calon and Green, 1987), which has also been imaged using seismic reflection (e.g., Thurlow, 1992). The recognition of thrust faults led to a thrust repetition model of the volcanic arc stratigraphy (e.g., Thurlow and Swanson, 1987). Following the 1984 termination of the base metal mining operations

in Buchans, advances in lithogeochemistry have enabled testing of the stratigraphic correlations (Jenner, 2000). The geochemical database collected by Jenner (2000) unveiled several issues in the Buchans Group stratigraphy not consistent with previous interpretation; however, was not detailed enough to fingerprint the various formations. This study incorporates petrographic (herein) and geochemical data (Chapter 3) to better constrain the relationships between the formations and thereby aid exploration.

2.3 Buchans Group

The Buchans Group (462-465 Ma; Compston, 2000; Zagorevski et al., 2007b): forms part of the Annieopsquotch Accretionary Tract (AAT: van Staal et al., 1998), a collage of accreted peri-Laurentian continental arcs and backarcs formed during the Early to Middle Ordovician (Figures 2.1 and 2.2). The AAT is bound to the west by the Lloyds River Fault and Hungry Mountain thrust (Thurlow, 1981; van Staal et al., 1998; Lissenberg et al., 2005) to the Notre Dame arc, and to the east by the Red Indian Line, a major suture zone separating rocks of peri-Laurentian and peri-Gondwanan affinity (van Staal et al., 1998). The constituent terranes of the AAT were accreted and imbricated along west-dipping, oblique-reverse faults that trend NE-SW in the Buchans area (Figure 2.1; e.g., Thurlow et al., 1992; Lissenberg et al., 2005; Zagorevski et al., 2007a).

The Buchans Group comprises a fault bounded arc terrane in the AAT of central Newfoundland and is structurally overlain by the Harry's River Ophiolite Complex (Zagorevski et al., 2010), and Notre Dame Arc above the Hungry Mountain Thrust (Zagorevski et al., 2008). To the south, it structurally overlies the Red Indian Lake Group (Zagorevski et al., 2006) along the Tilley's Pond/Powerline fault. To the east it is structurally overlain by the Mary March Brook Formation along the Airport thrust (Zagorevski et al., 2010; Figure 2.1). The Buchans Group and adjacent units are typically regionally metamorphosed to prehnite-pumpellyite and greenschist facies, although they locally reach amphibolite facies metamorphism in proximity to the Silurian Topsails Intrusive Suite and along some major thrust faults (e.g., Hungry Mountain Thrust: Thurlow, 1981).

The Buchans Group is subdivided into the Lundberg Hill, Ski Hill, Buchans River, and Sandy Lake formations (Figure 2.3) which group felsic and mafic rocks together (Table 2.1: Thurlow and Swanson, 1987). This grouping of 'local' mafic volcanic rocks within regional felsic volcanic formations creates ambiguity in the current study area (i.e., Lundberg Hill Formation) and makes correlations adjacent to the Lucky Strike deposit difficult. The majority of the massive sulfide deposits in the group occur within the Buchans River Formation, which is mainly exposed in a structural window of an antiformal thrust stack with north-dipping ore-bearing duplexes (Figures 2.3 and 2.4: Calon and Green, 1987). The least structurally disrupted ore-bearing duplex (e.g., Lucky Strike duplex; Calon and Green, 1987) hosts the majority of the previously mined deposits in the Buchans camp, including Lucky Strike, Old Buchans, Rothermere, and Maclean. The Lucky Strike duplex is folded over the culmination of the thrust stack in the Lucky Strike area where it locally shows south-dipping attitudes (e.g., Figures 2.3 and 2.4: Thurlow, 1992). The Oriental orebodies, although lying in a separate duplex, are thought to represent thrust-repeated Buchans River Formation and, as such, have been interpreted to occur on the same horizon as the other deposits (Calon and Green, 1987). The complex structural history of the region obscures many of the primary volcanic and sedimentary features and stratigraphic relationships; however, several synvolcanic faults have been identified and an extensional channel/caldera model has been suggested for the Buchans Group (e.g., Henley and Thornley, 1981; Kirkham and Thurlow, 1987).

2.4 Lundberg and Engine House zones

The area surrounding the historic Lucky Strike massive sulfide deposit is divided into the northwest dipping Lundberg Zone and the south dipping Engine House Zone (Figures 2.5-2.7). These sequences, previously referred to as the *intermediate footwall,* locally comprise "a complex, poorly understood stratigraphic package which has been altered extensively and modified significantly by faults" (Thurlow and Swanson, 1987). Identifying the original rock types is difficult because of the pervasive alteration. However, the altered mafic volcanic rocks have been grouped

with the Ski Hill Formation and the felsic volcanic rocks with the Buchans River Formation (Thurlow and Swanson, 1987). The Lundberg Zone includes rocks belonging to both formations, with stockwork-style mineralization occurring within the Ski Hill Formation and to a lesser extent within the Buchans River Formation, and "exhalative" mineralization occurring exclusively within the Buchans River Formation (Figures 2.5-2.7). The Lundberg Zone polymetallic stockwork was previously named the 'Lucky Strike Stockwork' and was thought to represent the stockwork to the Lucky Strike massive sulfide deposit (Jambor, 1987). However, it is never observed in connection with the Lucky Strike deposit, being separated by a several meter thick unit of strongly foliated green felsic tuff that forms the immediate structural (and presumed stratigraphic) footwall to the deposit. To the east of Lucky Strike, the stockwork is in abrupt contact with barren rock interpreted to be a flat lying fault (Jambor, 1987). Nevertheless, massive sulfide ore occurs locally in the Lundberg Zone and is considered to belong to part of the horizon that hosts the majority of deposits in the camp.

The Engine House Zone contains a polymetallic stockwork that is similar to but more isolated than the Lundberg Zone, lacks exhalative mineralization and is separated from the Lundberg Zone by the Airport Thrust (Thurlow et al., 1992).

2.5 Lundberg Zone Lithologies

The stratigraphy of the Lundberg Zone, as herein defined (Figures 2.5 and 2.6), consists of seven NW-dipping units that range from the basaltic pillows at the stratigraphic base of the zone, the 'lower' and 'upper' basaltic andesite, sedimentary sequences, rhyodacite to rhyolite and rhyolitic tuff.

Basaltic pillow breccia

The pillow breccia unit, which forms the stratigraphic base of the Lundberg Zone, consists of scoreacous basaltic pillow fragments that display asymmetrically chilled margins characteristic of

fragmented pillow margins, flows, or bombs (Figure 2.8A). Contacts with the overlying basaltic andesite are sheared and rarely marked by abundant diabase sills.

Basaltic andesite with interlayered chert, mafic breccia, and turbidite

Lower Member

The lower basaltic andesite member overlies the basaltic pillow breccia in the Lundberg Zone and is chiefly composed of pillow basalt with mafic breccia, turbidites and chert (Figure 2.8). Contacts between these lithologies are marked by sharp, often scoured basal contacts where mafic breccia or turbidites overlie chert and planar contacts where chert overlies mafic breccia or turbidites.

The chert unit is up to 34.7 m thick and ranges from grey, beige, olive green, pale yellow, orange, hematitic red, and dark purple-black (Figure 2.8B). The different coloured chert units are characteristically laminated to thinly bedded, with beds up to 3 cm thick. A gradational colour change from lighter grey and green with patchy hematitic reds and oranges, to dark purple-black with hematitic laminae occurs within the thicker chert unit. Contacts between chert beds are typically sharp and planar, but rare contacts are defined by ball and pillow structures suggesting siliciclastic sedimentation and later silicification (Figure 2.8B).

The pillow basalts overlie chert across a contact intruded by diabase. Pillow selvages are on the order of 3-4 cm thick and form predominantly black, arcuate bands and triple junctions, although various shades of red and purple are observed. Larger pillows up to 0.7 m thick are typically the least altered and exhibit a greenish grey colour, whereas smaller pillows, on the order of 0.3 m thick are typically altered. The observed dimensions could reflect the diameter of small pillows or the cross section of much larger pillow tubes. Within ‘pillows’, an increase in alteration and carbonate-filled amygdales is observed towards selvages.

The mafic breccia is an altered, medium grained, feldspathic unit containing subrounded scoriaceous basalt clasts and common chloritic mudstone interbeds <10 cm thick (Figure 2.8C). Clast abundance ranges from <5 to 30 %, with clasts typically averaging 3-4 cm in diameter but

locally reaching 20 cm in diameter. The clasts have sharp, irregular contacts and consist of carbonate infilled scoriaceous basalt with 1-2 mm diameter amygdales (Figure 2.8C). Where in contact with chert beds, the mafic breccia locally forms meter scale beds which have scoured basal contacts, reversely graded bases (diminishing concentration of basalt clasts towards lower contact) and normally graded tops. Rare rounded chert clasts occur near the top of the breccia.

The mafic-derived thickly-bedded turbidites consist of stacked greenish grey T_{ad}, T_{bd}, T_{abd}, or T_{acd} divisions of the Bouma sequence (Bouma, 1962). Individual stacks average approximately 1 m thick, but reach up to 2.1 m and are summarized in Table 2.2. These turbidites display typical divisions of the Bouma sequence; however, Tc layers (thin beds) may represent Ta layers because of the lack of observed cross-stratification.

Upper Member

The upper basaltic andesite overlies the lower member in the Lundberg Zone but is absent at the same stratigraphic position in the Engine House Zone (e.g., lower half of Figure 2.7). It consists primarily of massive to feldspar porphyritic and amygdaloidal basaltic andesite with common hyaloclastite and flow breccia with rare clinopyroxene-rich intervals (Figure 2.9A). At its stratigraphic top, the basaltic andesite is slightly more andesitic. Contacts between the upper and lower basaltic andesite members are heavily altered and marked by a significant decrease in tuffaceous rocks.

The massive basaltic andesite is characterized by beige to black colour with <5 to 30% white, pale yellow, or green to black, unaltered to altered feldspar or clinopyroxene phenocrysts and/or glomerocrysts (average <2 mm, but locally reach up to 3 mm). The matrix has a predominantly trachytic fabric of variably altered feldspar microlites with a tabular to less common skeletal crystal morphology. The groundmass is typically altered to chlorite or quartz-sericite assemblages, with quartz-sericite often completely replacing the groundmass and creating a pseudo-felsic appearance.

In amygdale-rich intervals, amygdales typically have a rounded morphology, average 1-2 mm in diameter, and consist of quartz-carbonate, chlorite, pyrite, and hematite (Figure 2.9B). In

such intervals, amygdale concentration typically averages approximately 15%, although highly vesicular to scoriaceous texture is common. Amygdales also commonly coalesce, forming irregular masses up to 2 cm, or entire zones of thin, elongated 'pipe vesicles' up to 2 cm. Spherical amygdales commonly display diffusely radiating quartz crystals, less common chlorite fans, and chlorite-rich cores with or without euhedral calcite or hematite crystals.

Hyaloclastite is a common feature, forming intervals from 30 cm thick to >10 m thick (Figure 2.9A). Basaltic-andesite fragments are exclusively black in colour and form arcuate to angular clasts averaging 1 cm but reaching 3 cm. The basaltic-andesite fragments are typically amygdaloidal, consisting mostly of quartz and carbonate. Mafic fragments have curviplanar to blocky margins with internal perlitic fracturing. Perlitic fracturing is defined by 60-100 μm wide concentrations of quartz and plagioclase crystals which cut plagioclase microlites displaying trachytic texture in massive and brecciated basaltic andesite. The hyaloclastite is commonly brecciated in situ, with angular clasts of various sizes ranging from <1cm up to decimetres and forming jig-saw-fit pattern.

Andesitic horizons form at the top of the sequence and consist of beige volcanic rocks with emerald green muscovite-altered feldspar phenocrysts (Figure 2.9C). The andesite is discontinuous throughout the stratigraphy and is often confused with basaltic andesite (see Chapter 3 for geochemical characterization).

Lower sedimentary sequence

The lower sedimentary sequence forms a conformable lens within the upper member of basaltic andesite with a measured thickness of at least 110 m at its thickest (Figure 2.7 and Figure 2.10). It comprises basal altered +/- graded rhyodacite-dominated breccia conformably overlain by a thick succession of siltstone with interstratified rhyodacite breccia and a massive rhyodacite-dominated breccia (Table 2.3). Although this sequence is lithologically similar to the upper

sedimentary sequence (Table 2.4), it clearly occupies a different stratigraphic position (e.g., Figure 2.7).

The basal altered rhyodacite-dominated breccia is matrix supported (70%) and contains three distinct clast populations. Rhyolitic to rhyodacitic clasts are most abundant (90%) and are typically cobble size (<20 cm). They are feldspar-phyric (5%) to aphyric with beige to brown or pink colours and subrounded clast boundaries (Figure 2.10A). The most common internal structure is mm-scale light beige to brown flow banding (Figure 2.10A). Basaltic clasts (10%) are medium to dark grey subrounded angular cobbles (~3-4 cm) to large pebbles (1 cm). The clasts are feldspar porphyritic (5-10%) to aphyric. Sulfide clasts/blebs are the least abundant (<1%), consisting of massive pyrite or galena, 1 cm or less in size. The matrix is pervasively altered, obliterating most of the primary textures. However, <1 cm angular lithic fragments (50%), similar in composition and proportions to the larger clast population are recognized. Black, irregular blocks, and rare curviplanar chloritic fragments which may represent hydrated and altered glass make up 10% of the matrix. The remainder is entirely silicified; however, it is likely composed of silt or sand-size detritus. Beds are typically massive, although clear reverse grading is observed over some beds that are up to 7.5 m thick.

Overlying the basal rhyodacite-dominated breccia is a thick succession, up to 25.3 m thick, of siltstone with discrete interbeds of rhyodacitic breccia or dispersed rhyodacitic clast horizons. Rhyodacitic breccia (15%) forms rare interbeds about 1 m thick in a massive grey-green siltstone matrix (Figure 2.10B). These beds are clast supported (>80%) and are dominated by 3 cm white aphyric rhyodacite clasts with rare (<1 cm) sphalerite-galena clasts in a black chloritic (+/- pyrite) siltstone matrix. Massive beds are most common, but normal and reversely graded beds are present. Lower contacts between these layers are typically sharp and scoured, and in rare cases the massive beds are underlain by plane-bedded siltstone to fine sandstone (Figure 2.10B). Upper contacts are typically sharp and irregular but also locally grade into diffuse clast-bearing horizons (10% clasts) above the main clast-supported bed.

The uppermost unit of the lower sedimentary sequence is a massive rhyodacite-dominated polymictic breccia (>85%) with interbedded, normally graded to planar-laminated sandstone to siltstone (<10%) and resedimented basaltic hyaloclastite (<5%: Figure 2.10C).

The massive rhyodacitic polymictic breccia consists of approximately 65% altered matrix, and 35% clasts. Clasts comprise four major types. The dominant clast population is flow banded rhyodacite (75%) defined by irregular light greyish white and dark grey bands. These clasts are subrounded and typically range from pebble to cobble (2-10 cm) size but reach up to boulder size (50 cm). Rare quartz-filled and s-shaped pipe amygdales are observed in the clasts. Basalt clasts (15%) form black, altered, angular, aphanitic to quartz-rich scoriaceous pebbles and cobbles (1-4 cm). Sandstone and siltstone clasts (5-10%) form fine, well sorted, subrounded pebbles (1 cm) with light altered margins. The least abundant are cherty rhyodacitic clasts (1%) that form angular to subangular beige to pink cobbles (2 cm). The matrix consists of coarse silt to sand-sized detritus.

The interbedded (<10%) sandstone and siltstone form the typical T_{ab} division of the Bouma sequence and consist of normally graded medium to fine sandstone averaging 10 cm in thickness grading upwards to a planar laminated horizon, averaging 5 cm in thickness with maximum thicknesses up to 20 cm (Figure 2.10C). Rare cross stratification is observed above planar laminated horizons forming the T_c division of the Bouma sequence; however, these are no more than 2 cm thick, and are rarely observed. T_{ab} division beds grade from thick (up to 25 cm) and abundant directly overlying the siltstone-dominated lower unit, to thinly-bedded (10-15 cm) and rare in the stratigraphically highest sections, marking a distinct change in depositional conditions. Similarly, the proportion of fine sandstone and siltstone clasts dramatically decreases away from the siltstone contact. Among the sandstone and siltstone resedimented mafic hyaloclastite forms rare 1-3m thick units characterized by basalt clasts with subangular clast morphologies and rare curviplanar margins (Figure 2.10C). Rare rhyodacitic clasts occur within these horizons.

Rhyodacite

The rhyodacite unit conformably overlies the upper basaltic andesite member in the Lundberg Zone and structurally overlies the pillow breccia in the Engine House Zone. The rhyodacite is weakly porphyritic and characterized by brecciation and intense hydrothermal alteration. Contacts between these two units are often obscured by a gradational colour change from light grey to dark grey/black due to alteration of the rhyodacite and underlying basaltic andesite, making separation of the units difficult. As well, the entire unit is locally sheared and altered in discrete zones up to 33 m thick. Many primary textures within the rhyodacite in both zones have been obliterated; however, careful study of small textural differences coupled with discrete alteration assemblages allow the separation of the rhyodacite from the upper basaltic andesite.

The rhyodacite typically comprises light beige to grey massive flows and breccia and is 0 to 30 m thick. It is commonly cherty, flow banded, and contains 5-15% variably altered feldspar (1-2 mm) and quartz (avg. 0.25-0.5mm, up to 1mm) phenocrysts. Quartz displays micropoikylitic, embayment and resorption textures. Locally, the rhyodacite grades vertically into rhyodacitic sandstone/wacke and siltstone.

Two types of intimately related breccia are observed within the rhyodacite which include autobreccia and jig-saw fit breccia. The autobreccia is characterized by blocky and angular rhyodacite clasts, 5-10 cm in diameter, occurring throughout the unit. In situ brecciation is characterized by jig-saw-fit texture of clasts averaging 4 cm but reaching up to 40 cm (Figure 2.11A). The rhyodacite is overlain by a discontinuous 0.1-3.9 m thick barite bed and/or volcano-sedimentary sequence (Figure 2.11B).

Upper sedimentary sequence

The upper sedimentary sequence consists of altered to unaltered matrix supported rhyodacite-dominated breccia overlain by siltstone intercalated with rhyodacite-dominated breccia or sandstone to siltstone breccia with rare rhyodacite clasts and largely unaltered rhyodacitic polymictic

breccia (Table 2.4). Although similar to the lower sedimentary sequence (Table 2.3), these units are immediately overlain by intensely altered rhyodacite tuff, and clast supported rhyodacite polymictic breccia, distinguishing them lithologically and stratigraphically. The upper sedimentary sequence overlies the basalt or rhyodacite with sharp and irregular contacts.

The basal rhyodacite-dominated breccia forms 2.1-14 m thick beds above a sharp and irregular contact with mafic breccia and consists of 70% silicified coarse silt to sand matrix and 30% clasts (Figure 2.11C). Four clast types were identified including: rhyodacite, basalt, sedimentary, and massive sulfide. 40-80% of the clast population comprises pink, beige, grey, and white angular to subrounded rhyodacite clasts with local flow banding. 20-30% of the clast population is black aphyric basalt or locally altered dark grey to beige carbonate infilled amygdaloidal basalt (<10%). Fine sandstone to dark grey siltstone comprise <10% and massive sulfide clasts <1%. The clast-size distribution is bimodal, consisting of 2-3 cm and 5-10 cm angular to subrounded lithic fragments, although the larger clast population is commonly absent.

Overlying the altered rhyodacite-dominated breccias across a sharp contact are siltstone and sandstone beds with variable felsic volcanic contributions or black mudstone. The thicknesses of these beds are also variable, forming 2-12 m successions of in situ brecciated sandstone and siltstone, black mudstone, or both (Figure 2.12A). The in situ breccia is composed of interlocking clasts of various grain sizes (medium sandstone to siltstone) with irregular to subangular clast margins. These subangular, typically fine sandstone to siltstone clasts, average 2-3 cm in size and locally display weak reverse grading (e.g., over 2 m) with the largest clast population ranging from 8 to 16 cm in a matrix of smaller clasts. Rare white rhyodacite (1-5%) and black aphanitic basalt (<1%) clasts in the sandstone breccia matrix are 4 cm or less in size. A gradation at the contact is observed in drill hole 3344 (westernmost hole) in which the proportion of rhyodacite clasts increases up stratigraphy forming a breccia composed of equal amounts of white rhyodacite and fine sandstone to siltstone clasts with a medium sandstone matrix. Black altered mudstone +/- fine sandstone is locally interstratified with the sandstone breccia forming beds up to 3.5 m thick.

The intensely altered rhyodacite tuff occurs only in the upper sedimentary sequence and overlies the sandstone to siltstone breccia across a sharp contact. It consists of foliated sericitized feldspar phenocrysts (>50%), rounded quartz phenocrysts (20%), lithic fragments, and abundant disseminated pyrite (Figure 2.12B). The lithic fragment assemblage is similar to the underlying sandstone/siltstone breccia, although many more clasts are chloritized, and the average size of clasts is smaller (< 1 cm). The matrix is composed of fine hydrothermally altered quartz or clay minerals and probably represents a volcanic ash component.

The rhyodacite polymictic breccia is the stratigraphically highest unit of the upper sedimentary sequence (Figure 2.12C). The upper contact of this unit is sharp and typically sheared, marked by rare barite-bearing massive sulfide and sulfide-rich clast zones up to 70 cm in thickness. The lower contact is sharp and irregular. The breccia beds are massive, clast-supported, normal or reversely graded, and typically consist of a single 5 m thick bed or two stacked beds. The breccia is characterized by >70% clasts in grey, pyritic siltstone to coarse sandstone matrix. Clasts typically show a bimodal size distribution with one population averaging <1 cm (pebble-sized) and the other from cobble to boulder-size (>5 cm up to 60 cm). Five distinct populations of clasts are recognized. Rhyolitic to rhyodacitic clasts (70%) are angular to subrounded, feldspar-phyric (<5 to 30%) to aphyric and cherty, and vary from red, beige, to grey in colour. Feldspar phenocrysts in the clasts most commonly have unaltered blocky crystal morphologies, although altered and glomeroporphyritic texture is present. Flow banding is rare in rhyolite clasts and is defined by alternating groundmass colour, as well as aligninment of amydgules. Basalt clasts (20%) are black in colour, commonly altered, sparsely plagioclase phyric, and contain 5-10% quartz, carbonate, and pyrite-filled amygdales. The groundmass consists of tabular plagioclase microlites and quartz amygdales but lacks trachytic texture typical of the basaltic andesite unit. 10-15% of the clasts consist of claystone and fine-grained sandstone. The claystone clasts are typically subrounded and consist of quartz and plagioclase grains ranging from <3 um up to 8 um with rare sulfide grains of pyrite with blebby sphalerite inclusions up to 24 um. Rare biotite-granodiorite clasts consist of

interlocking, 0.18 mm crystals of weak to intensely sericitized feldspar laths, unaltered irregular quartz, and lesser chlorite pseudomorphs as observed in thin section. Massive sphalerite, galena, chalcopyrite, and pyrite clasts are rounded, <1cm in diameter, and typically have indistinct margins; however one massive sulfide clast was found that is 22 cm in diameter. The matrix of the breccia is composed mostly of angular quartz and feldspar grains and lithic fragments (0.3 mm average) displaying both volcanic (embayment and resporption) and plutonic (e.g., granophyric) textures in a selectively sericitzed clay matrix (45%).

Rhyolite

The uppermost rhyolite unit structurally overlies the upper sedimentary sequence in the Lundberg Zone. The rhyolite is aphanitic to quartz-feldspar porphyritic and is typically massive near the base and brecciated in the stratigraphically higher sections and is interlayered with crystal-rich tuff. The lower contact with rhyodacite and the upper sedimentary sequence is typically sheared, altered, and largely obscured by late diabase.

Massive rhyolite contains 30 to 70 % euhedral to subhedral white feldspar phenocrysts, (<2 mm) commonly displaying glomeroporphyritic texture. Rounded, grey quartz phenocrysts (<2mm) range in abundance from <5 to 30% but typically <10% (Figure 2.13A). Flow banding is common within the massive unit and is defined by alternating red and black bands averaging 1 cm thick. Other textures observed in drill core and in thin section include granophyre, graphic intergrowths, perlite, and embayed and resorbed phenocrysts. Embayed and resorbed quartz and feldspar are particularly common in all slides; however, perlitic fracture is extensive only in the massive flow banded unit and in sections containing granophyric texture. Epidote, prehnite, and pumpellyite were identified in thin section as metamorphic replacement of felsic glass. Rare primary amphibole phenocrysts were observed which are commonly pseudomorphed by chlorite.

Brecciated rhyolite is characterized by both aphanitic and porphyritic subrounded rhyolitic clasts highlighted by alteration (Figure 2.13B). Rhyolitic clasts (10-50%) average 3-5 cm in size, but

locally are 10 cm (Figure 2.12B). In rare sections, 10 cm subangular, altered feldspar-phyric basalt clasts are observed with altered margins up to 4 cm thick. Crystal-rich rhyolitic tuff occurs throughout the unit. It typically contains >70% feldspar with lesser quartz phenocrysts and rare angular jasper and rhyolite clasts <1cm in diameter (Figure 2.13C).

2.6 Engine House Lithologies

Six lithologies are recognized in the Engine House Zone (Figure 2.7): basaltic pillow breccia, tuffaceous sediments with locally interstratified aphyric rhyodacite, rhyodacite tuff, flow-banded rhyodacite autobreccia, tuffaceous sediments, and quartz-phyric rhyodacite (previously referred to as the prominent quartz sequence: Thurlow and Swanson, 1981). All contacts are inferred to be structural except between the pillow breccia and tuffaceous sediments, and the rhyodacite tuff and flow-banded rhyodacite autobreccia. Pillow breccia and various tuffaceous sediments and rhyodacite tuff are observed up section in H-08-3366 above a diabase dike where they may represent a structurally repeated succession (Figure 2.7). Contacts between these units in H-08-3366 are conformable. All units within the Engine House Zone are flat lying except the upper quartz-phyric rhyodacite, which is south dipping, and cuts across the other lithologies along a south-dipping shear zone.

Basaltic pillow breccia

The pillow breccia unit within the Engine House Zone is identical to that of the Lundberg Zone and is characterized by carbonate-infilled scoriaceous pillow fragments with distinct chilled margins. It occurs at the base of the Engine House Zone and in the middle of the section (Figure 2.14A)

Tuffaceous sediments with locally interstratified rhyodacite

The tuffaceous sediments are about 10 m thick and overlie the pillow breccia along a <1cm fault gouge contact with no apparent shearing. This unit is characterized by grey to black or beige, laminated to thinly bedded tuffaceous mudstone (85%), coherent aphyric rhyodacite, and

interstratified thinly bedded tuffaceous mudstone and thin (<5 cm) sandstone (15%) (Figure 2.14B). The laminated mudstone is homogenous and strongly altered giving an apparent coherent texture; making it difficult to distinguish from aphyric rhyodacite.

Rhyodacite tuff

The rhyodacite tuff lies above a sheared contact with the tuffacacous sediments (Figure 2.14C). The rhyodacite tuff is up to 10 m thick and is characterized by 10% rhyolite clasts (2-10 cm) within a highly altered clay/ash matrix. Rhyolite clasts are typically subrounded and aphyric to weakly feldspar- and quartz-phyric. The matrix is characterized by <5% quartz crystals averaging <2mm; however, local quartz-rich (45%) beds are observed with individual crystals 0.5-1 cm wide (e.g., H3404, similar to the previously described 'prominent quartz sequence': Thurlow and Swanson, 1981). The rhyodacite tuff also contains up to 15% black lithic grains and rare rhyolite grains (1mm).

Rhyodacite autobreccia with interstratified rhyodacite tuff

The rhyodacite autobreccia conformably overlies the rhyodacite tuff in the Engine House Zone. It is characterized by autobrecciated to in-situ brecciated aphyric rhyodacite with local flow banding and rhyodacite tuff clasts (Figure 2.14C). Interstratified crystal-poor rhyodacite tuff layers are present locally which form silt-sized banded units similar to the tuffaceous sediments and interstratified rhyodacite observed lower in the succession. This unit hosts the Engine House polymetallic stockwork.

Southern sedimentary sequence

The southern sedimentary sequence is a structurally emplaced succession (e.g., H-08-3366) representative of rocks observed at the base of the Engine House Zone. It consists of the previously defined units: tuffaceous sediments (5.5 m thick) overlain by pillow breccia (4.5 m thick) and interstratified rhyodacite tuff and aphyric rhyodacite (12.5 m thick: Figure 2.15A). These rocks are overlain by interstratified beige tuffaceous sandstone and black mudstone up to 26.8 m thick above a

minor (10 cm) weak fault gouge contact. Tuffaceous sandstone typically forms up to 1 m thick beds that are normally graded with varying grain sizes from fine pebble conglomerate and very coarse sandstone, to coarse or medium sandstone at upper contacts. Mudstone beds are 0.5 cm to 3.3 m thick and display many soft sediment deformation features, including rare flame structures (Figure 2.15B). Three distinct facies are recognized within this sedimentary unit: massive to normally graded tuffaceous sandstone beds with rare mudstone interbeds and sharp, irregular basal contacts; black mudstone; alternating layers of mudstone (4 cm thick) and sandstone (1-3 cm thick).

Quartz-phyric rhyodacite tuff (formerly prominent quartz sequence)

The quartz-phyric rhyodacite tuff structurally overlies the southern sedimentary sequence across a 3-6 m thick shear zone containing both lithologies (Figure 2.15C). This unit is characterized by 15-20% white, rounded to rare pseudohexagonal quartz fragments, 0.5-1 cm in diameter, and 15% altered, blocky to angular feldspar fragments, 1-2 mm in length. All thin sections show clear volcaniclastic textures. The matrix is composed of clay minerals (85%), probably representing a large volcanic ash component. Rounded to angular quartz and feldspar grains (0.1 mm) comprise the remainder (15%). The pyroclast assemblage consists of mostly juvenile to slightly rounded aphyric to QFP rhyolite (15%) and a significant component (10%) of pumiceous fiamme clasts which suggests a pyroclastic origin.

2.7 Summary of the Lithology and Stratigraphy of the Lundberg and Engine House zones

The rocks surrounding the Lucky Strike deposit have been subdivided into seven major NW-dipping units: pillow breccia, lower and upper basaltic andesite, lower sedimentary sequence, rhyodacite, upper sedimentary sequence, and rhyolite (Figures 2.6 and 2.7). The pillow breccia unit consists of scoreacous pillow fragments which display distinct chilled margins with decreasing amygdale size. The lower basaltic andesite overlies an altered and weakly sheared contact and is

composed of mafic breccia with lesser pillow basalts, silicified siliciclastic rocks, and associated turbidites.

The upper basaltic andesite overlies a heavily altered contact with the underlying lower basaltic andesite and is marked by a significant decrease in the abundance of mafic breccia and fine grained sedimentary rocks (Figure 2.16A). It consists primarily of massive and brecciated basaltic flows and hosts the Lundberg Zone stockwork mineralization at the top of the unit. The upper basaltic andesite contains a conformable sedimentary lens which consists of interlayered felsic-dominated polymictic breccia and siltstone. This "sedimentary" sequence contains rare, <1 cm massive sulfide clasts.

The upper basaltic andesite is conformably overlain by a discontinuous autobrecciated rhyodacite which grades laterally to a <5 to 30 m thick 'upper sedimentary sequence' adjacent to drill holes 3378 and 3406 in cross section B-B' (Figures 2.6 and 2.16B). In H-08-3406, a vertical gradation from autobrecciated rhyodacite to rhyodacitic wacke and siltstone is observed. The upper sedimentary sequence consists of fine sandstone/siltstone breccia overlain by a sheared rhyodacite tuff and felsic-dominated polymictic breccia. This sequence is considered to be the Lucky Strike ore horizon. It is in sheared contact with the overlying rhyolite unit and a thick interval of late diabase (Figure 2.16C). The hanging-wall rhyolite unit consists of feldspar and quartz porphyritic flows with locally interlayered crystal-rich rhyolite tuff overlain by brecciated rhyolite flows capping the local stratigraphy.

The Engine House Zone is separated from the Lundberg Zone across the Airport Thrust (Figures 2.4 and 2.7). Here, the pillow breccia unit is characterized by pillow fragments with chilled amygdaloidal margins. Tuffaceous sediments, which consist of bedded mudstone and thin normally graded sandstone/greywacke, overlie the pillow breccia along a 1 cm fault gouge contact. Rhyodacite tuff structurally overlies the tuffaceous sediments and is characterized by rhyodacitic fragments in an altered clay (ash) matrix. Conformably overlying the rhyodacite tuff is flow banded rhyodacite and interstratified rhyodacite tuff which hosts the Engine House stockwork. The flow-

banded rhyodacite is in sheared contact with either the southern sedimentary sequence and/or quartz-phyric rhyodacite tuff. The southern sedimentary sequence consists of tuffaceous sediments that are conformably overlain by basaltic pillow breccia, interstratified 'tuffaceous sediments and rhyodacite tuff', and sandstone and mudstone above a <5 cm fault gouge contact. Quartz-phyric rhyodacite tuff structurally caps the Engine House succession (Figure 2.15C).

Correlation with the Buchans stratigraphy

Lundberg Zone

Thurlow and Swanson (1987) defined 4 formations within the Buchans Group (Table 2.1 and Figure 2.5). Barbour et al. (1989) logged the pillow breccia and lower basaltic andesite units as Sandy Lake Formation (SLF), the structurally overlying upper basaltic andesite as the Ski Hill Formation (SHF), and the overlying rhyodacite, upper sedimentary sequence, and rhyolite as the Buchans River Formation (BRF).

In the Lucky strike area, the base of the SLF consists of "felsic pyroclastic rocks (some with prominent quartz phenocrysts), polylithic breccia-conglomerate, arkose, wacke, siltstone and graded pumiceous pyroclastic flows" (Thurlow and Swanson, 1987). This contrasts with the pillow breccia and lower basaltic andesite that were also classified as SLF by Babour et al (1989). Thurlow and Swanson (1987) identified bedded tuffaceous sedimentary rocks with multicoloured mudstone-chert and basaltic pillow lava units as distinct units which are grouped here as part of the Lundberg Hill Formation. These units were observed at the base of the Lundberg and Engine House zones in this study. Including these units in the redefined Lundberg Hill Formation (LHF) removes the need for a previously proposed thrust contact (Figure 2.5: Old Buchans of Barbour et al., 1989) and results in a simpler stratigraphic succession within the Lundberg Zone. The upper basaltic andesite unit identified as SHF is therefore not thrust-repeated stratigraphy within the Lucky Strike duplex as suggested by Calon and Green (1987). A conformable sedimentary lens within the Ski Hill basalt was not previously described, but it may correlate with the "marginal Footwall Arkose" which

locally underlies the 'Intermediate Footwall' in the Lucky Strike area (Thurlow and Swanson, 1981). The conformable contact between the lower sedimentary sequence and the upper basaltic andesite indicate that no thrust faults are required and either the BRF is interfingered with SHF (i.e., time transgressive) or there are other sequences similar to BRF lower in the stratigraphy. Towards the top of the mafic succession, andesite was identified which is slightly more fractionated than the upper basaltic andesite. This horizon forms only part of the previous 'Intermediate Footwall' (e.g., Figure 1.6). The SHF is conformably overlain by the rhyodacite and upper sedimentary sequence which host the Lucky Strike deposit and are grouped into the BRF.

Barbour et al. (1989) grouped the rhyolite unit with the BRF, and Thurlow and Swanson (1981) included it with the Lucky Strike ore horizon (Figure 2.5). This study demonstrates that the rhyolite unit is quartz-feldspar porphyritic, whereas structurally underlying felsic rocks are largely aphyric. The observed fault contact, interpreted as a thrust fault between the BRF and overlying rhyolite, precludes the rhyolite being part of the SLF as an out-of-sequence thrust would be required to emplace young over old. In the classification of Thurlow and Swanson (1987) the rhyolite would have to be placed into LHF. However, grouping of major mafic and felsic volcanic centres is undesirable under stratigraphic code. The simplest solution is to reserve the LHF for mafic rocks interbedded with chert and place quartz-phyric volcanic rocks in the newly proposed "Lucky Strike hanging-wall succession". The closest geographic feature to these rocks is the Lucky Strike open pit which serves as a type-locality and gives its informal name (Figure 2.4). This informal name is appropriate until recognition of its original stratigraphic position is established to the west of Sandy Lake. Overall, the stratigraphy proposed by (Thurlow and Swanson, 1987) is supported by this study; the modifications proposed herein clarifies the definition of the units allowing extrapolation to camp scale.

Engine House Zone

The stratigraphy of the Engine House Zone has not been firmly established as Thurlow and Swanson (1981, 1987) focused on development of more regional units. Preliminary correlations

were made by Kowalik et al. (1981), but these predated the study of Thurlow and Swanson (1987). As in the Lundberg Zone, the pillow breccia unit was previously classified as the Footwall Basalt (e.g., Kowalik, 1981); although the drilling was not deep enough to be certain of this grouping. The lack of unique lithological associations (e.g., multicoloured chert) precludes it from being assigned to the LHF, as in the Lundberg Zone. The simplest solution is that the pillow breccia represents a lateral facies of the SHF.

The conformably overlying tuffaceous sedimentary rocks and interstratified rhyodacite were not previously assigned to a formation; however, the faulted basal contact and the association with felsic volcanic rocks suggest that they belong to the BRF. The structurally overlying rhyodacite is grouped with the Intermediate Footwall and BRF, consistent with previous classification of Thurlow and Swanson (1987). All remaining structural units, in the Engine House Zone including the quartz-phyric rhyodacite, were grouped as 'dacitic pyroclastics' by Kowalik et al. (1981), and are grouped here with the BRF.

The quartz-phyric rhyodacite forms part of the former 'prominent quartz sequence' that was historically assigned to the LHF klippe south of Lucky Strike (e.g., felsic volcanic rocks; Figure 2.4 and 2.15C; Thurlow, 1992). These rocks lack any distinctive facies associations; however, lithogeochemical results (Chapter 3) indicate that this unit belongs to BRF. The remaining lithologies are interpreted to reflect the primary stratigraphy as observed in the Lundberg Zone, with lateral facies variations. Therefore, the Engine House and Lundberg Zones represent the same stratigraphic horizon.

Correlation with other deposits in the Buchans Mining Camp

The ores of the Buchans Mining Camp were classified as stockwork, in situ (i.e., ~massive), or transported ore (e.g., Jambor, 1987). The stockwork ore occurs exclusively adjacent to the Lucky Strike and Oriental orebodies. The Lundberg Zone mineralization is characterized by polymetallic stockwork predominantly hosted in the SHF, and to a lesser extent BRF, and exhalative

mineralization hosted exclusively in BRF (e.g., Figure 2.6). The stratigraphic setting of the stockwork is consistent with it being a peripheral zone to the Lucky Strike deposit. The exhalative mineralization correlates with both the North orebody and Lucky Strike, Rothermere, and Maclean ore horizons within the BRF (e.g., BRF: Figure 2.5).

The North Orebody is the stratigraphically lowest orebody in the Buchans camp, occurring on a separate ore horizon from the other deposits at the base of the Buchans River Formation (Jambor, 1987) and correlates to the lowermost polymictic breccia of the upper sedimentary sequence at Lundberg (e.g., Figure 2.5), although no in situ ore has yet been found on this horizon. The North orebody is overlain by siltstone and felsic tuff which form the footwall of the Two-level/Lucky Strike orebody and hosts the Rothermere and Maclean (Binney, 1987), and Clementine and Oriental orebodies (Thurlow and Swanson, 1981).

2.8 Conclusions

The Lundberg Zone is characterized by lateral continuity of stratigraphic units over the entire study area (800 x 500 m). The stratigraphic succession includes chert-basalt of the LHF, basaltic andesite of the SHF, felsic volcaniclastic rocks of the BRF, and rhyolite of the newly proposed Lucky Strike hanging-wall succession. The Engine House Zone is located structurally below an overthrusted quartz-phyric unit of the BRF. This relationship is confirmed by geochemical results of Chapter 3.

The Engine House Zone lies within the same structural panel as the Lundberg Zone; however, it comprise a lateral facies variation of the Lundberg Zone. The observed stratigraphic relationships generally agree with earlier interpretations, but the recognition of distinct mafic and felsic units, including sulfide-bearing horizons, within the BRF and SHF has important implications for exploration within the camp. In the Lundberg Zone the SHF basalt host the majority of the polymetallic stockwork, and the BRF volcaniclastic rocks hosts the exhalative mineralization and nearby Lucky Strike massive sulfide. The presence of sulfide clasts within a volcaniclastic lens in

the SHF (lower sedimentary sequence) suggests that massive sulfide mineralization may not be limited to the BRF and that multiple ore horizons may exist.

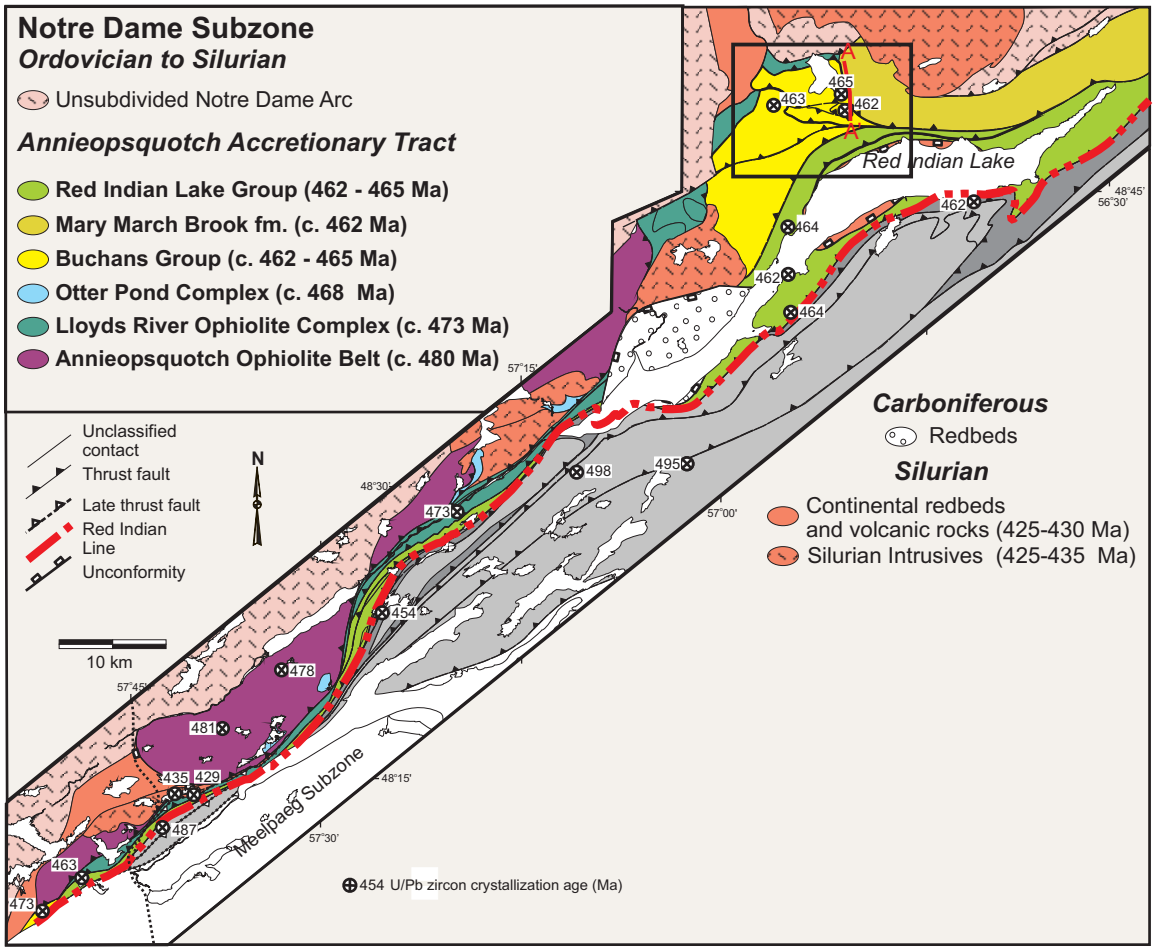

Figure 2.1: Geology of the Annieopsquotch Accretionary Tract (AAT). The AAT is a thin (8-15 km thick) accretionary tract consisting of arc and back-arc volcano-sedimentary units. An interpretation of section A-A' is displayed in Figure 2.2 (Zagorevski et al., 2006).

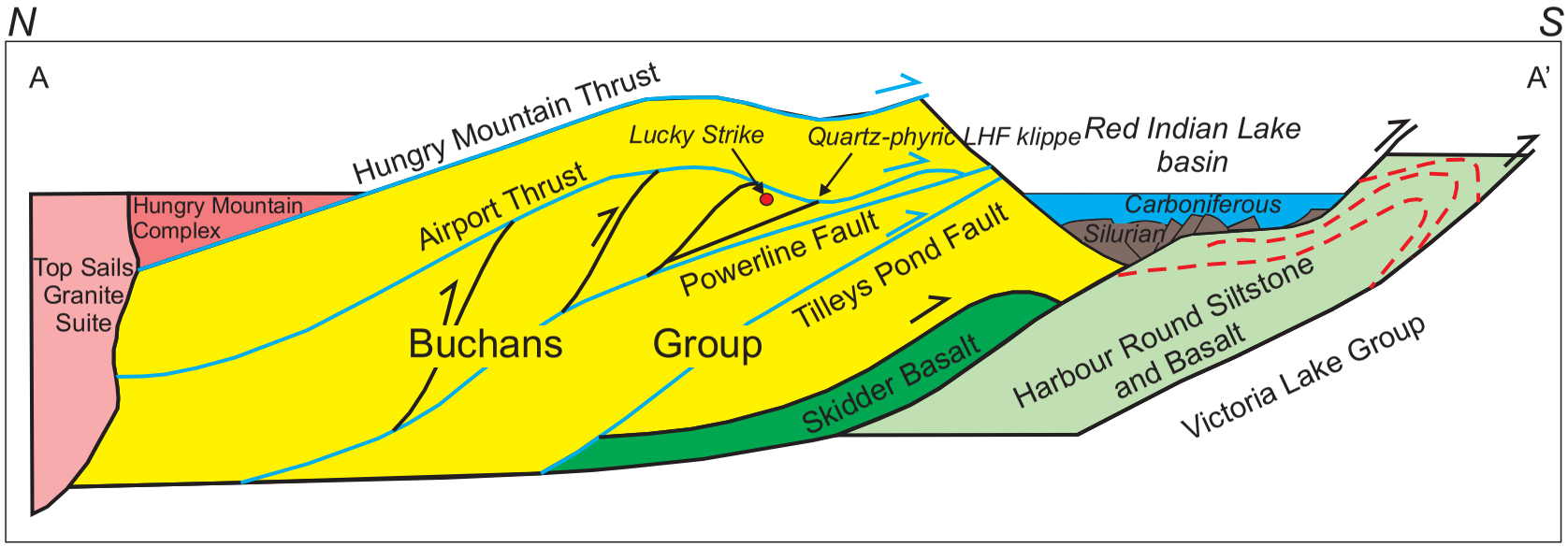

Figure 2.2: Schematic cross-section of the antiformal thrust stack model proposed for the Buchans area from seismic and geological data (Thurlow et al., 1992) showing the position of the Lucky Strike deposit. The Lucky Strike deposit lies in the middle of an antiformal culmination centred on the town of Buchans. The klippe in the middle of the section above the airport thrust is interpreted as the quartz-phyric rhyodacite which structurally overlies the Engine House Zone shown in Figure 2.4.

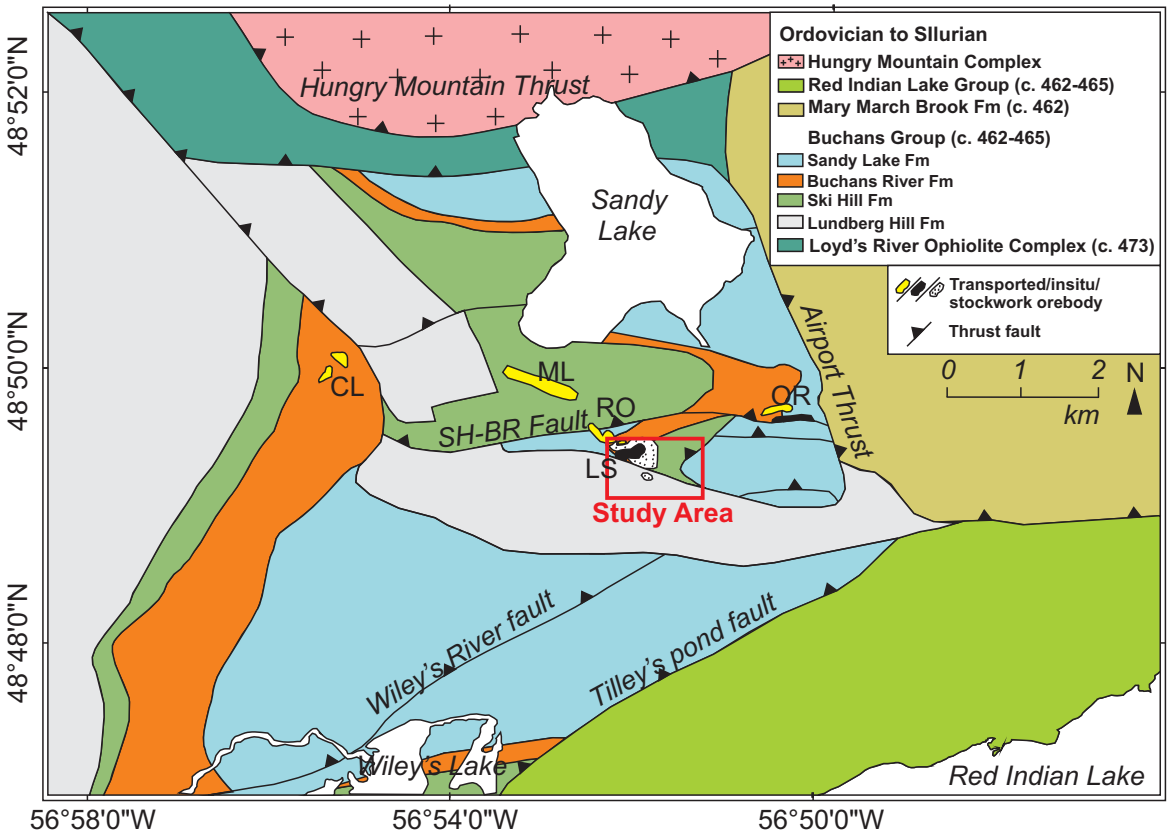

Figure 2.3: Compilation map of Buchans geology by Thurlow and Swanson (1987), Thurlow et al., (1992), and Zagorevski (2009). The mineral deposits (yellow) in Buchans are located along two broadly NW-and NE-trending channels extending away from the Lucky Strike deposit (LS). Rothermere (RO) and Maclean (ML) lie in the NW channel, whereas Oriental (OR) and several smaller deposits lie in the NE channel. The Clementine (CL) prospect lies west of the main deposits.

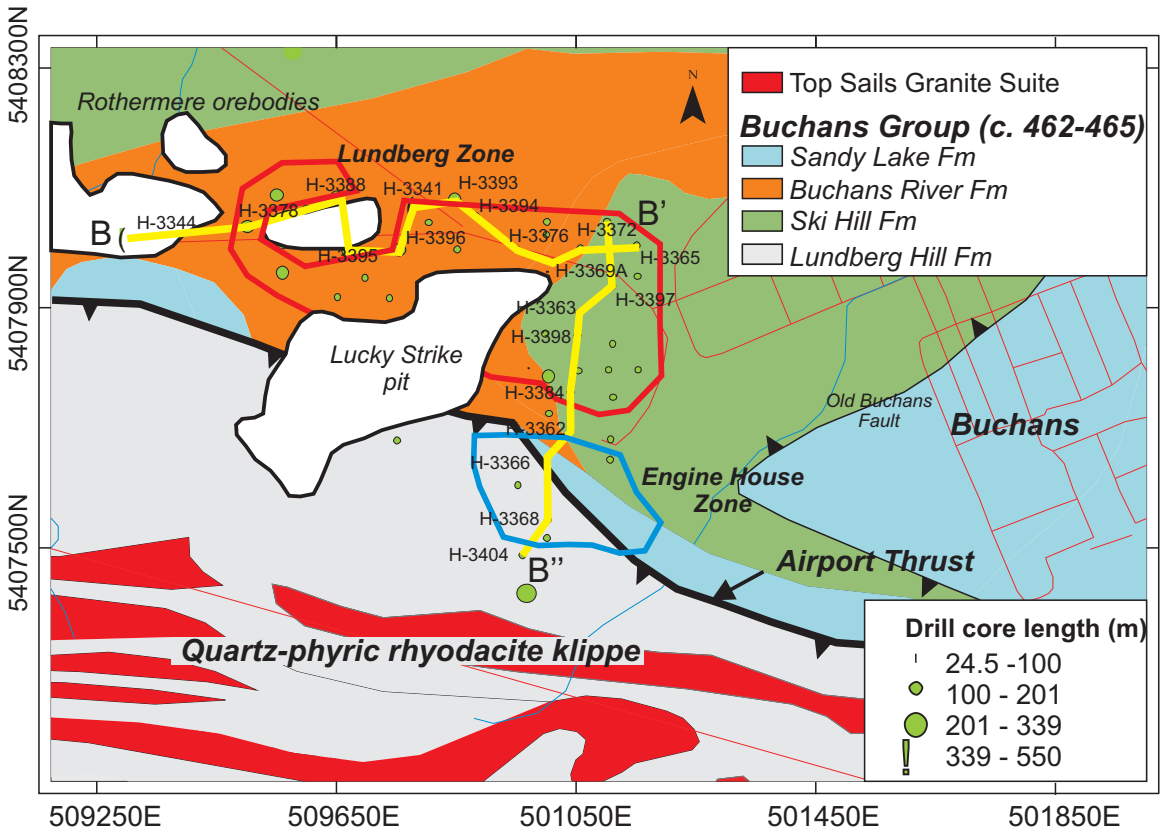

Figure 2.4: Close-up of Figure 2.3 from Thurlow (1992) and Thurlow and Swanson (1987) showing the limits of drilling in the Lundberg and Engine House zones (Webster and Barr, 2008). The Lundberg Hill Formation on this map is that defined by Thurlow and Swanson (1987); however, it has identical geochemistry to that of the Buchans River Formation (Chapter 3) and is classified as Buchans River Formation herein. Cross sections B-B' and B'-B" are represented in Figures 2.7 and 2.8, respectively, and incorporate this reclassification. The UTM datum is NAD 1983.

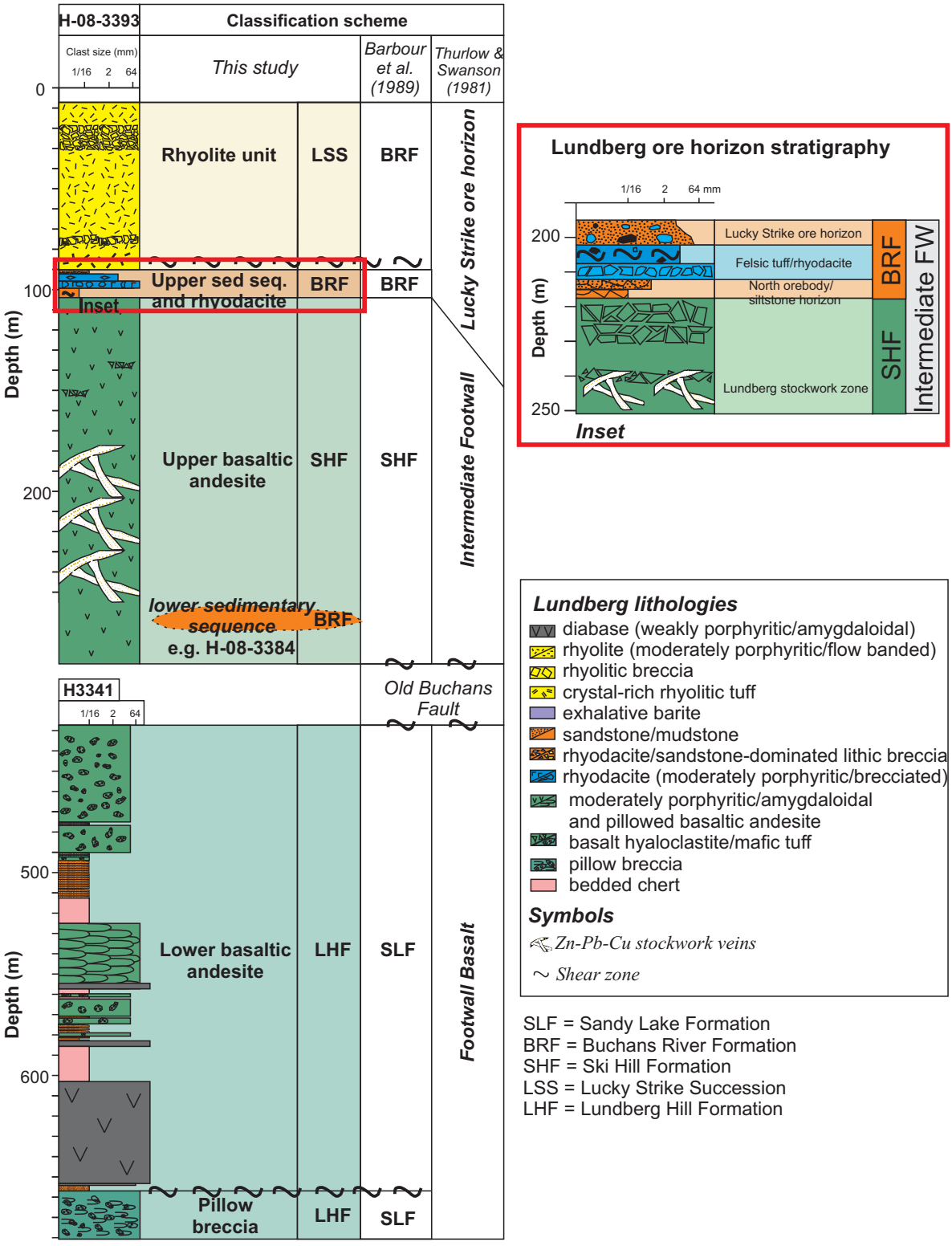

Figure 2.5: Stratigraphic nomenclature in the Lundberg Zone area showing its history and development. Details of the ore horizon stratigraphy are shown in the inset. The stratigraphic position of the Lucky Strike ore horizon is identical to that of the Two-level, Rothermere,Oriental, Maclean, and Clementine deposits. The North orebody lies at a slightly lower stratigraphic position than the Lucky strike ore horizon.

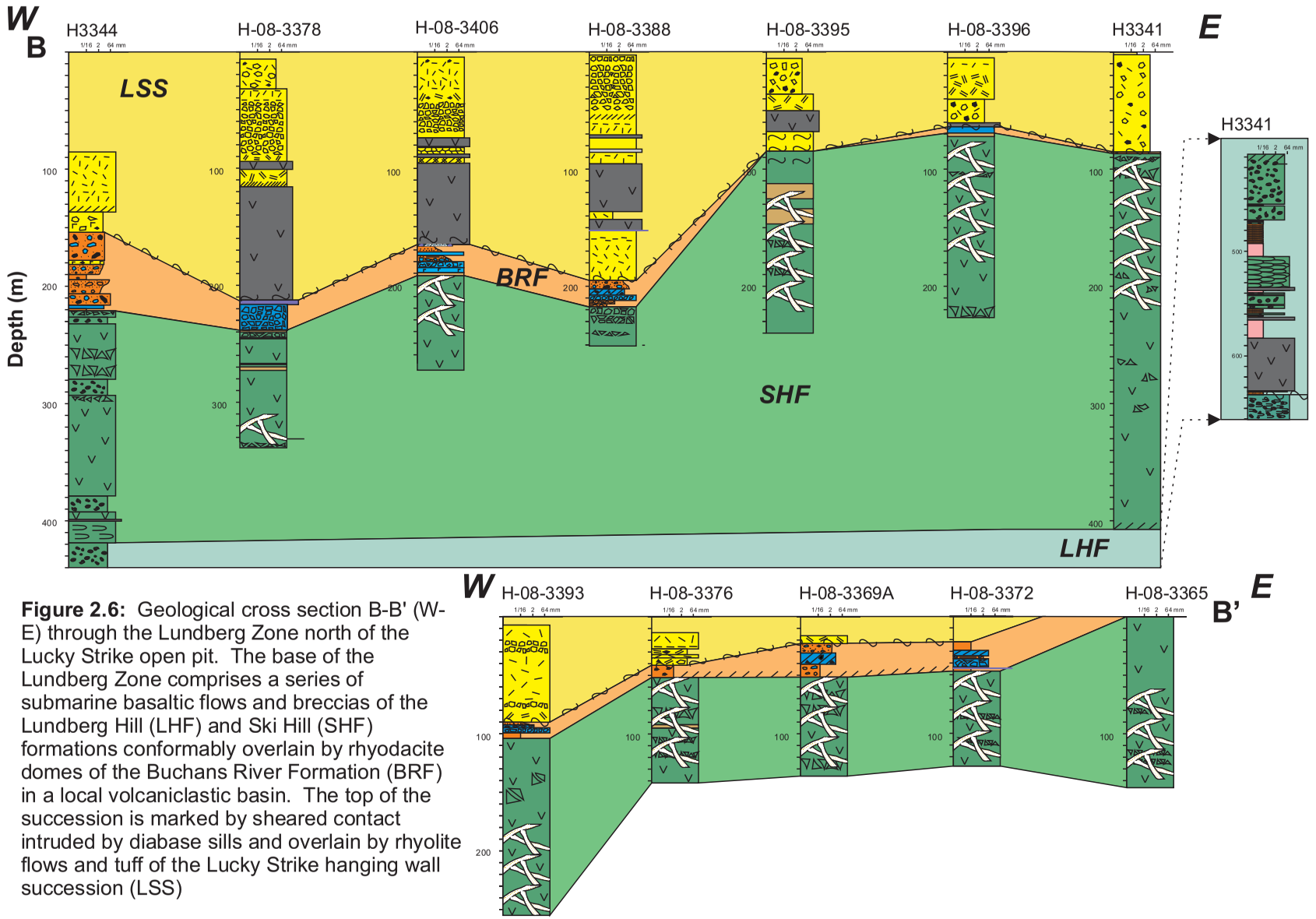

Figure 2.6: Geological cross section B-B' (W-E) through the Lundberg Zone north of the Lucky Strike open pit. The base of the Lundberg Zone comprises a series of submarine basaltic flows and breccias of the Lundberg Hill (LHF) and Ski Hill (SHF) formations conformably overlain by rhyodacite domes of the Buchans River Formation (BRF) in a local volcaniclastic basin. The top of the succession is marked by sheared contact intruded by diabase sills and overlain by rhyolite flows and tuff of the Lucky Strike hanging wall succession (LSS)

Lundberg lithologies


diabase/intermediate dike (weakly porphyritic/amygdaloidal)


rhyolite (moderately porphyritic/flow banded)


rhyolitic breccia


crystal-rich rhyolite tuff


exhalative barite


'hydrothermal upflow zone'


sandstone/mudstone


sandstone/polylithic breccia


rhyodacite (moderately porphyritic/brecciated)


rhyodacite (aphyric/rhyodacite tuff)


moderately porphyritic/amygdaloidal and hyaloclastite basalt


bedded chert


mafic tuff/pillow breccia

Symbols


Zn-Pb-Cu stockwork veins

Shear zone


Brittle fault zone

Lithological legend of the various rock types and lithofacies which occur in the Lundberg and Engine House zones.

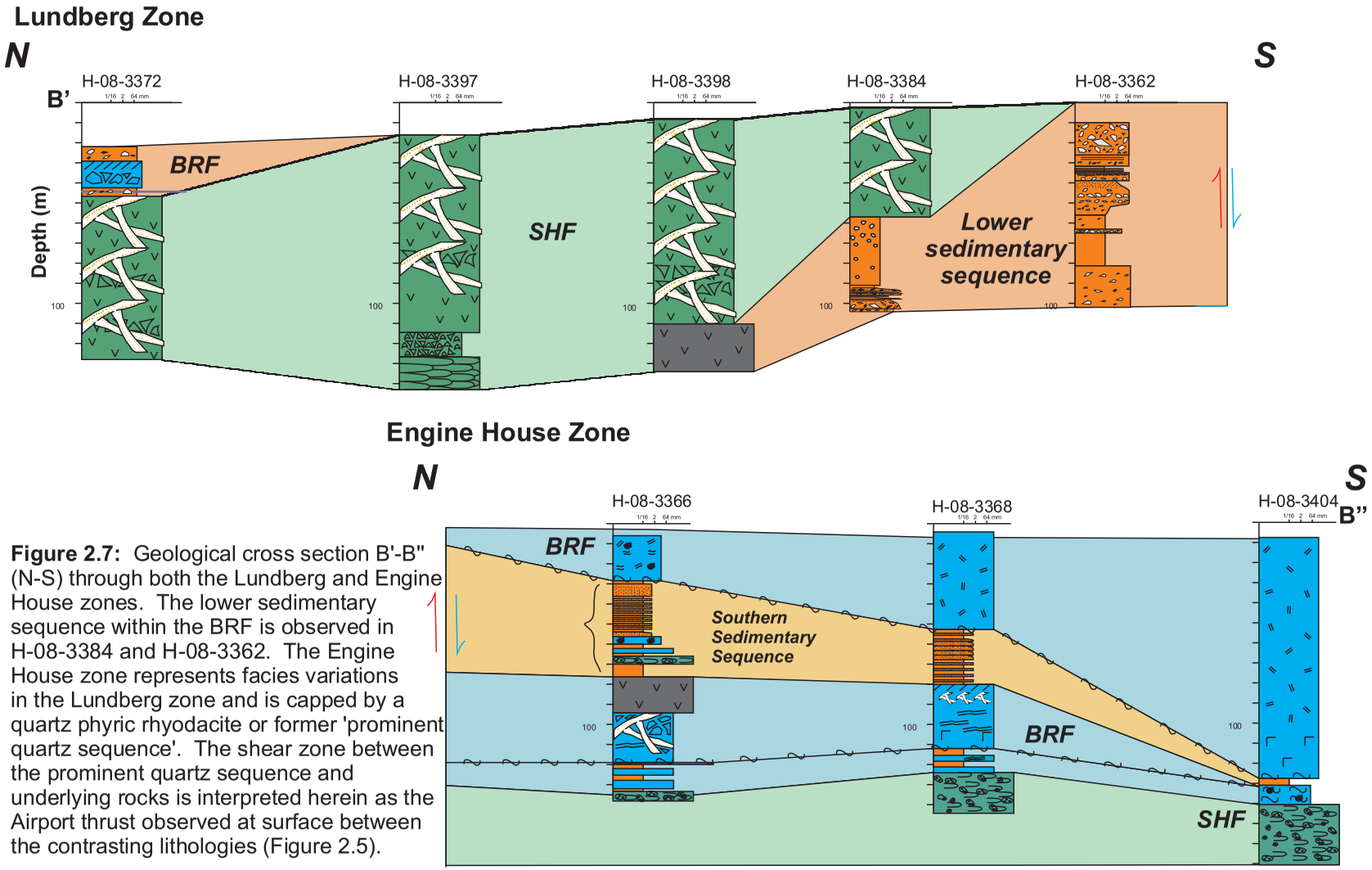

Figure 2.7: Geological cross section B'-B" (N-S) through both the Lundberg and Engine House zones. The lower sedimentary sequence within the BRF is observed in H-08-3384 and H-08-3362. The Engine House zone represents facies variations in the Lundberg zone and is capped by a quartz phyric rhyodacite or former 'prominent quartz sequence'. The shear zone between the prominent quartz sequence and underlying rocks is interpreted herein as the Airport thrust observed at surface between the contrasting lithologies (Figure 2.5).

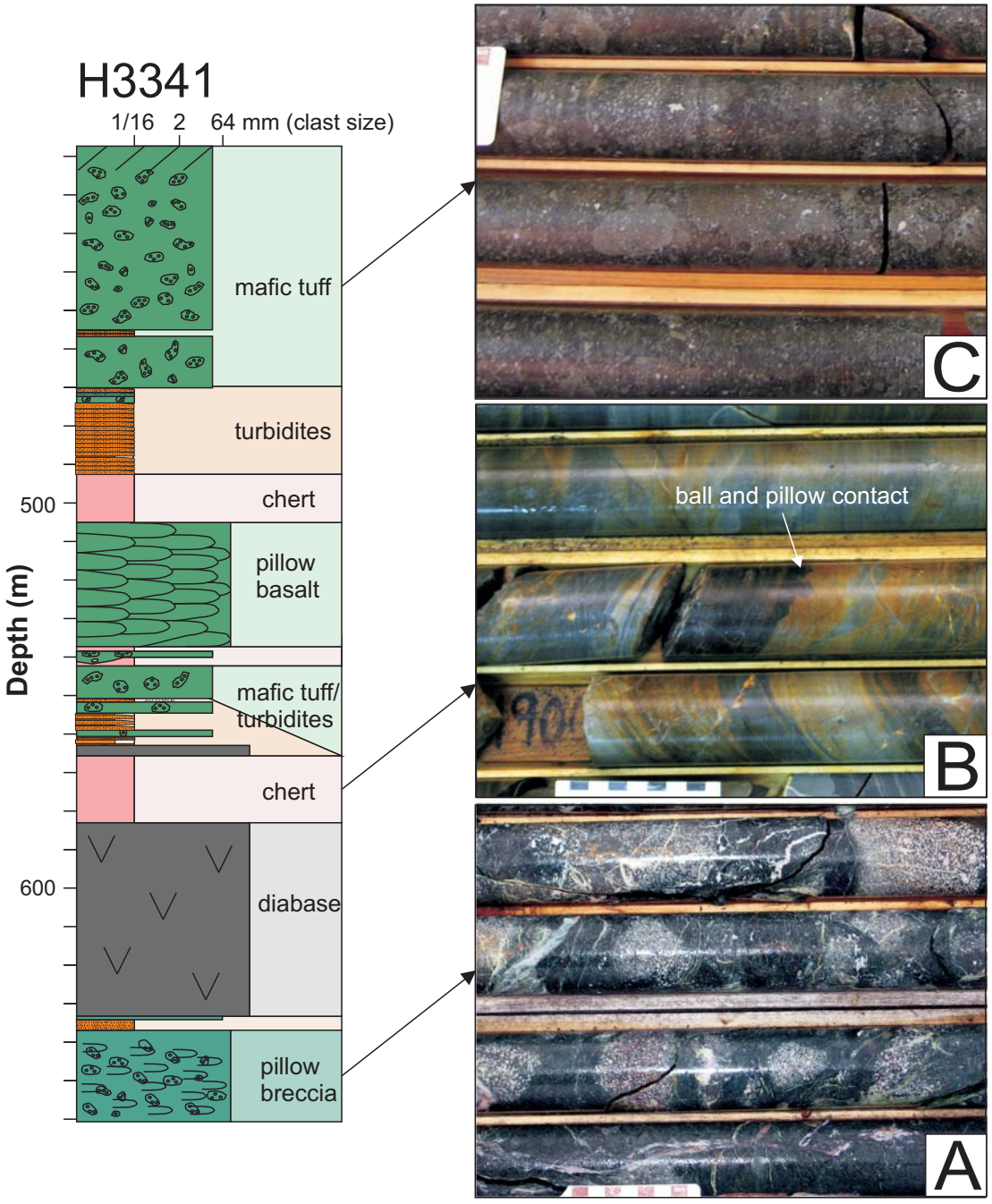

Figure 2.8: Summary of the stratigraphic relationships of the lower basaltic andesite unit. A. Pillow breccia unit with distinctly chilled margins evident in some clasts (e.g., hole 3368;125 m; top right). B. Ball and pillow structure within 'bedded chert' indicating siliciclastic sedimentation and later silicification (hole 3341; 579.3 m). C. Mafic tuffaceous unit with unique ungraded scoriaceous basalt clasts (H3344; 259.2 m).

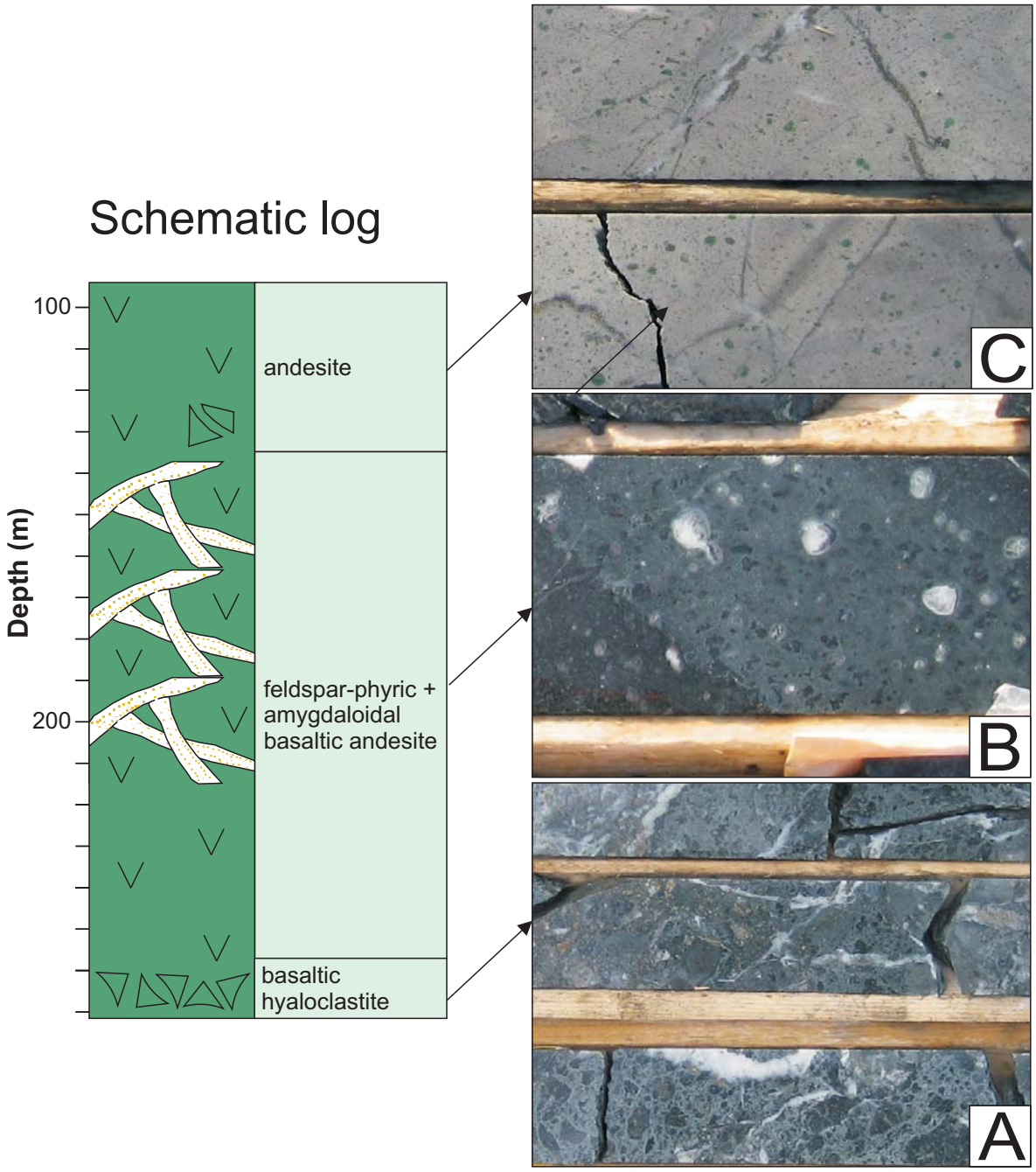

Figure 2.9: Summary of the stratigraphic relationships of the upper basaltic andesite unit. A. Hyaloclastite with in situ brecciation of highly amygdaloidal basalt (quartz-hematite-carbonate-chlorite alteration; H3396; 227 m). B. Feldspar porphyritic and quartz-carbonate altered amygdaloidal upper basaltic andesite (H3386; 141.5 m). C. Emerald green muscovite-altered feldspar phenocrysts of the andesite unit (fractionated basaltic andesite: see Chapter 3).

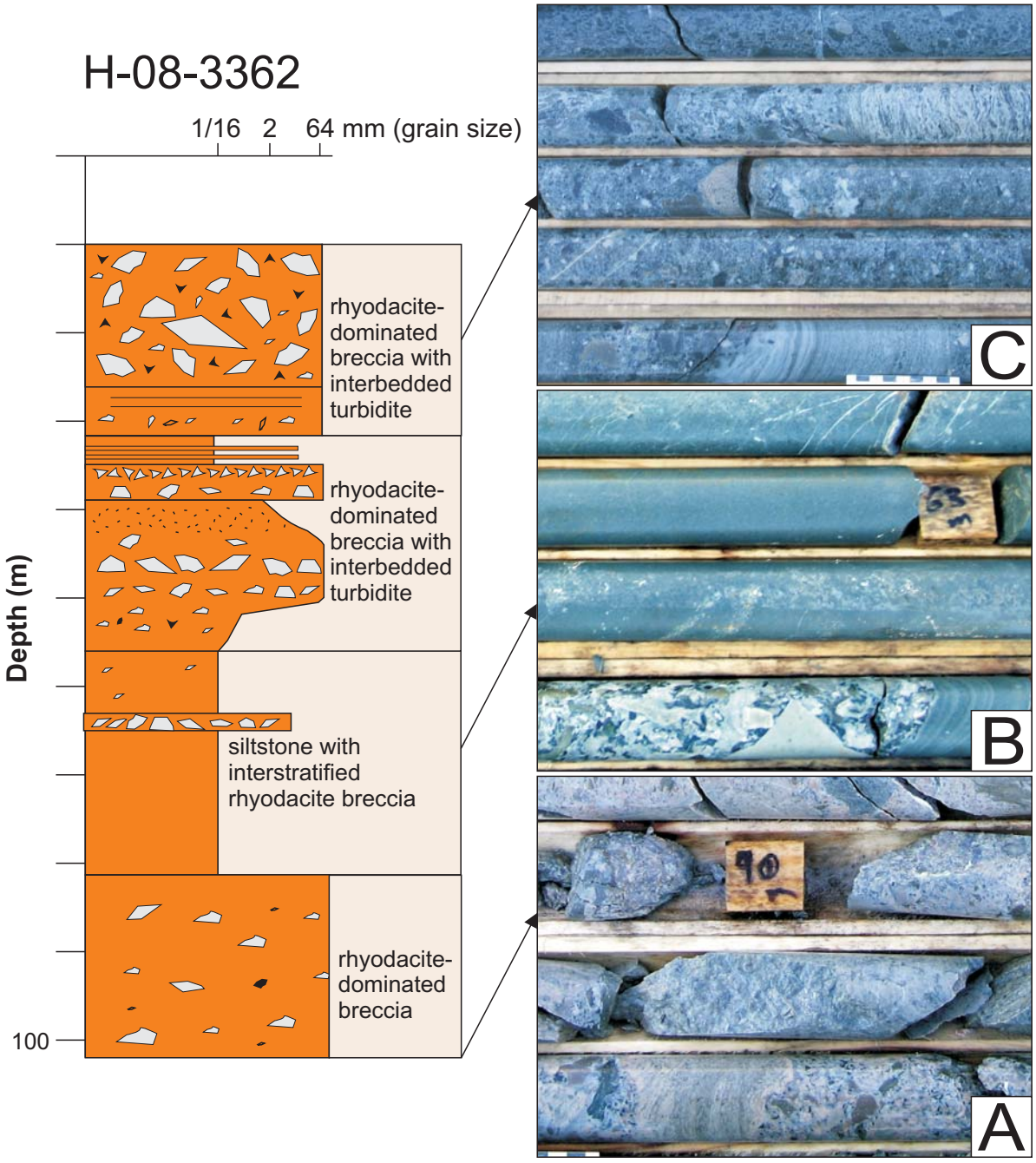

Figure 2.10: Summary of the stratigraphic relationships of the lower sedimentary sequence. The sequence records a shift from proximal rhyodacite dominated breccia (A: H3362; 90 m) to more distal massive siltstone (B: H3362; 65 m). The occurrence of rhyodacite mass flow breccias with interbedded turbidites at the top of the unit suggests reactivation of the volcanic edifice C: Tabc division turbidite among polymicitc debris flow (H3362; 28 m). The resedimented hyaloclastite is observed in the top row of 2.10C, highlighting the increase in mafic clasts in the upper portions of the lower sedimentary sequence.

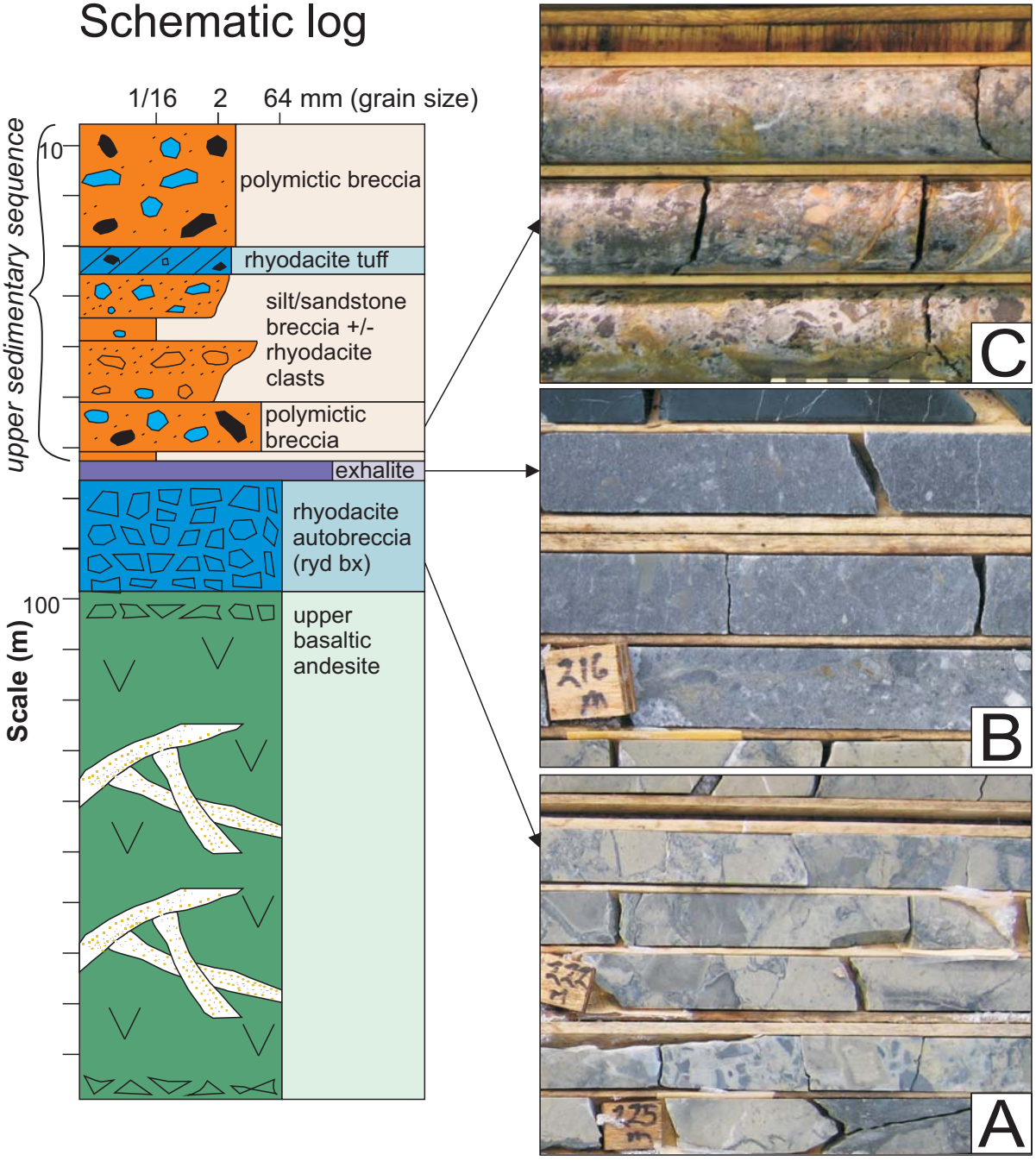

Figure 2.11: Stratigraphic position of the rhyodacite, exhalite, and heavily altered basal polymictic breccia of the upper sedimentary sequence. A. Insitu jigsaw-fit rhyodacite breccia with a silicified fine-grained matrix (H3378; 220m). B. Bedded barite with rare rhyodacite clasts, large euhedral barite crystals, and disseminated sphalerite and galena (H3378; 216 m). C. Silicified basal polymictic breccia of the upper sedimentary sequence (H3344; 210 m).

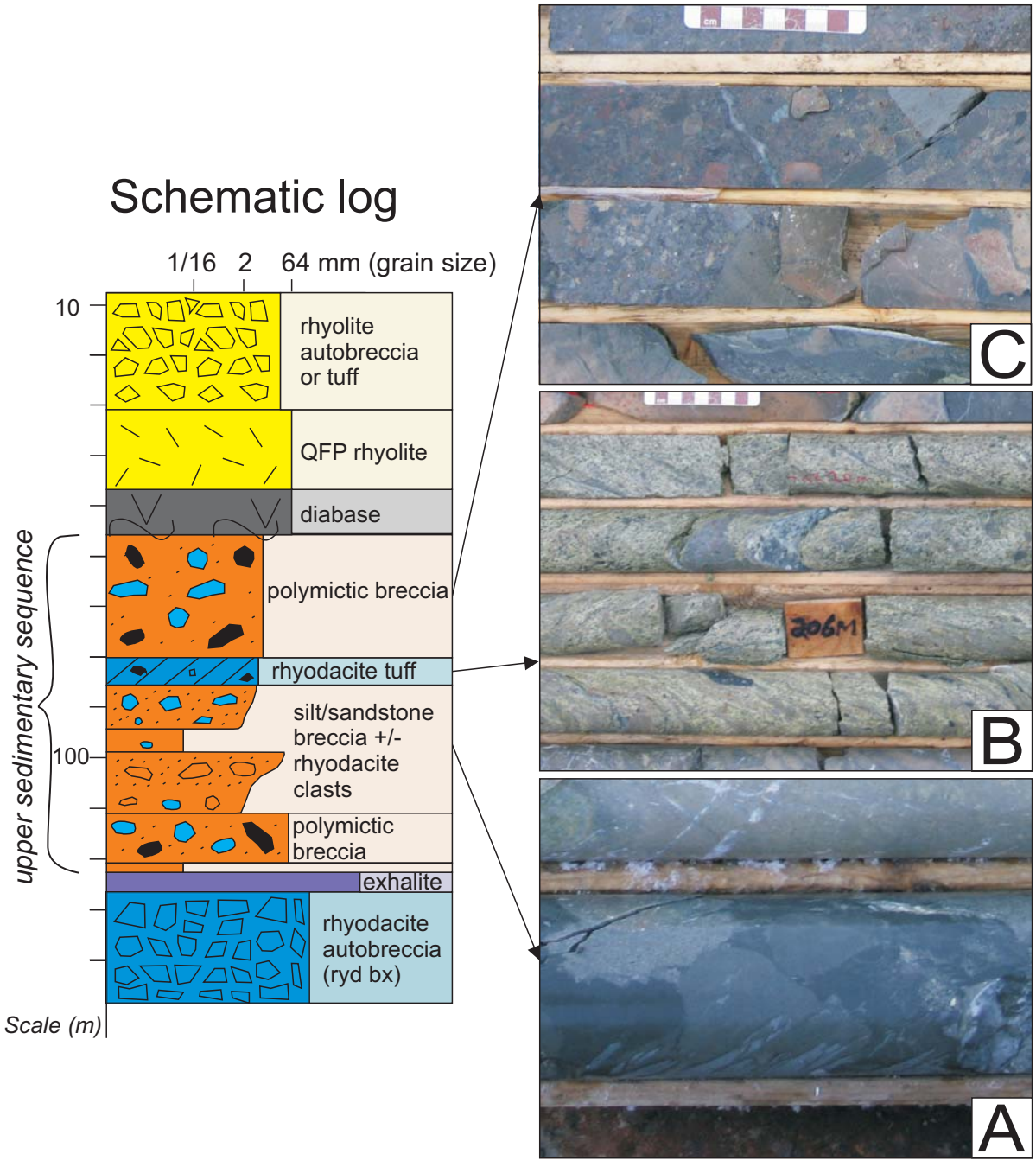

Figure 2.12: Summary of the stratigraphic relationships of the upper sedimentary sequence. A. Brecciated fine sandstone and siltstone formed by slumping of unconsolidated sediments (H3388, 213 m). B. Crystal-rich rhyodacitic tuff with lithic fragments and fiamme? (H3388; 206m). C. Polymictic breccia with rare 1 cm massive sphalerite-galena clasts (top left) and abundant angular rhyodacitic clasts (H3388; 197 m).

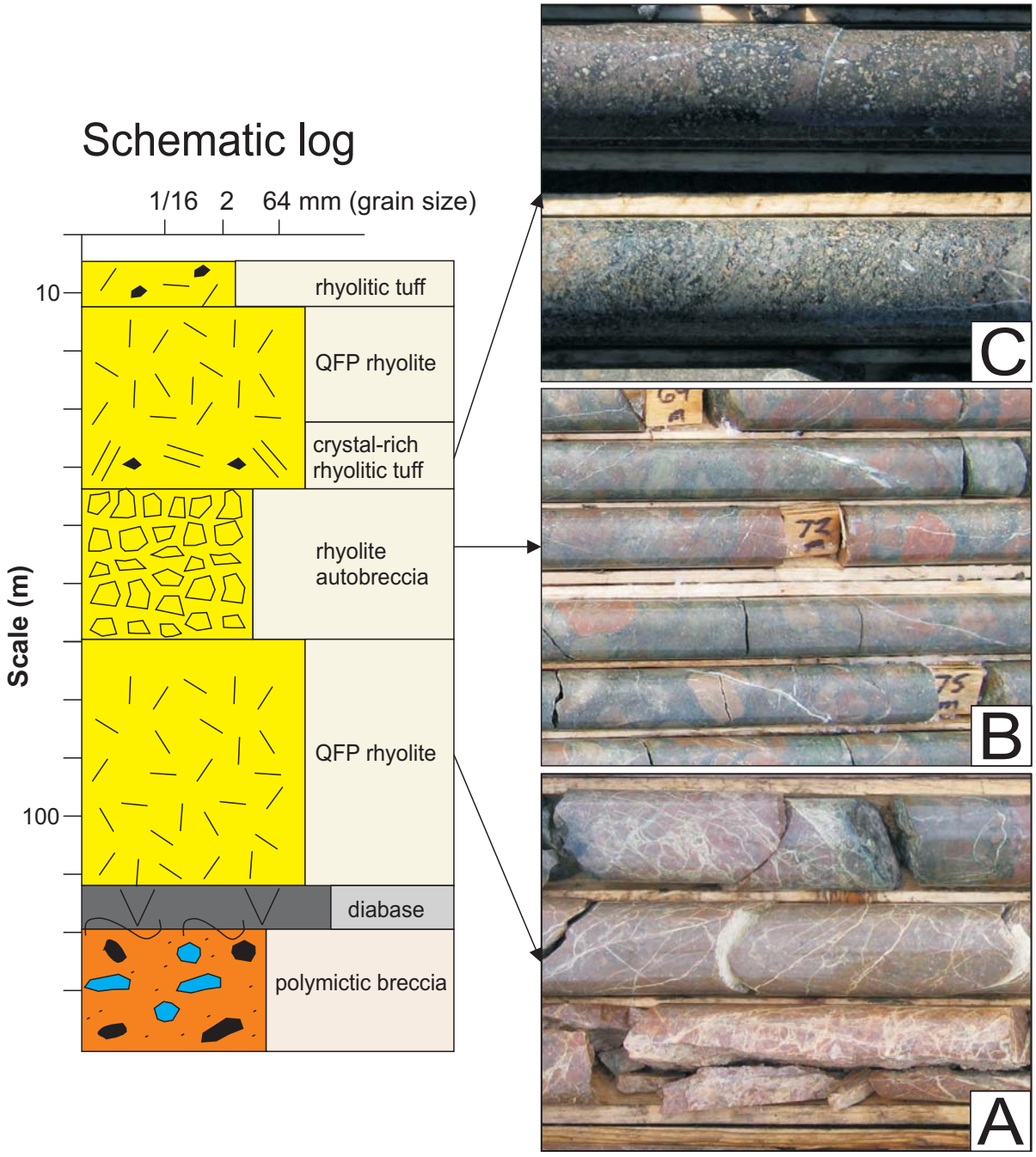

Figure 2.13: Summary of the stratigraphic relationships of the rhyolite unit. A. QFP rhyolite cut by sericite-carbonate veins (H3396; 10 m). B. Autobrecciated rhyolite with characteristic fine-grained chlorite-altered matrix (H3378; 69 m). C. Rhyolitic, feldspar-rich tuffaceous volcaniclastic. The groundmass is altered to a fine, dark chlorite (H3393; 88 m).

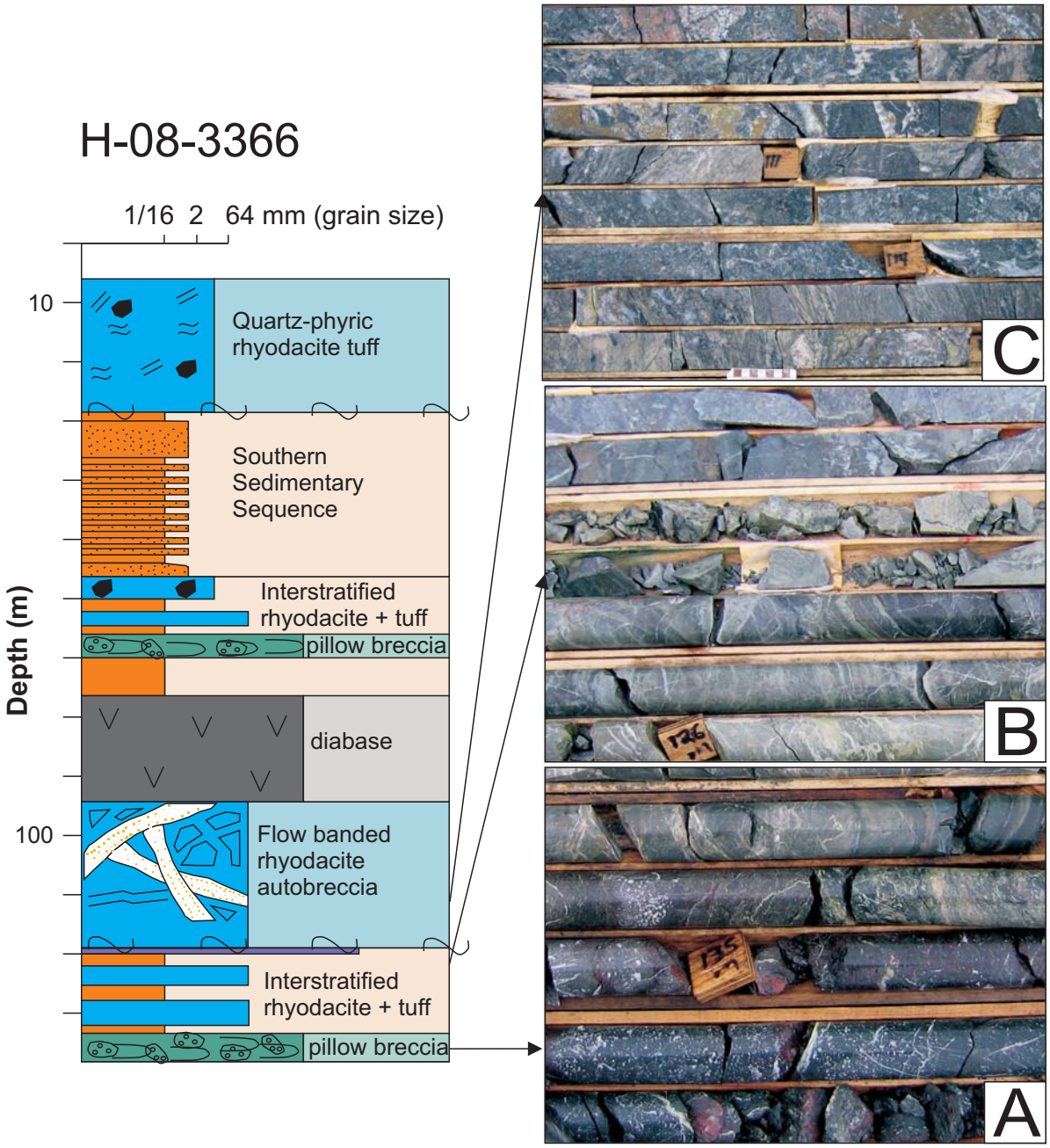

Figure 2.14: Summary of lithologies of the Engine House Zone. A. Pillow breccia with unique carbonate-scoriaceous pillow fragments (H3366; 135 m). B. Interstratified rhyodacite and bedded rhyodacite ash tuff. Locally overlying the ash tuff (top row) is barite horizon similar to the Lundberg zone (H3366; 126 m). C. Sheared contact between the barite and flow banded rhyodacite autobreccia and tuff which hosts the chalcopyrite-rich Engine House stockwork zone (H3366; 114 m).

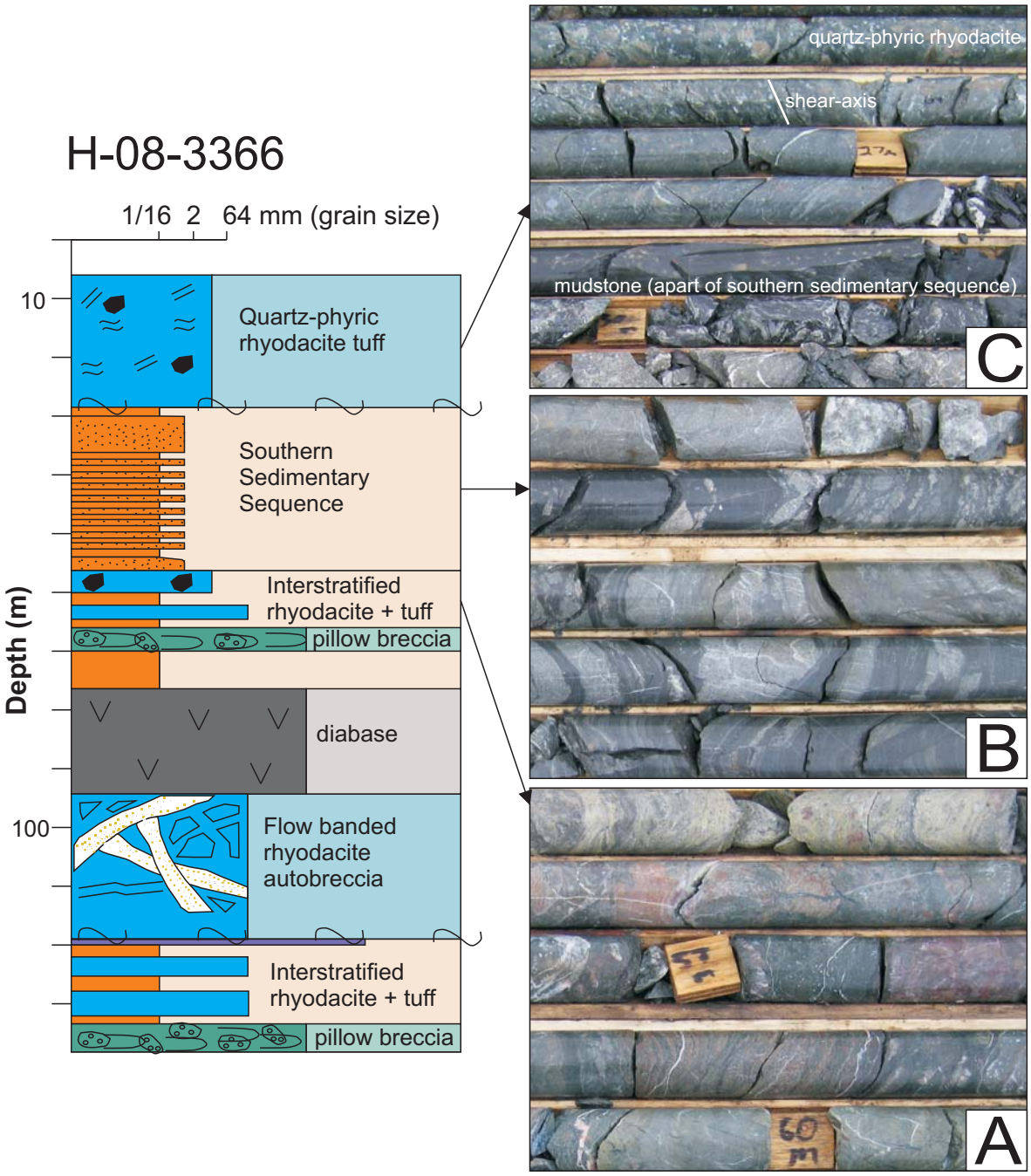

Figure 2.15: Summary of the southern sedimentary sequence lithologies and capping quartz-phyric rhyodacite tuff of the Engine House Zone succession. A. Interstratified rhyodacite tuff (top 3 rows) and aphyric rhyodacite (bottom row) (H3366; 57 m). B. Tectonically re-worked volcanogenic sandstone and layered mudstone (H3366; 45 m). C. Sheared contact between the southern sedimentary sequence and quartz phyric rhyodacite. The quartz phyric rhyodacite displays clear pyroclastic texture (e.g., pumice fiamme) and sheared quartz phenocrysts (H3366; 27 m).

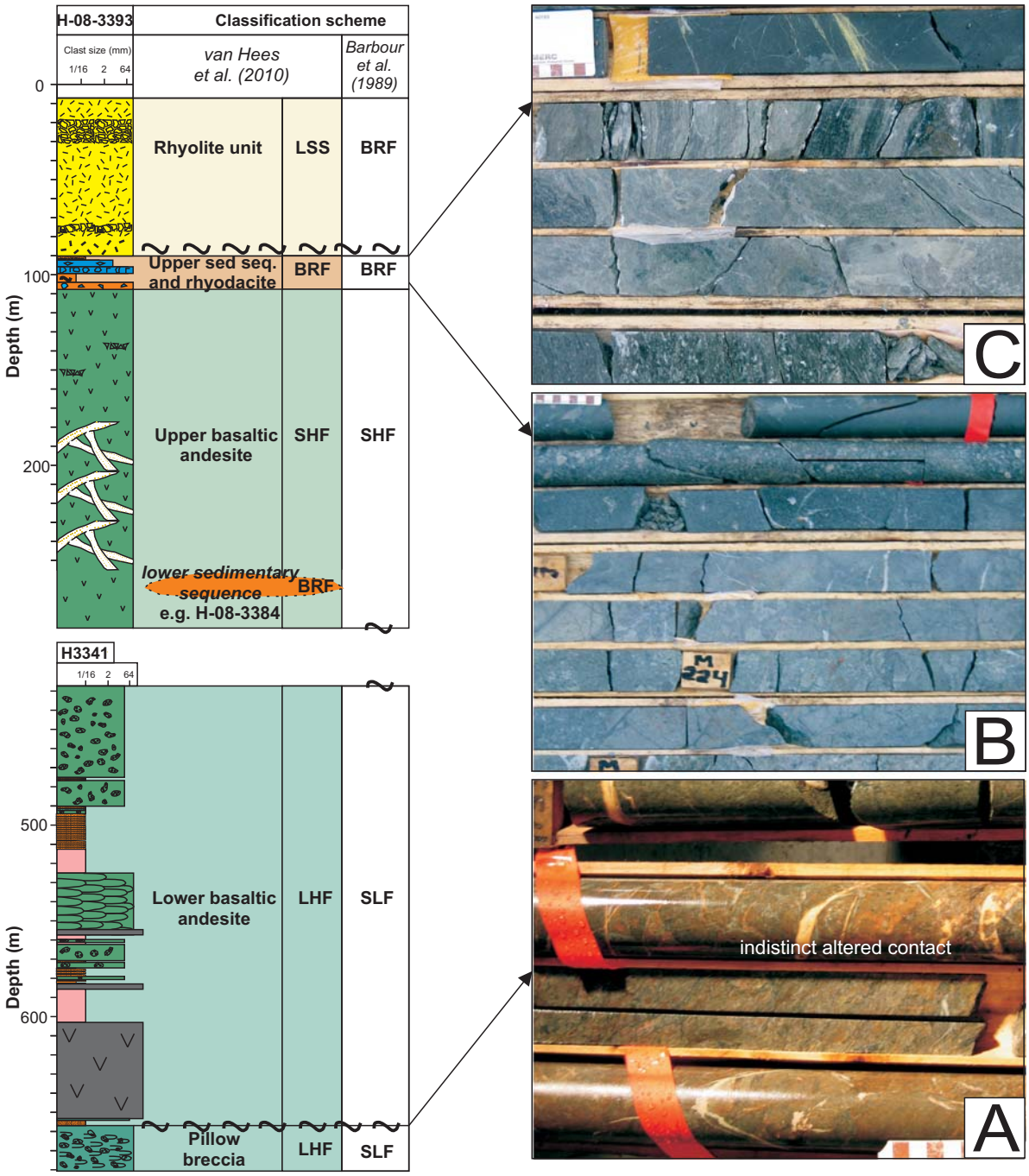

Figure 2.16: Summary of the Lundberg zone succession including photographs of the 3 observed major contacts. A. Heavily altered contact between the lower and upper basaltic andesite (H3344; 1406 m). B. Conformable contact of the upper basalt and upper sedimentary sequence with rare rhyodacite clasts in a moderately poorly sorted sandstone matrix grading up to rhyodacitic breccia (H3388; 220 m). C. Diabase overlying sheared rhyodacite (H3396; 65 m).

Table 2.1: Buchans Group stratigraphy (Thurlow and Swanson, 1987)

Formation	**Estimated Thickness**	**Lithologies**
Sandy Lake	2000 m	Basaltic pillow lava, pillow breccia intertonguing with coarse grained, redeposited clastic rocks of felsic volcanic derivation (arkosic conglomerate, arkose, wacke, siltstone). Locally abundant tuff, breccia, polylithic pyroclastic breccia and tuffaceous sedimentary rocks.
Buchans River	400 m	Felsic tuff, rhyolite, rhyolite breccia, pyritic siltstone, wacke, polylithic breccia-conglomerate, granite boulder conglomerate, high-grade in silty and transported sulphide orebodies.
Ski Hill	1000 m	Basaltic to andesitic pyroclastic rocks, breccia, pillow lava, massive flows. Minor felsic tuff.
Lundberg Hill	1000 m	Felsic pyroclastic rocks, coarse pyroclastic breccia, rhyolite, tuffaceous wacke, siltstone, lesser basalt, minor chert and magnetite iron formation.

Table 2.2: Summary of turbidite features within the lower basaltic andesite

Turbidite Division	Average thickness (m)	Average grain size (mm)	Contact	Grain sorting	Sedimentary structures
T_a	0.05-2	0.42	sharp	moderate	coarse-tail to normally graded
T_b	0.05-0.2	0.25	gradational	well	planar laminae
T_c	<0.05	0.21	gradational	well	none
T_d	0.02-0.61	<0.0625	sharp	well	diffuse laminae, flames (<1cm)

Table 2.3: Characteristics of Lower sedimentary sequence breccias

Lithology	Matrix	Clast type and abundance	Contacts
rhyodacite-dominated breccia	matrix supported (70%) consists of <1 cm angular lithic fragments and altered glass shards	90% rhyodacite clasts 10% basaltic clasts <1% sulphide clasts	undrilled lower (BOH) sharp, conformable upper
siltstone with interbedded rhyodacite breccia	siltstone	clast supported (>80%) 100% rhyodacite clasts <1% sulphide clasts	sharp, +/- scoured basal sharp & irregular, or gradational upper
massive rhyodacite- dominated breccia with interbedded turbidite	matrix supported (65%) coarse silt to sand-sized detritus	75% flow banded rhyodacite 15% basalt 10% sedimentary 1% cherty rhyodacite	gradational lower eroded upper (TOH)

Table 2.4: Characteristics of upper sedimentary sequence lithologies

Lithology	Matrix	Clast type and abundance	Contacts
rhyodacite-dominated breccia	silicified coarse silt to sand-sized	matrix supported (70%) 40-80% rhyodacite 20-30% basalt <10% scoreacoues basalt <10% sedimentary <1% massive sulphide	sharp, irregular lower gradational upper
sandstone to siltstone breccia	sandstone/siltstone	brecciated coarse silt to sandstone	sharp lower sharp upper
rhyodacite tuff	alteration: quartz + clay	>50% feldspar phenocrysts 20% quartz phenocrysts 10% lithic fragments	sharp lower sharp upper
rhyodacite polymictic breccia	pyritic siltstone to coarse sandstone	clast supported (>70%) Rhyodacitic (60-70%) Basalt (15-20%) 10-15% sedimentary 1% biotite-granodiorite 2% massive sulphide	sharp and irregular lower sharp, +/- sheared upper

Chapter 3: Chemostratigraphy of Mineralized and "Barren" Volcanic rocks within the Lundberg and Engine House Zones

3.1 Abstract

The primary stratigraphy within the Buchans Mining Camp has been long known to control the distribution of mineral deposits. A predictable geochemical stratigraphy would thus be an invaluable tool in exploration. The Lundberg and Engine House Zone polymetallic stockworks are hosted by Ski Hill Formation (SHF) basaltic andesite and andesite, and to a lesser extent, Buchans River Formation (BRF) rhyodacite. The Lucky Strike hanging-wall succession (LSS) rhyolite structurally caps the mineralization. These rocks have well-defined calc-alkaline trends with high La/Yb ratios and well defined Nb, Zr, Eu, and Ti anomalies characteristic of a volcanic arc setting. The andesite formed by fractionation of the basaltic andesite and occurs towards the top of the mafic pile and marks the contact between the SHF and BRF providing a great stratigraphic and geochemical vector to ore. The geochemical differences between the rhyodacite and rhyolite units may be explained by either multiple partial metls or shallow fractional crystallization. The rhyolite of the LSS has an overall depletion in HREE relative to the BRF rhyodacite providing a strong geochemical fingerprint for barren (LSS) versus mineralized (BRF) stratigraphy. Host rocks of the Oriental and Maclean mine sequences and Clementine prospect are geochemically identical to the host rocks of the Lundberg Zone indicating that geochemistry of felsic volcanic rocks can be used for exploration in Buchans to identify prospective units.

3.2 Introduction

Geochemistry is an invaluable tool for delineating both regional tectonic environments (e.g., Swinden, 1991) and local stratigraphic units (e.g. Swinden et al., 1989) favourable for VMS mineralization. Within the Buchans Mining Camp, local stratigraphy is known to control the location of VMS deposits (Thurlow and Swanson, 1987); thus, lithogeochemical fingerprinting may aid in targeting new VMS mineralization. However, few geochemical studies have been undertaken

to test the geochemical characteristics of the lithostratigraphic units hosting mineralization. Initial studies concentrated on mineralized versus barren assemblages; however, no distinguishing geochemical signatures were found (Strong, 1984). Jenner (2000) defined multiple "cycles" of volcanism that occur throughout different stratigraphic units, but found limited potential for geochemistry as exploration tools or chemostratigraphic markers. The apparent diversity of "cycles" within petrographically similar units may suggest that correlations based solely on field mapping are not entirely correct.

This chapter aims to re-evaluate the stratigraphy in close proximity to the historic Lucky Strike deposit and in the least structurally disrupted duplex of the Buchans Mining Camp based on detailed sampling and analysis of the volcanic rocks. The stratigraphic succession in proximity to Lucky Strike is shown to be predictable both petrographically and geochemically. In particular, the felsic volcanic rocks associated with mineralization have geochemical fingerprints that are distinct from barren felsic volcanic rocks. These results are compared to other mineralized zones in the Buchans Group to test their applicability to other ore horizons and as camp-scale exploration vectors.

3.3 Sampling and Analytical Methods

Eighty three whole rock samples were collected from drill core adjacent to the Lucky Strike pit to characterize the different stratigraphic units (Figures 3.1 and 3.2). Whole rock samples were collected from the majority of stratigraphic units: upper basaltic andesite (SHF), rhyodacite from the lower sedimentary sequence (BRF) lens within the upper basaltic andesite, rhyodacite autobreccia (BRF) above the basaltic andesite, rhyodacite from the upper sedimentary sequence (BRF) adjacent to rhyodacite autobreccia, quartz-phyric rhyodacite tuff (BRF), rhyolite (LSS), and late diabase dykes (Figures 3.1 and 3.2). These samples ranged from weakly altered with most primary volcanic textures preserved to intensely altered with no original textures preserved.

All analytical work was carried out at Activation Laboratories Ltd., Ancaster Ontario. Results are presented in Appendix 3.1. A combination of lithium metaborate/tetraborate fusion ICP-

ES and trace element ICP-MS were used to analyse major and trace elements, respectively. Samples were crushed using mild steel to <1.7 mm, mechanically separated with a rifle splitter, and pulverized to <105 microns. Mild steel may introduce up to 0.2 wt% Fe contamination. Pulverized samples were first mixed with lithium metaborate/tetraborate then placed in an induction furnace. The fused product was then dissolved with 5% nitric acid and spiked with standards to cover the entire mass range. The solution was then analyzed by ICP-ES and ICP-MS after 3 blanks and 3 controls were first prepared and analyzed. After the samples were run, two additional controls were analyzed. A duplicate or split sample was analyzed every 15 samples for additional quality control (Appendix 3.2).

3.4 Lithogeochemistry

In studies of subgreenschist metavolcanic rocks in VHMS districts elements such as SiO_2, CaO, Na_2O, and MgO have been shown to be mobile under original hydrothermal conditions (e.g., Lentz, 1998), whereas TiO_2, Zr, Nb and REE remain immobile (e.g.,Whitford et al., 1988). The geochemistry of volcanic rocks in the Lundberg and Engine House zones are in agreement with these studies and generally show Zr and TiO_2 immobility (e.g. Figure 3.3A). The LREE are weakly mobile, but are still representative of primary values (Figure 3.3B), whereas HREE remain highly immobile (Figure 3.3C). The primary geochemistry of these heavily altered volcanic rocks is therefore best illustrated by the compatible (e.g. TiO_2) and incompatible (e.g. HFSE and REE) immobile elements (e.g., Barrett and Maclean, 1994). The compositions of altered and least-altered samples are presented in Table 3.1. Tectonic discrimination diagrams are presented in Figures 3.4 to 3.7 and 3.9, f-series rhyolite classication in 3.10, and normal mid-ocean ridge basalt (NMORB) multi-element plots (Sun and McDonough, 1989) in Figures 3.8 and 3.11.

Upper basaltic andesite (SHF)

The upper basaltic andesite has a wide range of Zr/TiO_2 and Nb/Y ratios which plot within the basaltic andesite and andesite fields of Winchester and Floyd (1977) (Figure 3.4). The andesitic

samples have slightly higher Zr/TiO_2 ratios but similar Nb/Y ratios compared to more primitive samples. The most primitive samples are clinopyroxene + feldspar-phyric rocks which have the lowest HFSE and REE abundance (e.g. Figure 3.4) and generally contain higher Cr (~175-520 ppm) and Ni (~50-130 ppm) than feldspar-phyric samples (<175ppm Cr, <50ppm Ni; Figure 3.5). The andesitic samples typically have undetectable Ni and Cr (<20 ppm); however, one sample has significant concentrations (e.g., sample 8; Figure 3.5). Andesite samples near the BRF-SHF contact have average Zr/TiO_2 values of 0.014 (range from 0.01-0.02; Figure 3.6). Both the basaltic andesite and andesite plot within the calc-alkaline basalt field on tectonic discrimination diagram of Cabanis and Lecolle (1989) (Figure 3.7).

NMORB-normalized multielement diagrams show enrichment in Th and LREE, distinct negative Nb, Zr, Eu, and Ti anomalies, and a flat HREE profile (Figure 3.8A). The andesite displays an identical but enriched profile (Figure 3.8A).

Rhyodacite from the lower sedimentary sequence (BRF)

One representative felsic clast (representative of 75% of the clast population) was sampled from the lower sedimentary sequence (G112, H-08-3362; Figure 3.1). The sample plots in the field of rhyodacite/dacite on the Winchester and Floyd (1977) discrimination diagram (Figure 3.4). The Zr/TiO_2 ratio (0.0423) is much higher than the upper basaltic andesite. On a NMORB-normalized multielement diagram, the rhyodacite is characterized by extreme Th and overall LREE enrichment and strong Nb, Ti and HREE depletion (Figure 3.8B). Ta/Yb plots indicate a volcanic arc affinity (Pearce et al., 1984) (Figure 3.9) and La/Yb ratios a FII rhyolite affinity as defined by Lesher et al. (1986) (Figure 3.10).

Rhyodacite (BRF)

One representative sample of the rhyodacite (G070) was taken from, H-08-3378 (Figure 3.1). Zr/TiO_2 (0.05) and Nb/Y (0.14) ratios for this sample are in the rhyodacite/dacite field on a Winchester and Floyd (1977) discrimination diagram (Figure 3.4). These ratios are similar to that of

the rhyodacite clast from the lower sedimentary sequence. The NMORB-normalized multielement diagram of the rhyodacite shows Th and LREE enrichment and Nb, Zr, Eu, and Ti depletion, and a flat but slightly enriched HREE profile relative to the rhyolite unit (Figure 3.8C). Ta/Yb plots indicate volcanic arc affinity (Figure 3.9).

Rhyodacite from the upper sedimentary sequence (BRF)

Twelve samples of rhyodacite tuff and one representative felsic clast (representative of >70% of the clast population; sample G030) were sampled from the polymictic breccia in the upper sedimentary sequence (Figure 3.1). Both plot within the rhyodacite/dacite field, defined by Zr/TiO_2 and Nb/Y ratios identical to the rhyodacite clast from the lower sedimentary sequence (Figure 3.4). Nb/Y values range from 0.10-0.20 well below the subalkaline-alkaline boundary (Nb/Y=0.7) reflecting a strong subalkaline composition. Zr/TiO_2 ratios average 0.042 (from 0.029-0.059) and are similar to the rhyodacite from the lower sedimentary sequence. NMORB-normalized multielement profiles are characterized by Th and LREE enrichment and Nb, Zr, Eu, and Ti depletion, and a flat but slightly enriched HREE profile compared to the rhyolite unit (Figure 3.8D). The rhyodacite from the upper sedimentary sequence can be further classified as FII-type based on chondrite-normalized La/Yb_N versus Yb_N values (Figure 3.10).

Quartz-phyric rhyodacite tuff (BRF)

The quartz phyric rhyodacite tuff plots in two discrete fields on Figure 3.4. This is the result of sampling of rhyodacite tuff with and without 1cm quartz crystals within the Engine House Zone; Zr/TiO_2 ratios average 0.0465 (quartz-phyric) and 0.0516 (not quartz-phyric). On NMORB-normalized multielement plots rhyodacite samples are enriched in Th and LREE and depleted in Nb, Zr, Eu, and Ti with flat HREE profiles; however, the samples without 1cm quartz crystals are distinctly depleted in HREE (Figure 3.8E).

Rhyolite (LSS)

The rhyolite unit has a distinct Nb/Y ratio (0.28) compared to rhyodacite from the lower sedimentary sequence, rhyodacite autobreccia conformable with upper basaltic andesite, and rhyodacite from the upper sedimentary sequence (Figure 3.4). Zr/TiO_2 ratios average 0.059 and range from 0.052-0.07. NMORB-normalized multielement plots of the rhyolite show Th and LREE enrichment and Nb, Zr, Eu and Ti depletion with concave up and depleted HREE profiles compared to all rhyodacite-like samples (Figure 3.8F). Ta/Yb ratios indicate a volcanic arc affinity and are distinctly higher thanall rhyodacite-like rocks (Figure 3.9).

Diabase

Two diabase samples (61, 101) were collected from separate horizons within the Lundberg Zone. Sample 61 was collected from the diabase occupying the shear zone separating the rhyolite unit from the upper sedimentary sequence (Figure 3.1), and sample 101 is from an intrusion within the lower basaltic andesite (Figure 3.1). Both diabase samples plot within the basaltic andesite field of Figure 3.4A. Zr/TiO_2 and Nb/Y ratios are 0.0054 and 0.131 (G061) and 0.0089 and 0.178 (G101), respectively. NMORB-normalized multielement plots of the diabase samples show Th and LREE enrichment and Nb, Zr, Ti and HREE depletion, similar to the upper basaltic andesite (Figure 3.11A). The diabase plots within the calc-alkaline field of Cabanis and Lecolle (1989; Figure 3.7). Sr concentrations are among the highest of all samples (>250ppm) and likely reflect the relative lack of alteration within the late dykes.

3.5 Lithogeochemical Stratigraphy of the Lundberg and Engine House zones

The upper basaltic andesite which conformably underlies the rhyodacite and upper sedimentary sequence (Figure 3.1) has typical calc-alkaline chemical characteristics. A slightly more fractionated basaltic andesite occurs at the top of the mafic pile. Felsic clasts in the lower sedimentary sequence within the basaltic andesite are identical to the overlying rhyodacite unit in

terms of their Nb/Y, Zr/TiO_2, and N-MORB-normalized multielement profile. However, the Nb/Y and/or Zr/TiO_2 ratios are distinctly higher than in some samples of the rhyodacite (G166, G177). The lower sedimentary sequence is enriched in HREE compared to the rhyolite, clearly distinguishing these as separate units. The trace element geochemistry of the felsic clasts in the lower sedimentary sequence suggest that they may have been derived from a source similar to the BRF rhyodacite autobreccia.

The upper sedimentary sequence conformably overlies the upper basaltic andesite and flanks the rhyodacite unit (Figure 3.1). The majority of samples from the upper sedimentary sequence are from tuffaceous layers; however, one representative felsic clast from the polymictic breccia was also sampled (G030; Figure 3.1). They have identical trace element profiles and Nb/Y and Zr/TiO_2 ratios and are distinct from the rhyolite unit. This suggests that the upper sedimentary sequence represents flanking volcaniclastic and pyroclastic deposits to a possible rhyodacite dome complex of the BRF.

The quartz-phyric rhyodacite structurally overlies the Lundberg/Engine House Zones across the Airport Thrust (e.g., LHF of Thurlow et al., 1992; Figure 2.4). These rocks have bimodal compositions (with and without 1 cm quartz crystals). The samples with 1 cm quartz crystals (former prominent quartz) have trace element profiles and Nb/Y and Zr/TiO_2 ratios identical to the rhyolite (LSS) unit. However, samples without 'prominent quartz' are identical to the rhyodacite autobreccia and flanking upper sedimentary sequence (rhyodacite tuff layers and aphyric rhyodacite clasts). The abundance of quartz crystals varies along this stratigraphic horizon, but the rhyodacite breccia geochemistry appears most representative of this unit. This unit is thus correlated with BRF rhyodacite and not the LHF of Thurlow et al. (1992). The alternative explanation is that it forms part of a klippe of Mary March Brook Formation (Zagorevski, 2009) as it shares some of the chemical characteristics of those rocks.

The rhyolite unit, which structurally overlies the upper sedimentary sequence across a shear zone intruded by diabase (Figure 3.1) is geochemically distinct from the felsic clasts in the lower sedimentary sequence, the rhyodacite autobreccia, and the felsic tuff layers and aphyric clasts of the

upper sedimentary sequence. This strongly suggests that the rhyolite unit originates from an unknown unit lower in the stratigraphy or outside of the study area. The diabase unit is geochemically similar to the basaltic andesite, but has a higher Zr content and no pronounced Eu anomaly. The diabase has slightly lower Zr/TiO_2 values than the upper basaltic andesite with over 2000 ppm more Ti and higher transition metal content.

Four geochemically distinct volcanic units are thus recognized from base to top within the Lundberg and Engine House stratigraphy: upper basaltic andesite, andesite or fractionated basaltic andesite, rhyodacite, and structurally emplaced rhyolite. The base of the Lundberg Zone (and Engine House Zone) is marked by extensive subaqueous, calc-alkaline basaltic andesite with fractionation occurring intermittently in the later stages of mafic volcanism. The conformable lower sedimentary sequence has chemistry identical to the rhyodacite and felsic material located at a higher position in the stratigraphy (Figure 3.1). Its position within the upper basaltic andesite indicates that rhyodacite volcanism of the BRF occured at several stratigraphic horizons, both within and above the upper basaltic andesite (SHF), and thus contemporaneously with the upper basaltic andesite. The rhyodacite and upper sedimentary sequence (both rhyodacite tuff and clasts) are interpreted to have formed from pyroclastic eruptions (rhyodacite tuff) and mass flows (polymictic breccia) flanking a growing rhyodacite dome (H-08-3378 to H-08-3406). The quartz-phyric rhyodacite (BRF) represents a lateral facies variation within Lundberg Zone units. The geochemistry of the rhyolite unit structurally overlying the upper sedimentary sequence is distinct, consistent with it being a structurally emplaced unit.

3.6 Implications for Buchans Group Stratigraphy

Previous classification of the Buchans Group places the upper basaltic andesite in the SHF, the lower sedimentary sequence, rhyodacite, upper sedimentary sequence, and quartz-phyric rhyodacite in the BRF. In Chapter 2, it was concluded that the rhyolite belongs to the Lucky Strike hanging-wall succession (LSS). The upper basaltic andesite was the only mafic volcanic unit studied

and therefore is most reasonably assigned to the SHF. The geochemistry of the felsic material in the lower sedimentary sequence lens is consistent with it being grouped with the rhyodacite and upper sedimentary sequence in the BRF. This study further suggests that rocks of the BRF are locally interfingered with basaltic andesite of the SHF. The quartz-phyric rhyodacite of the Engine House Zone also belongs to the BRF. The different geochemistry of the rhyolite unit compared to the rhyodacite, upper sedimentary sequence, and quartz-phyric rhyodacite suggests that the LSS is a separate unit.

A comparison of geochemical data within rocks from elsewhere in the Buchans camp was made using the geochemical database of Zagorevski (2008). No differences were observed between the REE profiles of the basalt from the Lundberg Zone (this study), two samples collected from the SHF north of the town of Buchans, and at the Clementine prospect (Figure 3.11D). Felsic volcanic rocks from the BRF and LSS at Oriental, Maclean, and Clementine are identical to those of the Lundberg and Engine House zones. Three samples from the Oriental area analyzed by Zagorevski (2008) are identical to the rhyodacite and rhyolite of the Lundberg Zone (Figure 3.11C). Two samples from the Clementine area and one from the Maclean extension ore horizon (Zagorevski, 2008) are also similar to rhyodacite of the BRF (Figure 3.11B and C). The overall consistency of the geochemistry of both mafic and felsic volcanic rocks throughout the camp suggests that the lithogeochemical stratigraphy of the Lundberg and Engine House zones may be used to target undiscovered resources outside the immediate area of Lucky Strike.

3.7 Genesis of Buchans Group Lithologies

The mafic rocks of the Lundberg Zone (upper basaltic andesite) have low REE concentrations and strongly depleted HFSE (e.g. Nb = ~0.2x NMORB) suggesting a source that is similar to, but more depleted than MORB (cf. Winter, 2001; Figure 3.8A). The lack of extreme HREE depletion indicates that garnet was not in equilibrium with the melt and constrains the depth of melting to < ~ 40km (Hart et al., 2004).

The geochemical variation within the Lundberg Zone may be explained by Fe-Ti fractionation or partial melting. The mafic-intermediate unit (andesite) plots on a separate alteration line from the basaltic andesite which indicates that it formed by shallow crystal fractionation of a basaltic andesite magma (Figure 3.3). The lack of various intermediate rock compositions (Daly Gap) may be explained by shallow fractional crystallization (Clague, 1987). The felsic units of the Lundberg Zone may have formed by either partial melting or fractional crystallization. The rhyodacite and rhyolite units have widely different La/Yb and Dy/Lu ratios (Figure 3.8) indicating that two separate melts may have been required. However, both the Zr/TiO_2 ratio versus depth plot (Figure 3.6) and the progressively deepening Ti anomaly in Figure 3.8 could be explained by Fe-Ti fractionation.

3.8 Implications for Exploration

VMS are commonly associated with large-scale alteration of host rocks at a break in mafic volcanism and the onset of felsic volcanic activity. However, subtle geochemical features within many stratigraphic units suggests that exploration should investigate each unit individually. The upper basaltic andesite is recognized to be equivalent to the SHF and is the main target for stockwork mineralization. The BRF rhyodacite autobreccia lies along the same stratigraphic horizon as the upper sedimentary sequence (part of the BRF), and is the main target for associated massive, exhalative, and transported sulfides. The upper sedimentary sequence is recognized as the main ore-horizon which produced all of the Buchans deposits and has favourable FII rhyolite geochemistry. Massive sulfide clasts within the BRF lower sedimentary sequence indicate contemporaneous sulfide deposition and resedimentation below the BRF-SHF contact. However, the LSS rhyolite, which structurally overlies the upper sedimentary sequence and rhyodacite has FI rhyolite geochemistry. Its distinctive chemistry indicates that it is structurally emplaced and unrelated to FII mineralization, although weak alteration (Chapter 4) indicates that it may be related to distal hydrothermal activity.

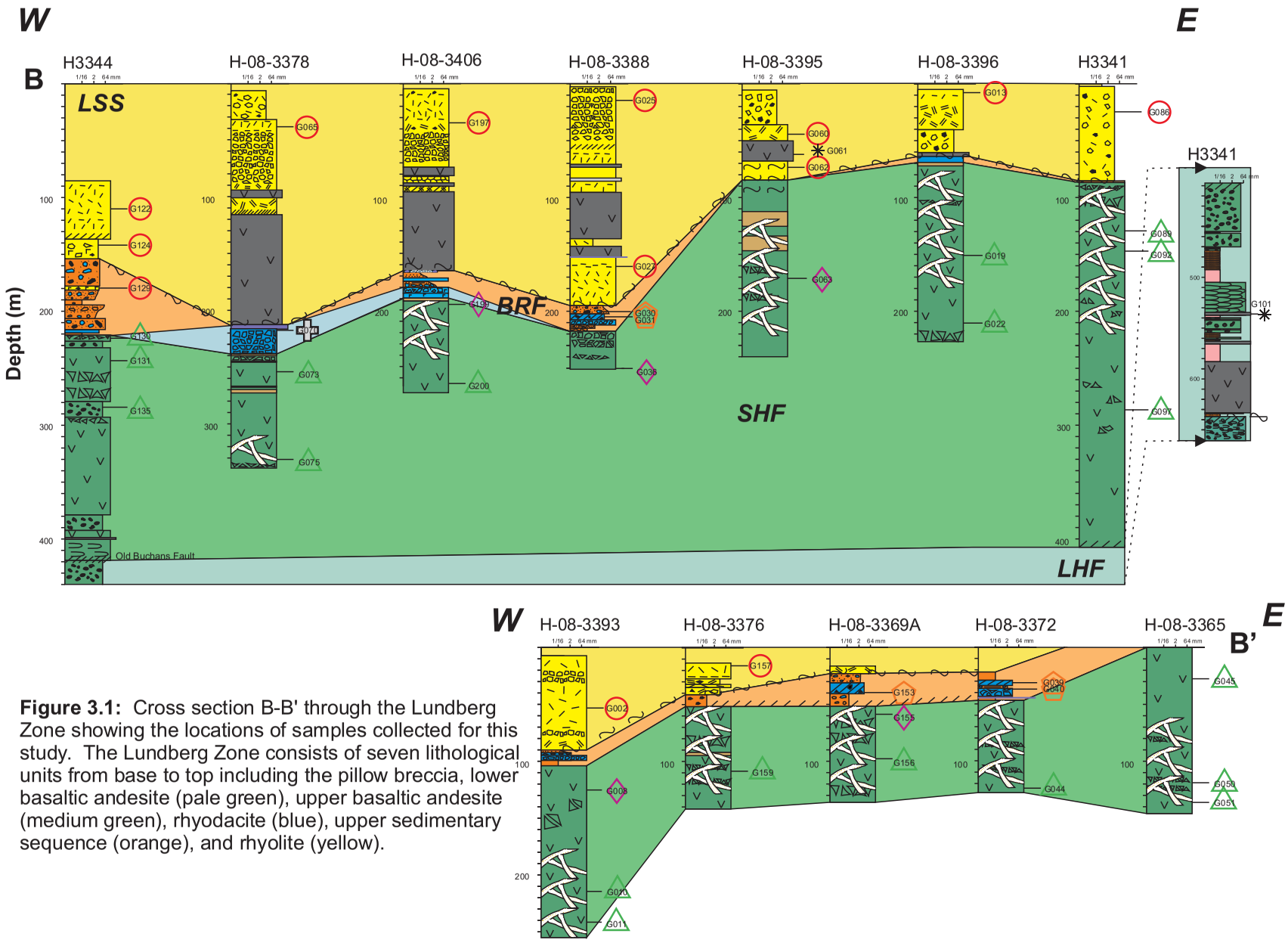

Figure 3.1: Cross section B-B' through the Lundberg Zone showing the locations of samples collected for this study. The Lundberg Zone consists of seven lithological units from base to top including the pillow breccia, lower basaltic andesite (pale green), upper basaltic andesite (medium green), rhyodacite (blue), upper sedimentary sequence (orange), and rhyolite (yellow).

Lundberg lithologies

diabase/intermediate dike (weakly porphyritic/amygdaloidal)
rhyolite (moderately porphyritic/flow banded)
rhyolitic breccia
crystal-rich rhyolite tuff
exhalative barite
'hydrothermal upflow zone'
sandstone/mudstone
sandstone/polylithic breccia
rhyodacite (moderately porphyritic/brecciated)
rhyodacite (aphyric/rhyodacite tuff)
moderately porphyritic/amygdaloidal and hyaloclatite basalt
bedded chert
mafic tuff/pillow breccia

Symbols

Zn-Pb-Cu stockwork veins

Shear zone

Brittle fault zone

Lithogeochemistry sample location

diabase

rhyolite

rhyodacite with 1 cm quartz phenocrysts

rhyodacite w/o 1 cm quartz phenocrysts

upper sedimentary sequence

rhyodacite

rhyodacite autobreccia

lower sedimentary sequence

andesite

basaltic andesite

Lithological legend of the various rock types and lithofacies which occur in the Lundberg and Engine House zones. 7 chemostratigraphic units were identified; the location of each sample is marked by its respective symbol.

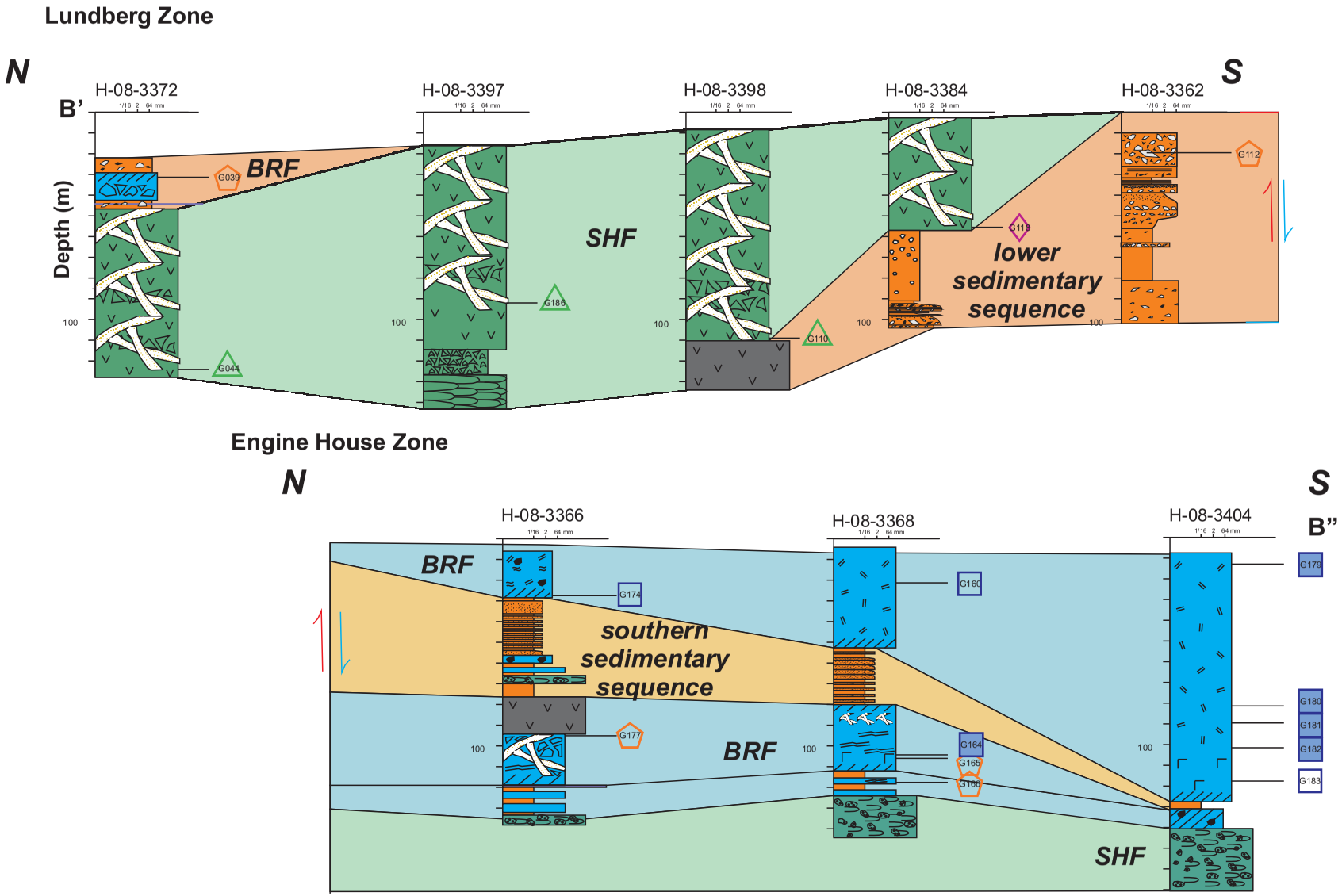

Figure 3.2: Cross section B'-B" through the Lundberg and Engine House zones showing the locations of samples collected for this study.

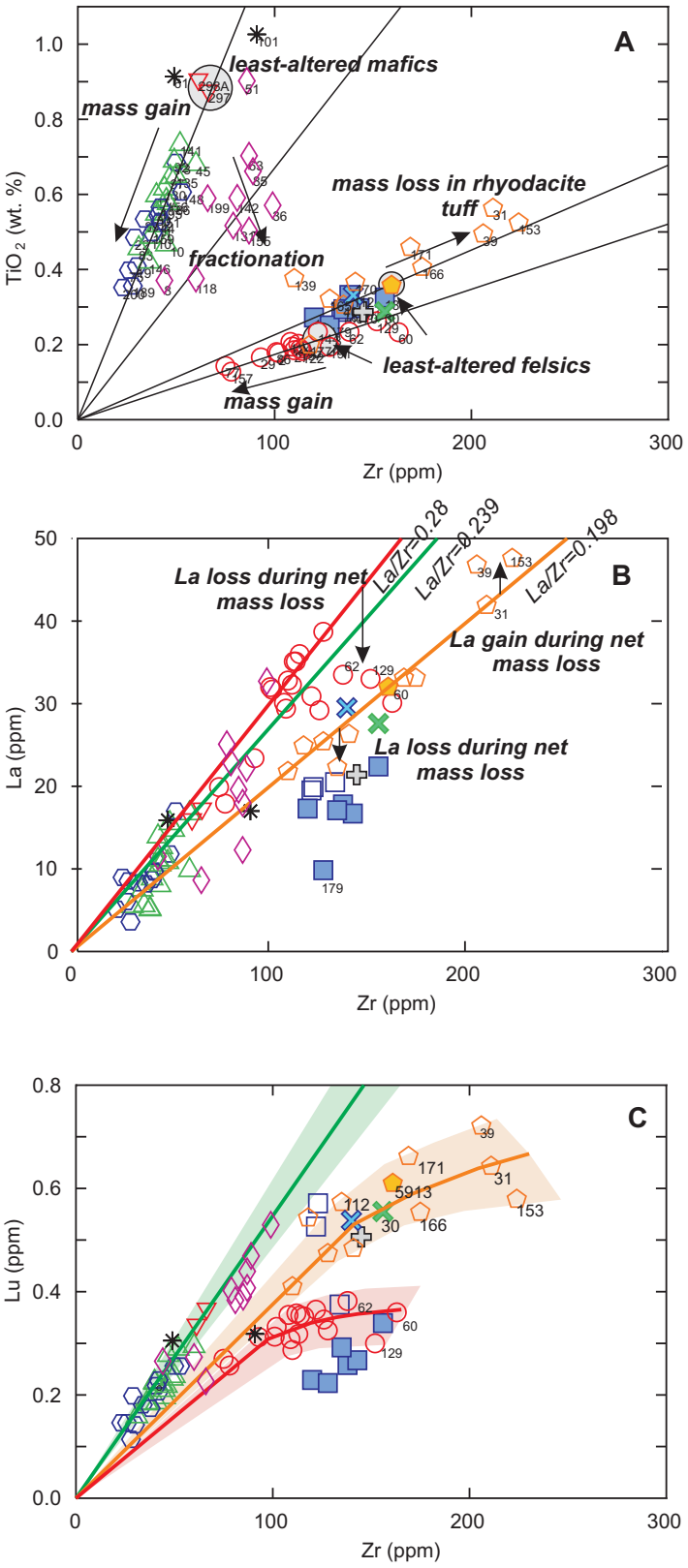

Legend

- diabase
- rhyolite
- rhyodacite with 1 cm quartz phenocrysts
- rhyodacite w/o 1 cm quartz phenocrysts
- upper sedimentary sequence
- rhyodacite
- rhyodacite autobreccia
- lower sedimentary sequence
- andesite
- basaltic andesite

Figure 3.3: A. TiO_2 versus Zr demonstrating immobility of the sample set and fractionation of the upper basaltic andesite. Variation in the TiO_2/Zr concentration along alteration lines that project through the origin depict dilution or concentration due to mass gain or loss during alteration, respectively. B. Plot of La versus Zr demonstrating minor mobility of La within the basaltic andesite and rhyolite units. Lines through the origin represent the average La/Zr content of the respective units. C. Plot of Lu versus Zr demonstrating the immobility of Lu. The shape of the felsic curves demonstrates the relative incompatibility of Zr and Lu.

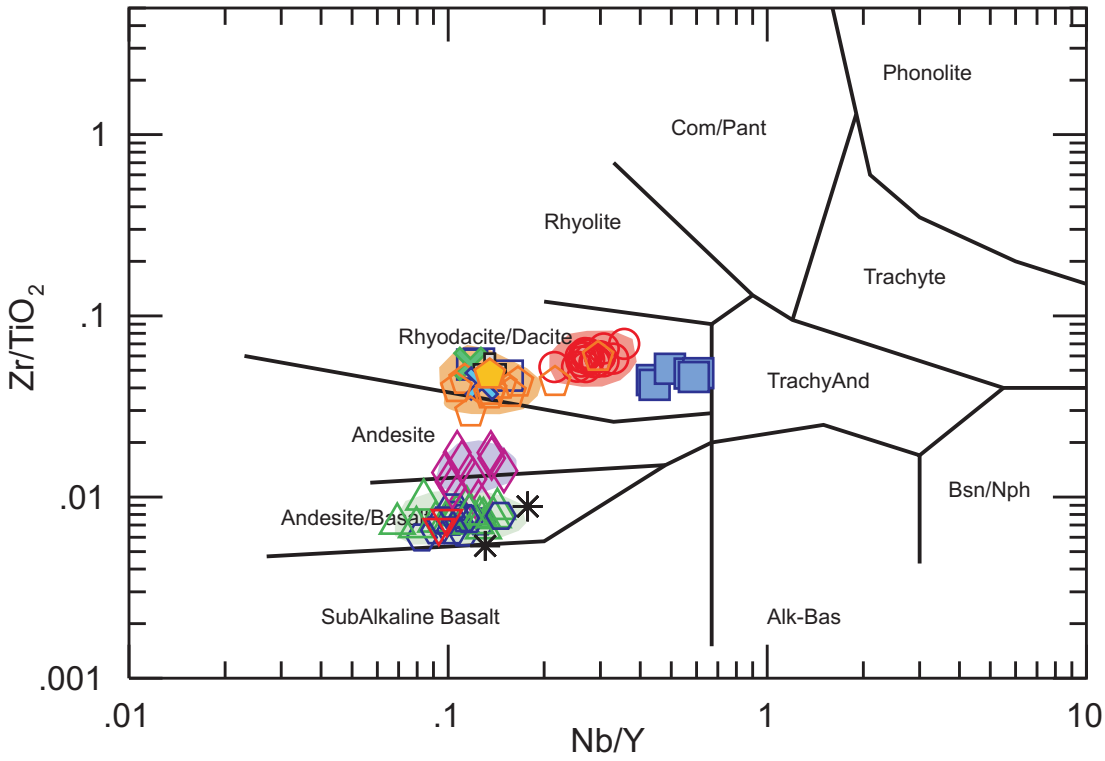

Figure 3.4: Winchester and Floyd (1977) discrimination diagram of the four main geochemical groups: basaltic andesite, andesite, rhyodacite, and rhyolite. A range of Zr/TiO_2 ratios observed between the basaltic andesite and andesite unit indicate fractionation of the basaltic andesite; however, the lack of any values between the andesite and felsic units indicate the felsic units were not part of a fractionated suite and probably were formed by partial melting.

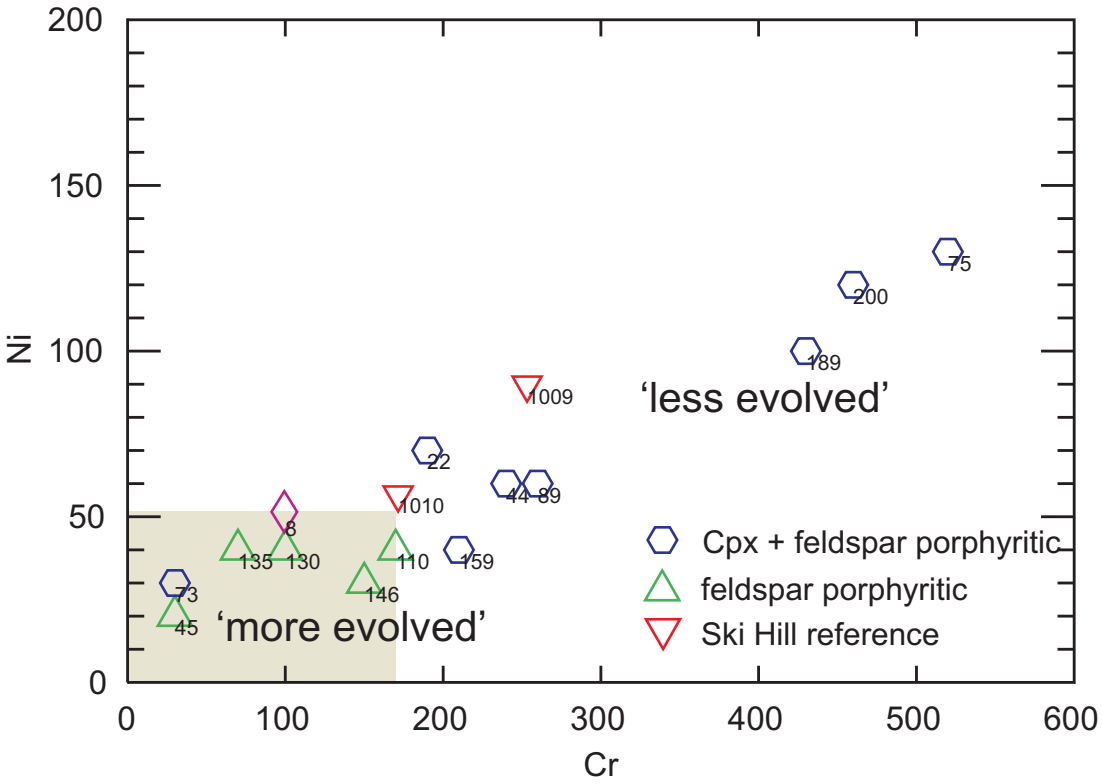

Figure 3.5: Cr versus Ni concentration in Clinopyroxene-feldspar phyric versus feldspar-phyric basaltic andesite. Clinopyroxene-bearing basaltic andesite has a more primitive composition (higher Cr and Ni concentrations) than the basaltic andesite with only feldspar phenocrysts.

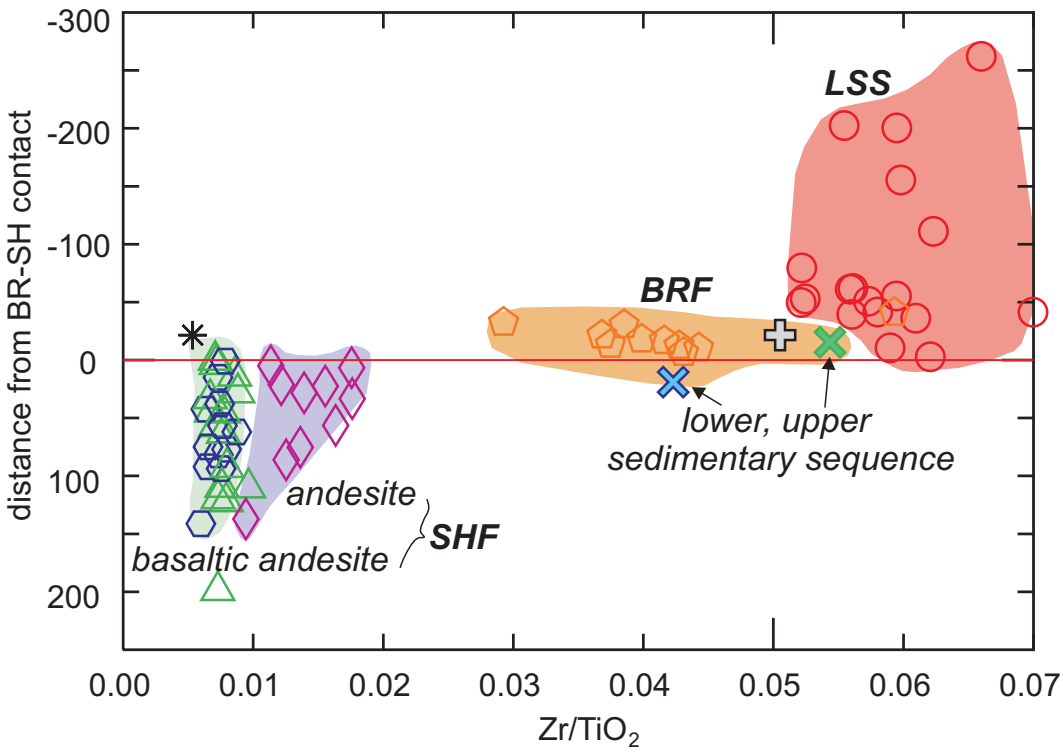

Figure 3.6: Zr/TiO_2 versus distance from the SHF-BRF contact. The plot distinguishes all rock units from the lowermost basaltic andesite and andesite, conformably overlying rhyodacite, and structurally overlying rhyolite. The andesite unit is clearly more abundant near the top of the mafic volcanic pile; whereas, mafic volcanic rocks are completely absent in the upper part of the stratigraphy. The rhyodacite and rhyolite units have different, but overlapping Zr/TiO_2 ratios indicating that they may be derived from a similar source.

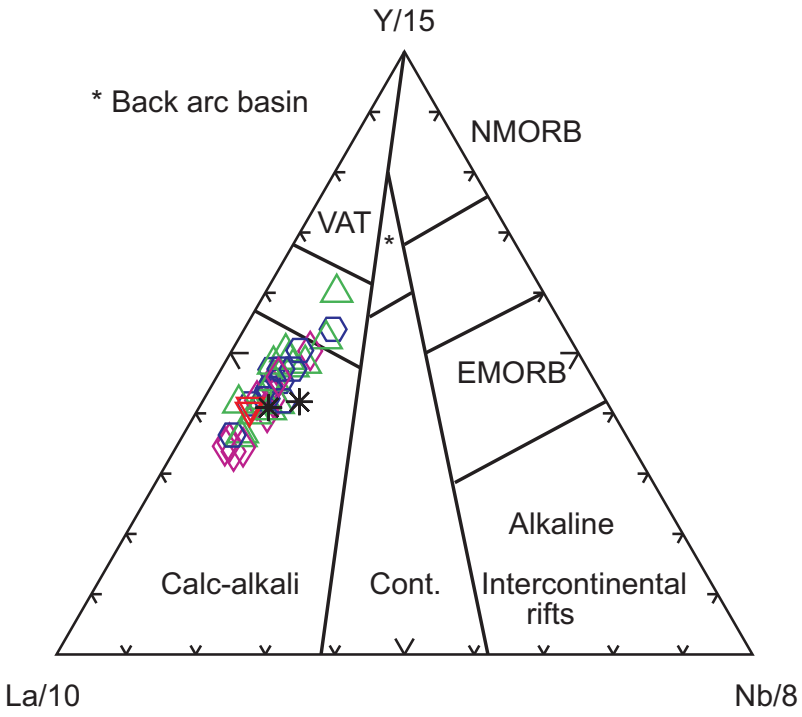

Figure 3.7: La-Nb-Y plot of Cabanis and Lecolle (1989) indicating a calc-alkaline arc setting for the basaltic andesite. The high La and low Nb content is characteristic of an arc setting where La is likely derived from metasomatism above the subducting plate and Nb is inherited from the mantle. The lower Y content distinguishes calc-alkaline from tholeiitic arc environments.
VAT = volcanic arc tholeiite
Cont. = continental crust

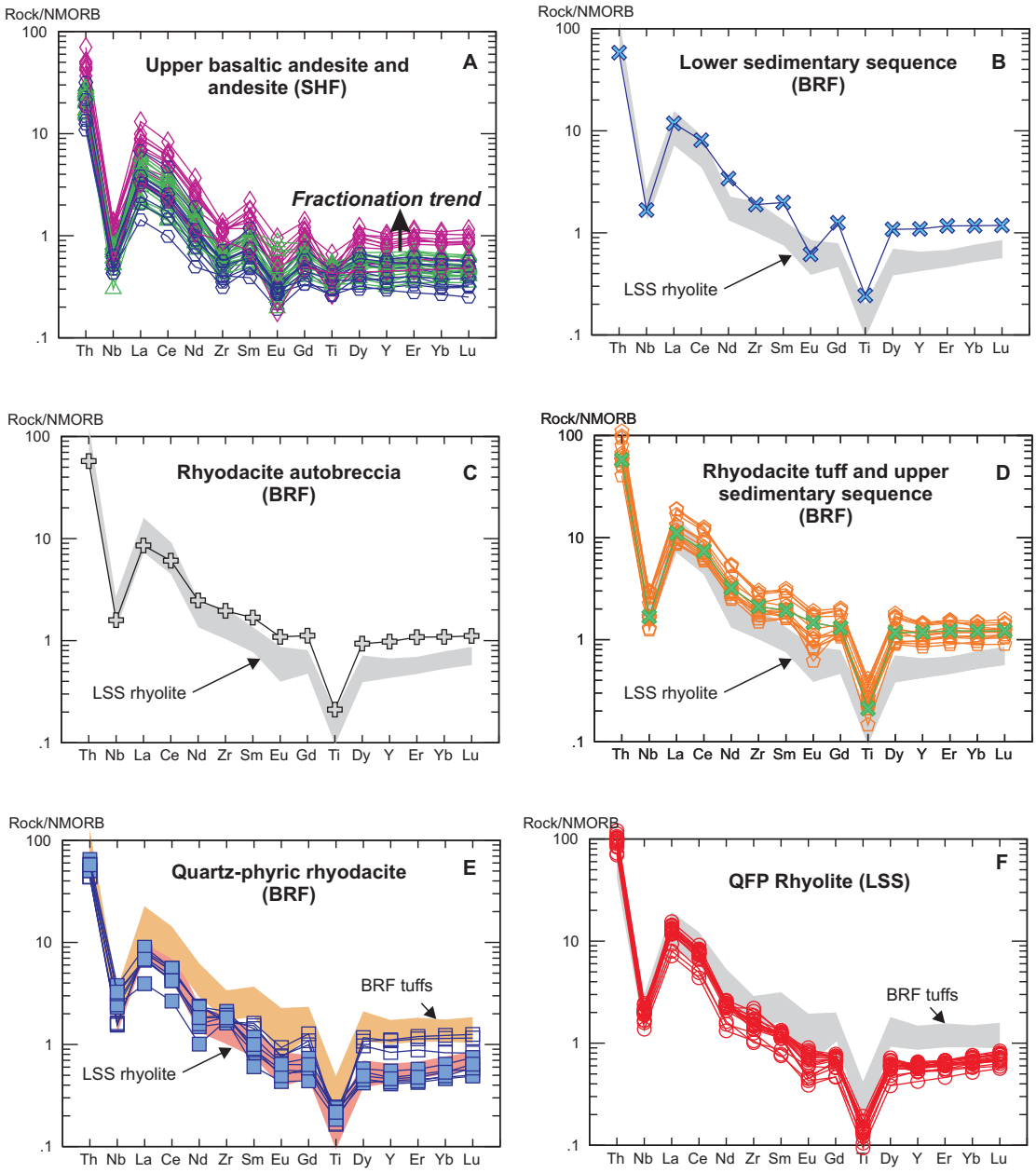

Figure 3.8: The andesite unit is determined to form by fractionation of the upper basaltic andesite. The lower sedimentary sequence, rhyodacite autobreccia, and rhyodacite tuff were determined to have identical geochemistry that is distinct from the rhyolite unit. All samples are normalized to NMORB of Sun and McDonough (1989). A. NMORB-normalized multielement plot of the upper basaltic andesite (SHF) demonstrating fractionation. B. NMORB-normalized multielement plot representing the clast population of the lower sedimentary sequence (BRF). The grey shading shows the range of REE values of the rhyolite unit. C. NMORB-normalized multi element plot of the rhyodacite autobreccia (BRF). The grey shading shows the range of REE values of the rhyolite unit. D. NMORB-normalized multielement plot of the upper sedimentary sequence and rhyodacite tuff units (BRF). The grey shading shows the range of REE values of the rhyolite unit. E. NMORB-normalized multielement plot of the structurally capping rhyodacite with (filled blue squares) and without (unfilled blue squares) 1 cm quartz phenocrysts of the Engine House zone (formerly named the 'prominent quartz sequence' by Thurlow and Swanson (1981) and the Lundberg Hill Formation by Thurlow and Swanson (1987)). F. NMORB-normalized multielement plot of the structurally emplaced rhyolite unit (LSS). The grey shading shows the range of REE values of the rhyolite unit.

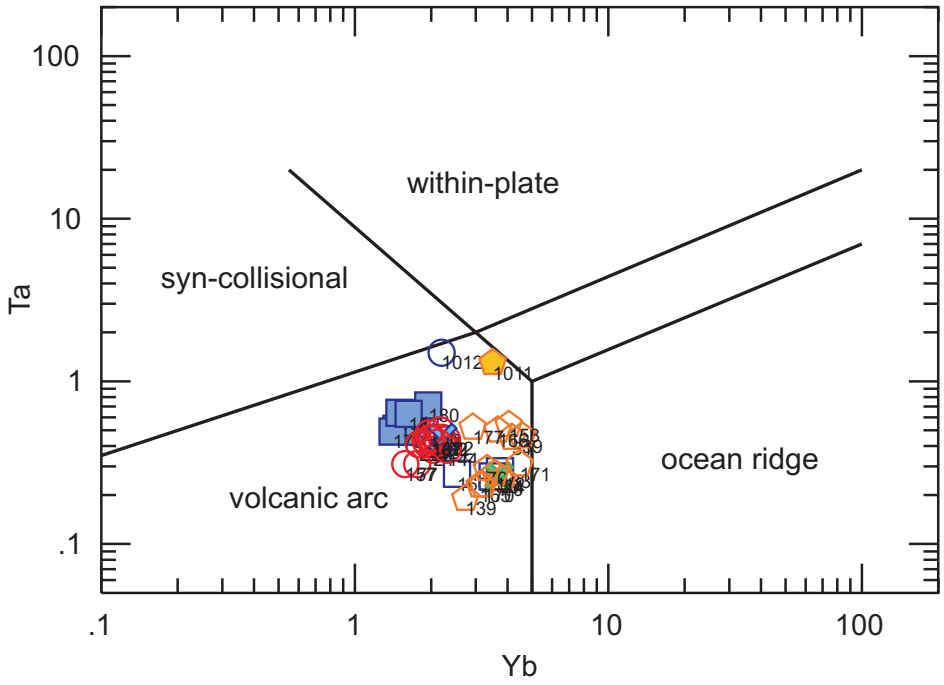

Figure 3.9: Ta versus Yb plot of felsic volcanic rocks of the Lundberg Zone. This plot indicates an I-type volcanic arc setting. Ta is analagous to Nb and is strongly depleted in arc volcanic rocks since it is not liberated during metasomatism of the mantle wedge or dehydration of the downgoing slab. Yb is a strongly compatible element and is retained in the source region.

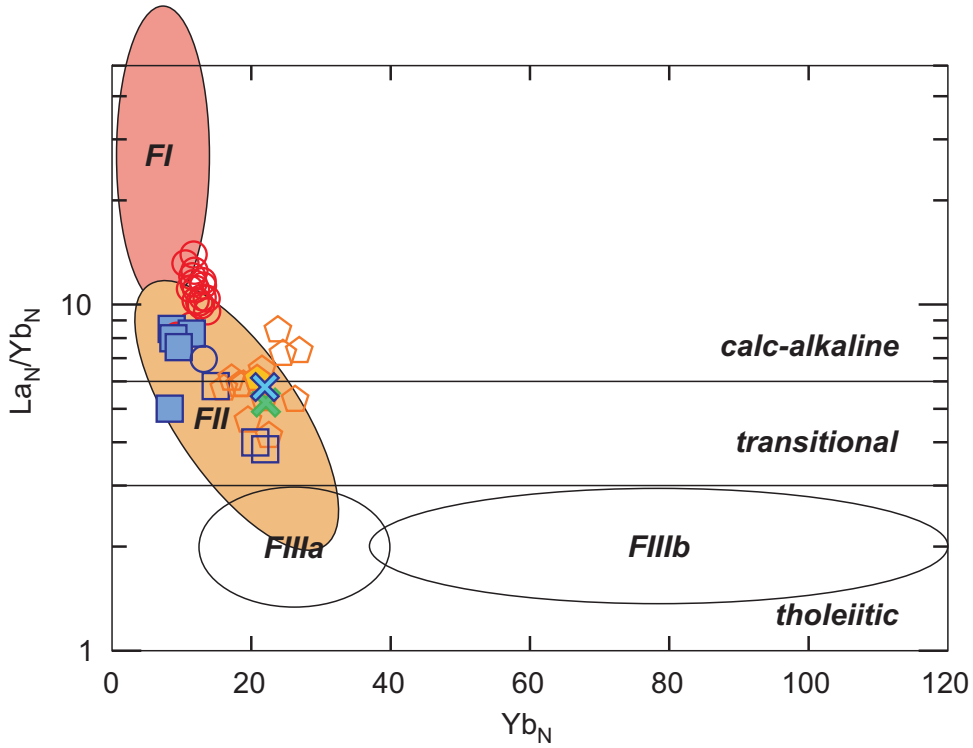

Figure 3.10: REE ratio diagram of Lesher (1986) discriminating transitional FI-FII (rhyolite) and FII (rhyodacite) affinities. This plot implies a shallower depth of melting for the rhyodacitic rocks compared with the the rhyolitic rocks (e.g., Hart et al., 1999). This plot originally used for Archean rocks has been expanded to include paleozoic volcanic suites (Piercey, 2007). La_N and Yb_N are chondrite normalized La and Yb concentrations.

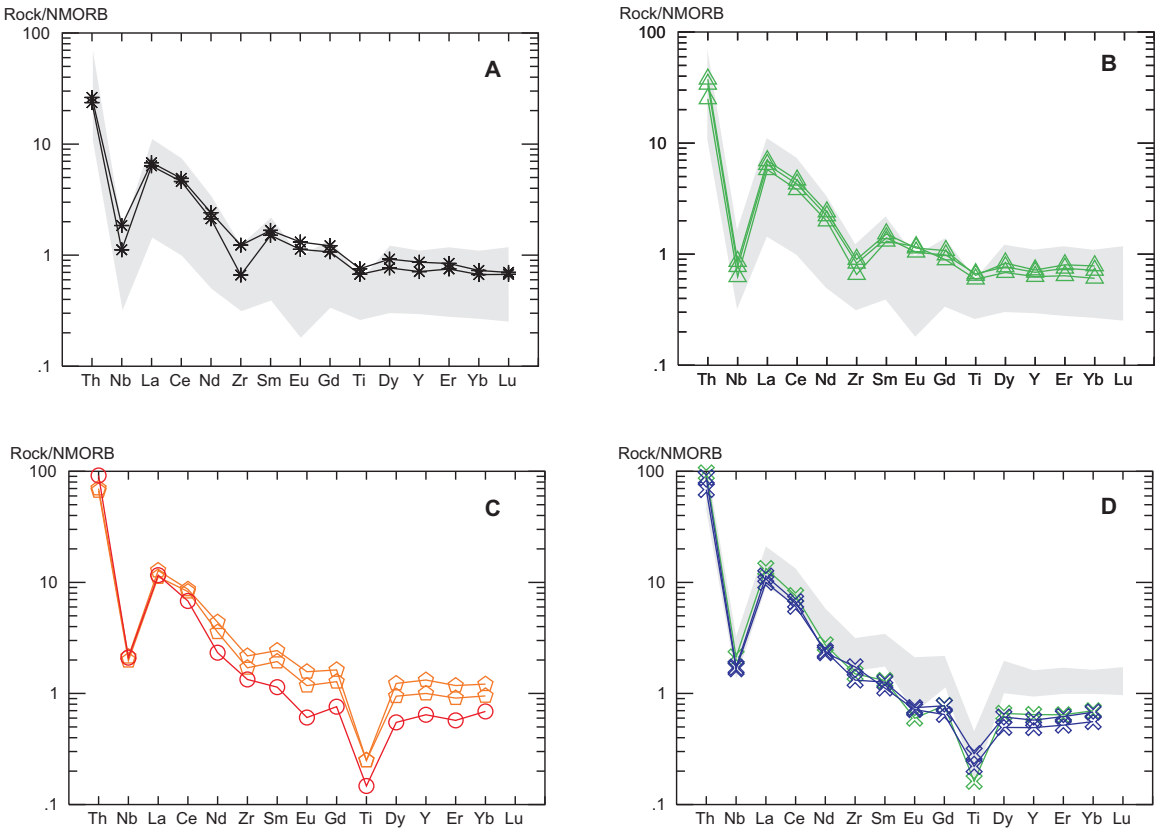

Figure 3.11: Comparison of Lundberg Zone host rock geochemistry to several other Buchans mines. Host rocks from these mines have identical geochemistry to the Lundberg Zone lithologies suggesting that the identified signatures may be used as a regional exploration tool. The above NMORB-normalized multielement diagrams are those constructed originally by Sun and McDonough (1989). A. NMORB-normalized multielement plot of the diabase. Shading represents basaltic andesite samples of this study. B. NMORB-normalized multielement plot of Clementine basalt. Shading represents basaltic andesite samples of this study. C. NMORB-normalized multielement plot of the Oriental felsic volcanic rocks, including both rhyodacite and rhyolite units. These rocks are identical to those observed in the Lundberg and Engine House zones. D. NMORB-normalized multielement plot of felsic volcanic rocks of the Maclean extension (blue) and one sample from Clementine (green). These rocks are identical to the rhyodacite from the Buchans River Formation within the Lundberg and Engine House zones. The grey shading represents the range of REE values of the rhyolite unit.

Table 3.1: Average compositions of altered (a) units of the Lundberg Zone versus unaltered (u) reference samples of the Buchans Group and unaltered rocks of this study

	SHF			OR	L. sed. seq.	Rhyodacite	U. sed. Seq.		Qtz-phy Rhyodacite		Rhyolite	
	u	a	f	u	a	a	Tuff	Clast	w 1 cm qtz	w/o 1 cm qtz	u	a
n	2	28	9	1	1	1	9	1	6	3	2	16
SiO_2	53.51	58.47	65.94	74	73.67	80.34	70.31	72.87	72.59	75.59	73.17	71.67
Al_2O_3	16.66	13.49	12.56	13.50	11.76	11.01	13.97	11.08	13.04	11.03	13.65	13.26
$Fe_2O_{3(T)}$	11.08	9.24	6.62	2.40	3.46	0.77	2.83	1.60	2.38	2.75	2.25	2.53
MnO	0.19	0.48	0.20	0.05	0.14	0.017	0.04	0.05	0.09	0.08	0.05	0.07
MgO	3.32	8.41	5.01	0.22	3.11	0.48	1.30	0.60	0.95	0.92	0.96	1.98
CaO	7.58	0.42	0.35	1.49	0.21	0.44	1.68	2.79	1.94	1.34	0.95	1.39
Na_2O	3.74	0.75	0.39	6.20	0.13	0.12	1.17	2.55	3.21	2.27	3.27	1.67
K_2O	0.74	1.30	2.26	1.01	2.59	3.29	3.05	2.20	1.60	1.44	3.08	2.88
TiO_2	0.89	0.55	0.53	0.34	0.33	0.287	0.42	0.29	0.30	0.25	0.21	0.19
P_2O_5	0.18	0.11	0.18	0.06	0.07	0.06	0.10	0.06	0.07	0.06	0.06	0.05
LOI	2.31	6.00	5.15	0.60	3.84	2.72	4.30	3.84	3.35	3.21	2.07	3.52
Zr/Y	3.19	3.12	3.78	4.35	4.58	5.29	4.88	4.70	10.62	4.57	6.69	7.06
Zr/TiO_2	0.01	0.01	0.01	0.05	0.04	0.05	0.04	0.05	0.05	0.05	0.06	0.06
Zr 63.85		42.29	76.89	161	140	145	166.56	156	136.67	126.33	118	114
La_N/Yb_N	5.23	4.73	5.42	6.20	5.91	4.62	6.27	5.34	7.48	4.54	10.45	10.83
La 16.65		9.62	18.59	32.00	29.50	21.40	33.14	27.60	16.86	19.97	33.00	30.32
Yb 2.29		1.44	2.44	3.70	3.58	3.32	3.76	3.71	1.61	3.26	2.27	2.00

u=unaltered

a=altered

n= number of samples averaged

f= andesite from this study

SHF = Ski Hill Formation

OR = Oriental 'Rhyolite'

Oxides are given in wt. % and trace elements as ppm

The unaltered Ski Hill Basalt reference is an average of RAX06297 and RAX06298A from Zagorevski (2008)

The unaltered Oriental 'rhyolite' reference is sample 5913 from Zagorevski (2008)

The unaltered rhyolite column is an average of RAX08G122 and RAX08G144 of this study

Unaltered samples were selected based on petrographic and CCPI and AI indices

La_N/Yb_N - are chondrite normalized values

Chapter 4: Alteration of the Lundberg and Engine House Zone Polymetallic Stockwork

4.1 Abstract

The Lundberg and Engine House zones form a peripheral polymetallic stockwork to the ~5.5 Mt Lucky Strike volcanogenic massive sulfide deposit, Buchans, Newfoundland. The stockwork is characterized by veins of massive pyrite, quartz-carbonate with disseminated or blebby sphalerite-galena-chalcopyrite, bladed barite and carbonate with disseminated or blebby sphalerite-galena-chalcopyrite, massive polymetallic sulfides, and narrow quartz-carbonate veins with little or no sulfide. Where present, the bladed barite and calcite occur at the top of the mineralized zone suggesting infiltration of seawater during the precipitation of barite and possibly boiling of the hydrothermal fluid and the precipitation of bladed calcite.

In the Lundberg Zone, stockwork mineralization is spatially associated with three footwall alteration facies within the upper basaltic andesite and andesite, as well as hanging-wall alteration in the upper sedimentary sequences and rhyolite units. Footwall alteration consists of a zoned alteration pipe which grades from a siliceous core zone in the center of the pipe, to an intense quartz-chlorite-sericite zone surrounded by moderate quartz-chlorite-sericite alteration towards the margins. In the hanging-wall, weak sericite +/- carbonate alteration occurs within the upper sedimentary sequence along the same stratigraphic horizon as the Lucky Strike deposit. The structurally emplaced rhyolite unit is weakly altered to fine-grained white mica (hereafter phengite), quartz, carbonate, and chlorite.

Intense quartz-sericite alteration associated with the siliceous core zone has Ishikawa (AI) indices greater than 90 and carbonate-chlorite-pyrite (CCPI) indices less than 65. Strong to intense quartz-chlorite-sericite alteration generally has AI and CCPI values greater than 90, characteristic of intense silicification, chloritization, and lesser sericitization. Within this zone, alteration indices decrease away from heavily mineralized areas and towards the Ski Hill – Buchans River Formation contact. Moderate quartz-chlorite-sericite alteration immediately surrounds this zone, and has much lower AI (65-90) and CCPI values (70-90). The rhyodacite units in the hanging-wall have AI and

CCPI typical of weak sericite-carbonate alteration. The rhyolite unit is characterized by CCPI and AI values intermediate between diagenetic and hydrothermal alteration, with a westward increase in alteration intensity. Mass balance calculations indicate gain of SiO_2, MgO, Fe_2O_3, K_2O, and Al_2O_3, and mass loss of CaO and Na_2O in the footwall alteration. These trends are characteristic of silicification, chloritization, and sericitization. Both felsic lithologies of the hanging-wall display no significant mass change.

In the Engine House Zone, rhyodacite in the footwall is cut by stockwork mineralization. In intensely mineralized zones, the rhyodacite displays intense quartz-sericite alteration similar to that of the siliceous core zone within the upper basaltic andesite (AI>90 and CCPI<90). The hanging-wall consists mostly of quartz-phyric rhyodacite. A range of diagenetic to weak hydrothermal alteration is observed, similar to that of the Lundberg Zone.

Shortwave infrared spectroscopy (SWIR) was used to characterize these assemblages. Relative proportions of chlorite and illite were calculated from the depths of chlorite and illite absorption features and gave results similar to least-squares normative mineralogy. Chlorite and white mica were easily identified with strong, contrasting absorption features; quartz addition dramatically decreased the slope of the spectra. Within the phengite-quartz-carbonate-chlorite alteration facies, shortwave infrared spectroscopy clearly identified phengite as the dominant muscovite, distinguishing proximal versus distal alteration in the thrust emplaced rhyolite unit. Shortwave infrared spectroscopy provides an additional exploration tool within the Buchans mining camp for defining proximal versus distal alteration facies.

4.2 Introduction

Intense alteration zones are observed within the peripheral stockwork surrounding the Lucky Strike deposits, the largest VMS deposit in the Buchans Mining Camp (Table 1.1). Limited studies of alteration at the Lucky Strike deposit have concentrated on the chemical composition of alteration in the Intermediate Footwall and the Lucky Strike and Engine House stockwork zones (e.g., Figure

1.6; Kowalik, 1981, Henley and Thornley, 1981). Henley and Thornley (1981) identified calcite, chlorite, epidote, hematite, illite, montmorillonite, muscovite, pyrite, and quartz by XRD. Hydrothermal chlorite and muscovite were also analyzed by electron microprobe (Henley and Thornley, 1981). However, they did not have enough drill hole constraints to construct detailed cross sections showing the distribution of alteration surrounding the Lucky Strike deposit. New drilling in 2008 provided an excellent opportunity to better constrain the alteration zonation, using petrography, shortwave infrared spectrometry, and whole-rock geochemistry (Figure 4.1).

4.3 Methods and Analytical Procedures

Two hundred samples and eighty three whole-rock analyses from twenty nine drill holes were examined to characterize the hydrothermal alteration and mineralization of the Lundberg and Engine House zones. Representative samples were taken of each volcano-sedimentary unit along W-E and N-S sections (e.g., Figures 3.1 and 3.2). Alteration and mineralization assemblages were first identified by field observation and petrography and then studied in greater detail with alteration geochemistry and shortwave infrared spectroscopy. Whole-rock lithogeochemical samples were analyzed at Activation Laboratories Ltd., Ancaster Ontario. A combination of ICP-ES and ICP-MS were used to analyze major and trace elements, respectively. Results are presented in Appendix 3.1. Duplicates were run every 15 samples for quality control (Appendix 3.2).

Shortwave infrared (SWIR) analyses were conducted on cut drill core surfaces and thin section blanks for two hundred samples. Results are presented in Appendix 4.1. This technique was particularly useful for identifying alteration mineralogy on a large number of samples which are generally characterized by a very fine grain size. Absorption features and their relative intensity/depth were extracted using "SpecWin ^{TM}" software. These data are presented in Appendix 4.2. The software first removes the continuum and then smooths the spectrum (Dr. Bill Peppin ASD, personal communication, 2010).

4.4 Mineralization within the Lundberg and Engine House zones

The mineralization that partly underlies the Lucky Strike deposit is a stockwork consisting of cross-cutting base metal veins which form a semi-concordant, wedge-shaped zone that is 360 m wide and thins out 600 m to the northwest (Thurlow and Swanson, 1981). The highest grade mineralization forms a northwest trend that cuts the Lucky Strike open pit (Figure 4.1). Lower grade stockwork mineralization extends to the northeast; however, no mineralization occurs southwest of the Lucky Strike glory hole. Zn concentrations versus depth are presented in cross section A to A' and A' to A" with overlaid alteration assemblages (e.g., Figure 4.2 and 4.3). Higher metal grades occur in areas of more intense alteration (e.g., H-3384, H3396, and H-3406). The correlation between Zn grade and other base and precious metals is presented in Figure 4.4.

The sulfide mineralogy of the Lucky Strike polymetallic stockwork consists of pyrite, chalcopyrite, sphalerite, galena, quartz, barite, chlorite, and calcite (Kowalik et al., 1981). Mineralization within the Lundberg and Engine House zones identified in this study consists of two types: exhalite and polymetallic stockwork. The exhalite consists of beds of light grey, fine-grained barite and sulfides with 5-10 vol. % rhyodacite clasts occur within the Buchans River Formation (BRF) at a number of positions (e.g., Figure 2.11B). Barite accounts for greater than 50 wt. % of these horizons, commonly as crystals up to 1 cm in size. The exhalative mineralization and underlying stockwork (e.g., H-08-3372) are locally separated by 1 m of metalliferous mudstone cut by pyrite veins at its base and overlain by 1 m of a sulfide-bearing pebbly greywacke, indicating that the stockwork and exhalative mineralization formed contemporaneously. However, the polymetallic stockwork veins cross-cut the upper portions of the Ski Hill Formation (SHF) basalts and rarely penetrate the BRF (Figure 3.1).

The stockwork can be divided into 2 broad zones: an upper pyritic and strong quartz-chlorite-sericite zone underlain by a polymetallic, intense quartz-chlorite-sericite zone (e.g., Figures 4.4 and 4.5). The upper zone is characterized by massive pyrite veins (Figure 4.6A). A distinctive

black chlorite zone commonly occurs at the transition of the two zones and contains more than 50% pyrite bound by strong quartz-chlorite-sericite alteration. Pyrite locally forms euhedra that vary from 1mm up to 1 cm in size (Figure 4.6B).

The majority of polymetallic veins occur in the intense quartz-chlorite-sericite zone. They consist of sphalerite, galena, pyrite, and chalcopyrite in a quartz-calcite-barite gangue. Stockwork veins have several different morphologies with internal mineral zonation and proximal (cm-scale) alteration haloes. Four types of polymetallic veins have been recognized from top to bottom: (1) quartz-carbonate-barite-sulfide, (2) quartz-carbonate-sulfide, (3) massive sphalerite veins, and (4) quartz dominant.

The quartz-carbonate-barite-sulfide vein type (~10%) is characterized by disseminated to blebby sphalerite and galena, with lesser pyrite and chalcopyrite, in a matrix of bladed barite, polycrystalline calcite, and hydrothermal quartz (Figure 4.6C). These veins are most common in the upper portions of the polymetallic stockwork zone. Individual blades of quartz and calcite are commonly 0.5 to1.5 cm in length and 2 mm in width; barite blades are much smaller (<1 cm in length and <0.5 mm in width). Proximal vein alteration is typically absent; however, some veins have 1 cm black chlorite margins (clinochlore-penninite: Henley and Thornley, 1981) and pyrite haloes.

The quartz-carbonate-sulfide vein type (~85%) occur below the bladed gangue zone and are characterized by fine-grained carbonate-quartz veins with blebby to disseminated sphalerite, galena, and chalcopyrite, and cubic pyrite (Figure 4.7A). Obvious zonation of sulfide and alteration minerals within these veins is rare; however, quartz, barite, galena, and sphalerite locally concentrate in vein cores, whereas carbonate and pyrite concentrate toward vein margins. No consistent alteration halo is observed adjacent to these veins, although rare <1 cm chlorite (e.g., clinochlore-penninite: Henley and Thornley, 1981) and pyrite haloes are observed. Instead chlorite or sericite is typically pervasive through drill core at the meter to decametre scale.

The massive sphalerite veins (~5%) occur in a similar position to the quartz-carbonate sulfide vein type and have massive irregular to blebby sphalerite cores surrounded by carbonate and minor quartz margins (Figure 4.7B). Proximal vein alteration consists of symmetric, ~2 mm thick chlorite-pyrite alteration haloes surrounded by up to 1 cm of sericite alteration (e.g., Figure 4.6B).

The last group of veins are small (<2 cm) quartz veins which may contain small amounts of sphalerite, galena, pyrite, and/or carbonate (Figure 4.7C). These veins typically have 1 cm sericite alteration halos and occur in the lower portions of the polymetallic stockwork zone and into the footwall.

Vein mineralogy

Pyrite is most abundant at the margins of the stockwork mineralization. In the core of the stockwork zone, chalcopyrite is associated with sphalerite and galena. In general, the grain size of vein sulfides increases towards the core of the stockwork.

Although it is most abundant at the margins of the Lundberg Zone, pyrite occurs in equal proportions to the other sulfides in the core of the Lundberg Zone (Figure 4.7C) and typically forms cubes that range from <0.1 mm to 2mm, and colloform texture locally (Figures 4.8A and 4.8B). Pyrite aggregates are commonly infilled by quartz, chlorite, and carbonate within or at the margins of veins (Figure 4.8D). This texture indicates that pyrite formed during or before the quartz-chlorite and quartz-sericite alteration marginal to veins. Inclusions of gypsum and galena within pyrite are also observed.

Sphalerite consists of irregular to elongate blebs of sulfide which is most common in the cores of veins where vein zonation is present (Figure 4.8E). It has characteristic chalcopyrite disease texture which consists of linear trains of chalcopyrite along pre-existing grain boundaries, reflecting replacement or coprecipitation of sphalerite and chalcopyrite (Figure 4.8F: Barton and Bethke, 1987). Replacement of sphalerite margins and cross-cutting blebs of chalcopyrite across sphalerite grains indicate the formation of chalcopyrite after sphalerite.

Galena forms irregular to elongate blebs, most commonly around quartz gangue (Figure 4.9A). Galena typically occurs towards the margins of zoned veins, but also locally in the cores. It replaces sphalerite and forms 'inclusions' in sphalerite (Figure 4.9B).

Chalcopyrite occurs as irregular blebs and is most commonly associated with sphalerite, galena, and pyrite in a quartz-carbonate gangue in the core of the Lundberg Zone (Figure 4.9B). At the margins of the Lundberg Zone it is more commonly associated with pyrite. Chalcopyrite is observed to replace sphalerite (Figure 4.9C), galena, pyrite, and chlorite.

Barite forms bladed crystals in veins in the upper portions of the polymetallic stockwork zone. Individual blades of barite range from <0.1 mm to 1mm wide and 1mm to 1 cm in length. Bladed barite aggregates may form clusters up to 2 by 3 cm. Barite blades are commonly partly to completely replaced by quartz +/- chlorite or carbonate and rarely by sulfide (Figures 4.9D and 4.10A to D).

Quartz is the most abundant gangue mineral in the veins and occurs throughout the entire stockwork. Quartz forms subhedral crystals that average 0.1 mm in size and are commonly associated with chlorite. It also commonly replaces barite or forms comb quartz on pyrite (Figure 4.10A and B).

Chlorite forms very fine-grained alteration on the margins on veins containing abundant pyrite; however, it may locally fill open space within veins (Figure 4.8D). Chlorite commonly surrounds quartz, barite, and pyrite.

Fine-grained muscovite (sericite) is rare within veins and more commonly forms alteration surrounding them. It is extremely fine grained and fills open space similar to chlorite.

Carbonate occurs as a late stage mineral which typically surrounds sulfides and is more abundant in the upper part of the Lundberg Zone. In the upper parts of the polymetallic zone, it replaces bladed barite to varying degrees (Figures 4.11A to D). Complete replacement of bladed barite and the formation of polycrystalline blades is the most common bladed texture, with relics of

the original barite preserved in few cores (Figures 4.11A and B). Here, calcite is observed to infill and locally replace barite along cleavage planes.

Generalized paragenetic sequence

A general paragenetic sequence may be developed based on replacement textures of gangue and sulfide minerals. Kowalik et al. (1981) placed chlorite before pyrite, quartz, chalcopyrite, sphalerite, galena, barite, and calcite. However, the replacement of barite by quartz (+ chlorite) and sulfide indicate that barite must have formed earlier. Chalcopyrite is observed to cut chlorite. The association of chlorite and comb quartz on pyrite cubes indicates that quartz and chlorite formed after pyrite. Sericite appears to have formed after quartz and chlorite.

4.5 Hydrothermal Alteration within the Lundberg and Engine House zones

Kowalik et al. (1981) placed the hydrothermal alteration within the Lundberg and Engine House zones surrounding the Lucky Strike in situ VMS deposit occurs mainly within their Intermediate Footwall (Figure 1.6). The Intermediate Footwall has been generally divided into the Ski Hill Formation (mafic rocks) and Buchans River Formation (felsic rocks). However, whole-rock geochemistry indicates that the upper parts of the Intermediate Footwall have distinctly higher Zr/TiO_2 ratios and are, in fact, slightly more fractionated than the underlying basaltic andesite (Chapter 3). Mineralization was previously thought to be restricted to the Intermediate Footwall; however, this study shows that thick sections of 'Intermediate Footwall' (andesite) overlie the stockwork mineralization.

A prograde hydrothermal alteration is preserved in which moderate quartz-chlorite-sericite is replaced by strong and intense quartz-chlorite-sericite, which is replaced in turn by intense quartz-sericite (siliceous core zone). Near the base of the quartz-chlorite-sericite altered upper basaltic andesite a combination of in situ and hyaloclastite breccias form a permeable horizon infilled with quartz and lesser chlorite (Figure 4.12A). Above the basaltic andesite breccias, the contacts of

andesitic flows are replaced by quartz-chlorite-sericite-pyrite (Figure 4.12B). In H-08-3395, in situ brecciation is more intense towards the top of the hole; these rocks are part of the siliceous core zone (Figure 4.12C). The contact between the strong and intense quartz-chlorite-sericite zones is typically gradational and marked by alternation of both assemblages; however, sharp contacts across black chlorite zones and/or mudstones are locally observed which may be attributed to primary lithological differences. Silicification is less obvious in the impermeable black pyritic mudstones (Figure 4.12C).

Lundberg Zone

Twenty nine drill holes were examined surrounding the Lucky Strike deposit to characterize the distribution of alteration facies (Figure 1.5, Figure 4.1). Three footwall and two hanging-wall alteration facies were identified: a siliceous core zone, strong to intense quartz-chlorite-sericite, and moderate quartz-chlorite-sericite in the footwall, and weak sericite-carbonate and phengite-quartz-carbonate-chlorite in the hanging-wall (Figure 4.2). The three footwall alteration facies occur within both the upper basaltic andesite and andesite units. The weakest alteration in the footwall consists of moderate (AI< 90) quartz-chlorite-sericite alteration and is most distal to stockwork mineralization, far west of the Lundberg zone in H-3344, to the east in H-08-3393 and H-08-3398, and to the south in H-08-3408. Moderately altered andesite occurs within H-3344. The strong to intense quartz-chlorite-sericite alteration forms a core zone of alteration within the basaltic andesite, with a distinct change from moderate to strong and intense (AI> 90) quartz-chlorite-sericite faices towards the northwest (Figure 4.3). A similar zonation is observed vertically, where intense quartz-chlorite-sericite at the base of the upper basaltic andesite grades upwards to a commonly >40 m thick strongly altered quartz-chlorite sericite zone (Figure 4.2). This zone has the appearance of being mostly sericitized and/or silicified; however, chlorite comprises a much larger percentage than can be recognized in drill core. The strongly altered andesite and basalt are typically not distinguishable; however; an emerald green muscovite identified as barium muscovite by Henley and Thornley (1981) is typically associated with andesite and is a useful discriminator of the transition from altered

intermediate to mafic rocks. The siliceous core zone locally occurs in the areas of highest Zn cut-off grades at the top of the basaltic andesite unit or within andesite (e.g., >3 wt. % Zn; compare Figures 4.1, 4.2, and 4.3). Here, it increasingly replaces the strong to intense quartz-chlorite alteration facies at shallower depths, grading through in situ brecciated basalt to an intensely silicified and/or sericitized rock.

The extent of alteration of the various rhyodacite units in the hanging-wall is dependent upon the primary lithology: autobreccia, polymictic breccia clasts, versus rhyodacite tuff of the upper sedimentary sequence. Alteration of the rhyodacite autobreccia is exclusively quartz-sericite-pyrite which is discordant across its lower contact. The matrix of the upper sedimentary sequence is largely unaltered with very weak sericite +/- carbonate, but clasts within this unit show both quartz-chlorite and quartz-sericite alteration. One sampled rhyodacite clast has significant sericite (~35%) and carbonate (~10%) alteration. The interstratified rhyodacitic tuff is altered to fine-grained green muscovite and significant carbonate (~10%).

The LSS rhyolite unit, which forms the structurally-emplaced hanging-wall to the Lucky Strike ore horizon is more altered than the upper sedimentary sequence. It shows a westward increase in alteration intensity from relatively unaltered in H-08-3376 and H-08-3393, to a hydrothermal phengite-quartz-carbonate-chlorite facies in H-08-3378 (Figure 4.2).

Engine House Zone

5 alteration facies were observed in the Engine House Zone: siliceous core zone, intense to strong quartz-chlorite-sericite, moderate quartz-chlorite-sericite, sericite-carbonate +/- chlorite, and chlorite-hematite. The lowermost pillow breccia is characterized by chlorite alteration and locally chlorite-hematite in H-08-3366. The tuffaceous sediments with interlayered rhyodacite are altered to strong quartz-chlorite-sericite which often obscures the primary volcaniclastic textures. The rhyodacite autobreccia unit, which hosts the Engine House Zone, is predominantly altered to a ‘siliceous core zone’. Towards the bottom of the unit, the rhyodacite autobreccia is interlayered with

tuffaceous rhyodacite which is only weakly altered (e.g., G164 versus G165). The southern sedimentary sequence is very weakly altered to sericite +/- quartz. The structurally capping quartz-phyric rhyodacite tuff unit is weakly altered to sericite-carbonate-chlorite.

Alteration petrography

Lundberg Zone

The mineralogy of the different host units of the alteration is summarized in Table 4.1. The mineralogy of the upper basaltic andesite consists of quartz, chlorite, and sericite, with lesser epidote, pyrite, K-feldspar, albite, and carbonate. Quartz ranges from 10 to 65 vol. % and occurs as alteration of primary volcanic glass, feldspar phenocrysts, and within amygdales. Primary igneous feldspar is present in significant amounts in least-altered samples (e.g., 20 vol. %) forming tabular microlites with rare skeletal texture (Figure 4.13A) and phenocrysts within eight least-altered samples which generally contain <30 vol. % quartz. Chlorite and sericite are abundant within the basaltic andesite in all but the least altered samples; however, few samples within more intensely mineralized zones contain more chlorite and sericite than samples towards the top of the basaltic pile. Sericite typically comprises 20 vol. % of the rock and variably alters primary volcanic glass, microlites, and phenocrysts (Figure 4.13B); however, several samples associated with intense silicification contain around 30 vol. % (and one over 50 vol. %). Chlorite typically comprises 35 vol. % and occurs as alteration of primary volcanic glass and clinopyroxene and feldspar phenocrysts, and in amygdales (Figure 4.13A). The lowest concentrations of chlorite are observed within intense (>50 % SiO_2) quartz alteration zones. Epidote commonly comprises 1-2 vol. % and occurs as small crystals or aggregates associated with groundmass chlorite. Intense quartz-sericite alteration of the basaltic andesite is clearly distinguished from the rest of the samples, containing >55 vol. % quartz and ~30 vol. % sericite.

A range of alteration characteristics is observed between the least and most fractionated basaltic andesite. The least fractionated basaltic andesites (lower Zr/TiO_2; Chapter 3) typically

preserve some tabular microlites, whereas more fractionated samples do not (Figure 4.13C). The fractioned andesite is altered to quartz, chlorite, and sericite which occur in the groundmass and in phenocrysts, with lesser chlorite, epidote, and rare carbonate. Samples range from 40 to 69 vol. % quartz. The concentration of sericite in the andesite is typically 25 vol. %. Chlorite is abundant in the majority of andesite samples and is strongly correlated with the concentration of quartz, although the most intensely silicified samples contain significantly less chlorite. Epidote typically comprises 2 vol. % and pyrite makes up a significant fraction (up to vol. 5 %) compared to all other lithologies.

The rhyodacite autobreccia sample from the Lundberg Zone is intensely altered to quartz-sericite (G070), containing 30 vol. % muscovite and >40 vol. % quartz.

The upper sedimentary sequence is altered to weak sericite +/- carbonate (Figure 4.13D). One rhyodacite clast from the upper sedimentary sequence (representative of >70% of the clast population) contains 20 vol. % muscovite indicating weak hydrothermal alteration. By contrast, one representative clast from the lower sedimentary sequence contains 25 vol. % muscovite and 10 vol. % chlorite typical of more strongly altered rhyodacite. Rhyodacite tuff from within the upper sedimentary sequence contains between 30 and 40 vol. % muscovite indicating similar degrees of hydrothermal alteration.

Samples of the LSS rhyolite unit in the structural hanging-wall contain phengite, quartz, carbonate, and chlorite, which increase in abundance to the west (Figures 4.2 and 4.14A to 4.14D). Phengite contents ranges from 4 to 30 vol. %, commonly as a replacement of feldspar phenocrysts, volcanic glass, or in perlitic fractures. Hydrothermal quartz that replaces volcanic glass (~10 to 25 vol. %) appears to mimic the primary volcanic texture with circular form and radiating extinction. Carbonate (0 to 10 vol. %) occurs as replacement of feldspar phenocrysts, volcanic glass, and as minor veins. Chlorite ranges from 0 to 15 vol. % and occurs as replacement of felsic glass.

Engine House Zone

The mineralogy of the interstratified tuffaceous sediments and rhyodacite unit, the rhyodacite autobreccia, and the structurally emplaced quartz-phyric rhyodacite tuff in the Engine House Zone is presented in Table 4.2. The altered rhyodacite from the interstratified tuffaceous sediments consists of a quartzofeldspathic matrix with carbonate, sericite, chlorite, and pyrite. The quartzofeldspathic matrix comprises over 85 vol. % of the rock and is weakly altered to carbonate (10 vol. %), sericite (2 vol. %) and chlorite (1 vol. %).

The aphyric rhyodacite autobreccia which hosts the Engine House Zone consists of a quartzofeldspathic matrix (58 to 79 vol. %) that has been altered to 15 to 25 vol. % sericite. One sample of rhyodacite tuff from above the autobreccia preserves the original clastic texture and contains sericite (10 vol. %) and carbonate (10 vol %) alteration.

The structurally-emplaced quartz-phyric rhyodacite tuff above the Engine House Zone consists of a quartzofeldspathic matrix altered to quartz and feldspar clasts, sericite, carbonate and chlorite. The primary quartzofeldspathic matrix comprises 30 to 85 vol. % of the rock depending on the degree of alteration.

4.6 Alteration Geochemistry

The geochemistry of the upper basaltic andesite, lower sedimentary sequence, rhyodacite autobreccia, upper sedimentary sequence, and rhyolite unit is variably affected by the hydrothermal alteration (Table 3.1). In the immediate footwall of the Lucky Strike horizon, SiO_2, MgO, and K_2O are enriched, whereas Al_2O_3, Fe_2O_3, CaO, and Na_2O are depleted relative to background samples (Table 3.1). SiO_2 is significantly enriched (up to 76.8 wt. %) exceeding concentrations observed in rhyolites. MgO is ~5 wt. % higher in altered samples and locally exceeds 14 wt. % in heavily chloritized samples. K_2O reaches 3.5 wt. % in sericite-rich zones devoid of chlorite. CaO is almost entirely leached from the footwall reflecting plagioclase destruction, except in few samples affected

by minor carbonate alteration. Na_2O is either completely removed (<0.1 wt. %) or unaffected by alteration.

The rhyodacite unit which corresponds to the Lucky Strike horizon is enriched in SiO_2 and K_2O but depleted in all other elements typical of intense quartz-sericite alteration. The lower and upper sedimentary sequences have higher concentrations of Fe_2O_3, MgO, and K_2O, but lower concentrations of Al_2O_3, CaO, and Na_2O than unaltered rhyodacite. The rhyolite unit is enriched in Al_2O_3, Fe_2O_3, MgO, and K_2O, and depleted in Na_2O.

Alteration indices and alteration intensity

Alteration box plots of samples from the Lundberg and Engine House zones illustrate the chloritization and sericitization trends (cf. Large et al., 2001a: Figure 4.15). The Box plot utilizes both the Ishikawa (AI) and carbonate-chlorite-pyrite (CCPI) alteration indices. The Ishikawa alteration index is a ratio of the elements gained (K_2O + MgO) over elements gained and lost (K_2O + MgO + Na_2O + CaO) during chloritization and sericitization (Ishikawa et al., 1976). Ratios between 20 and 65 represent approximate primary compositions, whereas values below 20 indicate albitization, and values over 65 sericitization depending on the starting composition. The carbonate-chlorite-pyrite (CCPI) alteration index is a ratio of elements gained (MgO + FeO) over elements gained and lost (MgO + FeO + Na_2O + K_2O). This index measures carbonate, chlorite, and pyrite because all these minerals may contain important MgO and FeO proximal to mineralization. Unaltered basalts have a CCPI between 70 and 90, but Ishikawa indicies less than 60.

The three different alteration zones within the basaltic andesite can be recognized in the alteration box plot (moderate quartz-chlorite-sericite, intense quartz-chlorite-sericite, and intense quartz-sericite) (Figures 4.15 and 4.16). Lateral and vertical variations in alteration intensity are displayed graphically in Figures 4.2 and 4.3. Vertical variations in alteration intensity are plotted separately in Figure 4.17. The moderately altered quartz-chlorite-sericite zone comprises samples from H-3344 located far west of the main Lundberg Zone and Lucky Strike open pit, H-08-3408

located southwest of Lucky Strike, and samples at depth within H-3341. These samples have AI values <80 and CCPI values <85 (Figures 4.15 and 4.16A to F). In general, alteration indices decrease towards the top of this zone (Figuress 4.17A and B). The strong to intense quartz-chlorite-sericite zone is by far the most dominant alteration within and surrounding the Lundberg Zone (Figures 4.2 and 4.3). Within this zone, alteration indices decrease laterally and vertically within the basaltic andesite; where samples are lighter coloured due to a change in the abundance of chlorite, sericite, and/or quartz (Figures 4.2 and 4.3, and 4.17C and 4.17D and 4.18). CCPI values range from 81 to 100 indicating near-complete to complete alteration of primary volcanic glass and phenocrysts to chlorite (Figure 4.18A to D). AI values range from 84 to 98 indicating minor variation in the abundance of sericite and chlorite. The intense quartz-sericite zone is observed immediately west of the Lucky Strike pit and overlies the intense quartz-chlorite-sericite zone (Figures 4.1 and 4.2). The AI values in this zone are typical of strongly altered volcanic rocks (>93); however, the CCPI values (<64) are similar to that expected in an unaltered basaltic andesite indicating that different alteration affected this zone (Figures 4.18E and F).

The three alteration zones within the andesite are also recognized in the alteration box plot (weak quartz-chlorite-sericite, strong to intense quartz-chlorite-sericite, and intense quartz-sericite) (Figure 4.15). The weakly altered andesite sample (131) is from H-3344 located far west of the main Lundberg Zone and has AI values <60 and CCPI values <65 (Figures 4.19A and B). This sample is macroscopically identical to strongly altered andesite (e.g., G008 and G036). The most common alteration of the andesite unit is strong to intense quartz-chlorite-sericite alteration which has AI values between 86 and 97 and CCPI values between 73 and 99 (Figures 4.18C and D). Hand samples of the andesite in this zone are various shades of grey to beige; samples which contain more chlorite are generally darker coloured. The intense quartz-sericite zone only occurs adjacent to highly mineralized zones above strongly chloritized rocks (Figures 4.19E and F). Alteration indices of the intense quartz-sericite alteration is similar to that of the basaltic andesite (AI values >91 and CCPI values <60).

One representative rhyodacite clast (representative of >70% of the clast population) from within the upper sedimentary sequence has a CCPI value of 32 and an AI value of 34, typical of unaltered rhyodacite. By contrast, one representative clast from the lower sedimentary sequence has CCPI value of 71 and an AI value of 94, more typical of intense quartz-sericite altered mafic rocks. Rhyodacite tuff from within the upper sedimentary sequence contains 30 to 40 vol. % muscovite and plots in the weakly sericitized field on the alteration box plot (Figures 4.15 and 4.20A and B). Rhyodacite rocks from within the Engine House Zone have different alteration patterns. They are either relatively unaltered (AI values <50) or intensely sericitized and/or silicified (AI values >85) (Figures 4.20C to F).

The rhyolite unit is unaltered to weakly sericitized and chloritized. The weakly altered samples (75>AI>60) occur in the hanging-wall above highly mineralized basaltic andesite; whereas, unaltered samples occur distal to mineralization (Figures 4.14A to D). Only a few samples of rhyolite associated with shear zones are notably chloritized and/or silicified in the central portion of the Lundberg Zone (e.g., 024, 062). Samples of quartz-phyric rhyodacite mimic the rhyolite alteration indices but the intensity of alteration is heterogeneous (Figure 4.21A to F).

Single-precursor mass-balance calculations

The single-precursor method developed by Maclean and Barrett (1993) is a useful tool for quantifying mass change in altered volcanic rocks and eliminates problems which occur when analyzing lithogeochemical data (e.g., closure). The method involves comparing all geochemical results to a suite of least-altered samples assuming immobility of one element within the altered rock. The principle of this method is that the ratio of an immobile element in the primary rock over altered rock (Z_o/Z_a) is equivalent to the ratio of mobile elements gained or lost during mass transfer. Multiplying the concentration of an element in the altered rock by the ratio of Z_o/Z_a provides an estimate of the absolute quantity of the element gained or lost relative to the concentration of the element in the least-altered equivalent (Co):

$$mass\ change = (\frac{Zo}{Za} * Ca) - Co$$

Values greater than zero thus reflect mass gain, and values less than zero mass loss.

Immobile elements and reference samples

Bivariate plots of immobile compatible versus immobile incompatible elements (e.g. TiO_2 or Al_2O_3 versus Zr) are the most useful diagrams for differentiating primary (e.g., fractionation) from secondary (e.g., net mass change) processes (Barrett and Maclean, 1994). Samples from the Lundberg and Engine House zones plot along a single alteration line on a TiO_2 versus Zr bivariate plot (e.g., Figure 3.3A: Chapter 3) clearly demonstrating Zr dilution and immobility. Zr was determined to be the most immobile element and was used for the mass balance calculation (Figure 4.22). Whole-rock compositions of the least-altered samples used for calculating mass balance are shown with the lithogeochemical data of Appendix 3.1. Unaltered Ski Hill basalt sample RAX06A298a from Zagorevski (2008) was used for basaltic andesite calculations. Unaltered fractionated basaltic andesite has not been identified in the Buchans Camp and no reference was available for comparison. Unaltered sample 5913 from the Oriental rhyolite (i.e., field classification of Zagorevski, 2008) was selected to compare with the rhyodacite unit. Unaltered rhyolite sample RAX08G122 from this study was used for the hanging-wall rhyolite calculations. Results are summarized graphically in Figures 4.22, 4.23, and 4.25, and tabulated in Appendix 4.3.

Major elements

Proximal alteration zones within the upper basaltic andesite adjacent to the Lundberg and Engine House stockwork show the greatest mass change. All major elements except CaO and Na_2O, which were lost, and TiO_2 and P_2O_5, which were immobile, were gained during alteration (e.g., Figure 4.23 and Figure 4.24A). SiO_2 shows the greatest mass increase within 200 m of the SHF-BRF contact (e.g., Figure 4.23A). MgO shows the second largest increase (on average 10g/100g), also within 200 m of the SHF-BRF contact. Al_2O_3 and Fe_2O_3 show smaller but consistent mass gains in these samples. K_2O shows a small increase in all samples of sericite alteration. CaO, and to a lesser

extent Na_2O, are entirely leached proximal to the Lundberg and Engine House stockwork zones within the upper basaltic andesite, consistent with destruction of plagioclase during sericitization.

Across the SHF-BRF contact a clear change in alteration style occurs within the hanging-wall rhyodacite (rhyodacite autobreccia, rhyodacite tuff, rhyodacitic polymictic breccia). In general, the rhyodacites experience a net mass gain of SiO_2 (12.75 wt. %), MgO (0.75 wt. %), and K_2O (1.9 wt. %). Elements lost include Al_2O_3 (0.7 wt. %) and Na_2O (5.1 wt. %). CaO is variably lost and gained, reflecting carbonate alteration (gains) and plagioclase destruction (losses).

Above the thrust contact, the LSS rhyolite unit displays an entirely different alteration style/intensity and mass balance. The major oxides show little mass change; however, MgO (+1.14 wt. %), CaO (+0.83 wt. %), Fe_2O_3 (+0.75 wt. %), and Na_2O (-3.2 wt. %) are affected. The gain of CaO contrasts sharply with the proximal alteration facies within the upper basaltic andesite which are entirely devoid of calcium. This is due to both the preservation of plagioclase and the addition of carbonate.

Alkaline earth elements (Cs, Rb, Sr, Ba)

The alkaline earth elements display variable mass change within the upper basaltic andesite proximal to stockwork veins (Figure 4.24B). The most notable changes are in Rb, Sr, and Ba which reflect the abundance of these elements in feldspar, muscovite, barite, and carbonate. In other samples Sr is nearly completely lost (e.g., -185 ppm or 94% of the original concentration), and Ba is anomalously enriched reflecting partitioning of Ba into muscovite. Mass gains of Cs are extraordinarily large (e.g., 2.2ppm or +1000% of the original concentration). Distal to stockwork veins within the rhyodacite unit, a similar pattern of enrichment and depletion is observed; however, the mass changes are typically much smaller. Within the rhyolite unit Sr is lost (e.g., -150 ppm or 63% of the original) and large variations in Ba are observed (-619 ppm to 2054 ppm or -50 to +100 % of the original concentration).

Metals

The transition metals are typically enriched within the upper basaltic andesite and rhyodacite units proximal to the ore zone. Zn (e.g., +650 %), Pb (e.g., +800 %), Cu (e.g., +400 %), Cr (e.g., +900 %), and Sc (e.g., +30 %) are especially enriched within the upper basaltic andesite (e.g., Figure 4.25A). The rhyodacite unit has a 5500% increase in Zn, and 700% increase in Pb content; however, Cu enrichment is limited to the footwall. Within the rhyolite unit, Zn is the only metal appreciably enriched (e.g., +130%).

Rare earth elements

In general, the rare earth elements are immobile in the Lundberg and Engine House zones. LREE (La through Gd) display minor mobility proximal to stockwork veins (e.g., -10 %). HREE are completely immobile (Tb through Lu) displaying mass changes typically lower than 1%. REE are also highly immobile in rhyodacite in the immediate hanging-wall of the Lundberg and Engine House zones, although samples of rhyodacitic tuff (e.g., 31, 39, 153) display small gains of La (e.g., Figure 4.25B). There is a slight mass loss of the LREE in thrust-emplaced LSS rhyolite and no change in HREE, reflecting the overall immobility of REE in all lithologies.

4.7 Least-Squares Normative Mineralogy

Normative proportions of hydrothermal phyllosilicates were calculated using a Microsoft Excel® based least-squares calculator (MINSQ) developed by Herrmann and Berry (2002). The process involves assigning the whole-rock major elements to minerals of known or assumed composition present in the sample. Microprobe analyses from Henley and Thornley were used where available; however, ideal stoichiometric formulae may also be used as an estimate. Residuals are then calculated which represent the difference between the actual whole-rock weight percentages and the estimated abundances of all the minerals in the calculation. The *solver* tool in Excel® is then used to perform a least-squares calculation and determine a unique solution of mineral proportions for which the sum of the squared residuals is as low as possible (Herrmann and Berry, 2002).

Selection of mineral compositions

The mineral assemblages used for the least-squares calculation were determined by petrography (Table 4.1). Minerals which comprised greater than one volume percent of the sample were included in the calculations. These were quartz, feldspar, sericite, chlorite, epidote, pyrite, and carbonate. Microprobe analyses taken from Henley and Thornley are listed in Table 4.3. All other minerals were assumed to be stoichiometric end members. For pyrite, the iron content was recalculated to Fe_2O_3. For normative calculations involving upper basaltic andesite, pycnochlorite (ore proximal) and ripidolite (ore distal) chlorite compositions from Henley and Thornley (1981) were chosen to represent variations in Mg and Fe content. The pycnochlorite data is from immediately below the Lucky Strike pit, whereas the data for ripidolite are from the transported Maclean deposit away from the most intense hydrothermal alteration zones. Although Henley and Thornley (1981) noted the presence of clinochlore within the Intermediate Footwall (andesite), clinochlore was not used in the normative calculation as this composition yielded no normative chlorite, even in andesites which contained 45 vol. % chlorite in thin section.

The muscovite composition within the Intermediate Footwall of Henley and Thornley (1981) was used in the normative calculation. Its low K_2O content is consistent with an illitic composition, as identified by SWIR within the upper basaltic andesite (see below). A regional metamorphic epidote from Henley and Thornley (1981) was chosen to represent epidote within the upper basaltic andesite. All other minerals were assumed to be stoichiometric and major oxide percentages were obtained from Mindat.org (accessed in 2010). For normative calculations involving rhyodacite, the chlorite (diabanite) composition of the 'ore dacite' (cf. Henley and Thornley, 1981) was used (Table 4.3). For normative calculations involving rhyolite samples, stoichiometric chamosite and chlinochlore compositions were used. Phengitic muscovite analyzed by Henley and Thornley (1981) was used for the sericite component because shortwave infrared analyses of the rhyolite suggest a phengitic composition (see below). Carbonate was an important constituent within both the rhyodacite and rhyolite; however, CO_2 was not analyzed. To estimate the concentration of a

hypothetical Fe and Mg-bearing carbonate, CaO was added in proportion to the molar ratio of a $(Mg,Fe)Ca(CO_3)_2$ carbonate. This decreased the amount of calculated epidote to a concentration in keeping with the observed abundance of carbonate and epidote in thin section. For normative calculation involving quartz-phyric rhyodacite samples, the rhyodacite and rhyolite normative calculations were used depending on the presence of large, 1cm quartz phenocrysts

Results

Normative calculations for twenty-five samples of upper basaltic andesite are presented in Table 4.4 and summarized in Figure 4.26. Quartz ranges from 18 to 55 wt. % in the upper basaltic andesite. The moderately altered samples (AI<73) contain significant amounts of unaltered feldspar consistent with microlites with well developed trachytic texture (14-29 wt. % albite) observed in thin section. Strong to intensely altered samples have about the same chlorite and sericite content as the moderately altered samples, but significantly lower feldspar. These samples show a clear trend of increasing chlorite content with increasing CCPI. Sericite and quartz concentrations, however, display no clear trend. The normative abundances of albite, sericite, and chlorite correlate with AI values (Figures 4.26 and Figure 4.27). The normative mineralogy of intense quartz-sericite altered samples (G083 and G146) is dominated by abundant quartz (~50 wt. %), muscovite (~20 wt. %), and little chlorite (8 wt. %), characteristic of pervasive silicification and sericitization, and low CCPI values.

Results of normative mineral calculations for nine samples of the andesite are presented in Table 4.4 and summarized in Figure 4.28. Normative quartz ranges from 27-54 wt. %, suggesting that quartz contents are overestimated in the petrography because of the difficulty of distinguishing very fine-grained quartz and feldspar. Where petrographic estimates of quartz are higher, the difference is usually made up by feldspar in the norm. Both K-feldspar and albite were identified in the norm calculations up to 16 wt. % for K-feldspar and up to 19 wt. % albite. Normative muscovite ranges from 3 to 29 wt. %, consistent with thin section observations. Normative chlorite abundances

were also similar to the abundances observed in thin section, although the choice of chlorite composition clearly affected the results, as noted above. Samples which do contain significant chlorite were best modelled by ripidolite and pycnochlorite.

Results of normative mineral abundances for thirteen samples of the rhyodacite are shown in Table 4.4 and summarized in Figures 4.29A to 4.29C. The mineralogy of the rhyodacite was largely controlled by the rock type (breccia vs. tuff); however, in general, calculated quartz contents averaged 50 wt. % and ranged from 26 to 65 wt. %. The rhyodacite tuff contained the least amount of quartz (21-30 wt. %). Sample G040 is a slightly different rhyodacite tuff and occurs below the main tuff horizon. It contains much more quartz than the other rhyodacite tuff and is macroscopically much lighter in colour. Samples that have intense quartz-sericite alteration (i.e., proximal to Engine House stockwork and within rhyodacite autobreccia of the Lundberg Zone (G070)) contain much more quartz (39-65 %). Albite is more abundant in unaltered and weakly altered samples, which have correspondingly lower concentrations of quartz, whereas K-feldspar was more abundant in samples with higher concentrations of quartz. Petrographic examination suggests that all K_2O is present in muscovite, and normative calculations of K-feldspar are probably incorrect for these samples. Normative muscovite is abundant in all the rhyodacite samples and averaged 24 wt. % and ranged from 16 to 48 wt. %. Calculated concentrations of chlorite are typically low in the rhyodacite units averaging only 4 wt. %, except in weakly and intensely altered zones; however, it averages <0.5% within 'unaltered' rhyodacite.

Results of normative mineral abundances for sixteen samples of rhyolite are presented in Table 4.4 and summarized in Figure 4.29D. Calculated concentrations of quartz averaged 43 wt. % and ranged from 35 to 60 wt. %. Both K-feldspar and albite were differentiated in the norm calculation and average 4 and 16 wt. %, respectively. Phengite was the dominant alteration mineral in the calculations, averaging 27 wt. % and ranging from 9 to 35 wt. %. Chlorite abundance was estimated to be up to 15 wt. % in several samples, but chlorite is generally low in this unit. The calculated carbonate contents were less than < 10 wt. %.

4.8 Shortwave Infrared Spectroscopy and Distribution of Alteration Minerals

Shortwave infrared (SWIR) spectroscopy is an emerging technique which has been used to differentiate proximal versus distal alteration facies in volcanic-hosted massive sulfide environments (e.g., Thompson et al., 1999; Yang et al., 2001; Jones et al., 2005), including in samples from the modern seafloor (e.g., Paulick and Bach, 2006; Hocking et al., 2010). Its rapid sampling time (5-10 s) and virtually no sample preparation make it an invaluable exploration tool as the spectra can be collected directly on cut drill core. This is the first application of SWIR in the Buchans Mining Camp.

SWIR spectroscopy measures the response of vibration of OH and H_2O bonds to shortwave infrared (1.3-2.5um) radiation (Hauf, 2005). Excitation of the sample by a light source produces different combinations of asymmetric/symmetric OH-stretching or H_2O structural bending which are observed as absorption features on a reflectance spectrum. The positions of the absorption features vary depending on the coordination of the OH and H_2O with different cations. In particular, bond lengths between cations and hydroxyl groups (or other anionic species such as SO_4, CO_3) control the wavelength position of absorption features. Free OH and H_2O have an absorption feature at ~1.4 um which corresponds to the smallest bond length. Interlayer H_2O has an absorption feature at ~1.9 um. AlOH has an absorption feature at 2.2 um, FeOH at ~2.29 um, and MgOH at 2.31 um, reflecting increasing cationic radii and increasing wavelength positions. The unique wavelength positions of hydroxyl bound to different cations thus allow the assessment of the crystal structure (e.g., octahedral vs. tetrahedral sites) of various alteration minerals including mica, chlorite, epidote, carbonate, and clay minerals.

The intensity of individual absorption features is generally proportional to the abundance of the alteration mineral with those specific bonds, but highly variable absorption coefficients hinder quantitative assessment of alteration mineral abundances. Mixtures of different minerals dramatically affect the shape of the spectra. One of the best examples is that of illite and chlorite

(e.g., Figure 4.30A and B). Illite has a much higher absorption coefficient than chlorite and will thus have a greater influence on the spectra and appear to be in greater abundance than actually present. However, some authors (e.g., Herrmann et al., 2001) were able to semiquantitatively (r=0.62-0.74) determine the relative abundances of white mica and chlorite. Spectral software (e.g., SPECWIN^{TM}) that generates hypothetical spectra for mixtures of white mica and chlorite can also be used to estimate relative abundances of minerals by comparison with spectra.

Reference spectra for various sericite and chlorite compositions

White mica and chlorite have markedly different SWIR spectra because of the different cations present in their respective crystal structures (Figure 4.30C and D). The most notable difference is the higher relative reflectance and sharpness of the absorption features in the white mica profile. In particular, white mica has a strong ~2180-2228nm AlOH absorption feature, whereas chlorite has distinctive 2235-2255nm FeOH and 2320-2360 nm MgOH absorption features (Herrmann et al., 2001).

Variation in the position of the AlOH absorption feature in white mica is attributed to the amount of octahedral Al in its crystal structure (Herrmann et al., 2001; Jones et al., 2005). Absorption features between 2180 and 2195 nm are consistently associated with high proportions of octahedral Al; whereas, features between 2116 and 2228 nm are consistently associated with low proportions of octahedral Al (Post and Noble, 1993; Herrmann et al., 2001; Jones et al., 2005). Typically, Na-bearing micas (exchange of K for Na in interlayer region) have high proportions of octahedral Al (2180-2195 nm), normal K-bearing micas (e.g., muscovite and illite) have 'normal' proportions of octahedral Al (2200-2208nm), and phengitic micas have low proportions of octahedral Al (2216-2228nm). Additionally, the proportion of octahedral aluminum is correlated with the amount of iron and magnesium in the mica structure (Jones et al., 2005). High proportions of octahedral Al (e.g., Na-mica) correlate with lower proportions of iron and magnesium, whereas low proportions of octahedral Al (e.g., phengite) correlate with higher proportions of iron and

magnesium. The position of the AlOH feature is therefore an indication of the composition of the white mica.

The different positions of the FeOH and MgOH absorption features in chlorite indicate the exchange of Mg for Fe in its structure (Jones et al., 2005). Generally, Mg-rich chlorite absorbs at shorter wavelengths than Fe-rich chlorite (Herrman et al., 2001, Jones et al., 2005). Unfortunately, muscovite and carbonate have absorption features at the same wavelength as the MgOH feature of chlorite so the degree of Fe and Mg exchange cannot be easily determined by SWIR in mixed assemblages (Herrman et al., 2001, Jones et al., 2005).

Spectral characteristics of altered samples from the Lundberg and Engine House zones

SWIR spectra for each chemostratigraphic unit (Chapter 3) were obtained to better characterize the alteration assemblages, and results are summarized in Figures 4.31 and 4.32. Different spectral responses were obtained for the phengite-quartz-carbonate-chlorite zone in the structurally repeated rhyolite unit (LSS), the weak sericite-carbonate zone within rhyodacite and quartz-phyric rhyodacite (BRF), and the quartz-chlorite-sericite altered rocks within the upper basaltic andesite and andesite units (SHF) (Figure 4.32).

SWIR spectra of the upper basaltic andesite (SHF) display varying contributions from chlorite, illite, and quartz (compare Figure 4.30 and Figure 4.33). The influence of chlorite and decreasing SiO_2 clearly shortens the wavelength of the ~1400 nm absorption feature of water. The spectrum for andesite is similar to that of the upper basaltic andesite but has a larger response from illite. The chlorite spectral response in both rocks is characterized by a strong positive slope from a ~1400 nm water feature through a ~2100 nm crest and a distinct trough between ~1908 nm and 1995 nm. The remainder of the profile has an overall negative slope from a ~2118 nm shoulder, reflecting a minor sericite component and two more strong absorption features at ~2250nm (FeOH) and ~2335nm (MgOH). The illite spectral response has a negative slope across the entire spectra. The first absorption feature at ~1410 nm is at a slightly higher wavelength than that of chlorite, but a

similar ~1908 nm feature is present reflecting the presence of interlayer water in both crystal structures. The tail-ends of the spectra are characterized by a distinct shoulder at ~2118 nm, descending to a strong ~2200 nm (AlOH) feature and an additional ~2343nm trough (secondary AlOH). Negative slopes across the entire spectra are correlated with wt. % SiO_2 (e.g., Figure 4.33).

SWIR spectra for the rhyodacite (BRF) have a distinctive illite signature with few samples containing both illite and minor chlorite (Figure 4.33). Carbonate was observed petrographically, but a characteristic absorption spectrum for carbonate was not observed. The spectra have negative slopes across the entire range and characteristic absorption features at ~1908 nm (interlayer water), ~2200 nm (AlOH) and ~2343 (secondary AlOH), typical of illite. Spectra with chlorite (e.g., ~2250 nm absorption feature) have variable positive slopes up to ~1700-1800 nm and tend to have absorption features with slightly shorter wavelengths.

SWIR spectra for the rhyolite unit (LSS) are of two types: a response dominated by phengitic illite and responses dominated by illite with minor chlorite (Figure 4.35). Carbonate had no apparent effect on the spectra. Both spectra have a sharp absorption feature at ~1415 nm, a strong asymmetric water feature at ~1908, and a small inflection at ~2118. However, phengitic illite has a much stronger positive iron slope over the first half of the spectrum and a displaced AlOH water feature at ~2218 nm in phengitic illite versus ~2205 nm in normal illite (inset: Figure 4.35). Minor chlorite is detected by a small inflection or absorption feature at ~2250nm. A secondary AlOH absorption feature is observed at ~2343nm in both types of spectra.

Correlation with mineral abundances

The relative abundance of an alteration mineral may be assessed by the depth of its characteristic absorption features (e.g., Herrmann, 2001). The depth of an absorption feature is affected by the relative reflectance or brightness of the sample which may be different for rocks with similar mineralogy. This is avoided by comparing the ratio of two distinct absorption features in a

single sample to the same features in another sample. The mineral proportions calculated in the previous section are used here for comparison.

Within the Lundberg and Engine House zones, chlorite, illite, phengite, quartz, and carbonate are the only significant alteration products. Chlorite, illite, and quartz were all observed on the SWIR profile; but carbonate was masked by the dominance of illite. Samples with more quartz had spectra with a different slope (e.g., Figures 4.33 to 4.35). The relative depths of the major AlOH and MgOH absorption features were used as proxies for illite and chlorite abundance (Figure 4.36). The position and depth of the MgOH feature may be affected by the secondary AlOH feature (~2343 nm) of illite, or CO_3 of carbonates; however, at lower wavelengths (to 2326 nm) the feature is dominated by MgOH. The ratio of the AlOH and MgOH absorption features were plotted against normative illite/chlorite ratios for all lithologies in the Lundberg and Engine House zones. The upper basaltic andesite shows good correlation between the normative abundance of muscovite/chlorite versus depth of the AlOH/MgOH feature ($r'=0.75$: Figure 4.36). No significant correlations (i.e., $r'>0.5$) were observed for the fractionated basaltic andesite, rhyodacite, or rhyolite units largely due to the low concentration of chlorite observed in these samples.

4.9 Summary and Conclusions

Five types of stockwork veins were identified in the Lundberg and Engine House zones: (1) massive pyrite, (2) quartz-carbonate veins with disseminated or blebby sulfides (85%), (3) quartz-carbonate-barite with disseminated or blebby sulfides (10%), (4) massive sphalerite-galena with minor carbonate-quartz (5%), and (5) small quartz-carbonate veins with little or no sulfide (<1%) (Figure 4.5). In general, bladed quartz, carbonate, and barite are observed at the top of the mineralized zones. The veins with massive gangue and abundant disseminated sulfides occur directly below the bladed barite and carbonate horizon. Thin veins with or without sulfides are observed both above and below the mineralized zone. The distinct change from massive to bladed minerals may reflect shallower depths in the volcanic succession and possible open-space filling

close to the paleoseafloor, similar to that observed in epithermal systems. Sulfur isotope work by Kowalik et al. (1981) confirms that the source of sulfate for barite was dominantly seawater. The presence of 'bladed calcite' may indicate a zone of boiling (e.g., Simmons and Christenson, 1994); however, the polycrystalline nature of the carbonate and the observed replacement of bladed barite by carbonate indicate that primary blades of calcite did not form. The conditions under which barite can dissolve and be replaced by calcite are indicated in Figure 4.37. This does not preclude boiling, however, and a zone of boiling may also explain the position of the quartz-sericite zone largely above the polymetallic stockwork (Drummond and Ohmoto, 1985). Exsolution of CO_2 would have raised the pH of the hydrothermal fluid and caused precipitation of sulfides in the stockwork while CO_2 gas may have caused acid alteration (quartz-sericite at a pH of 4-4.5) in the overlying rocks (Drummond and Ohmoto, 1985). Thus, chlorite which forms at a pH of 4.5-5.5, may have formed after boiling and release of CO_2 from the 'residual' hydrothermal fluid.

Five alteration facies were identified within the host lithologies of the Lundberg and Engine House zones: siliceous core zone, moderate quartz-chlorite-sericite, strong to intense quartz-chlorite-sericite, weak sericite-carbonate, and phengite-quartz-carbonate-chlorite. These alteration facies form pipe-like alteration around the Lundberg and Engine House zones (Figure 4.38). The moderate quartz-chlorite-sericite alteration facies forms the weakest footwall alteration most distal to mineralization. The strong to intense quartz-chlorite-sericite occurs inside the envelope of moderately altered basalt and is cut by stockwork mineralization. Intense quartz-chlorite-sericite alteration is cut by quartz alteration which forms the siliceous core. The siliceous core zone is the most intense alteration within the Lundberg and Engine House zones and forms by replacement of the quartz-chlorite-sericite facies, mostly within basaltic andesite. The strongly altered quartz-chlorite-sericite zone mostly occurs within the andesite and rhyodacite, but is locally discordant into the upper basaltic andesite. The upper sedimentary sequence is altered to weak sericite-carbonate; however, all primary textures are preserved and alteration. The phengite-quartz-carbonate-chlorite zone occurs within the rhyolite unit of the Lucky Strike hanging-wall succession and rhyodacite tuff

unit of the Engine House Zone (BRF). Alteration intensity increases westward in the phengite-quartz-carbonate-chlorite zone within the hanging-wall rhyolite unit, and represents distal hydrothermal alteration of uncertain spatial relationship to ore.

Stockwork mineralization occurs in basaltic andesites with CCPI and AI values higher than 90. At depth and marginal to the Lundberg and Engine House zones, CCPI values are lower than 90 and AI values greater than 60. Significant mass change occurred within the Lundberg and Engine House zones (e.g., Figure 4.23). All units are characterized by net mass gain of SiO_2, Al_2O_3, MgO, Fe_2O_3, and K_2O, and loss of CaO and Na_2O associated with chloritization and sericitization in the footwall. Alteration changes were broadly uniform across much of the Lundberg and Engine House zones, with lower overall mass gains at greater distances from the mineralization. In contrast to the other lithologies, the rhyodacitic tuff in the hanging-wall shows a net mass loss of SiO_2, and a gain of K_2O, MgO, and Fe_2O_3. The remaining rhyodacite samples experienced much less mass change than in the upper basaltic andesite, possibly owing to the primary composition of the rhyodacite (e.g., higher quartz). The rhyolite unit showed variable mass gains and losses; only two samples showed Fe and Mg enrichment adjacent to shear zones.

A strong, negative correlation between the abundance of albite and the Ishikawa alteration index within basaltic andesite suggests that albite destruction is the main mechanism for formation of sericite and/or chlorite (e.g., Figure 4.27A). Sericite forms principally by the replacement of albite (Gifkins et al., 2005):

(1) $3NaAlSi_3O_8$ (albite) + $K^+ + 2H^+ \rightarrow KAl_3Si_3O_{10}(OH)_2$ (sericite) + $6SiO_2$ (quartz) + $3Na^+$

Chlorite forms by the replacement of albite or sericite (Gifkins et al., 2005):

(2) $2NaAlSi_3O_8$ (albite) + $3Mg^{2+} + 2Fe^{2+} + 14H_2O \rightarrow Mg_3Fe_2Al_2Si_3O_{10}(OH)_2$ (chlorite) + $3H_4SiO_4$ (aq) + $2Na^+ + 8H^+$

(3) $2KAl_3Si_3O_{10}(OH)_2$ (sericite) + $3H_4SiO_4$ (aq) + $9Mg^{2+} + 6Fe_2+ + 18H_2O \rightarrow$ $3Mg_3Fe_2Al_2Si_3O_{10}(OH)_8$ (chlorite) + $2K^+ + 28H^+$

Moderate correlations are observed between the abundance of chlorite + sericite and the Ishikawa alteration index (e.g., Figure 4.27B) which indicates that these alteration minerals formed by the destruction of albite (reaction 2). Formation of chlorite by the replacement of sericite (reaction 3) is common in prograde hydrothermal assemblages since sericite forms at lower temperatures than chlorite; however, chlorite is abundant even in moderately altered zones, and veins of chlorite are observed to cut sericite altered phenocrysts. The lack of correlation between the normative abundance of chlorite and sericite further indicates that reaction 3 was negligible. Two different alteration paths are suggested for moderately versus intensely altered basaltic andesite, suggesting that they may reflect paragenetically distinct stages of alteration (e.g., Figure 4.27B). The siliceous core zone may form by 2 reactions (Gifkins et al., 2005):

(4) $Mg_3Fe_2Al_2Si_3O_{10}(OH)_8$ (chlorite) + $4H_2O$ + $10H^+$ → $3SiO_2$ + $3Mg^{2+}$ + $2Fe^{2+}$ + $2Al(OH)_3$(aq)

(5) H_4SiO_4 (aq) → SiO_2 + $2H_2O$

Reactions 4 is the most likely to have formed the intense quartz alteration in the core of the Lundberg Zone consistent with the observed replacement of chlorite and aluminum leaching from the host rocks. However, reaction 5 is also plausible, since H_4SiO_4 was likely liberated from the host rocks during the chloritization of albite (reaction 2) which would have occurred prior to extensive silicification in the core of the deposit (e.g., Figure 4.12C).

The formation of carbonate within stockwork veins is attributed to magmatic input of CO_2 +/- Ca (Kowalik and Sawkins, 1981). Carbonate alteration observed within the hanging-wall likely formed by interaction between hydrothermal fluids and bicarbonate in seawater causing supersaturation of carbonate and subsequent precipitation (cf. Large et al., 2001). In the rhyolite unit, lateral flow of this mixed fluid through the permeable tuff likely precipitated sericite and carbonate into the matrix and around volcanic clasts.

The discrete zonation of alteration minerals from intense quartz-sericite assemblages higher in the Lundberg Zone to quartz-chlorite-sericite lower in the stratigraphy indicates increasing

temperature and pH of the hydrothermal fluids with depth (e.g., Schardt et al., 2001). The intense quartz and illite (sericite) facies likely precipitated at a pH between 4 and 4.5 and temperatures <250°C, whereas the quartz –chlorite-sericite assemblage likely formed at pHs of 4.5 to 5.5 and temperatures between 250° and 350°C (Schardt et al., 2001). Most mineralization occurs near the transition between these two zones. The lack of abundant chalcopyrite supports the moderate temperature and pH of the hydrothermal fluids.

Shortwave infrared spectra of the altered samples are dominated by chlorite, illite (hydrated muscovite) and quartz (e.g., Figures 4.33 to 4.35), and the different alteration assemblages are clearly distinguished by SWIR. The andesite has a higher percentage of quartz, causing the slope of the spectra to shift from positive to negative across all wavelengths measured. These samples also have a much larger proportion of muscovite. Spectra of the rhyodacite have a much larger contribution from illite, and few samples contain chlorite. The hanging-wall rhyolite has a similar spectrum, but the AlOH absorption feature occurs at higher wavelength (~2218nm) indicative of phengitic illite rather than normal potassic illite/muscovite; normal potassic illite/muscovite is found proximal to ore, whereas phengitic compositions are more distal. As this was the first attempt to use SWIR in the Buchans camp, the results have important implications for possible future application in the area.

4.10. Comparison to Other Kuroko-type Deposits and Genetic Implications

The similarity between the Buchans orebodies and the Miocene Kuroko deposits of Japan was recognized by some of the earliest workers in the camp (e.g., Thurlow et al., 1975; Thurlow and Swanson, 1981) and names for different types of Buchans ore were previously derived from Kuroko nomenclature: kuroko or 'black ore' (sphalerite-galena rich), oko or 'yellow ore' (chalcopyrite-rich), and keiko (siliceous stockwork ore) (Ohmoto et al., 1983). The polymetallic stockwork (sphalerite > galena > chalcopyrite > silver > gold) to the Buchans ores, however, has several differences from that of a typical Kuroko deposit. The Lundberg and Engine House zones form an elongate (~600 m along

strike) and wide (~450m), polymetallic stockwork in contrast to the much narrower (<100m), pipe-like, chalcopyrite-rich stockworks of Kuroko deposits (e.g., Deposit 4, Kosaka mine: Urabe et al., 1983). The overlying and offset Lucky Strike massive sulfide deposit is 400 m in length and was described as having "sheet like" morphology with transported ore extending well beyond its margins (Jambor, 1987). The black ores of the Kuroko deposits are identical to the polymetallic massive sulfide observed within the Lucky Strike deposit. However, unlike the Kuroko deposits, yellow (oko) ore is rare at Lucky Strike (Thurlow and Swanson, 1981), indicating a lower temperature of ore formation. Anhydrite/ gypsum-rich ore is also absent at LS possibly because of low temperatures or dissolution of anhydrite below 150°C at seafloor pressures (cf. Haymon and Kastner, 1981). However, baritic ore occurs across the top of the Lundberg and Engine House zones, similar to many Kuroko deposits.

The host rock controls on mineralization at LS and in the Kuroko deposits appear to be similar. However, an obvious synvolcanic fault that could have controlled the hydrothermal upflow has not been identified. A syn-volcanic fault could be envisaged running SE-NW in the same orientation as the longest dimension of the Lundberg Zone, as the alteration is symmetrical around this axis of most intense mineralization (e.g., Figure 4.38).

The Kuroko-type deposits of the Cambrian Mount Read Volcanic Complex of Western Tasmania provide another excellent comparison to the Buchans Mining Camp. VMS deposits of the Mount Read belt range from Cu, Zn-Cu, and Zn-Pb-Cu types with varying amounts of Ag and Au and have varying morphologies from lens-shaped to sheet like (Zn-Pb-Cu and Zn-Cu type; e.g., Roseberry, Hellyer, Que River, Thalanga), to pipes and stringer deposits (Cu-Au type; e.g., Mount Lyell and Highway Reward: Large et al., 2001b). The Lucky Strike orebody, as well as the Cu-Zn Skidder and Cu-rich Mary March prospects, most closely resemble the polymetallic lens and sheet-like deposits (e.g., Roseberry, Hellyer, Que River, Thalanga) which are interpreted to have formed at shallow water depths of 500 to ~1000 m (Large et al., 2001b).

A comparison of the alteration characteristics of Roseberry and Western Tharsis (Mt. Lyell) with the Lundberg Zone in Table 4.5. Alteration at the Hellyer polymetallic VMS deposit was modelled by Schardt et al. (2001) who determined that the character of the alteration assemblages was controlled by 3 factors: temperature, pH, and redox state of the hydrothermal fluid.

The alteration mineralogy observed at Hanging-wall and Battle Mountain orebodies at Myra Falls are similar to that of Buchans; however several differences must be noted. The footwall Price Andesite is heavily altered to sericite, quartz, and lesser carbonate, with chlorite proximal to the HW and Battle orebodies (Jones et al., 2005). Here, chlorite content is greatest immediately adjacent to the core of the deposit (Table 4.5). In felsic lithologies sericite, quartz, pyrite, chlorite, epidote, calcite, and dolomite are dominant (Jones et al., 2005). At Buchans, chlorite is developed mainly within upper basaltic andesite and is uniformly distributed beneath the Lucky Strike deposit. In the rhyodacite and rhyolite units at LS, a very similar alteration assemblage is observed containing quartz, sericite, and lesser chlorite, and carbonate (Table 4.5). At Myra Falls, the composition of the muscovite (and thus the wavelength of the AlOH absorption feature) is a distinctive marker of proximal versus distal alteration. In proximal alteration zones, the AlOH absorption feature of the Price Andesite is characteristic of sodic muscovite (<2200 nm), whereas in distal alteration zones it is typical of normal K-muscovite (~2205). By contrast, samples of moderate to intensely altered basaltic andesite proximal to mineralization in the Lundberg Zone have normal to slightly phengitic, K-muscovite compositions and AlOH wavelengths identical to regional mafic samples from Myra Falls. The disparity between these values is the result of differing primary composition of the host rocks, or concentration of paragonite (Na/Na + K) and/or phengite (Fe + Mg or Si/Al) in the hydrothermal fluid (Herrmann et al., 2001; Jones et al., 2005).

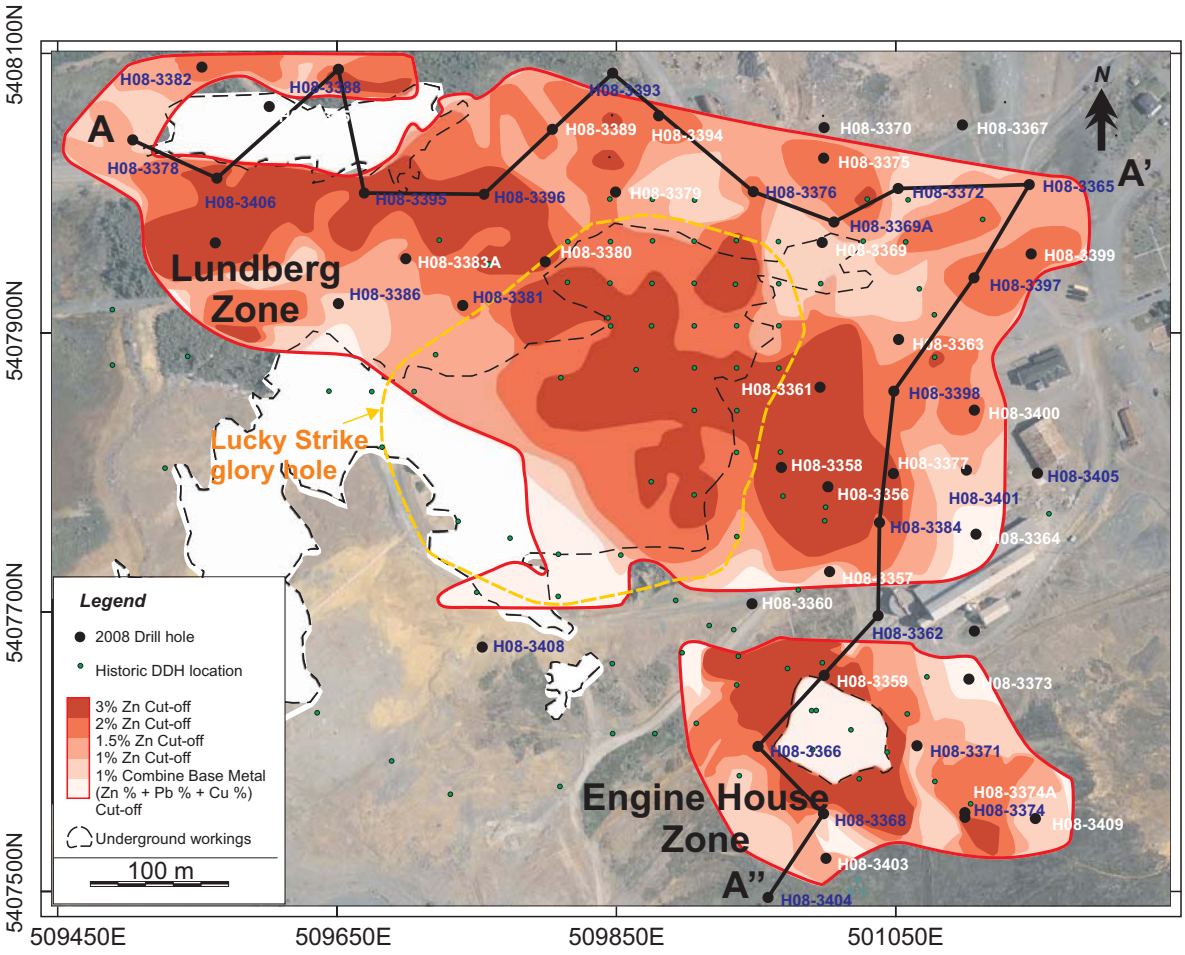

Figure 4.1: Schematic map of cut-off grades for Zn and combined base metals (Zn wt. % + Pb wt. % + Cu wt. %) projected to surface in the Lundberg and Engine House zones. Logged drill holes are highlighted in navy blue. Cross section A-A' is presented in Figure 4.2. The UTM datum is NAD 1983 (Modified from Webster and Barr, 2008).

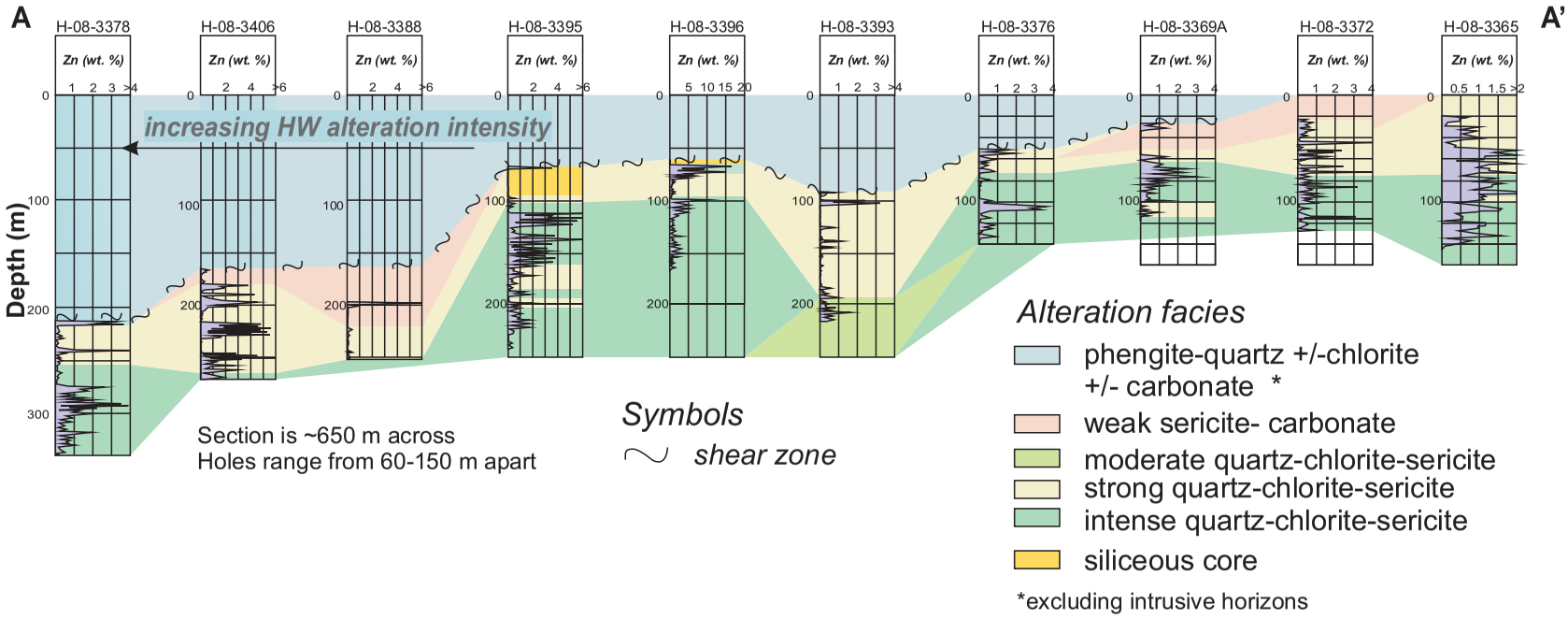

Figure 4.2: Cross-section A to A' showing the relationship between mineralization and alteration within the Lundberg Zone. Five main alteration facies were identified: a siliceous core zone, strong to intense quartz-chlorite-sericite, moderate quartz-chlorite-sericite, weak sericite +/- carbonate, and phengite-quartz-carbonate-chlorite. The siliceous core zone and the strong to intense quartz-chlorite-sericite zones are cut by stockwork mineralization, whereas the overlying weak sericite +/- carbonate facies is associated with massive sulfide. The phengite-quartz-chlorite-carbonate facies is not associated with any significant mineralization.

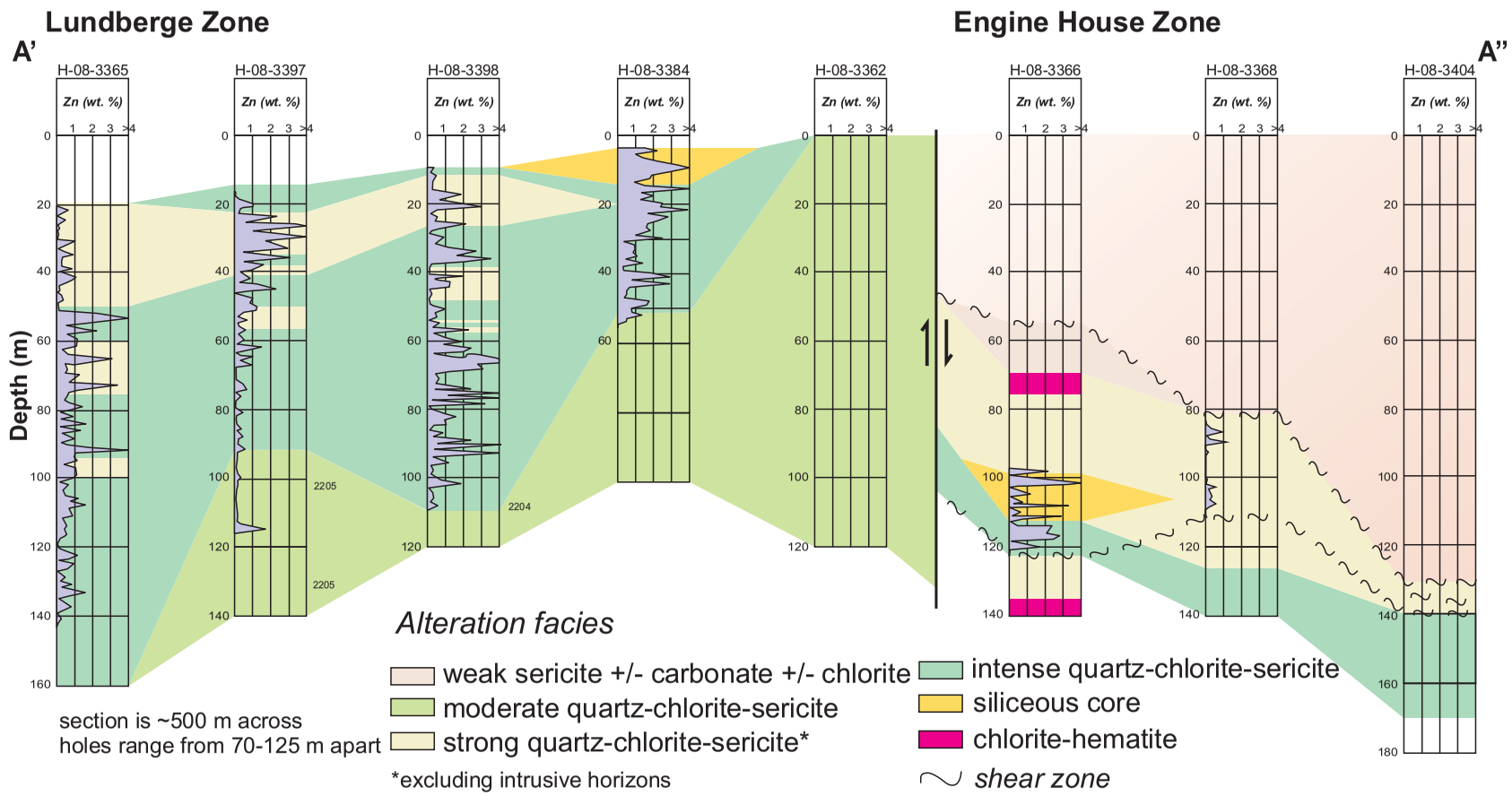

Figure 4.3: Cross section A' to A", from northeast to southwest, shows the relationship between mineralization and alteration within the Lundberg and Engine House zones. Alteration facies display an increase in alteration intensity from moderately altered to strongly and intensely altered quartz-chlorite-sericite facies towards the northeast (A'). The Engine House Zone has similar alteration to the Lundberg Zone except for much different sericite compositions in their respective structurally-emplaced assemblages.

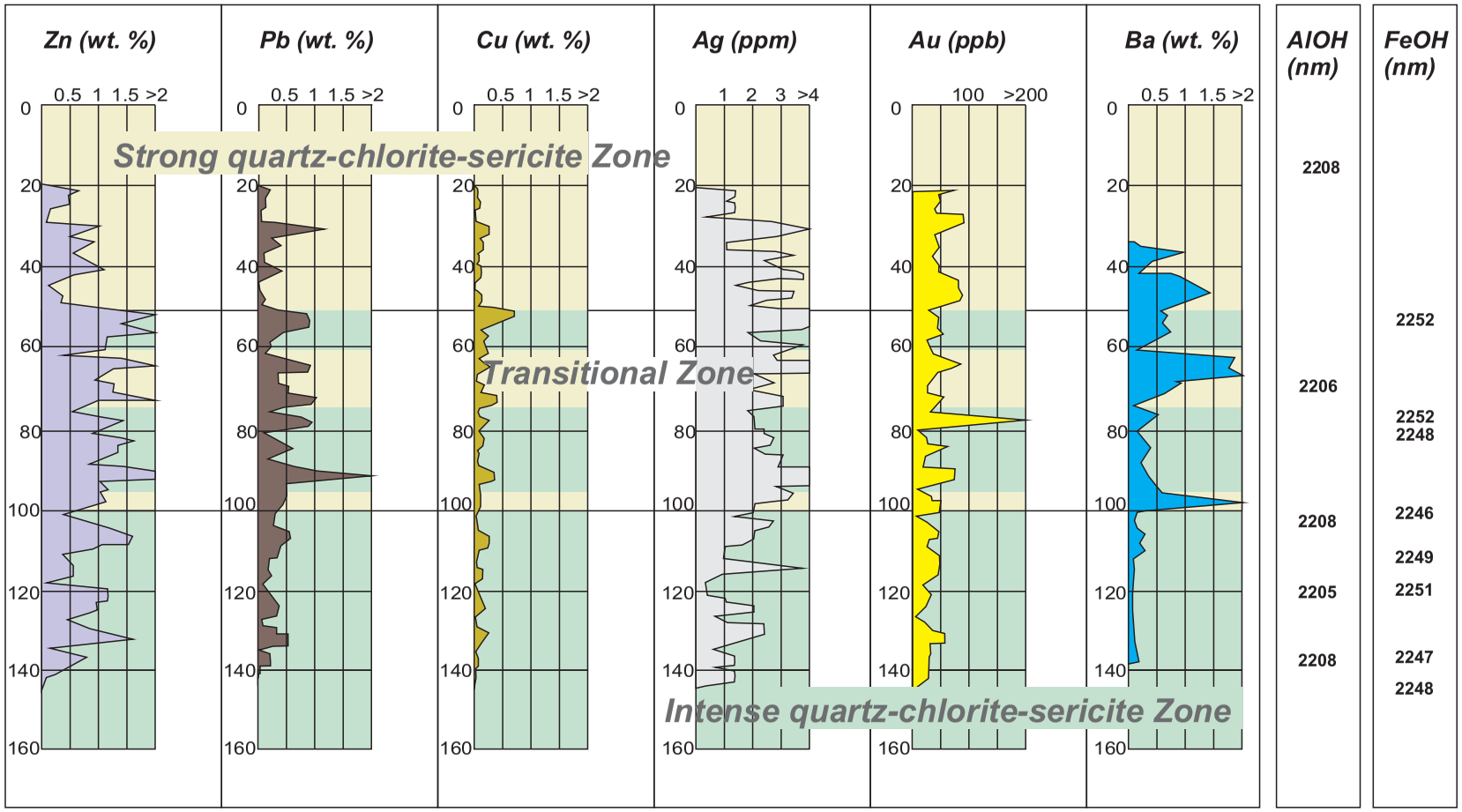

Figure 4.4: Base and precious metal grades in H-08-3365 showing metal enrichments in all zones. However, high concentrations of Ba are clearly associated with strong quartz-chlorite-sericite alteration. No systematic changes in AlOH or FeOH absorption features are observed. Alteration intensity decreases from intense to strong quartz-chlorite-sericite alteration towards the top of the hole.

Vein Types of the Lundberg Zone

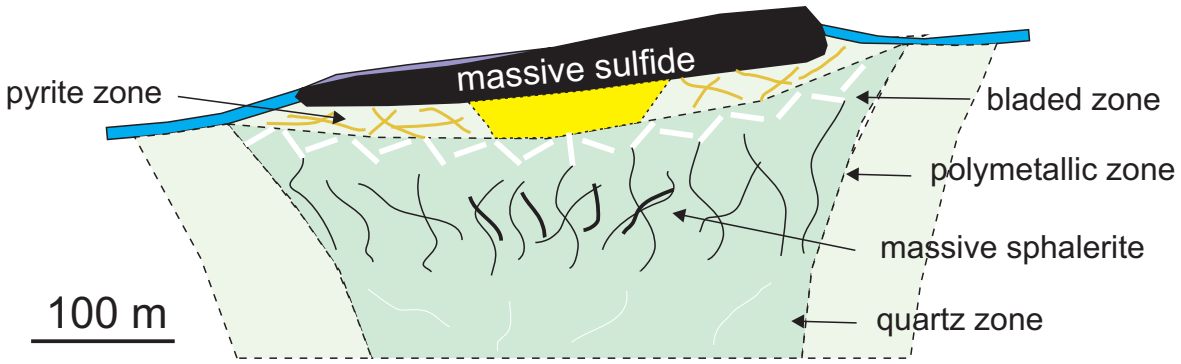

Figure 4.5: Schematic diagram of the various vein types of the Lundberg Zone. There are five main vein types: Massive pyrite, bladed barite and calcite, polymetallic, massive sphalerite-galena, and quartz-dominant. Massive pyrite veins occur in strongly altered basaltic andesite which are lighter in colour than the underlying, more intensely altered rocks. The bladed vein type consists of polymetallic veins, which have a bladed barite and calcite gangue. The polymetallic vein type consists of sphalerite, galena, chalcopyrite, and pyrite in a quartz and carbonate gangue. Massive sphalerite veins occur locally in a similar position to the polymetallic vein type. Quartz-dominated veins occur at the bottom of the stockwork zone, where mineralization terminates.

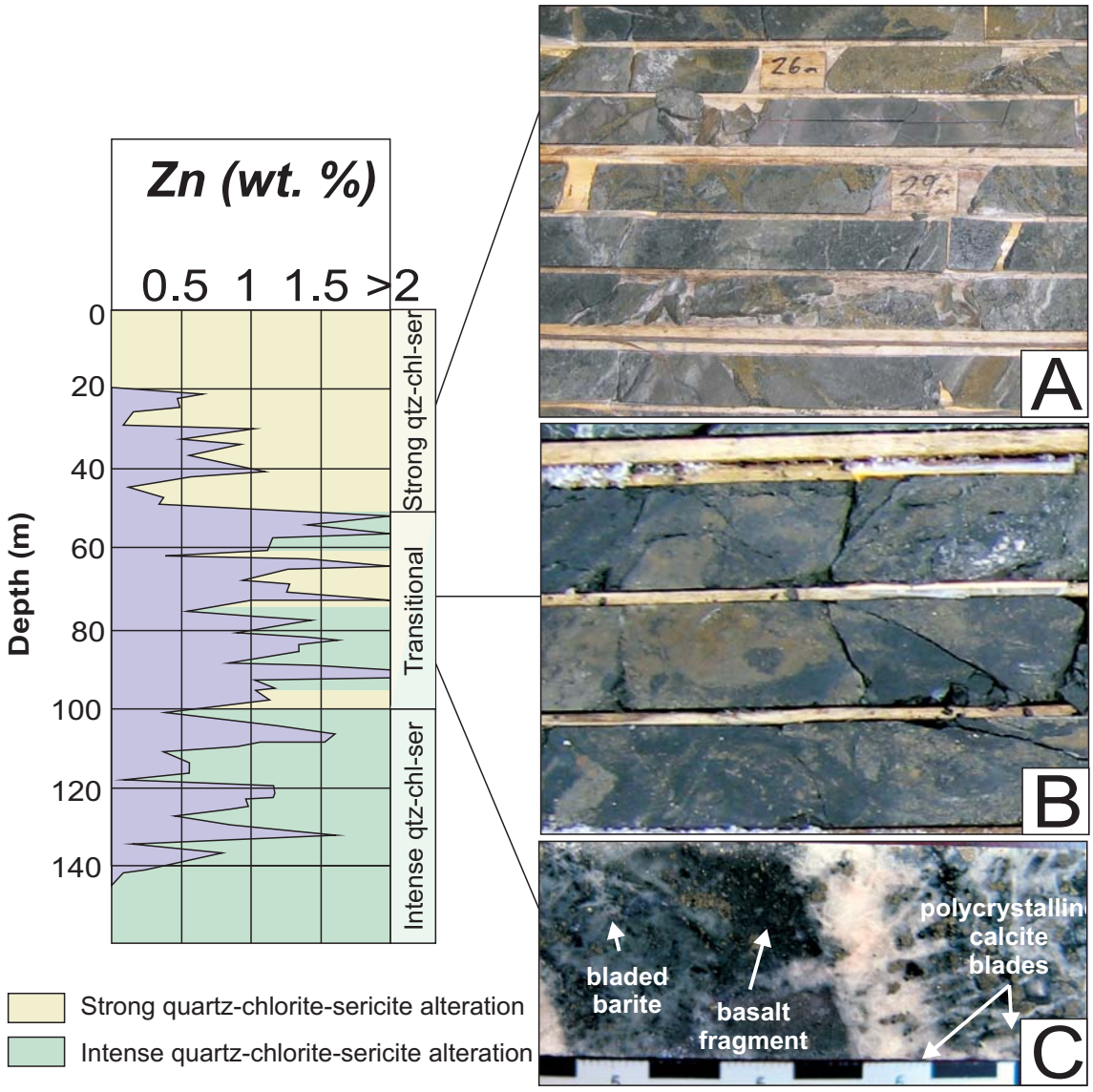

Figure 4.6: Photographs of alteration and mineralization of the Lundberg zone. A. Massive pyrite veins located at the top of the quartz-sericite zone. Sphalerite is present microscopically (i.e., Zn = 0.5 wt. %: H3365; 25 m). B. Semimassive sulfide zone consisting of >50 % pyrite in a chloritic mudstone (H3395; 121 m). C. Polycrystalline calcite blades and bladed barite surrounding a basalt fragment. Bladed barite forms smaller grey or white blades than calcite. Calcite forms large blades perpendicular to the basalt fragment infilling space clearly occupying a separate macroscopic habit (H3398; 21.5 m).

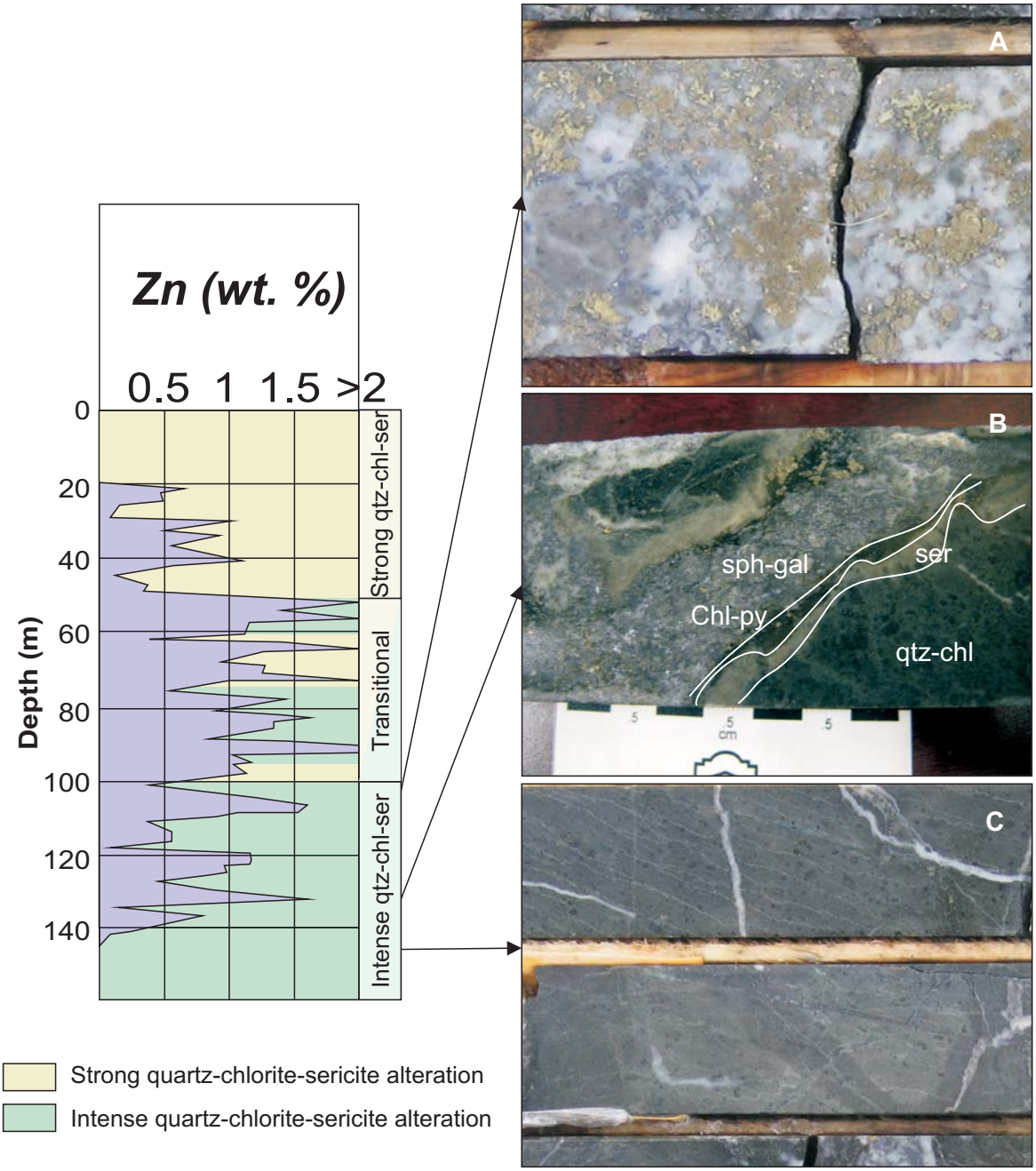

Figure 4.7: Summary of vein types within the Lundberg Zone. A. Disseminated to blebby sphalerite, galena, chalcopyrite, and euhedral pyrite within a massive quartz-carbonate matrix (H3378; 294 m). B. Proximal alteration of a massive sphalerite vein. The vein is bordered first by chlorite (cf. clinochlore: Henley and Thornely, 1981) and pyrite, then by sericite. Intense quartz-chlorite alteration is observed as "background" alteration (H3341; 131 m). C. Quartz-carbonate vein type cutting pervasive quartz veinlets (H3378; 297 m)

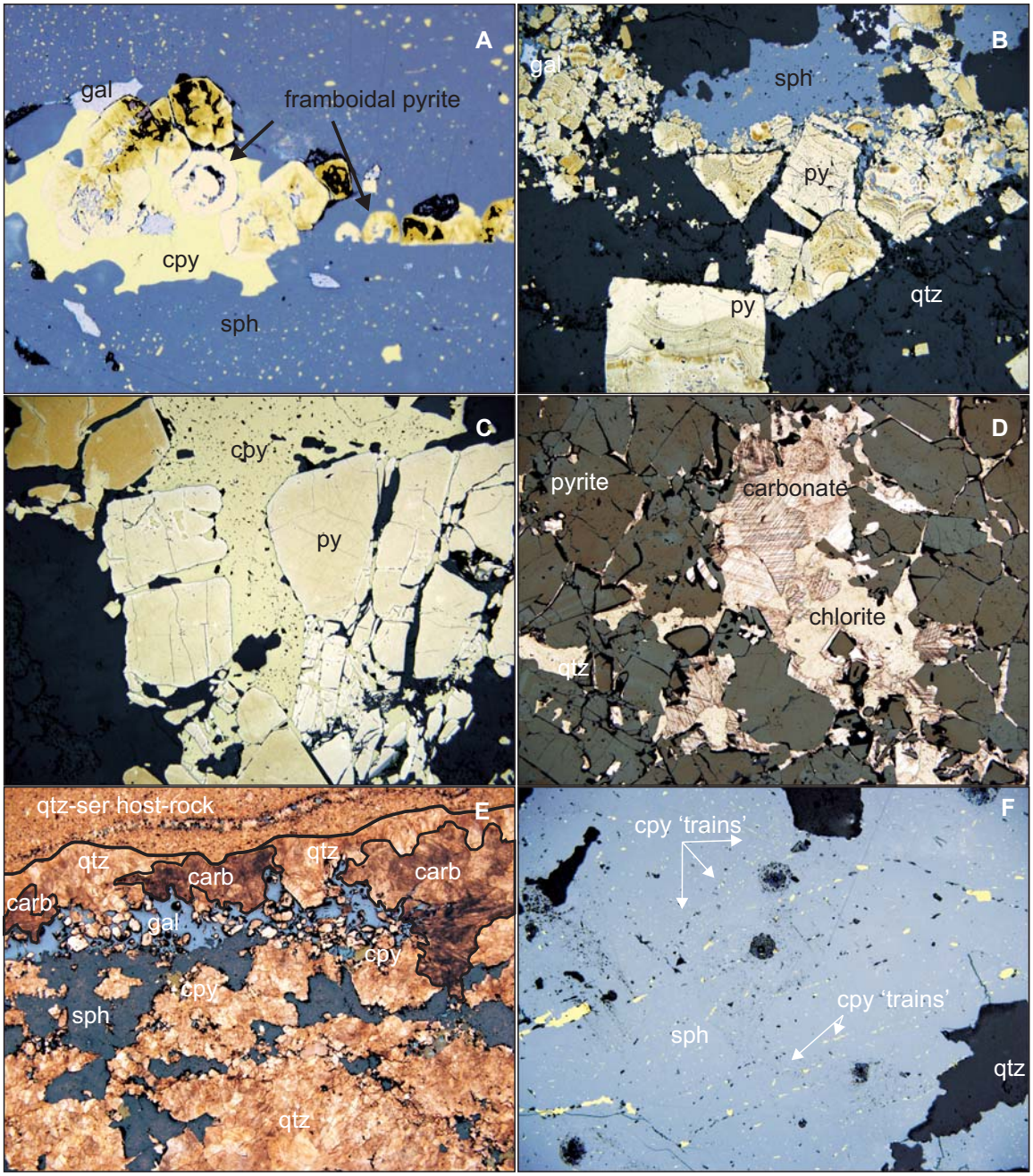

Figure 4.8: A. Colloform pyrite associated with chalcopyrite and galena within spaherite. Field of view is 0.43 mm. Taken under reflected light (H3341; 142 m). B. Colloform growth textures in pseudo-cubic pyrite. Field of view is 0.88 mm. Taken under reflected light (H3341; 167.5 m). C. Close association between pyrite and chalcopyrite at the upper margin of the polymetallic sulfide zone (H3341; 92.75 m). D. Association between pyrite, carbonate, and chlorite in a pyrite-rich vein. Pyrite clearly formed earliest; quartz, carbonate and chlorite filling the void space. Field of view is 1.75 mm, taken under mixed transmitted and reflected light (H-08-3365; 100 m). E. Zonation within a sulfide-bearing vein. Quartz precipitated on the vein wall followed by carbonate, galena, sphalerite, chalcopyrite. Field of view is 1.75 mm, taken under mixed transmitted and reflected light (H3398; 22 m). F. Chalcopyrite disease texture in sphalerite. Chalcopyrite blebs form linear 'trains' which precipitated along previous grain boundaries. The formation of this texture is attributed to replacement or coprecipitation of sphalerite by chalcopyrite (H3341; 126.5 m).

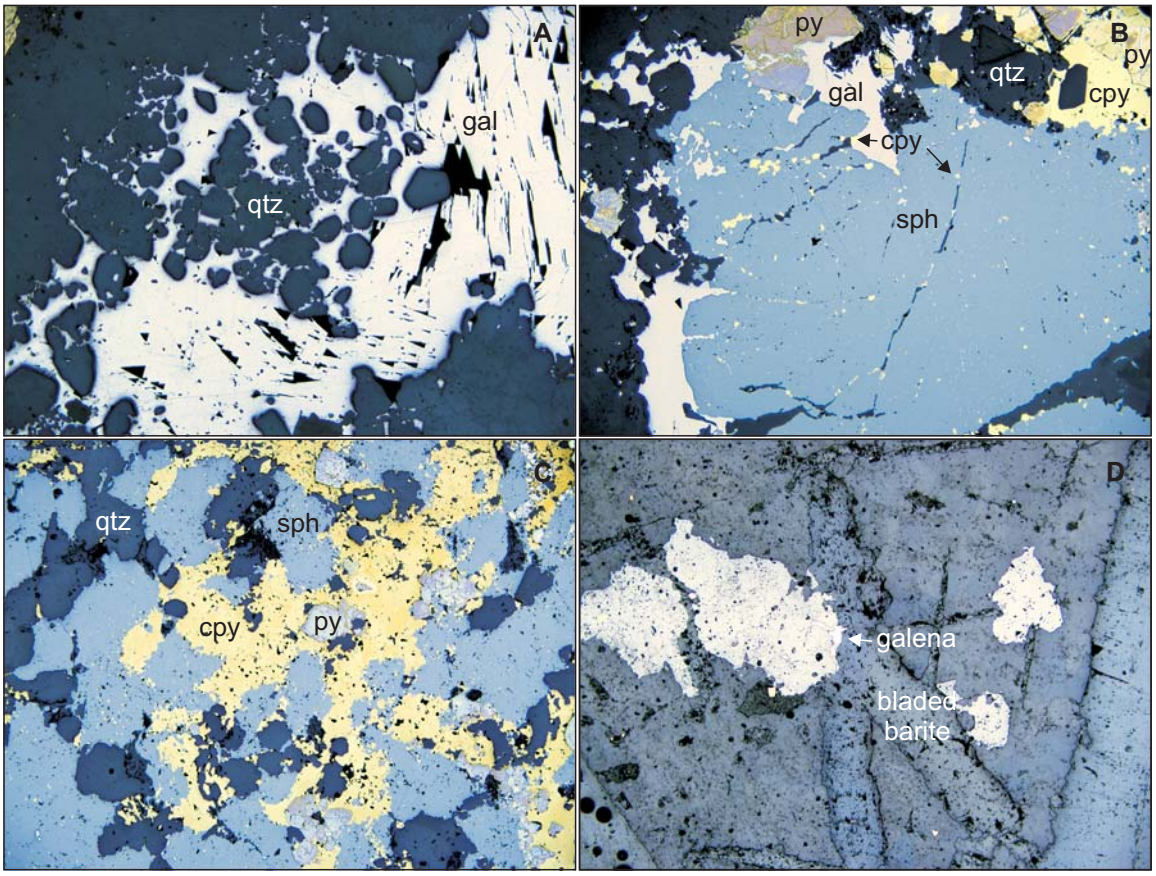

Figure 4.9: A. Typical growth of galena around quartz gangue. Field of view is 1.75 mm, taken under reflected light (H3341; 142 m). B. Association between the sulfides in the Lundberg and Engine House zones. Both galena and chalcopyrite are observed to infill pyrite and replace sphalerite. Chalcopyrite is observed to partly replace galena (upper middle). Field of view is 1.75 mm, taken under reflected light. C. Extensive replacement of sphalerite by chalcopyrite. Field of view is 1.75 mm, taken under reflected light (H3341; 144 m). D. Replacement of bladed barite by sphalerite. Field of view is 1.75 mm, taken under reflected light (H3398; 21.5 m).

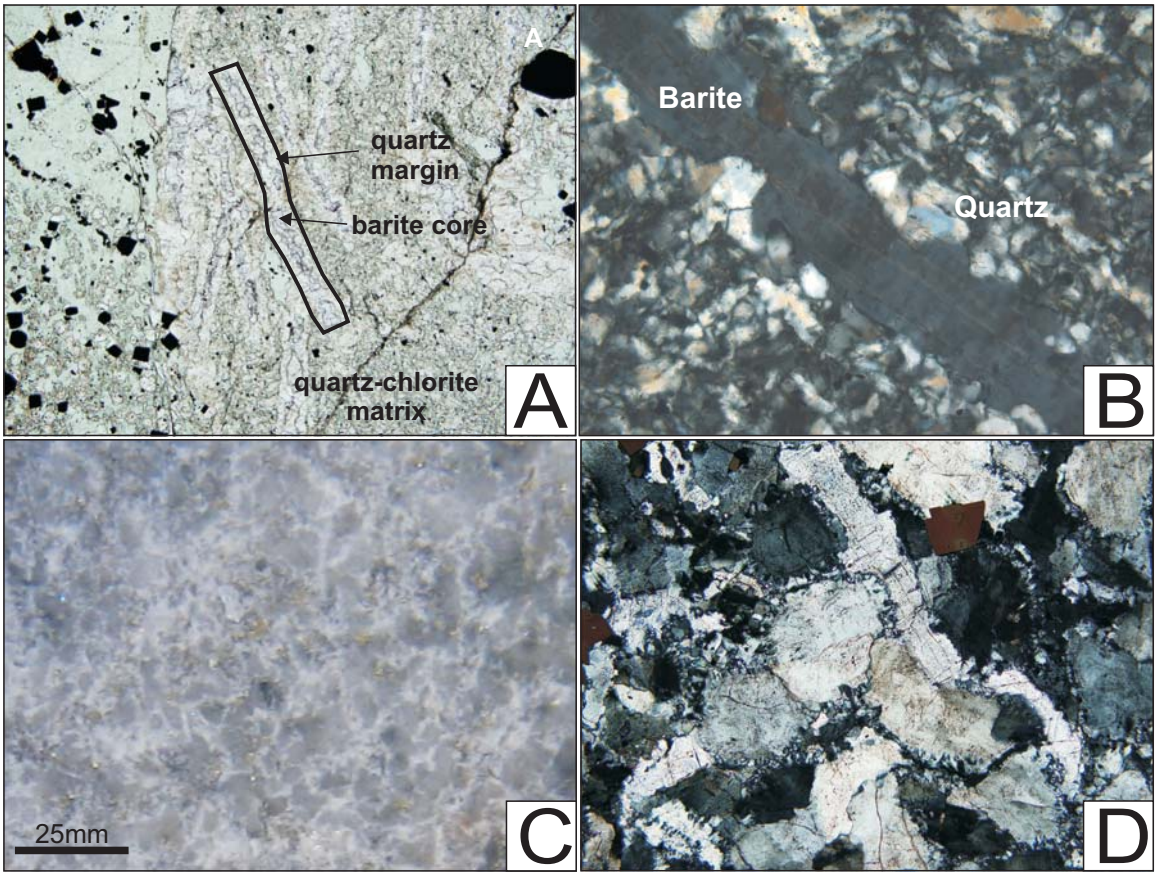

Figure 4.10: A. Bladed barite formed in the intense quartz-chlorite-sericite alteration zone. Barite is clearly replaced by quartz. Field of view is 1.75 mm, taken under plane polarized light (H3341; 330 m). B. Minor replacement of bladed barite by quartz. Field of view is 0.875mm; taken under crossed nicols (H3341; 93m). C. Intergrowth of bladed barite (white) and quartz (grey) within a polymetallic vein. Disseminated sphalerite, galena, and pyrite form the majority of the sulfide species. Barite forms an apparent interstitual texture around quartz (H3341; 90.5m). D. Photomicrograph of bladed barite and quartz intergrowth texture as shown in C. Quartz clearly replaces barite; a texture not apparent from macroscopic observation. Field of view is 0.875mm; taken under crossed nicols (H3341; 90.5m).

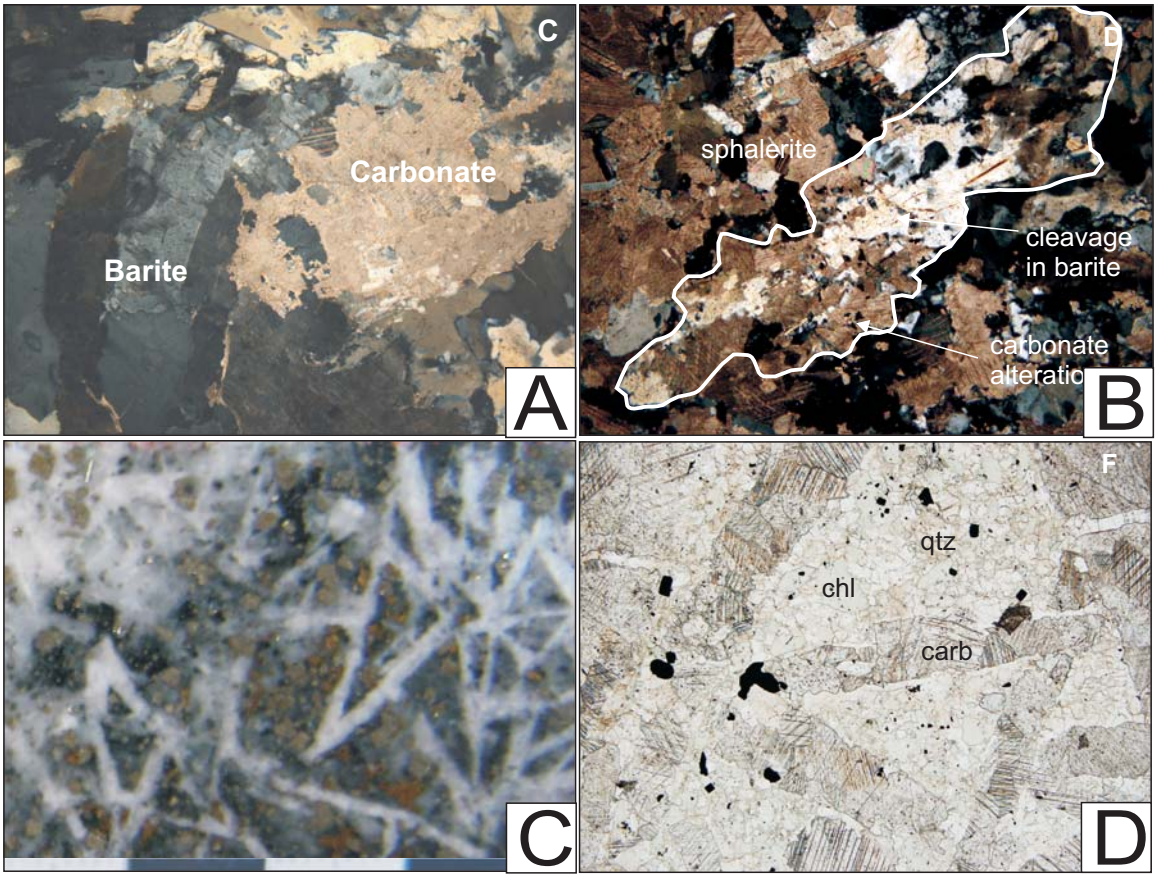

Figure 4.11: A. Partial replacement of bladed barite by carbonate. Field of view is 1.75 mm, taken under crossed nicols (H3341; 87.5 m). B. Partial replacement of bladed barite by carbonate. Carbonate typically alters barite along fracture and cleavage planes; however this rare example shows replacement of the majority of a blade. Field of view is 0.875 mm, taken under crossed nicols (H3341; 87.5 m). C. Bladed polycrystalline calcite within the upper portion of the Lundberg polymetallic stockwork. Disseminated pyrite and minor chlorite comprise an unusually large volume of this photo (H3398; 21.5 m). Scale is in centimetres. D. Bladed polycrystalline calcite in a quartz and chlorite gangue. Field of view is 1.75mm; taken under plane polarized light (H3365; 78 m).

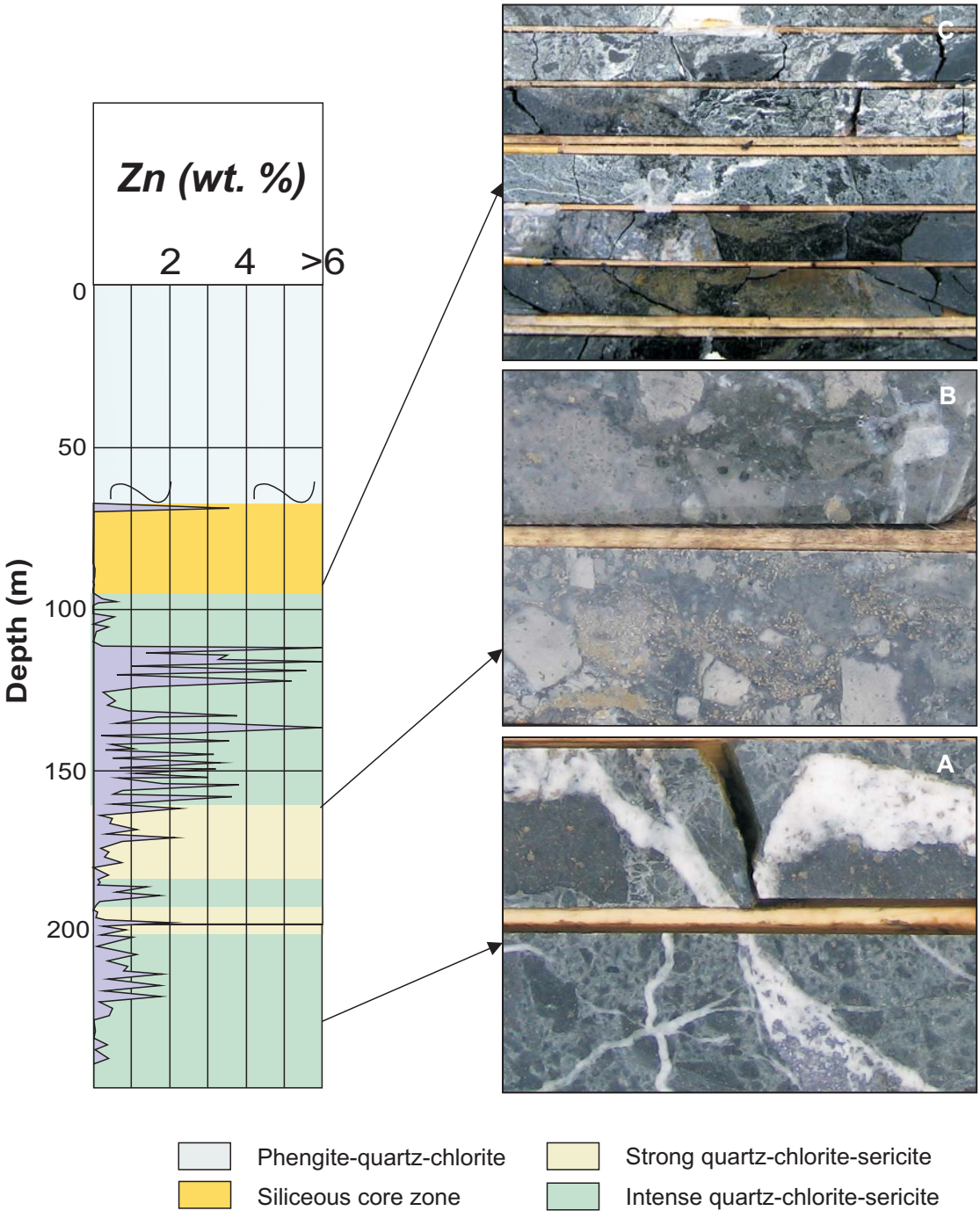

Figure 4.12: A. Quartz infilling of intensely altered quartz-chlorite-sericite basaltic breccia (H3378; 242 m). B. Strongly quartz-chlorite-sericite altered andesite flow margin altered to chlorite-pyrite within the matrix (H3395; 125 m). C. Intense quartz-sericite alteration in the siliceous core zone predominates and begins to replace quartz-chlorite-sericite altered basalt fragments above a chlorite-pyrite altered mudstone (H3398; 84 m).

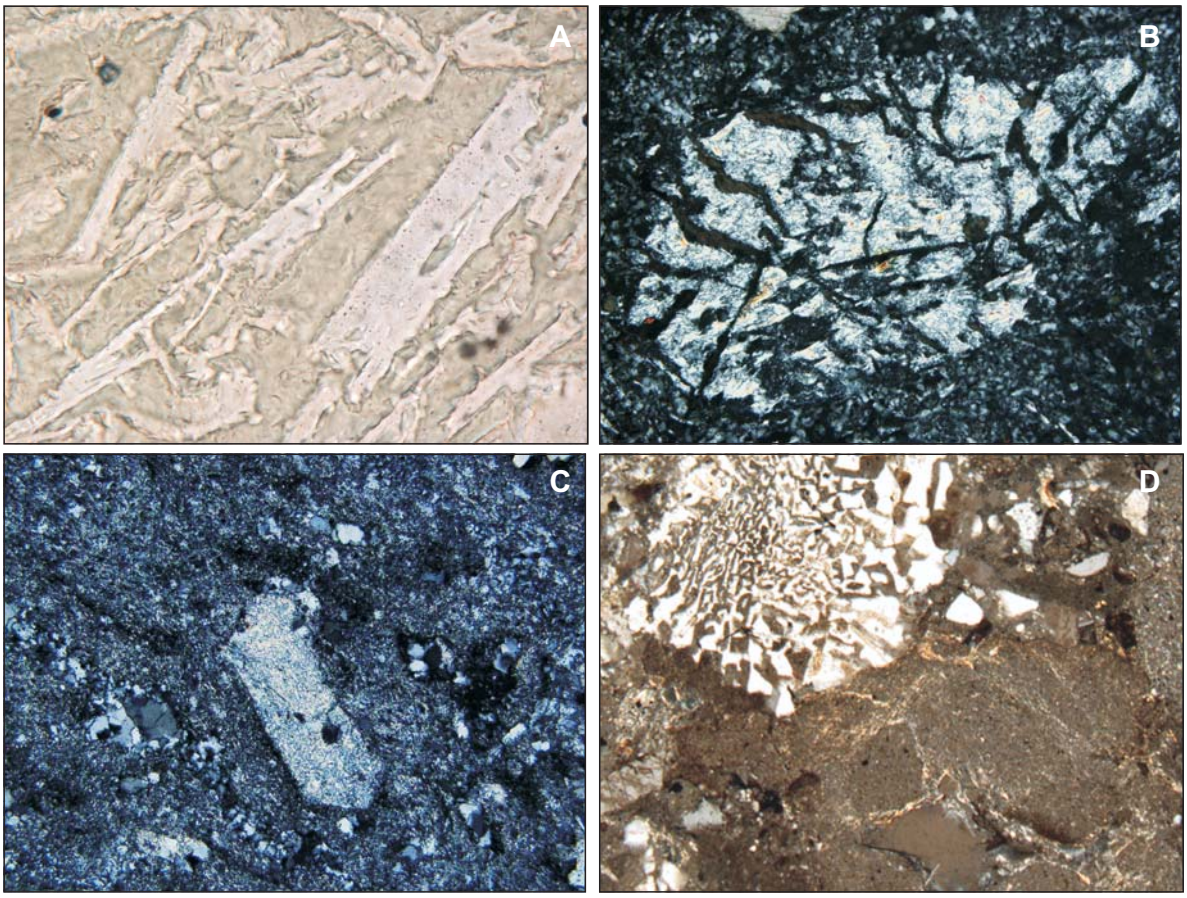

Figure 4.13: A. Skeletal texture of feldspar microlites in basaltic andesite surrounded by chloritized glass. The field of view is 0.175 mm. Taken under plane polarized light. B. Sericitized feldspar phenocrysts cut by chlorite veins emanating from a predominantly chlorite-quartz groundmass within the upper basaltic andesite. The field of view is 0.875 mm. Taken under crossed nicols. C. Sericitized feldspar phenocryst and quartz-sericite altered groundmass within the andesite. Field of view is 1.75 mm. Taken under crossed nicols. D. Weak sericite alteration within the upper sedimentary sequence. A granophyric clast is observed in the upper left. Field of view is 1.75 mm. Taken under crossed nicols.

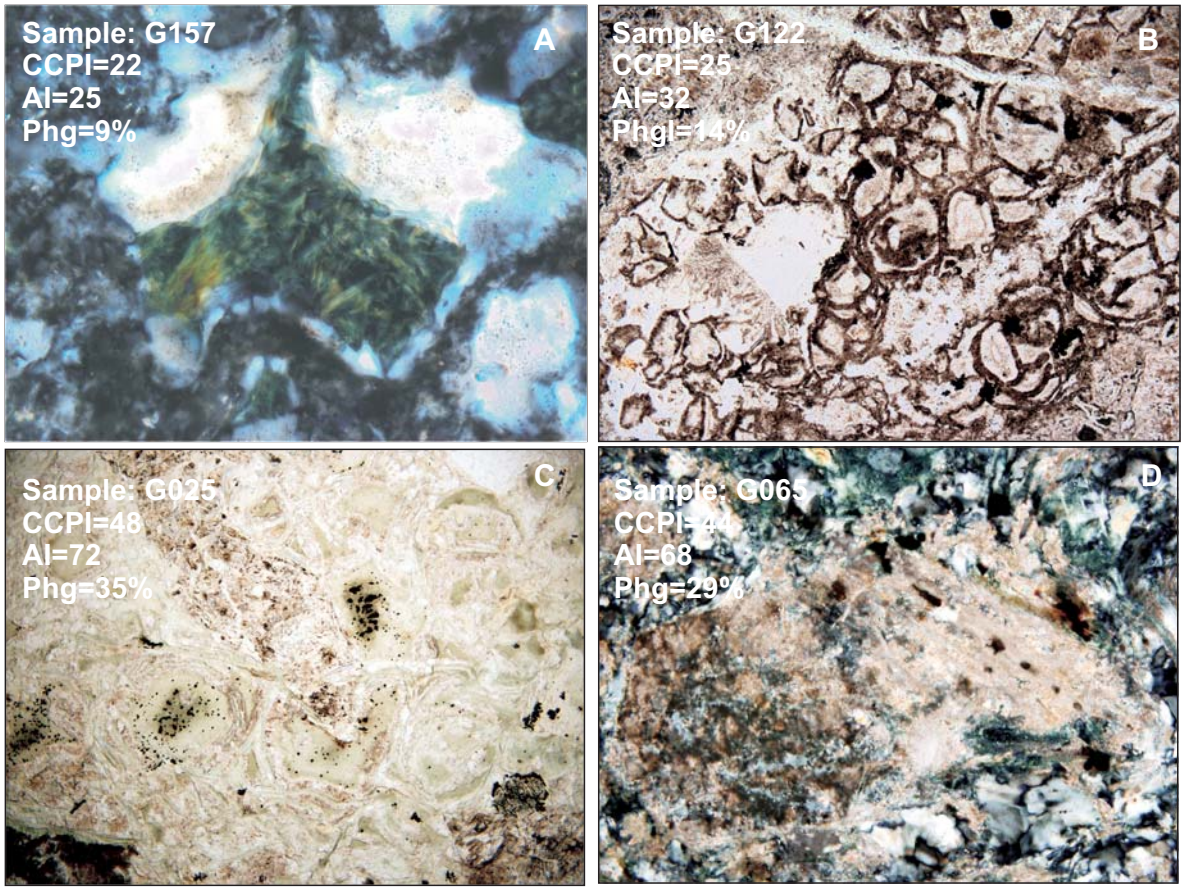

Figure 4.14: A. Minor phengite in least-altered rhyolite in the eastern part of the Lundberg Zone. Perlite is not observed in this least-altered zone. Field of view 0.175 mm, taken under plane polarized light (H3376; 16m). B. Clay-altered perlite rims characteristic of unaltered rhyolite. Chlorite locally alters perlite cores. Field of view is 0.35 mm, taken under plane polarized light (H3344; 110m). C. Strongly chloritized perlite cores with quartz-sericite +/- carbonate rims. Field of view is 0.175 mm, taken under plane polarized light (H3388; 15m). D. Nearly completely carbonitized feldspar phenocrysts. Chlorite abundance is slightly lower farthest west; however carbonate alteration increases significantly. Field of view is 0.875 mm, taken under crossed nicols (H3378; 39m).

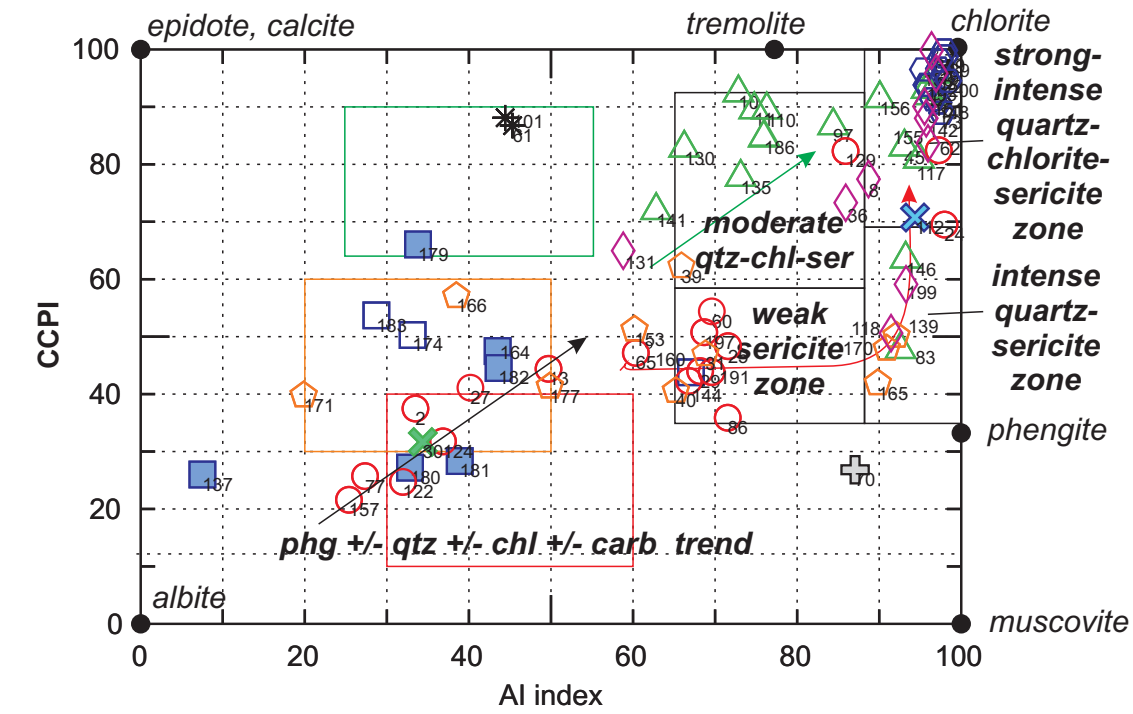

Legend

- diabase
- rhyolite
- rhyodacite with 1 cm quartz phenocrysts
- rhyodacite w/o 1 cm quartz phenocrysts
- upper sedimentary sequence
- rhyodacite
- rhyodacite autobreccia
- lower sedimentary sequence
- andesite
- clinopyroxene-phyric basaltic andesite
- basaltic andesite

Figure 4.15: Alteration box plot of the Lundberg and Engine House zones. The basaltic andesites are the most intensely chloritized; however, few samples show weaker alteration distal to stockwork mineralization. The rhyodacites are unaltered to strongly sericitized, and the rhyolite unit is weakly sericitzed or albitized. Al index = (K_2O + MgO) wt. % / (K_2O + MgO + Na_2O + CaO) wt. %; CCPI = (MgO + FeO) wt. % / (MgO + FeO + Na_2O + K_2O) wt. %. Numbers are sample numbers as displayed in Chapter 3.

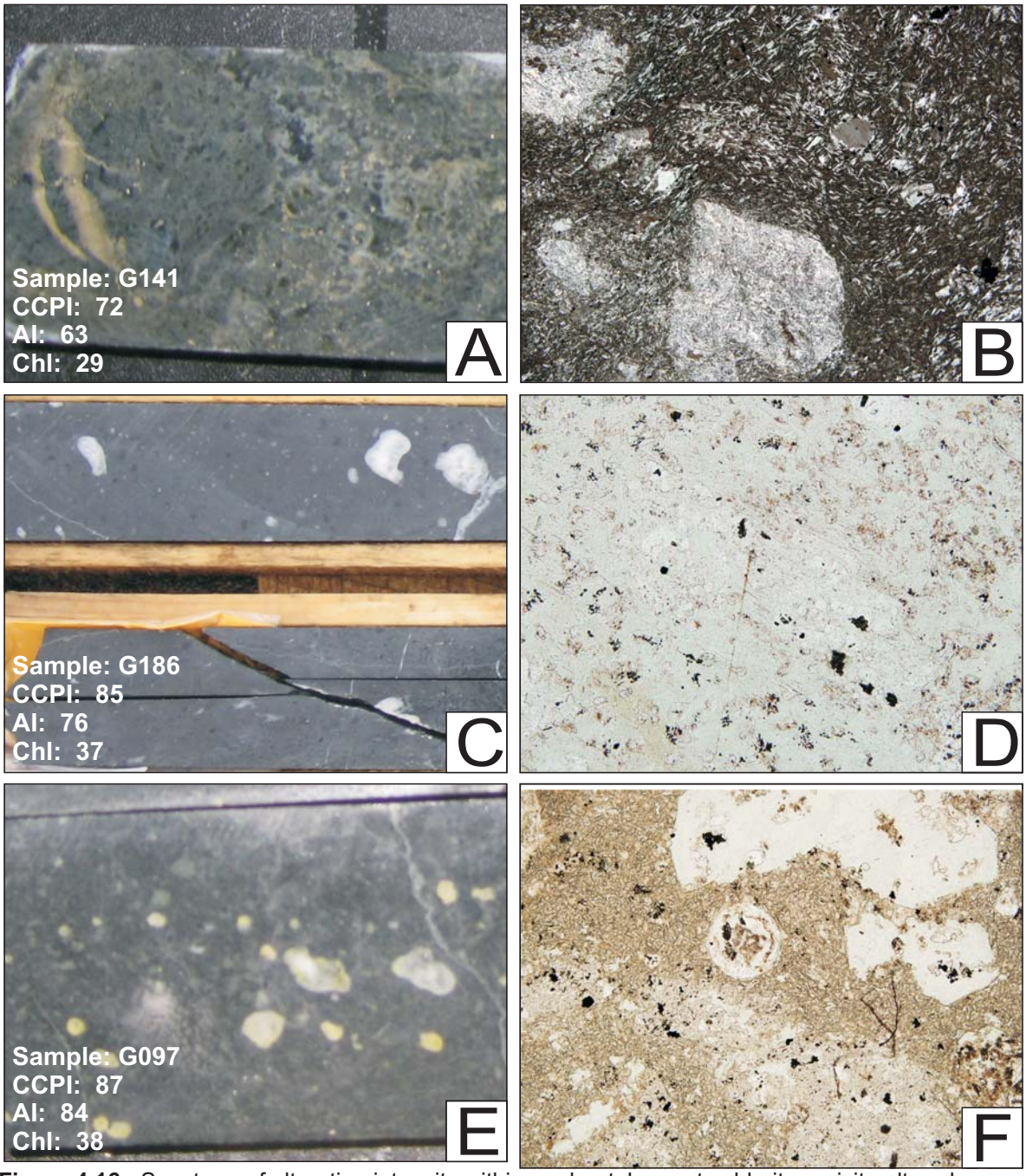

Figure 4.16: Spectrum of alteration intensity within moderately quartz-chlorite-sericite altered basaltic andesite. A. The least altered basalt is medium green-grey and contains 29 wt. % chlorite (H3408; 168.8m). Diameter of core is 4.7cm. B. Photomicrograph of G141 as shown in A. Well-preserved trachytic texture of feldspar microlites around sericitized feldspar phenocrysts in a strongly chloritized groundmass. Field of view is 1.75mm; taken under crossed nicols. C. Medium to dark grey basaltic andesite (H3397; 92m) .Diameter of core is 4.7cm. D. Photomicrograph of G186 as shown in C. Quartz-sericite altered feldspar phenocrysts partially replaced by chlorite. The groundmass comprises abundant chlorite, sericitized feldspar microlites, and clusters of epidote/fe-oxide. Field of fiew is 0.875mm; taken under plane polarized light. E. Medium-dark green-grey basaltic andesite (H3341; 286m). Diameter of core is 4.7cm. F. Photomicrograph of G097 as shown in E. Quartz-sericite alteration of feldspar phenocrysts is most common; although chlorite alteration is also observed. Feldspar microlites are replaced by chlorite. Quartz forms a major component of the groundmass. Field of view is 1.75mm; taken under crossed nicols.

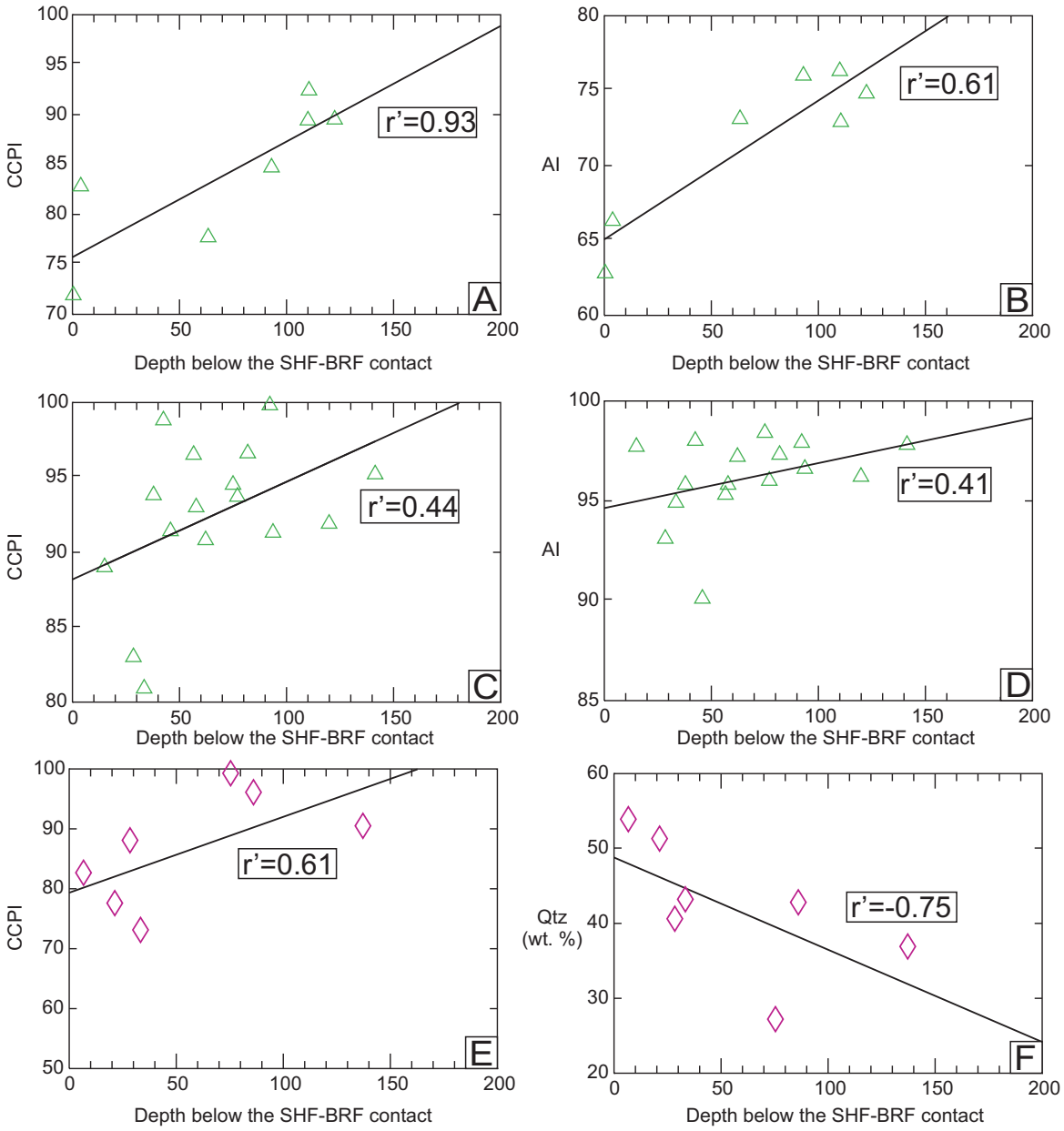

Figure 4.17: Alteration indices versus depth within the basaltic andesite and andesite units. A. CCPI values of the moderately altered basaltic andesite strongly increase below the Ski Hill Formation - Buchans River Formation contact. B. AI values of the moderate quartz-chlorite-sericite altered basaltic andesite, generally increase with depth. C. CCPI values of the strong to intense quartz-chlorite-sericite facies decreases towards the hanging-wall. In hand sample, basaltic andesite with lower CCPI are lighter coloured. D. AI values of the strong to intense quartz-chlorite-sericite facies have a moderate, positive correlation with depth. E. CCPI values of the andesite unit have a fairly strong positive correlation with depth. In hand sample, andesite with lower CCPI is more beige in colour, and lacks greenish-grey hues. F. Quartz concentration versus depth in the andesite unit. Intense silicification occurs towards the upper contact of the andesite and imparts a typical silicified appearance.

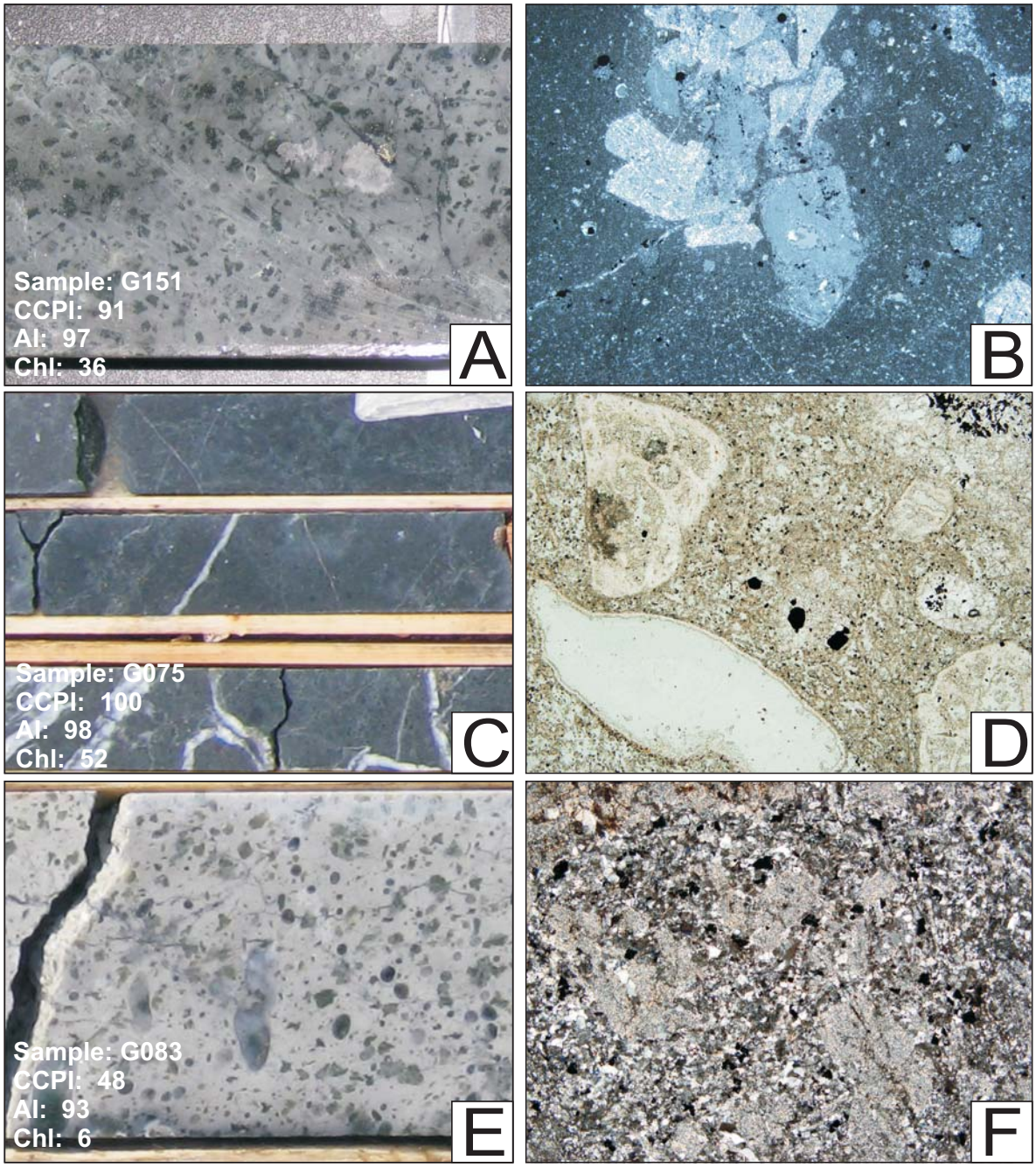

Figure 4.18: Photographs of intensely altered quartz-chlorite-sericite and quartz-sericite facies basaltic andesite. Macroscopic core diameter is 4.7cm in all photos; field of view in all photomicrographs is 1.75mm. A. Intensely altered quartz-chlorite-sericite facies basaltic andesite. Its lighter colour is consistent with abundant sericite, and smaller CCPI values than darker samples. B. Photomicrograph of G151 as shown in A. Feldspar phenocrysts are altered to sericite or chlorite. Taken under plane polarized light. C. Intensely altered quartz-chlorite-sericite basaltic andesite. Its darker colour is consistent with abundant chlorite, and large CCPI values. D. Photomicrograph of G075 as shown in C. The groundmass is entirely altered to quartz (dusty brown) and chlorite (green). Quartz fills multiple cores within feldspar phenocrysts characteristic of open space filling. Taken under plane polarized light. E. Photograph of the intense quartz-sericite alteration facies. F. Photomicrograph of G083 as shown in E. Near-complete replacement of feldspar phenocrysts and the groundmass by quartz and sericite. Taken under crossed nicols.

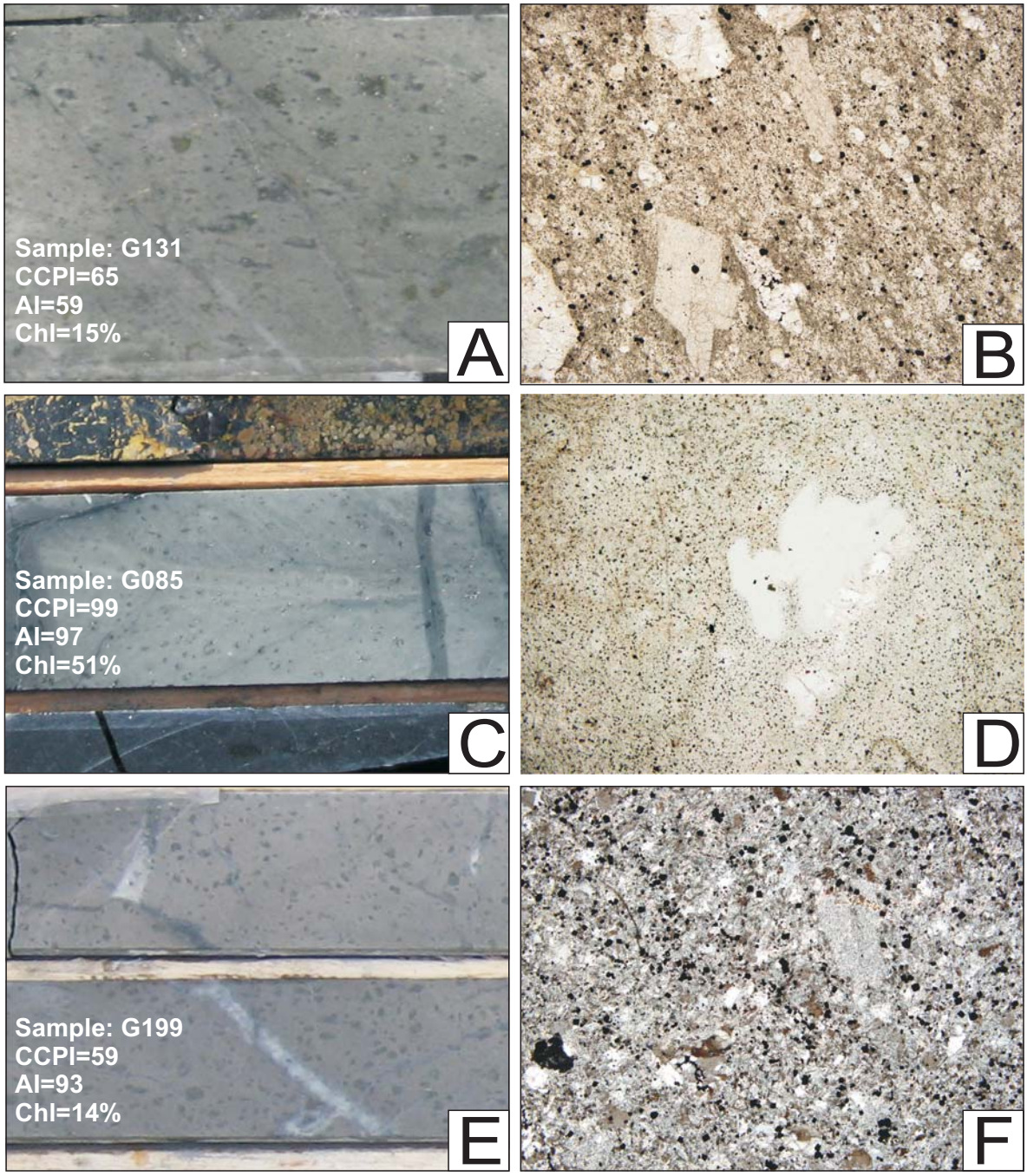

Figure 4.19: Mineralogical variation of the highly altered andesite unit. A. Photograph of least-altered andesite (H3344; 243m). Diameter of core is 4.7cm. B. Photomicrograph of G131 as shown in A. Sericite is the most commons alteration mineral replacing feldspar phenocrysts and microlites. Field of view is 1.75mm; taken under plane polarized light. C. Intense quartz-chlorite-sericite altered andesite (H3386; 150m). Diameter of the core is 4.76 cm. D. Photomicrograph of G085 (same as in A). Chlorite comprises ~50 wt. % of the rock and completely replaces relict feldspar phenocrysts and volcanic glass. Quartz and pyrite also replace relict feldspars and glass. Field of view is 0.875mm; taken under plane polarized light. E. Intense quartz-sericite altered andesite (H3406; 195m). Diameter of core is 4.7cm. F. Photomicrograph of G199 as shown in E. Quartz-sericite alteration completely replaces relict feldspar phenocrysts and volcanic glass. Chlorite occurs as replacement of volcanic glass and is dark grey-black. Pyrite is the predominant opaque mineral (<5%). Field of view is 1.75mm; taken under crossed nicols.

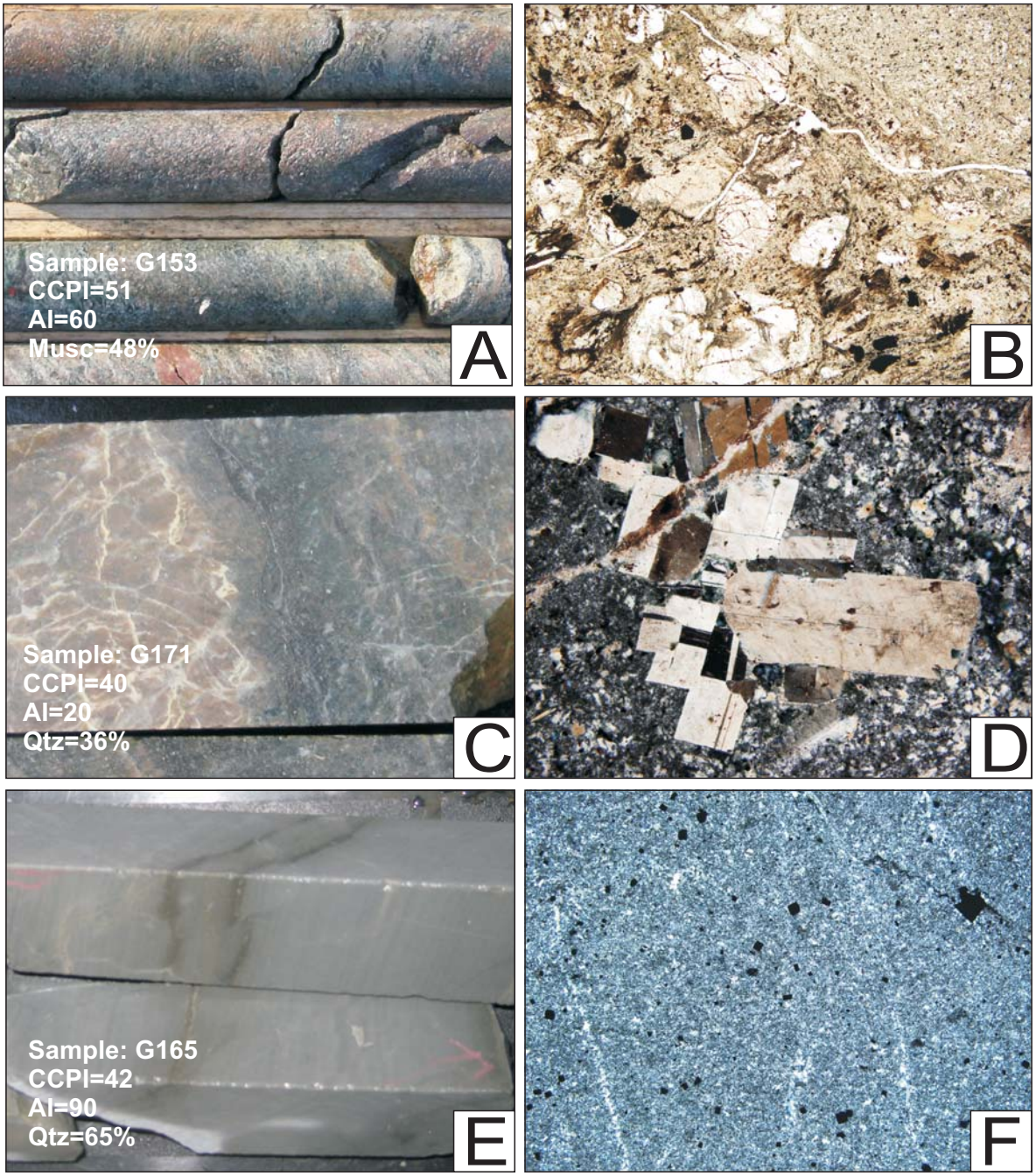

Figure 4.20: Mineralogical variation within the altered rhyodacite units of the Lundberg and Engine House zones. A. The rhyodacite tuff of the upper sedimentary sequence is uniformly altered to sericite-carbonate (H3369A; 40m) B. Photomicrograph of sample G153 as shown in A. The rhyodacite tuff is characterized by abundant quartz crystals in a highly sericitized matrix. Field of view is 1.75mm; taken under plane polarized light. C. Unaltered rhyodacite from the interstratified rhyodacite and tuffaceous sediments unit of the Engine House Zone. This sample lies stratigraphically below the intensely mineralized and altered rhyodacite autobreccia proximal to the Engine House stockwork (H3371; 86m) D. Photomicrograph of sample G171 as shown in C. Plagioclase glomerocrysts are pristine and display albite twinning. Field of view is 0.875mm; taken under crossed nicols. E. Intensely sericitized and silicified rhyodacite proximal to the Engine House stockwork (H3368; 106m) F. Photomicrograph of G165 as shown in E. Intense silicification and sericitization destroy all primary texture. Field of view is 1.75mm; taken under crossed nicols.

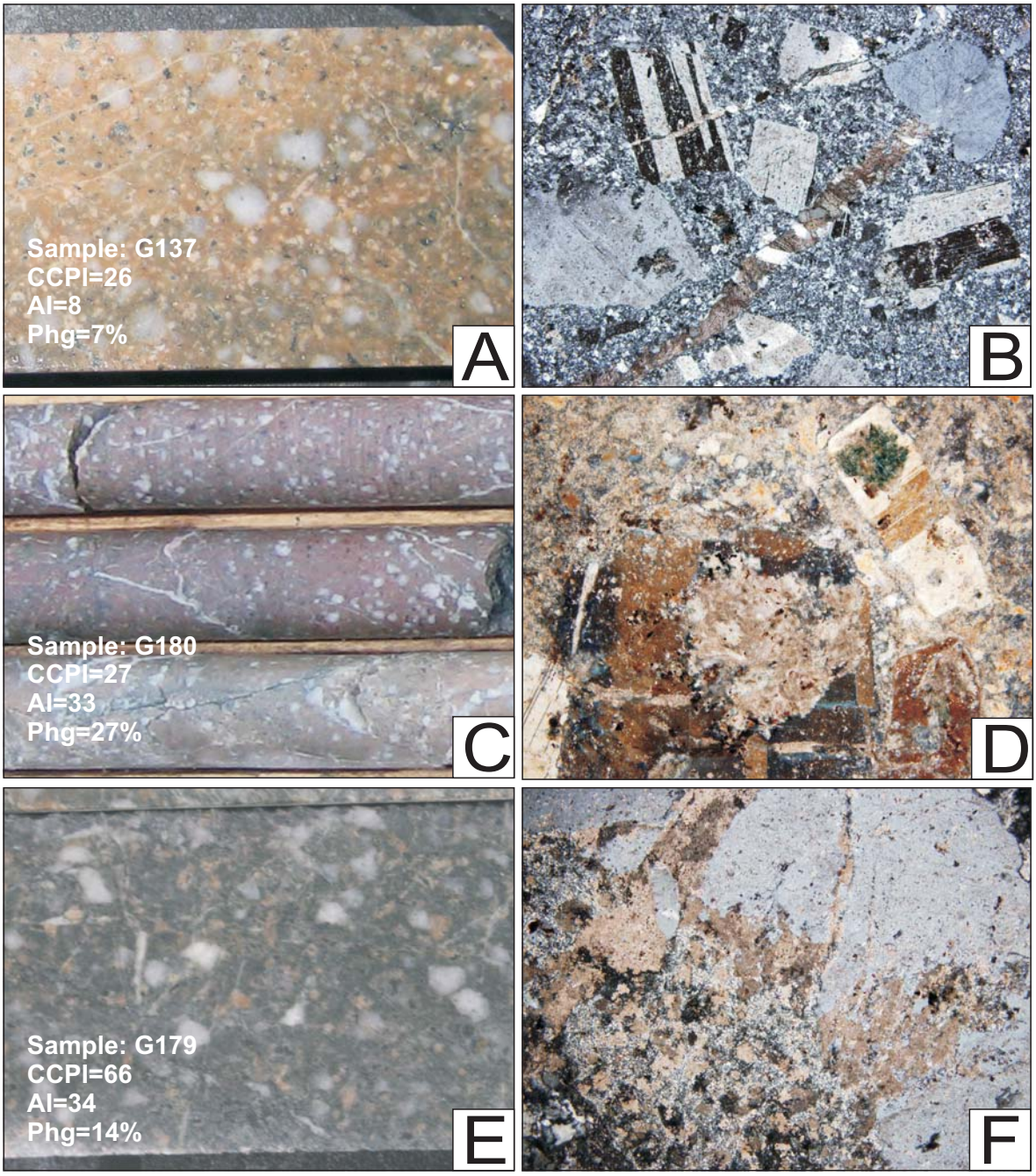

Figure 4.21: Heterogeneous alteration of the quartz-phyric rhyodacite. A. Albitized quartz-phyric rhyodacite. Diameter of core is 4.7cm (H3408; 25m) B. Photomicrograph of G137 as shown in A. Weakly sericitized plagioclase crystals display albite twinning in a quartz-albite matrix. Field of view is 1.75mm; taken under crossed nicols. C. Phengite-carbonate-chlorite altered quartz-phyric rhyodacite. Diameter of core is 4.7cm (H3404; 82m). D. Photomicrograph of G180 as shown in C. Strong carbonate and chlorite alteration of plagioclase crystals in a phengite-carbonate-chlorite altered matrix. Field of view is 0.875mm; taken under crossed nicols. E. Phengite-carbonate-chlorite altered quartz-phyric rhyodacite. (H3404; 13m). F. Photomicrograph of G179 as shown in E. Phengite-carbonate-chlorite alteration of a plagioclase crystal. This sample has similar alteration to that of G180; however, alteration is more intense here, and more fine-grained chlorite is observed. Field of view is 0.875mm; taken under crossed nicols.

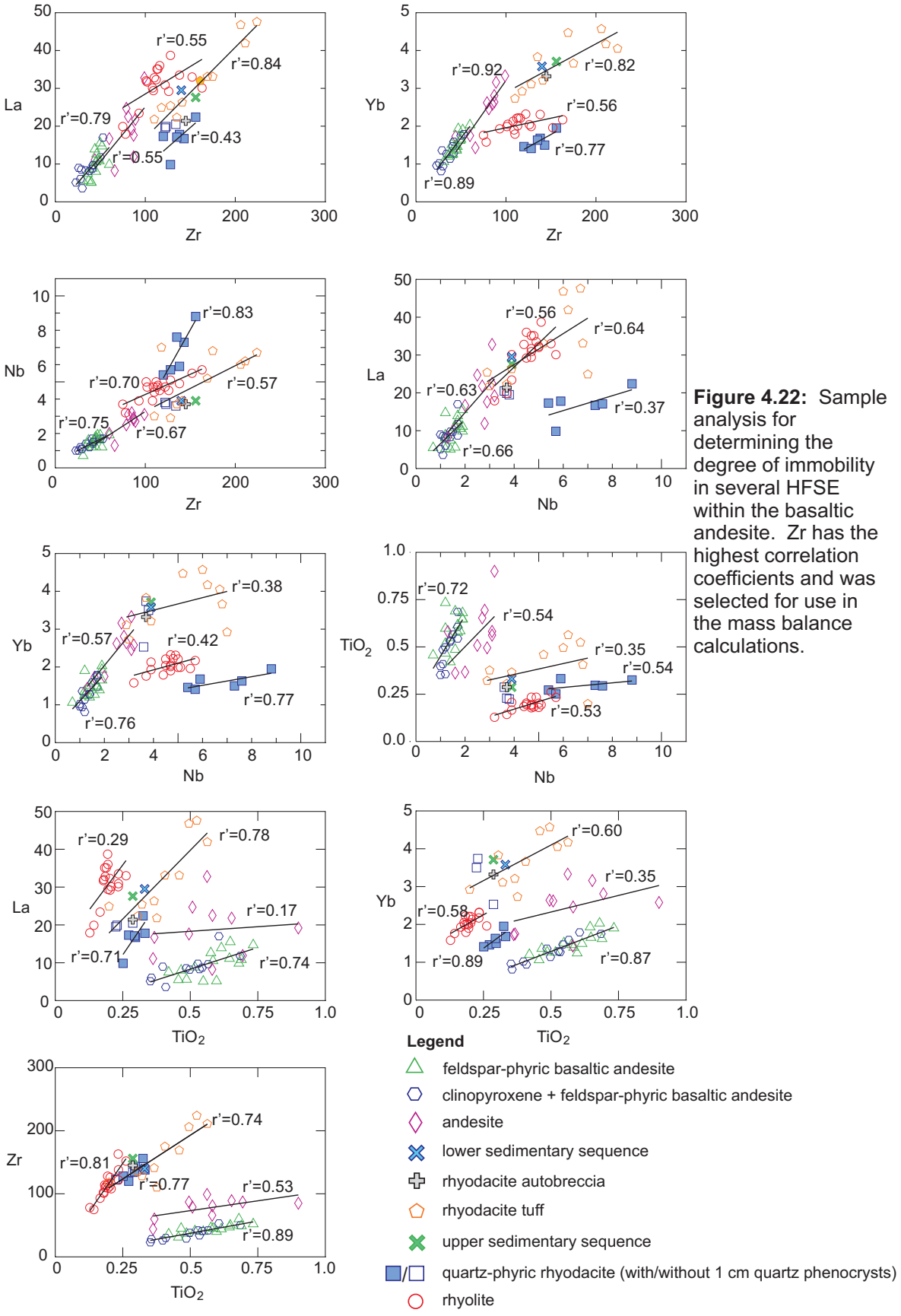

Figure 4.22: Sample analysis for determining the degree of immobility in several HFSE within the basaltic andesite. Zr has the highest correlation coefficients and was selected for use in the mass balance calculations.

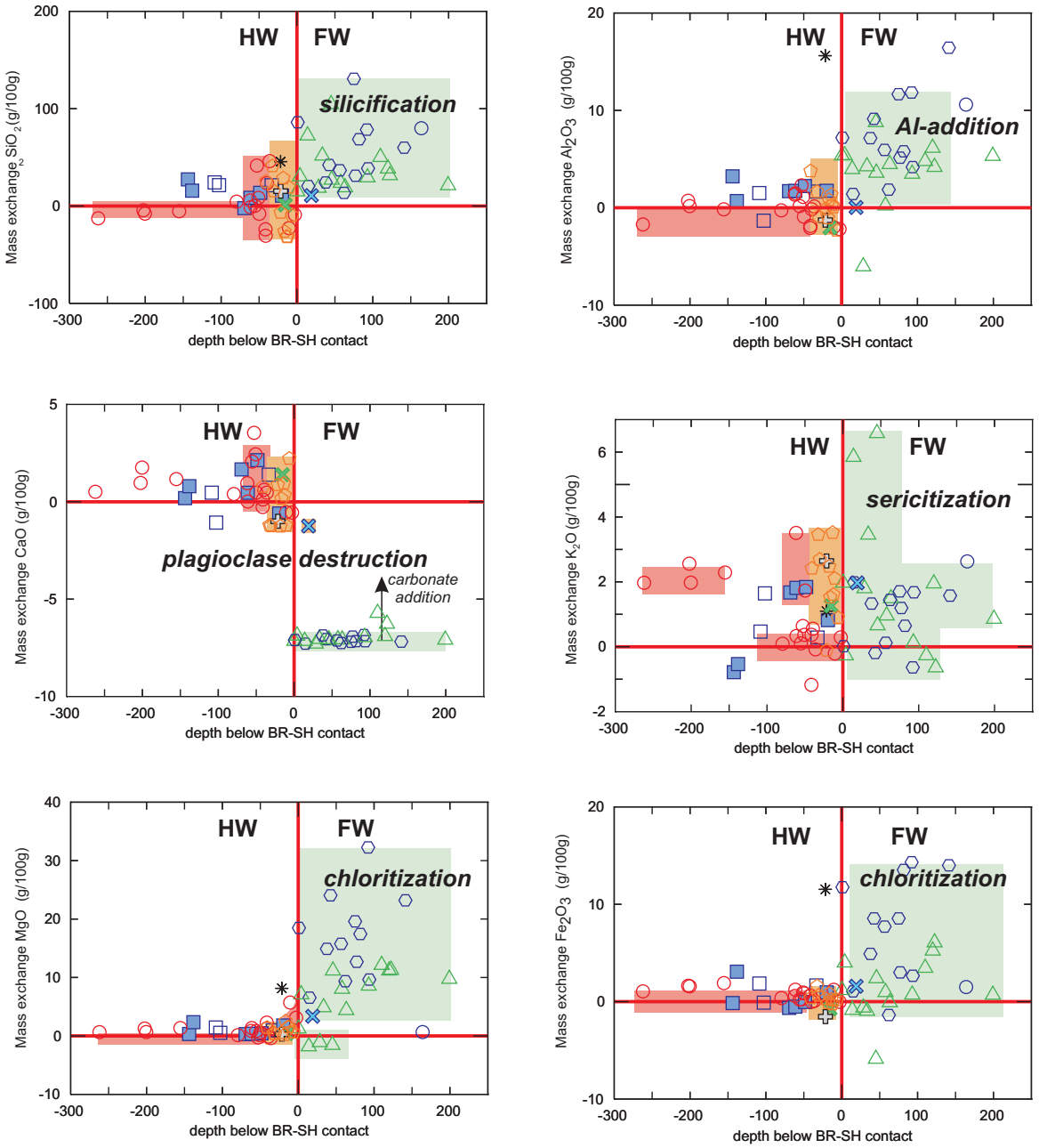

Figure 4.23A-F: Mass balance results of major elements in the Lundberg and Engine House zones. Basaltic andesite shows the largest mass change with a net mass gain. All major elements display mass gain except for CaO and to a lesser extent Na_2O (not shown) which are completely stripped in the proximal alteration pipe. The rhyodacite and rhyolite units display variable mass change which is much less than in the basaltic andesite. Addition of K_2O occurs in all rhyodacite, whereas the rhyolite displays K_2O enrichment higher in the stratigraphy. All other elements show variable additions or depletions, except for Fe_2O_3 and MgO which display little change.

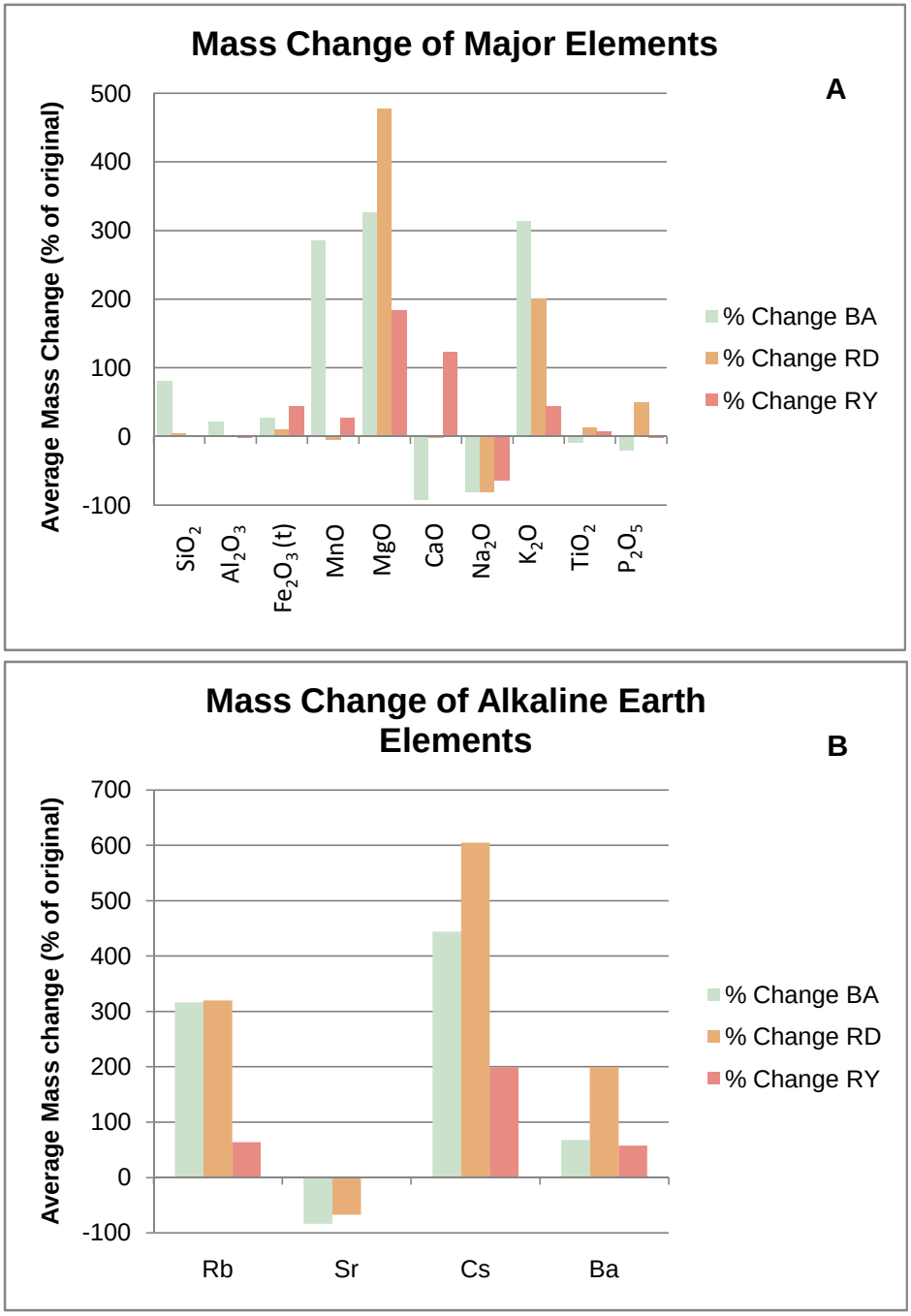

Figure 4.24: Mass balance of major and trace elements of the basaltic andesite (BA), rhyodacite (RD), and rhyolite (RY) units. A. The basaltic andesite has mass gain (SiO_2, MgO, K_2O) and loss (CaO and Na_2O) consistent with silicification, chloritization, and sericitization. The rhyodacite has large gain of MgO and K_2O, and loss of Na_2O, characteristic of sericitization and chloritization. The rhyolite has smaller mass gains of MgO and K_2O, and a unique gain of CaO, consistent with the observed carbonate alteration. B. Rb, Cs, and Ba, are gained in all rock types, reflecting the partioning of these trace elements into sericite. Sr was nearly completely lost within the basaltic andesite and rhyodacite units, reflecting the destruction of primary feldspar.

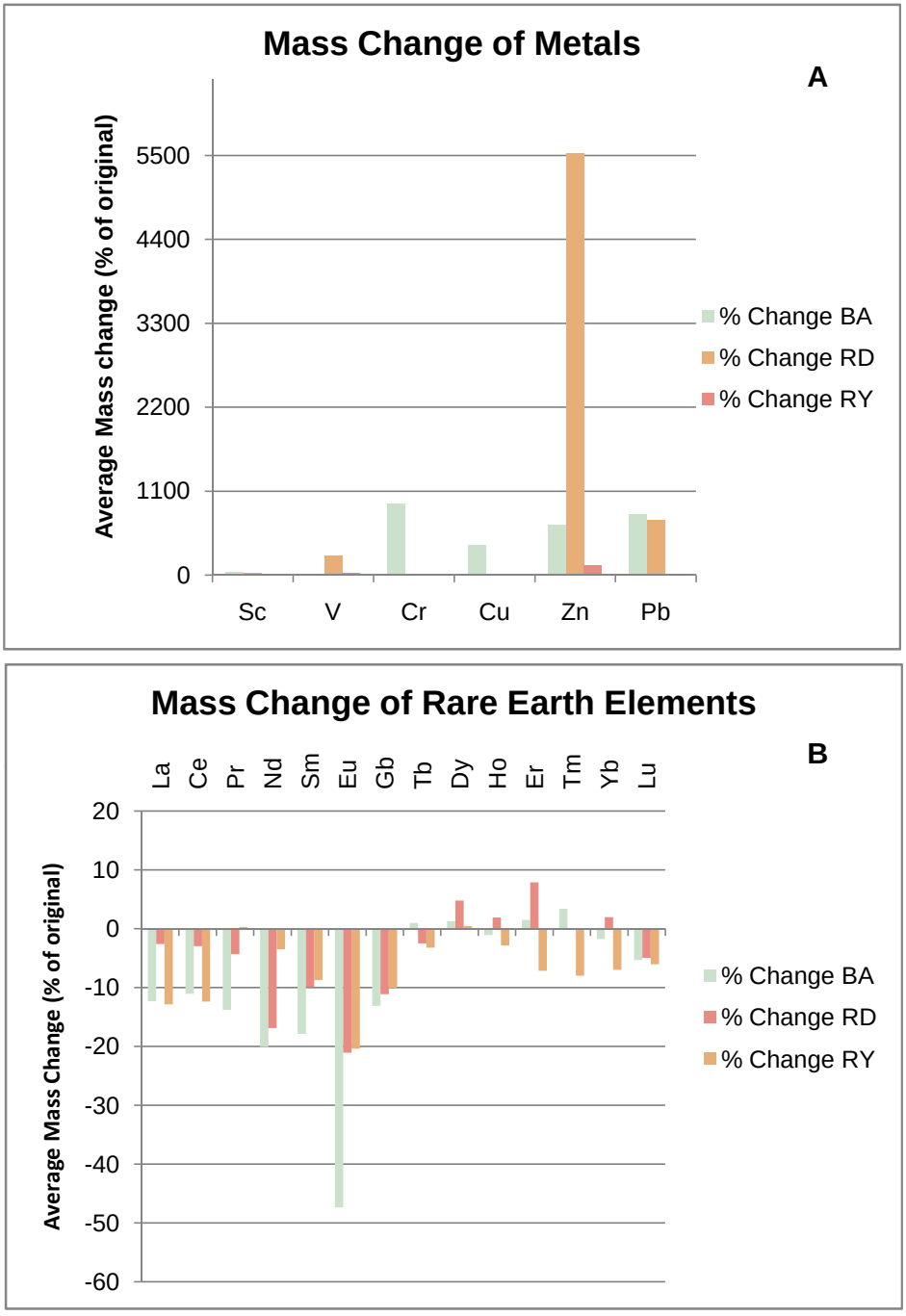

Figure 4.25: Mass balance of trace elements within the basaltic andesite (BA), rhyodacite (RD), and rhyolite (RY) units. A. The footwall basaltic andesite and ore-horizon rhyodacite units have large gains of metal; however, copper is restricted to the footwall basaltic andesite. The hanging-wall rhyolite unit also has mass gain of metallic elements (e.g., 200% Zn); however, small compared to the other two units. B. Rare earth elements within the Lundberg and Engine House zones are generally immobile. LREE display a ~10% loss in all units, whereas, HREE are immobile.

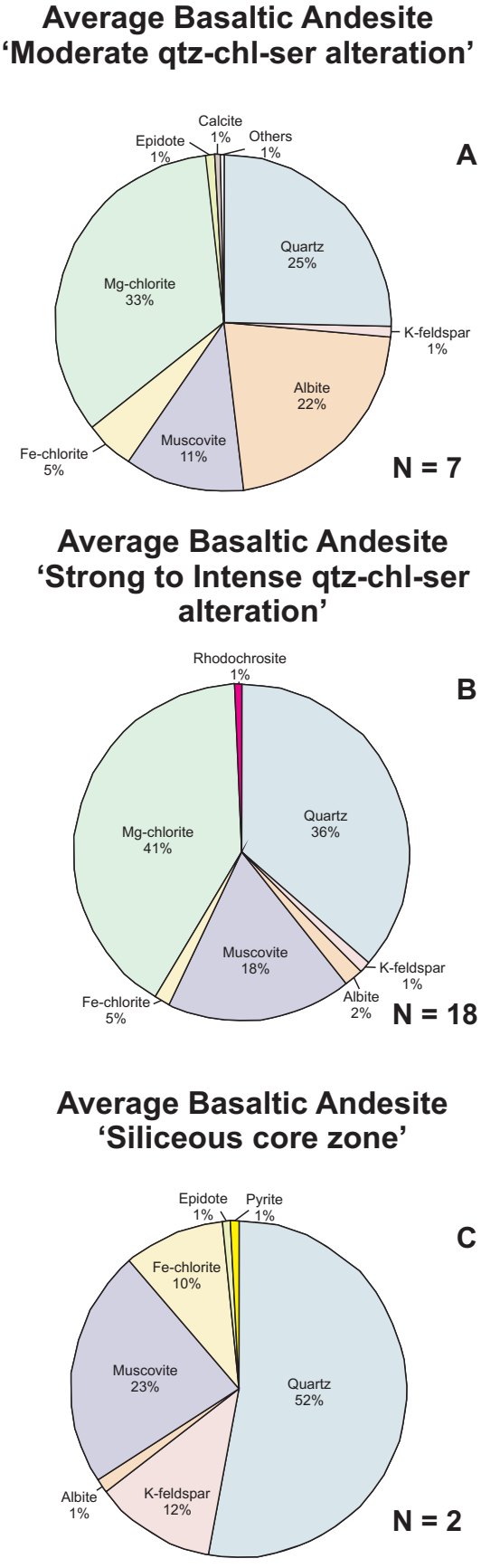

Figure 4.26: Normative mineralogy of the various alteration zones of the upper basaltic andesite unit. A. The moderately altered basaltic andesite consists mostly of quartz, Mg-chlorite, albite, and muscovite. Albite forms as phenocrysts and microlites in the groundmass. Chlorite forms as replacement of volcanic glass and muscovite forms as alteration of albite phenocrysts and/or microlites. This zone comprises the most distal alteration and forms on either side of the strong to intense quartz-chlorite-sericite altered zone. B. Over 95% of the strong to intense quartz-chlorite-sericite zone consists of quartz, chlorite, and sericite. Alteration intensity increases towards the core of the zone, where stockwork mineralization is most intense. By contrast, alteration intensity decreases towards the top of the basaltic andesite. C. The intense quartz-sericite or 'siliceous core zone', has very different mineralogy compared to the other footwall alteration zones. Over 75% of basaltic andesite in this zone is made up of quartz and muscovite.

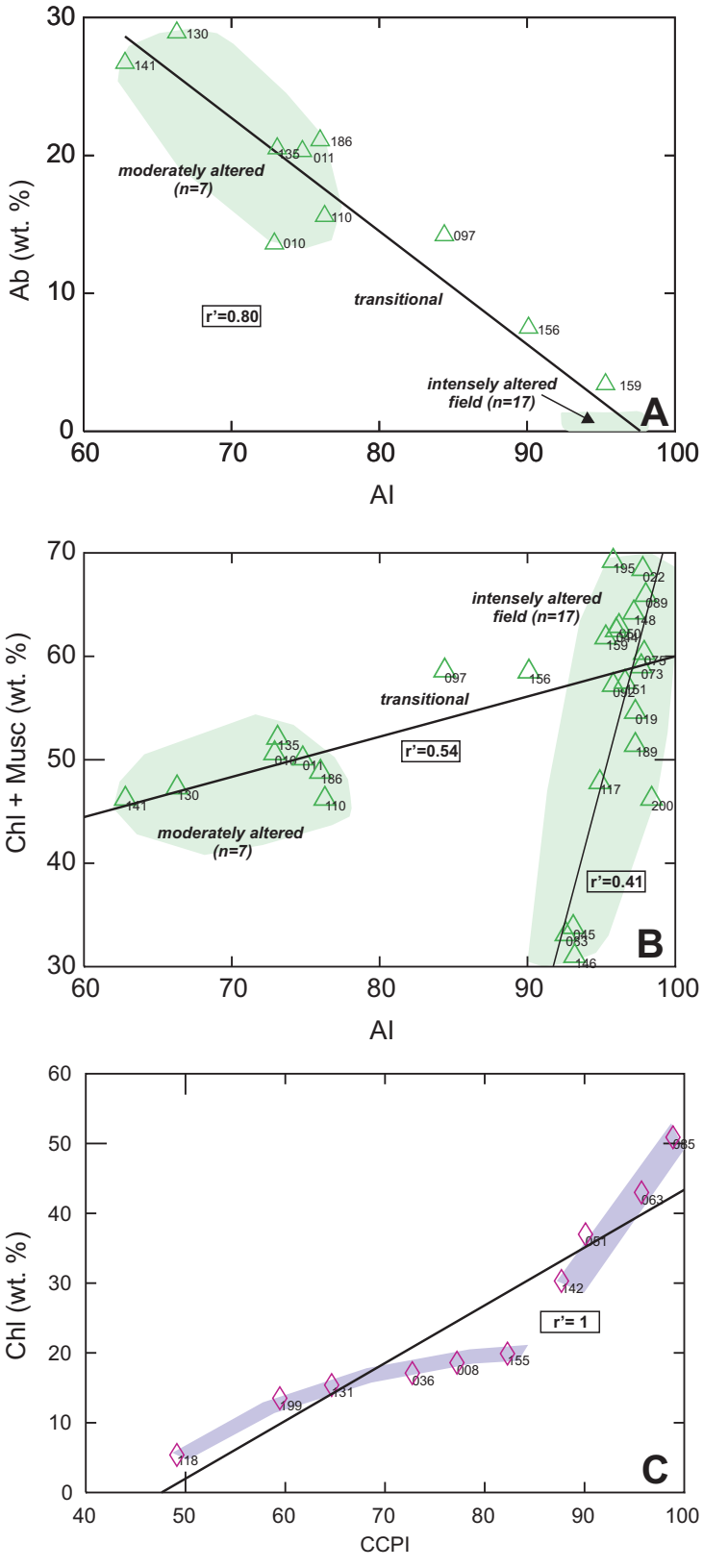

Figure 4.27: Mineralogical variations versus alteration intensity. A. The Ishikawa alteration index is negatively correlated with the abundance of albite indicating that the destruction of albite is more intense in highly altered zones. The moderate quartz-chlorite-sericite facies (AI<90) are the least-altered in the Lundberg Zone; however, these samples contain up to 46 wt. % chlorite. B. The Ishikawa alteration index is moderately correlated with the abundance of chlorite + muscovite, indicating that the replacement of albite by chlorite and muscovite was a dominant reaction. Two correlation coefficients are shown; one for samples with AI<90, the other for AI>90. C. Chlorite abundance versus CCPI in the andesite unit; a perfect correlation exists, indicating that CCPI is controlled by the abundance of chlorite. No samples contain between 20 and 30 wt. % chlorite. Samples with less than 20 wt. % chlorite show a logarithmic increase of chlorite abundance with increasing CCPI, whereas samples with more than 30 wt. % chlorite define a linear curve with a significantly larger, positive slope.

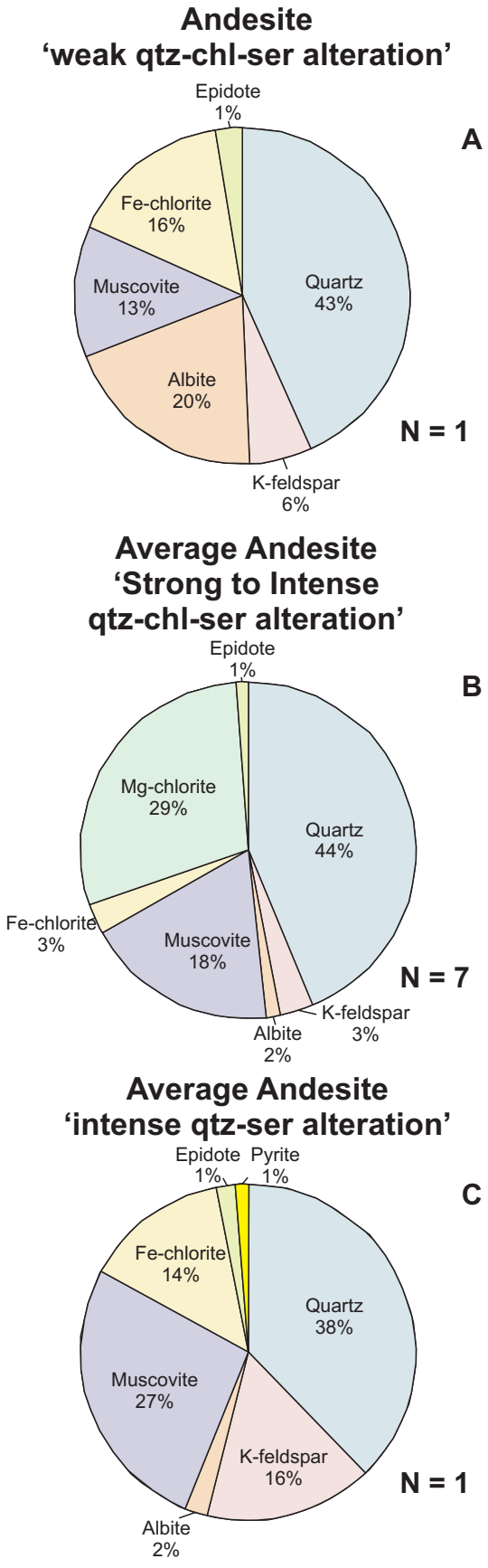

Figure 4.28: Normative mineralogy of the various alteration facies of the andesite unit. In hand sample, the andesite unit is largely indistinguishable from the basaltic andesite; however, the mineralogy of the various andesite facies is much different than that of the basaltic andesite making them easy to separate by the norm calculation. A. Only one weakly altered andesite sample was located in the suite of rocks analysed. It contains 18 wt.% more quartz than least-altered basaltic andesite, clearly distinguishing them as separate units. Fe-chlorite apparently comprises a major component of the rock (16%); however, a subequal proportion of Mg and Fe-chlorite is more likely since pyrite was unrecorded by the calculation (pyrite comprised 5% of the petrographic abundance). B. Strong to intense quartz-chlorite-sericite alteration of the andesite unit. Although the average quartz concentration is not much higher than that of weakly altered andesite, it reaches up to 54 wt. % locally, indicating large amounts of quartz addition. Chlorite abundance is also highly variable, ranging from 17-50 wt. %, and is directly correlated to the CCPI index which ranges from 73 to 96 within this facies. C. Intense quartz-sericite alteration of the andesite unit. Muscovite comprises 27 wt. % of this sample which occurs near the top of the footwall. This sample is located above the most intense mineralization of the Lundberg Zone.

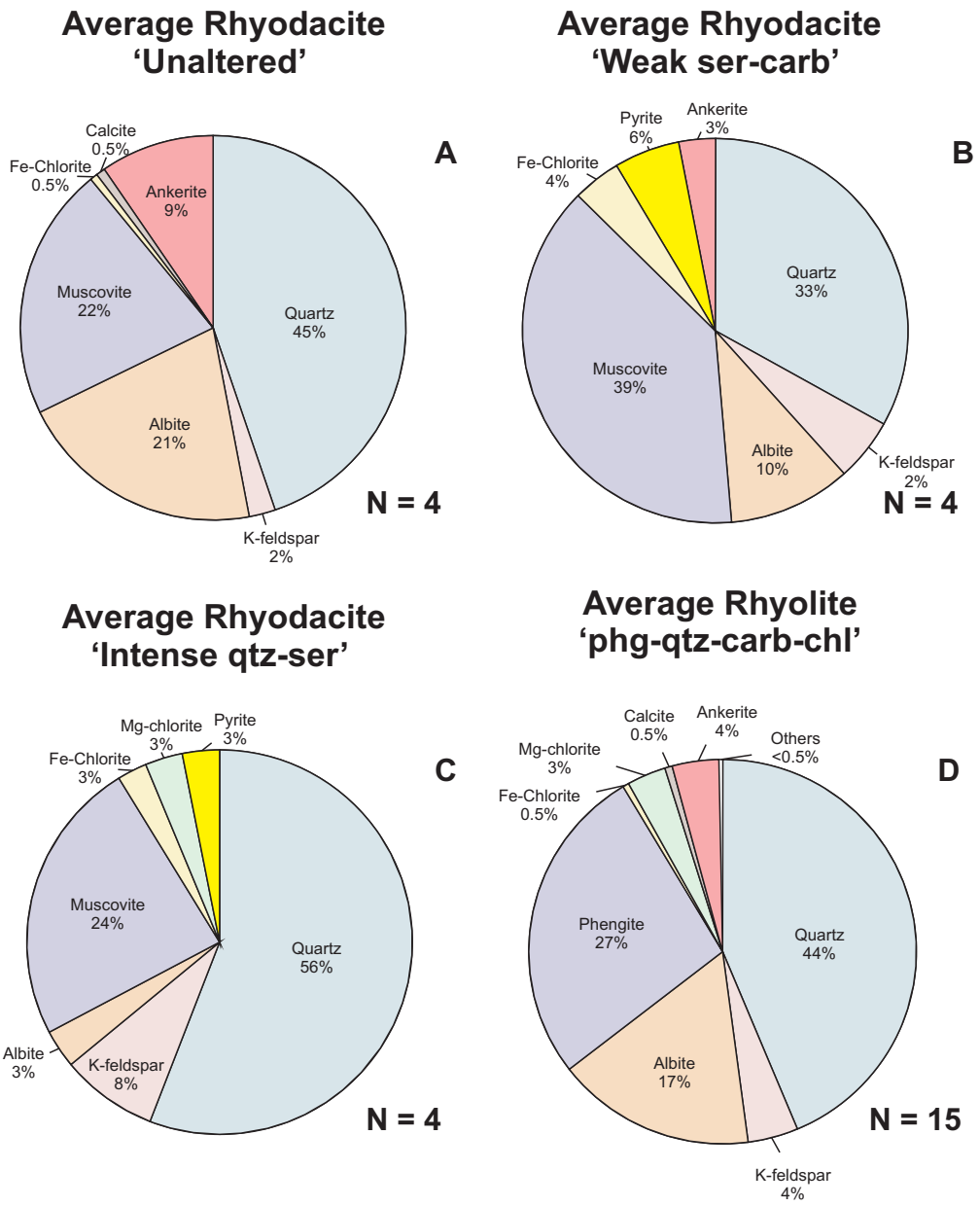

Figure 4.29: Normative mineralogy of rhyodacite units from the Lundberg and Engine House zones. A. Unaltered rhyodacite from the Engine House Zone and one sample from the upper sedimentary sequence of the Lundberg Zone. These samples are composed mostly of quartz, muscovite, and albite. All samples contain significant carbonate; a unique feature of the hanging wall lithologies. B. Rhyodacite tuff from the Lundberg Zone. The tuff contains more muscovite, but less quartz and albite than unaltered rhyodacite of the Engine House Zone. Pyrite is apparently anomalous; however, petrographic abundances were much lower, and the excess iron present in this sample is likely attributes to either ankerite, or minor talc veins which were not accounted for in the norm. C. Intense quartz-sericite alteration of aphyric/autobrecciated rhyodacite of the Engine House Zone. Quartz and muscovite comprise >80% of the mineralogy within this zone which is cut by polymetallic stockwork. D. Weakly altered rhyolite unit of the Lundberg Zone. The rhyolite has a similar mineralogy to that of unaltered rhyodacite; however, the composition of the sericite within the rhyolite is phengitic, rather than normal K-muscovite. Alteration intensity within the rhyolite unit increases towards zones of intense mineralization in the underlying footwall. This suggests that this structurally-emplaced assemblage may not be far travelled.

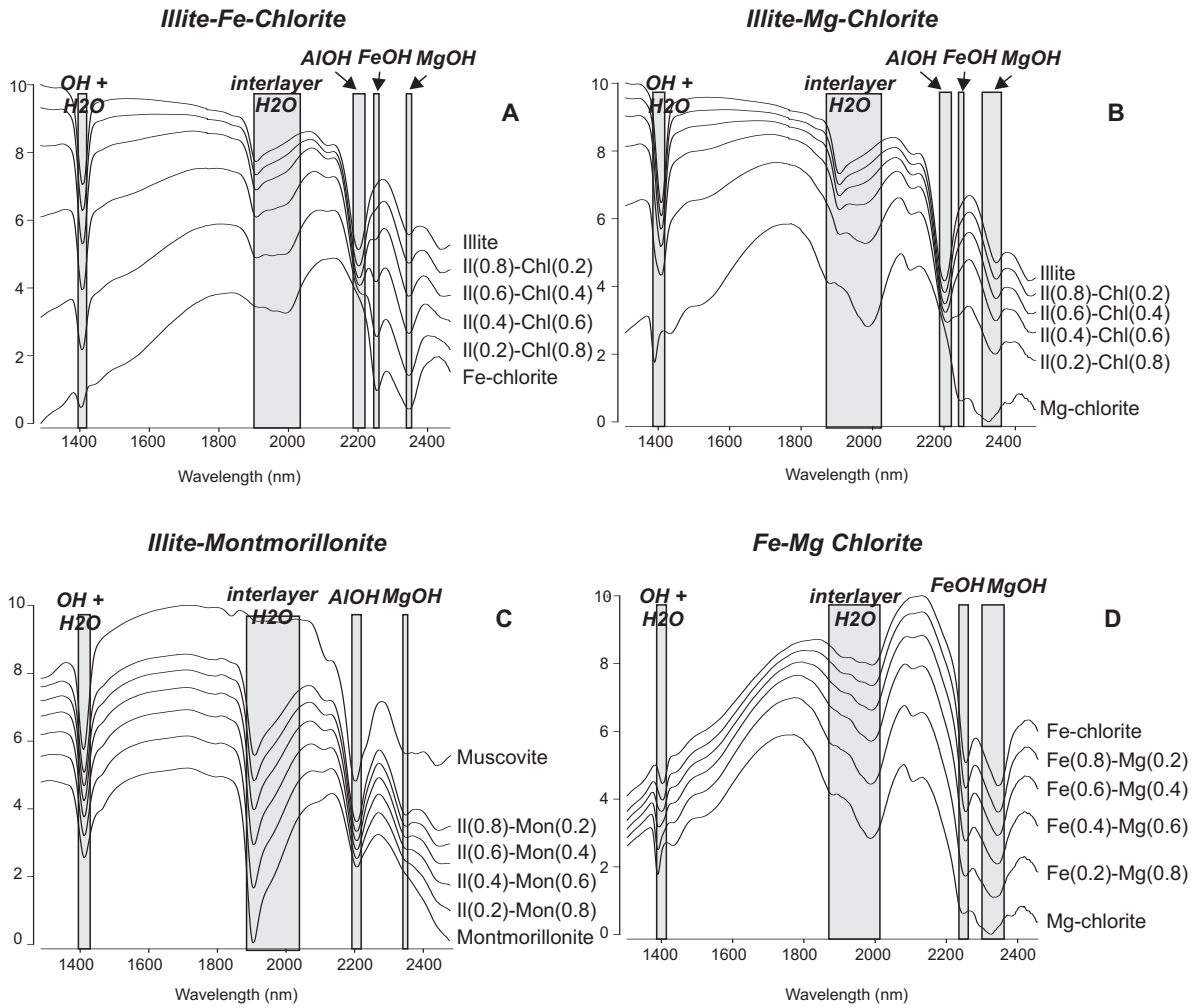

Figure 4.30: Examples of calculated absorption spectra (SWIR) for variable mixtures of alteration minerals. A. Illite and Fe-chlorite. Note the disappearance of the AlOH absorption feature, the addition of an FeOH feature, the changing slope and shape of the interlayer water feature. B. Illite and Mg-chlorite are observed. The FeOH feature is much less prominent, the slope begins to decrease at shorter wavelengths, and the ~1400 nm water feature is more pronounced. C. Illite and montmorillonite. A secondary AlOH/MgOH absorption feature occurs at ~2340 nm. Note that muscovite does not contain an interlayer water feature which clearly differentiates illite from muscovite. D. Fe-chlorite and Mg-chlorite. Fe-chlorite has an overall steeper slope to longer wavelengths than Mg-chlorite with absorption features at longer wavelengths.

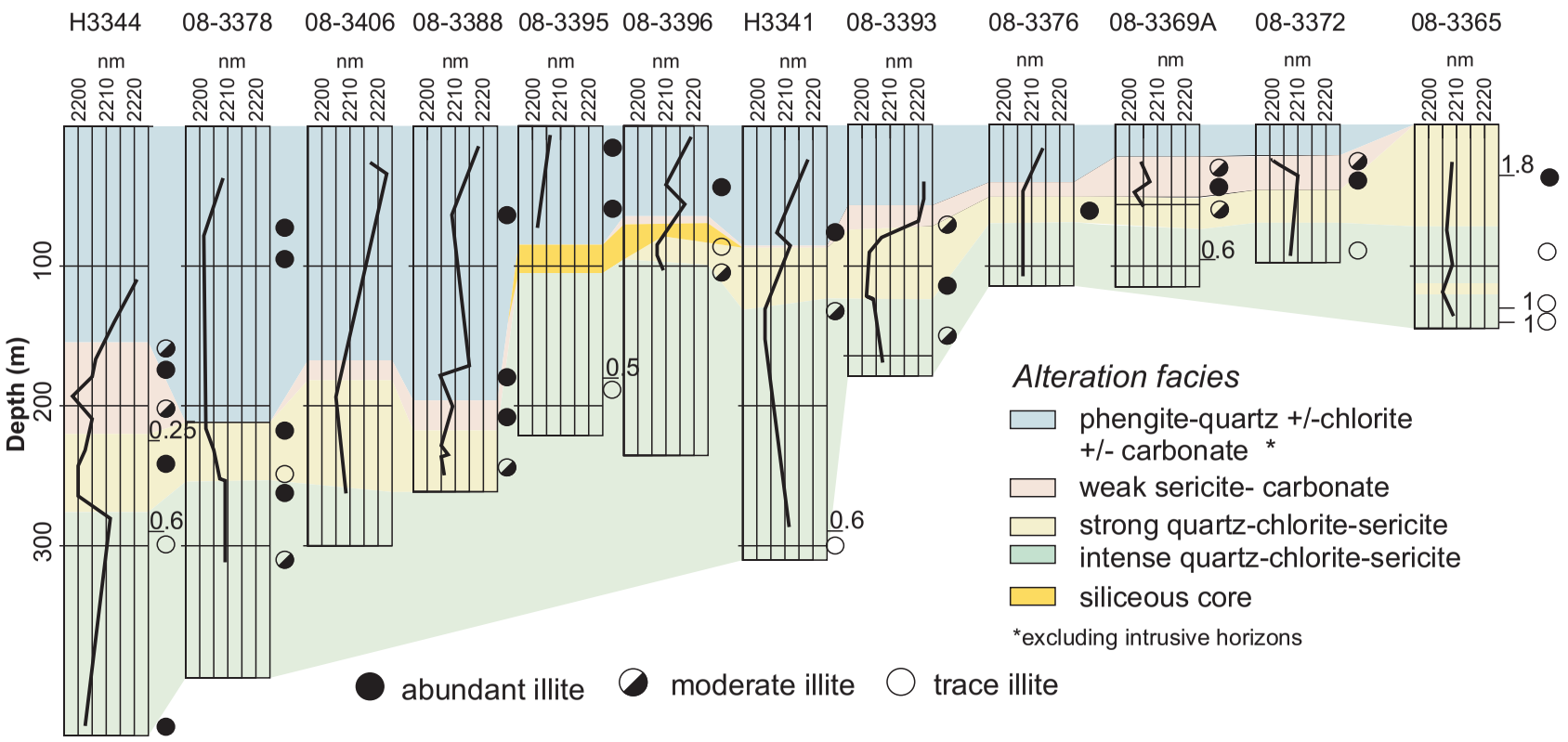

Figure 4.31: Summary of short wave infrared data in the Lundberg Zone along cross section A to A'. Depth plots show the variation of the AlOH absorption feature within different alteration assemblages. Compositions of sericite are estimated by their AlOH wavelength; values >2116 are phengitic; whereas values <2116 are illitic. Illitic composition predominate in the footwall and within the weak sericite +/- carbonate hanging wall; whereas, phengitic compositions predominate in the structurally emplaced hanging-wall. Relative abundances of illite are estimated by the intensity of characteristic absorption features. Values cited are ratios of illite over chlorite calculated as the depth ratio of their respective absorption features.

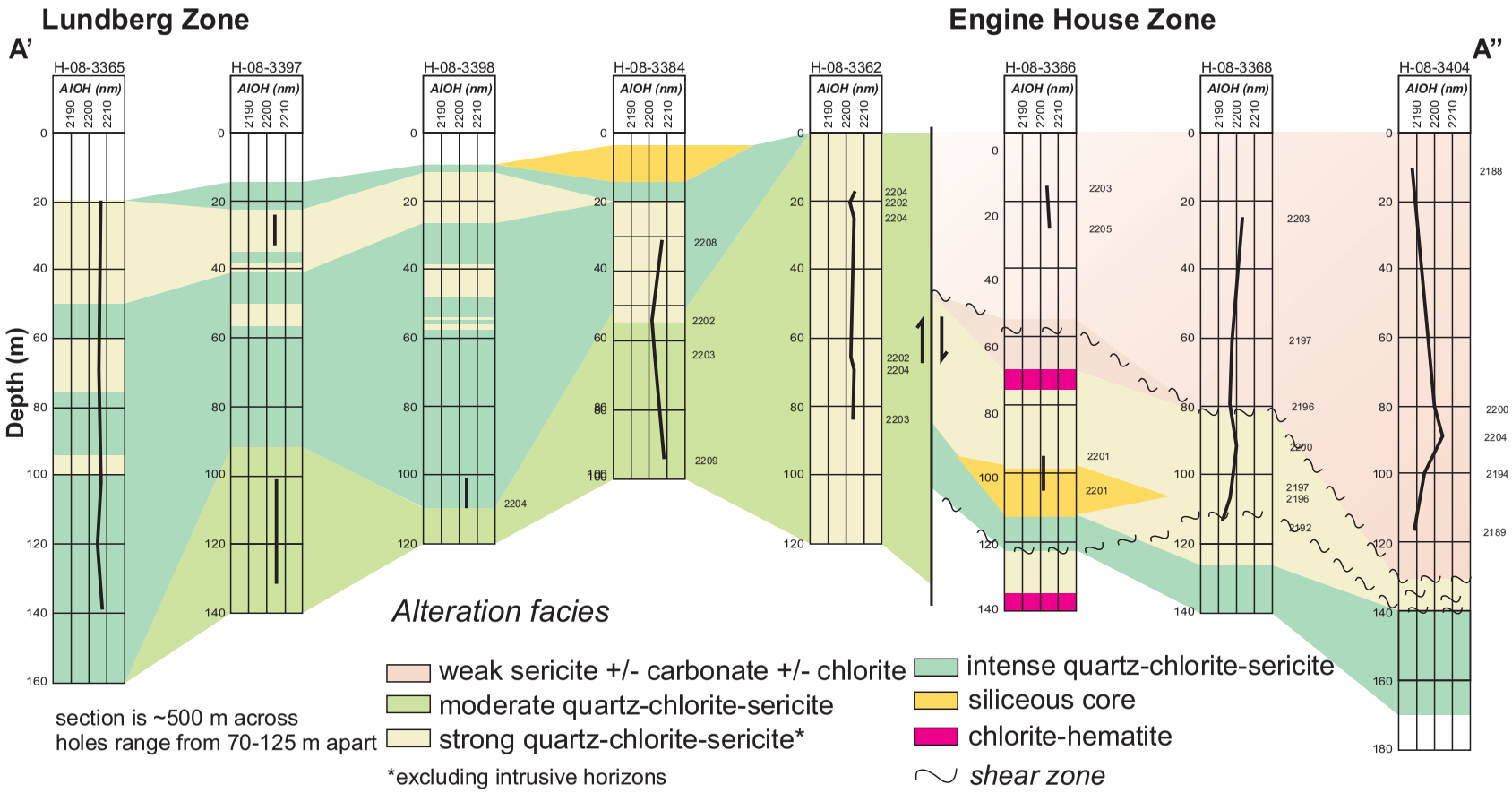

Figure 4.32: Cross section A' to A" showing variation in the AlOH absorption feature in different alteration facies of the Lundberg and Engine House zones. The length of the AlOH absorption feature gives a rough composition of sericite. The sericite within the moderate and strong to intense quartz-chlroite-sericite alteration facies are similar to normal muscovite; whereas, compositions in the thrust-emplaced sericite-carbonate +/- chlorite assemblage are normal to sodic. This composition contrasts markedly with the phengitic composition observed in the thrust-emplaced rhyolite unit in the Lundberg Zone.

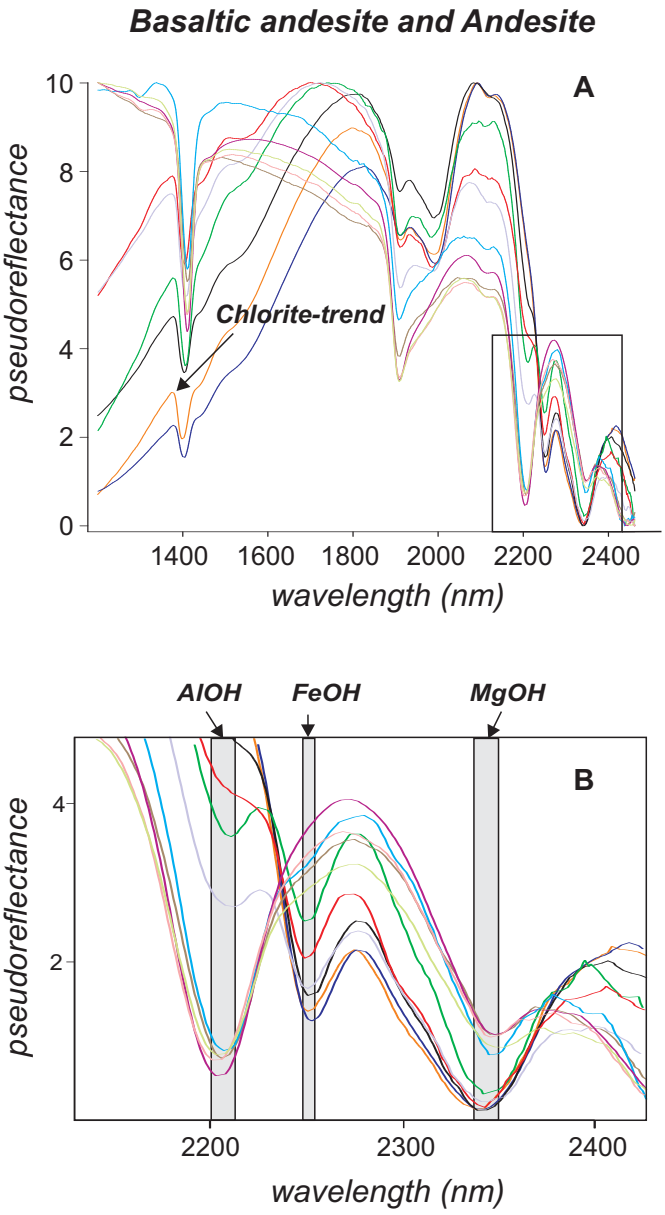

Legend

Sample #	SiO_2	MgO	Fe_2O_3
RAX08G010	50.63	9.18	11.67
RAX08G089	50.96	14.57	10.45
RAX08G156	56.61	10.19	9.49
RAX08G051	58.75	7.0	10.07
RAX08G063	60.73	9.1	10.66
RAX08G142	62.22	7.89	6.88
RAX08G199	65.62	1.06	6.05
RAX08G045	67.67	2.07	9.82
RAX08G008	69.67	0.52	8.66
RAX08G118	75.31	0.54	2.89
RAX08G083	76.67	0.84	2.52

Figure 4.33: A. The basaltic andesite and andesite units display absorption features typical of both illite and chlorite (compare with Figure 4.17). The addition of chlorite clearly shifts the ~1410 nm water feature of illite to smaller wavelengths. The slope of the profile is strongly correlated with wt. % SiO_2. B. Inset from 4.20A. The shift of the AlOH and MgOH feature to longer wavelength reflects the increasing chlorite content of the sample, whereas, an increase in the FeOH feature wavelength relfects increasing illite.

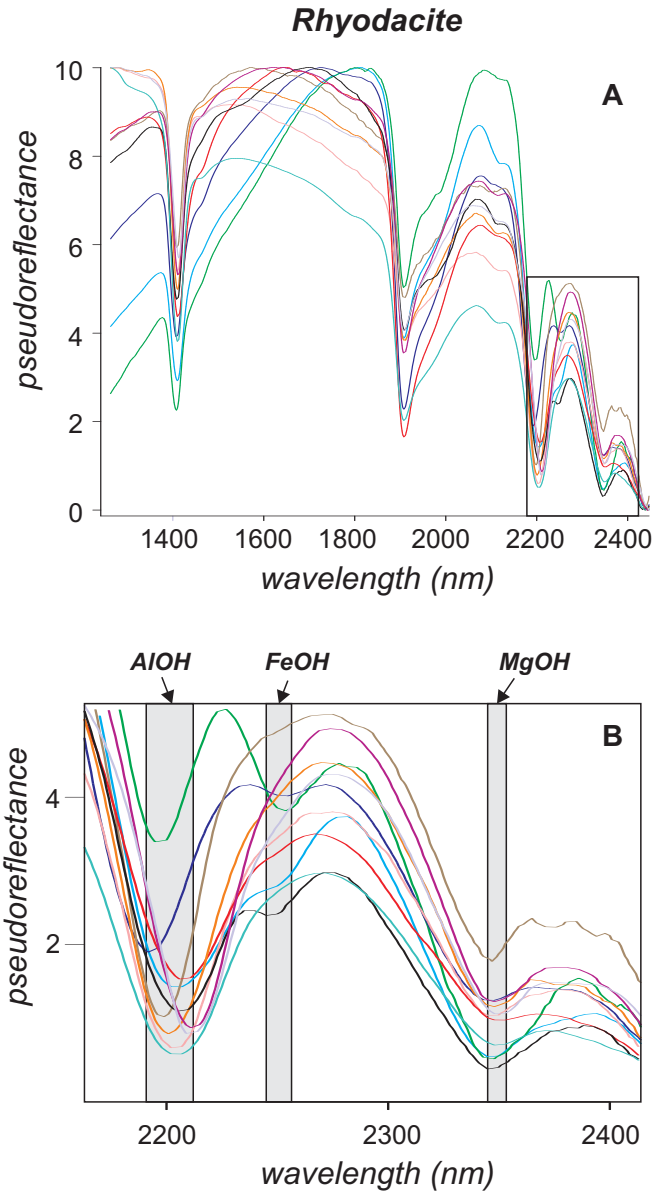

Legend

Sample #	SiO_2	MgO	K_20
RAX08G153	58.71	2.33	3.64
RAX08G166	69.8	0.9	2.07
RAX08G171	70.68	0.79	0.94
RAX08G177	72.73	1.19	2.51
RAX08G030	72.87	0.6	2.2
RAX08G112	73.67	3.11	2.59
RAX08G040	78.1	0.48	2.61
RAX08G170	78.25	0.47	3.24
RAX08G139	78.61	0.45	3.05
RAX08G070	80.34	0.48	3.29
RAX08G165	81.53	0.32	2.77

Figure 4.34: A. The rhyodacite-like units have absorption features dominated by illite; however, minor chlorite is typically present. The slope of the profile is strongly correlated with wt. % SiO_2. B. Inset from 4.12A. The shift of the AlOH feature to longer wavelengths reflects the increase of the illite content of the sample and is strongly correlated to wt. % K_2O. The shift of the FeOH feature to longer wavelength reflects a decrease in chlorite content and is strongly correlated with wt. % MgO and FeO

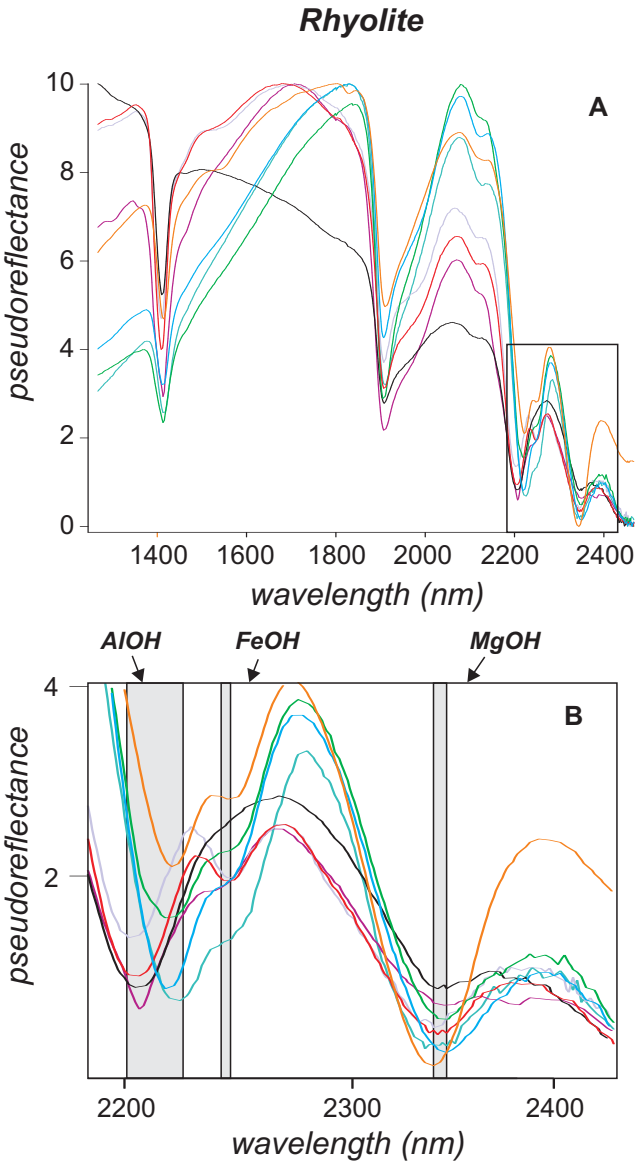

Legend

Sample #	SiO_2	MgO	Fe_2O_3	K_20
RAX08G062	63.1	7.67	3.57	2.27
RAX08G025	69.19	1.84	3.3	4.56
RAX08G191	69.87	1.42	3.13	4.55
RAX08G013	70.3	1.88	2.89	2.31
RAX08G024	72.85	4.11	1.89	2.62
RAX08G002	74.47	0.7	2.39	2.19
RAX08G077	76.6	0.23	1.29	1.79
RAX08G029	80.21	0.4	1.4	2.15

Figure 4.35: A. The rhyolite unit has an absorption spectrum similar to the rhyodacite unit and contains illite and chlorite; however, the position of the AlOH absorption occurs at longer wavelengths in the rhyolite unit, indicative of a phengitic composition of illite. B. Close-up of the longer wavelengths of 4.22A. The majority of the rhyolite samples have a ~2216 nm or longer AlOH absorption feature characteristic of phengite. Several samples have a distinctive ~2250 nm feature characteristic of chlorite.

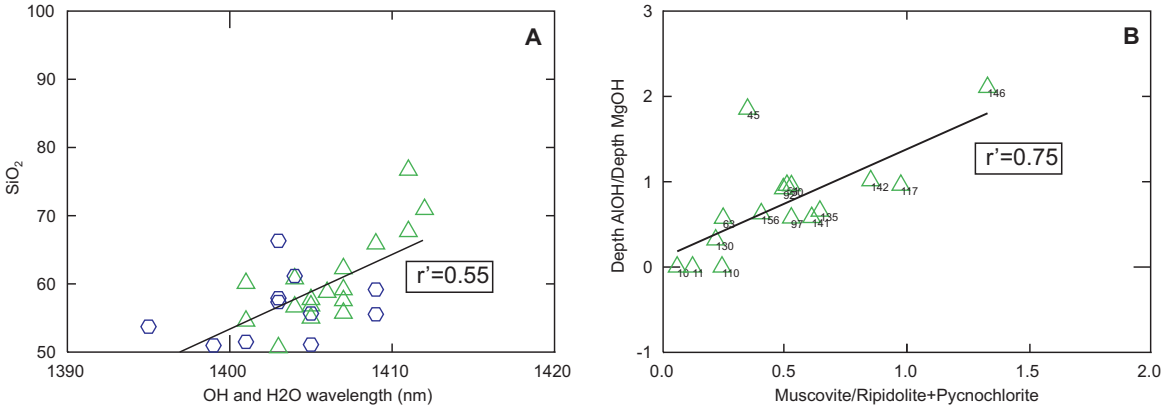

Figure 4.36: A. Plot of SiO_2 (wt. %) versus wavelength of the ~1400 nm water feature. Strong positive correlation between SiO_2 (decreasing chlorite) and the wavelength of the ~1400nm absorption feature is evident. Chlorite thus has the effect of lowering the wavelength at this position. B. A moderately positive correlation exists between the normative mineral proportions of chlorite and muscovite, and the ratio of the AlOH/MgOH absorption features of illite and chlorite. This indicates that the short wave infrared spectrometer can semiquantitatively determine the abudance of illite and chlorite in the Lundberg and Engine House zones.

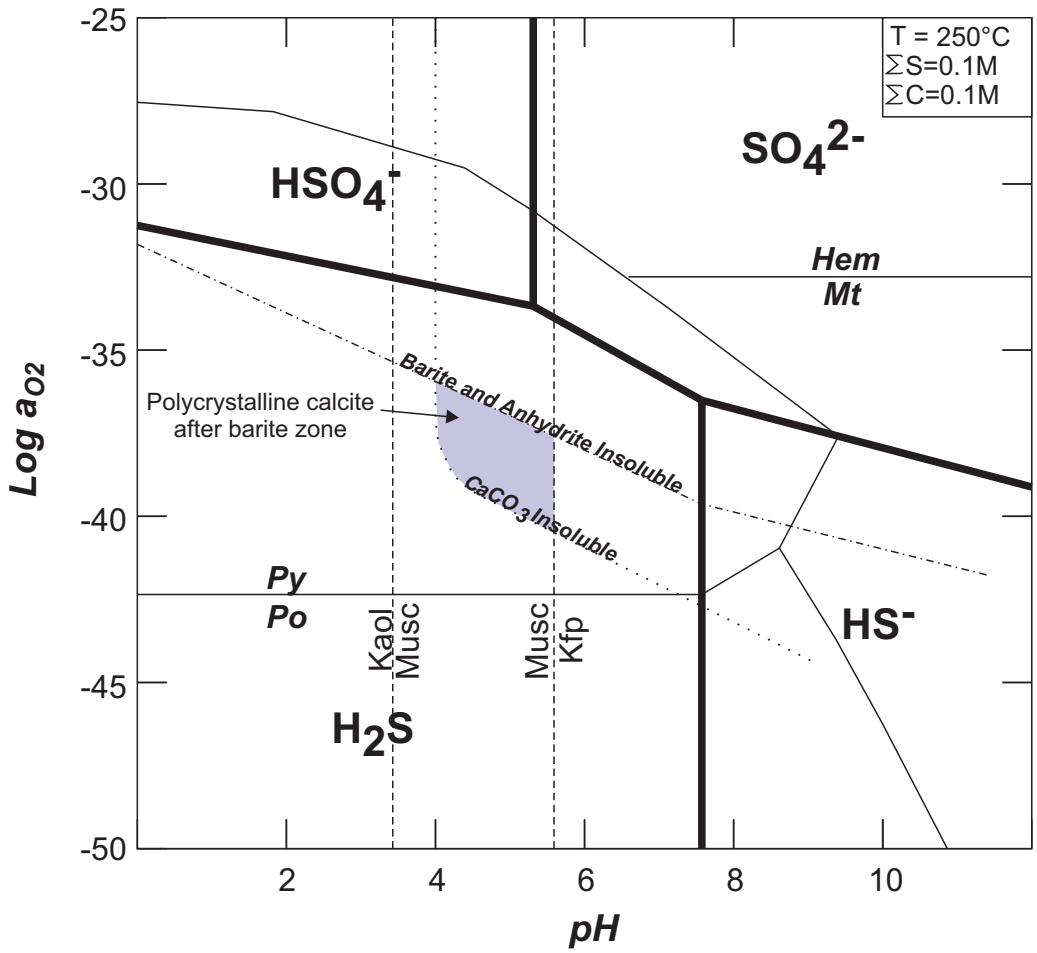

Figure 4.37: Oxygen activity versus pH illustrating the active sulfur species and mineral stability of the hydrothermal fluid during the formation of the Lundberg polymetallic stockwork. The solubility contours for barite and calcite show the conditions where carbonate may have replaced barite in the Lundberg Zone. The $CaCO_3$ insoluble curve is modelled at $mCa^{2+} = 10^{-1}$, the muscovite stability field at $mK^+ = 0.5$, and the bariteand anhydrite insoluble curve at $mBa^{2+} = 10^{-3}$ for barite and $mBa^{2+} = 10^{-1}$ for anydrite (from Crerar and Barnes,1976).

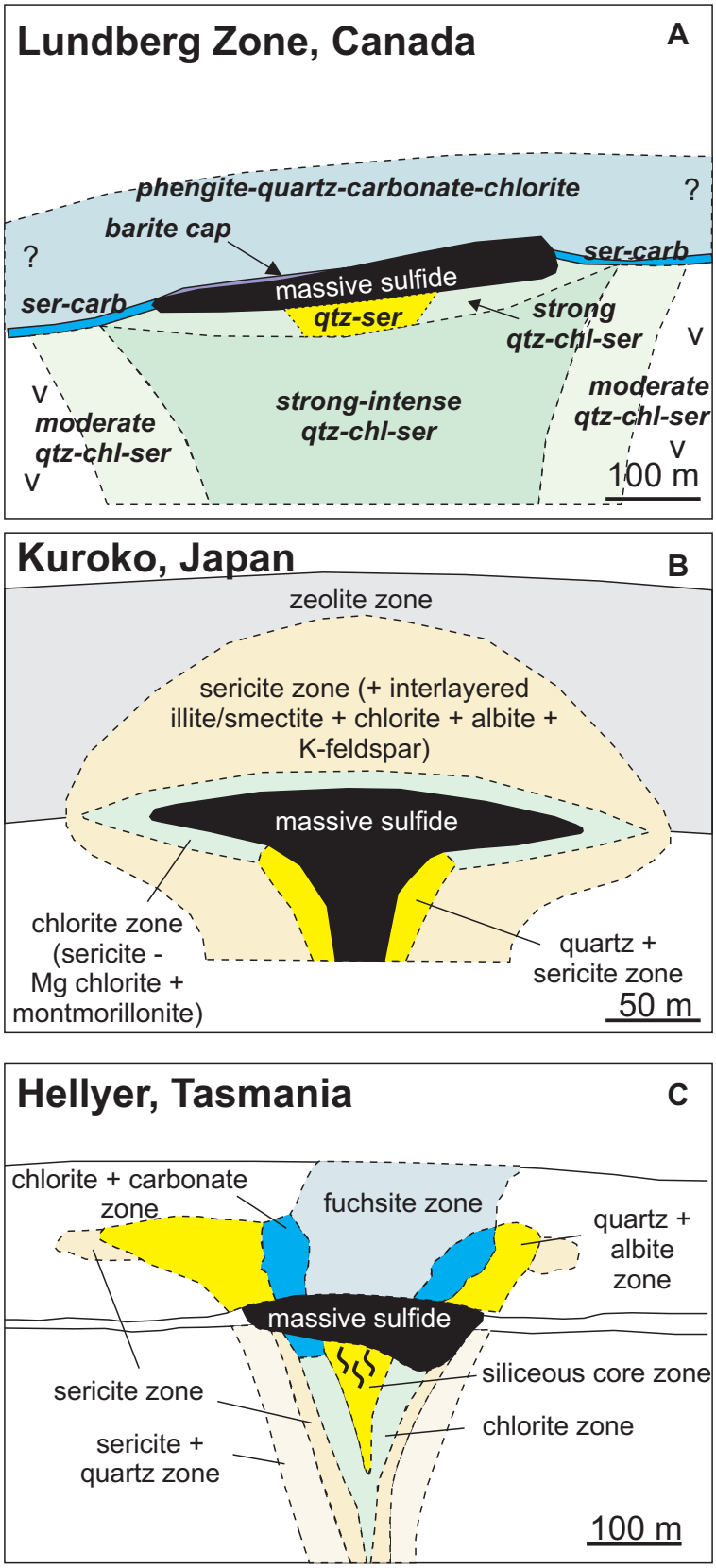

Figure 4.38: Comparison of Paleozoic VMS deposit models to the Lundberg and Engine House zones. A. Schematic drawing of the various alteration zones of the Lundberg and Engine House zones relative to the position of the Lucky Strike massive sulfide orebody. Quartz, chlorite, and sericite are the main alteration minerals in the footwall. By contrast, sericite and carbonate form the main hanging wall alteration. The large amount of stockwork observed around Lucky Strike (i.e. within the entire strong-intense quartz-chlorite-sericite alteration zone), is in distinct contrast with the sizes observed in the Kuroko District. B. The Kuroko deposits of Japan have several differences from the Lundberg Zone. The most notable, is the abundance of sericite-dominated assemblages marginal to mineralization. In the Lundberg Zone, chlorite comprises a greater proportion than the other alteration minerals in all but the intense quartz-sericite zone . C. The Kuroko-type Hellyer VMS deposit of Western Tasmania provides a similar comparison to the Lundberg Zone. The stockwork mineralization at Hellyer is much less extensive than at Lundberg, and the alteration pipe surrounding Hellyer contains sericite-dominated assemblages, largely absent in Buchans.

Table 4.1: Mineralogy of the altered volcanic units of the Lundberg Zone based on petrography

Basaltic Andesite (quartz-chlorite and quartz-sericite alteration)							
Sample Name	Quartz	Feldspar	Muscovite	Chlorite	Epidote	Pyrite	Carbonate
RAX08G130	10	35	5	50	0	0	0
RAX08G141	20	45	7	25	2	1	0
RAX08G135	20	20	10	45	5	0	0
RAX08G195	22.5	0.0	25	50	2	0.5	0
RAX08G097	25	15	15	44	0.5	0.5	0
RAX08G011	25	20	8	44	1	1	1
RAX08G148	30	15	30	25	0	0	0
RAX08G156	30	1	29	27	12	1	0
RAX08G010	30	15	5	45	2	2	1
RAX08G022	30	0	20	45	5	0	0
RAX08G044	35	0	25	38	0	2	0
RAX08G089	35	0	15	49	0	0.5	0
RAX08G045	40	0	52	0	0.5	7.5	0
RAX08G151	40	5	18.5	35	1	0.5	0
RAX08G073	40	0	19	40	0	1	0
RAX08G050	40	0	25	45	1	1	0
RAX08G110	45	20	0	30	2	3	0
RAX08G117	45	0	20	30	0	5	0
RAX08G019	45	0	15	34	5	1	0
RAX08G092	48.5	0	15	33	5	0.5	0
RAX08G075	50	0	0	49	0	1	0
RAX08G200	55	0	15	29	0	1	0
RAX08G146	57	0	30	5	3	5	0
RAX08G189	60	1	0	35	3	1	0
RAX08G083	65	0	29	5	0	1	0

Andesite (quartz-chlorite and quartz-sericite alteration)							
Sample Name	Quartz	Feldspar	Muscovite	Chlorite	Epidote	Pyrite	Carbonate
RAX08G085	40	0	0	50	10	0	0
RAX08G063	50	0	10	35	3	2	0
RAX08G051	45	0	20	30	3	2	0
RAX08G142	47	0	30	20	2.5	0.5	0
RAX08G131	47	0	25	20	2	5	0
RAX08G036	49.5	0	30	15	5	0.5	0
RAX08G008	53	0	30	10	3	4	0
RAX08G155	62	0	25	10	2.5	0.5	0
RAX08G199	40	0	50	5	1	4	0
RAX08G118	68.5	0	30	0	1	0.5	0

Table 4.1: Mineralogy of the altered volcanic units of the Lundberg Zone based on petrography

Rhyodacite (quartz-sericite-carbonate alteration)								
Sample name	Sample type	Quartz/ feldspar	Muscovite	Chlorite	Epidote	Pyrite	Carbonate	Talc
RAX08G030	clast	66.5	20	0	3	0.5	10	0
RAX08G040	tuffaceous sediment	75	20	0	1	2	2	0
RAX08G112	clast	64	25	10	0	1	0	0
RAX08G039	tuff	57	30	3	0	0	5	5
RAX08G070	breccia	67.5	30	0	1	1	1	0
RAX08G153	tuff	48	40	0	2	0	10	0

Rhyolite (phengite-quartz-carbonate-chlorite alteration)							
Sample name	Quartz/ feldspar	Phengite	Chlorite	Epidote	Pyrite	Carbonate	Clay/Fe oxide
RAX08G157	85	4	1	0	0	0	10
RAX08G065	68	5	15	0	0	10	2
RAX08G122	80	5	5	0	0	0.5	10
RAX08G002	80	9	1	10	0	0	3
RAX08G077	77	10	0	3	0	10	3
RAX08G129	75	10	0	1	0	4	10
RAX08G013	68	12	15	0	0	0	5
RAX08G025	66	15	6	3	0	10	5
RAX08G029	65	15	5	5	0	10	2
RAX08G144	75	15	9	0	0	1	0
RAX08G024	80	20	0	0	0	0	5
RAX08G191	60	20	10	5	0	0	5
RAX08G124	75	24	0	0	0	1	0
RAX08G197	63	30	1	2	0	4	1
RAX08G086	68	30	1	0	0	1	0

Table 4.2: Mineralogy of the altered volcanic units of the Engine House Zone based on petrography

Rhyodacite (sericite-carbonate alteration)							
Sample name	Sample type	Quartz/ feldspar	Muscovite	Chlorite	Epidote	Pyrite	Carbonate
RAX08G171	autobreccia	58	15	0	2	0.5	24.5
RAX08G166	interstratified tuffaceous sediments horizon	67	10	0	3	0	20
RAX08G177	autobreccia	63	25	0	2	0	10
RAX08G139	autobreccia	79	20	0	0	1	0
RAX08G165	coherent	79	20	0	0	1	0
RAX08G170	autobreccia	73	23	0	2	2	0

Quartz-phyric rhyodacite (sericite-quartz-carbonate-chlorite alteration)							
Sample name	Matrix	Qtz clasts	Fspar clasts	Muscovite	Chlorite	Pyrite	Carbonate
RAX08G174	77	15	5	3	0	0	0
RAX08G179	40	18	18	3	17	0	0
RAX08G137	58	10	20	8	1	0	3
RAX08G160	50	18	18	8	6	0	0
RAX08G183	70	5	3	10	2	0	10
RAX08G164	85	0	0	15	0	0	0
RAX08G180	30	32	8	15	5	0	10
RAX08G181	30	15	15	30	1	0	10

Table 4.3: Summary of microprobe data of altered volcanic rocks of the Lundberg Zone and surrounding area (Henley and Thornley, 1981)

	Mafic		IFW	IFW	Rhyodacite	Stockwork zone		IFW	Felsic
	pycnochlorite	ripidolite	clinochlore		diabantite	clinochlore	penninite	muscovite	phengite
Specimen	542-816	2666-3250	2889-083	2889-083	2878-309	LS 1	LS 2	2878-406	2837-1208
n	4	15	16	1	1	1	1	2	1
SiO_2	30.08	26.80	29.08	31.52	38.19	34.0	31.0	49.28	51.94
TiO_2	0.01	0.05	0.03	0.04	0.05	-	-	0.10	0.00
Al_2O_3	16.72	20.05	20.60	23.93	26.22	17.2	18.4	34.21	30.80
$Fe_2O_{3(T)}$	26.28	32.41	17.37	15.42	16.48	12.45	10.22	1.00	4.21
FeO	23.65	29.16	15.63	13.88	14.83	11.20	9.20	0.90	3.79
MnO	0.27	0.98	0.53	0.47	0.31	-	-	0.05	0.00
MgO	18.38	13.80	22.19	18.46	8.84	24.80	26.35	1.24	2.35
CaO	0.33	0.04	0.08	0.07	0.07	0.00	0.34	0.15	0.13
Na_2O	0.06	0.01	-	-	-	0.06	0.06	-	0.09
K_2O	0.01	0.00	0.00	3.33	-	-	0.02	7.70	8.95
Total	89.50	90.89	88.14	88.37	91.93	87.26	85.37	93.73	98.08

† Fe2O3=1.1113*FeO

Table 4.4: Normative mineral proportions within altered volcanic rocks of the Lundberg Zone

Basaltic Andesite																
Sample Name	Qtz	Kfspar	Ab	Musc	Rip	Pyc	Chl	Ep	Py	Cal	Rc	Total	SSR	AI	CCPI	VA
RAX08G141	17.6	5.2	26.9	17.5	28.7	0	28.7	1.7	0.4	0.3	0.0	96.6	0.9	62.8	71.9	
RAX08G135	22.3	1.0	20.7	20.4	1.4	30.3	31.7	0.0	0.0	0.2	0.3	96.6	0.5	73.1	77.7	
RAX08G130	21.9	0.0	29.1	8.4	2.2	36.7	38.9	0.0	0.0	0.2	0.5	99.1	0.7	66.3	82.8	
RAX08G186	27.9	0	21	12.31	0	36.5	36.5	0.0	0.0	0.2	0.4	98.7	5.0	76.0	84.7	1
RAX08G110	33.6	0.0	15.8	9.0	0.0	37.2	37.2	0.0	0.0	1.1	0.0	96.6	6.9	76.3	89.4	
RAX08G011	24.3	0.0	20.5	5.4	0.0	44.7	44.7	0.0	0.0	0.7	0.3	95.9	2.3	74.8	89.5	
RAX08G010	24.7	0.0	13.8	4.5	0.0	46.1	46.1	4.0	0.0	0.7	0.2	91.5	2.2	72.9	92.4	
RAX08G117	43.5	4.7	0.6	23.6	0.0	24.2	24.2	0.0	0.0	0.2	0.1	96.9	0.6	94.9	80.9	
RAX08G045	49.9	10.4	0.0	8.7	25.1	0.0	25.1	0.0	1.4	0.3	0.0	95.9	3.8	93.1	83.0	
RAX08G097	23.6	0.0	14.4	20.2	0.0	38.4	38.4	0.0	0.0	0.1	0.4	97.1	8.6	84.4	86.7	
RAX08G073	34.3	2.5	0.0	22.0	0.0	37.0	37.0	0.0	0.0	0.0	0.3	96.2	1.1	97.7	89.0	
RAX08G148	30.9	0.0	0.4	26.1	0.0	38.1	38.1	0.0	0.0	0.0	0.4	96.0	15.5	97.2	90.8	
RAX08G151	37.5	0.0	0.4	21.1	0.0	36.4	36.4	0.0	0.0	0.0	0.4	95.9	3.1	96.6	91.3	
RAX08G156	30.5	0.0	7.7	16.8	0.0	41.7	41.7	0.0	0.0	0.1	0.5	97.3	8.6	90.1	91.4	
RAX08G050	34.5	0.0	0.0	21.7	0.0	41.2	41.2	0.0	0.0	0.2	0.3	97.8	2.6	96.2	91.9	
RAX08G092	38.0	0.0	0.4	18.9	0.0	38.3	38.3	0.0	0.0	0.1	0.4	96.2	3.6	95.8	93.0	2
RAX08G044	32.2	0.0	0.8	21.0	0.0	41.5	41.5	0.0	0.0	0.1	0.5	96.3	10.9	96.0	93.7	
RAX08G195	25.3	0.0	1.2	21.9	0.0	47.3	47.3	0.0	0.0	0.1	0.6	96.4	14.2	95.8	93.8	
RAX08G200	49.7	0.0	0.0	14.0	0.0	32.2	32.2	0.0	0.0	0.0	0.3	96.2	7.2	98.4	94.5	
RAX08G022	26.3	0.0	1.4	18.6	0.0	49.8	49.8	0	0.0	0.0	1.0	97.2	11.2	97.8	95.2	
RAX08G159	30.1	0.0	3.6	13.4	0.0	48.4	48.4	0.0	0.0	0.0	0.7	96.1	8.7	95.3	96.5	
RAX08G019	39.2	0.0	0.2	8.0	0.0	46.6	46.6	0.0	0.0	0.0	0.3	94.4	2.0	97.3	96.6	
RAX08G189	43.2	0.0	1.1	9.1	0.0	42.3	42.3	0.0	0.0	0.0	0.4	96.2	4.5	97.3	98.0	
RAX08G089	27.7	0.0	1.3	13.6	0.0	52.3	52.3	0.0	0.0	0.0	1.0	95.8	35.8	98.0	98.8	
RAX08G075	34.0	0.0	0.0	8.3	0.0	52.0	52.0	0.0	0.0	0.0	1.1	95.4	35.6	97.9	99.8	
RAX08G083	55.1	8.7	1.3	27.2	5.9	0.0	5.9	1.0	0.3	0.2	0.0	98.8	0.4	92.6	47.7	3
RAX08G146	48.5	14.1	1.3	17.7	13.3	0.0	13.3	0.0	1.2	0.2	0.0	96.4	2.3	93.2	63.5	

Qtz = quartz, Kspar = k-feldspar, Ab = albite, Musc = muscovite

Rip = ripidolite, pyc = pycnochlorite, Ep = epidote, Py = pyrite, Cal = calcite

Rc = rhodochrosite, SSR = sum of squared residuals, VA = visual alteration.

1 = moderate quartz-chlorite-sericite alteration, 2 = strong to intense quartz-chlorite-sericite alteration

3 = intense quartz-sericite alteration

Andesite																
Sample Name	Qtz	Kspar	Ab	Musc	Rip	Pyc	Chl	Ep	Py	Cal	Rc	Total	SSR	AI	CCPI	VA
RAX08G131	42.1	5.9	19.2	12.3	15.4	0.0	15.4	2.2	0.2	0.0	0.0	97.5	0.4	59.1	64.6	1
RAX08G036	42.9	1.8	5.3	29.1	0.0	17.1	17.1	0.0	0.0	0.5	0.0	96.7	2.5	86.1	72.7	
RAX08G008	51.0	13.3	2.3	4.9	18.6	0.0	18.6	3.0	2.0	0.0	0.0	95.1	6.8	88.7	77.2	
RAX08G142	40.3	0.0	0.0	25.9	0.0	30.3	30.3	0.0	0.0	0.2	0.2	97.0	6.1	95.9	87.7	
RAX08G051	36.6	2.8	0.0	18.1	0.9	36.1	37.0	0.9	0.0	0.0	0.4	95.8	0.8	95.9	90.1	2
RAX08G155	53.6	3.0	0.0	19.7	0.0	19.9	19.9	0.0	0.0	0.2	0.1	96.6	0.4	95.9	82.3	
RAX08G085	26.9	0.0	2.0	15.2	0.0	50.9	50.9	0.0	0.0	0.1	0.5	95.7	47.4	96.8	98.9	
RAX08G063	42.5	0.2	0.0	10.6	0.0	43.0	43.0	0.0	0.0	0.1	0.3	96.6	2.3	96.9	95.7	
RAX08G199	36.6	15.8	2.1	26.4	13.5	0.0	13.5	1.9	1.1	0.0	0.0	97.35	2.2	93.3	59.4	3

Qtz = quartz, Kspar = k-feldspar, Ab = albite, Musc = muscovite

Rip = ripidolite, pyc = pycnochlorite, Chl = Rip + Pyc, Ep = epidote, Py = pyrite, Cal = calcite

Rc = rhodochrosite, SSR = sum of squared residuals, VA = visual alteration.

1 = weak quartz-chlorite-sericite alteration, 2 = strong to intense quartz-chlorite-sericite alteration

3 = quartz-sericite alteration

Table 4.4: Normative mineral proportions within altered volcanic rocks of the Lundberg Zone

Rhyodacite																
Sample name	Qtz	Kspar	Ab	Musc	Rip	Dia	Ep	Py	Cal	Ank	Rc	Total	SSR	AI	CCPI	VA
RAX08G030	46.6	4.9	21.4	16.6	0.0	0.0	0.0	0.0	1.3	8.7	0.5	100.0	1.8	34.4	31.7	
RAX08G171	35.5	0.0	38.3	16.1	0.0	1.1	0.0	0.0	0.0	9.0	0.0	100.0	2.7	19.9	39.8	1
RAX08G177	45.9	3.9	17.6	24.1	1.3	0.0	0.0	0.0	0.0	6.9	0.2	99.9	0.2	49.9	41.3	
RAX08G166	50.7	0.0	6.0	29.1	0.0	0.0	0.0	0.0	1.3	12.7	0.2	100.0	5.7	38.5	57.1	
RAX08G040	53.7	7.2	13.2	18.2	4.2	1.5	0.0	0.2	0.0	0.8	0.0	99.0	0.2	65.2	40.5	
RAX08G153	26.2	0.0	12.2	48.1	1.8	0.0	0	0.0	0.0	10.6	0.3	99.1	1.0	60.2	51.3	2
RAX08G039	30.4	0.0	11.2	42.6	7.1	0.0	0.0	8.7	0.0	0.0	0.0	100.0	2.0	65.9	62.3	
RAX08G031	20.8	14.0	4.4	46.0	1.2	0.0	0.0	13.2	0.4	0.0	0.0	100.0	1.0	68.8	47.0	
RAX08G070	39.4	5.7	9.6	35.4	0.0	0.0	0.0	9.5	0.4	0.0	0.0	95.5	4.1	87.1	26.8	
RAX08G165	64.8	6.7	0.0	21.5	2.1	3.3	0.0	0.3	0.0	0.3	0.1	99.2	0.4	89.8	41.9	3
RAX08G170	57.9	10.0	1.6	20.3	3.9	4.5	0.0	0.3	0.0	0.3	0.1	99.0	0.5	90.9	47.9	
RAX08G139	59.6	9.8	1.1	18.3	4.1	4.7	0.0	0.4	0.0	0.2	0.2	98.4	0.5	92.1	50.2	
RAX08G112	55.4	3.3	0.6	26.0	10.8	0.0	0.0	0.0	0.0	0.9	0.0	97.1	1.8	94.4	70.7	4

Qtz=quartz, Kspar=k-feldspar, Ab=albite, Musc=muscovite, rip=ripidolite, dia=diabnite

Ep=epidote, Py=pyrite, Cal=calcite, ank=ankerite, Rc=rhodochrosite

SSR=sum of squared residuals, VA = visual alteration.

1 = unaltered to weakly altered rhyodacite, 2 = weak sericite-carbonate-chlorite altered rhyodacite tuff

3 = intense quartz-sericite alteration, 4 = intense quartz-sericite-chlorite

Rhyolite																
Sample name	Qtz	Kfspar	Ab	Phg	Cham	Clin	Cal	Ank	Rc	Ep	Py	Total	SSR	AI	CCPI	VA
RAX08G157	55.2	2.3	30.7	9.1	0.0	0.0	0.0	2.7	0.0	0.0	0.0	100.0	0.5	25.4	21.6	
RAX08G077	51.4	1.0	22.5	16.5	0.0	0.0	3.4	4.7	0.5	0.0	0.0	100.0	5.0	27.3	25.7	
RAX08G122	34.8	4.9	42.8	13.6	1.3	0.0	0.0	2.6	0.1	0.0	0.0	100.0	0.1	32.0	24.7	
RAX08G002	45.0	0.0	24.0	23.2	0.0	0.0	1.9	5.9	0.0	0.0	0.0	100.0	7.7	33.5	37.5	
RAX08G124	41.6	2.1	32.0	19.4	0.6	0.0	0.0	4.2	0.1	0.0	0.0	100.0	0.2	36.8	31.8	
RAX08G029	60.6	0.0	4.5	31.5	0.0	0.0	1.7	1.3	0.4	0.0	0.0	100.0	1.7	40.2	41.1	
RAX08G013	34.7	0.7	30.4	24.6	1.6	3.5	0.0	2.7	0.1	0.0	0.0	98.3	0.1	49.7	44.4	
RAX08G144	41.5	7.6	12.3	31.4	1.1	0.0	0.0	4.8	0.3	0.0	0.0	99.1	0.2	66.8	42.3	1
RAX08G065	37.8	0.0	4.4	29.0	0.0	23.9	0.4	0.0	0.0	0.0	0.0	100.0	0.9	68.2	44.0	
RAX08G197	40.0	9.3	8.8	31.0	1.3	1.3	0.0	7.5	0.3	0.0	0.0	99.5	0.3	68.7	50.8	
RAX08G191	39.9	10.4	10.3	30.1	1.8	0.0	0.0	5.5	0.3	0.0	0.0	98.3	0.2	69.6	43.8	
RAX08G086	40.7	14.7	9.5	28.3	0.0	0.0	0.0	5.7	0.3	0.0	0.0	99.2	0.3	71.5	35.9	
RAX08G025	39.6	8.6	7.8	34.8	0.7	1.1	0.0	6.7	0.3	0.0	0.0	99.7	0.3	71.6	48.4	
RAX08G129	38.8	0.0	10.8	33.8	0.0	12.3	1.1	0.0	0.3	0.9	0.0	98.1	5.5	85.9	82.3	
RAX08G024	50.6	0.0	2.9	32.8	0.0	10.5	0.3	0.0	0.1	0.0	0.0	97.2	2.4	98.0	69.5	

Qtz=quartz, Kspar=k-feldspar, Ab=albite, Phg=phengite, cham=chamosite, Clin=clinochlore

Ep=epidote, Py=pyrite, Cal=calcite, ank=ankerite, Rc=rhodochrosite

SSR=sum of squared residuals, VA = visual alteration.

1 = phengite-quartz-carbonate-chlorite alteration

Table 4.4: Normative mineral proportions within altered volcanic rocks of the Lundberg Zone

Quartz-phyric Rhyodacite (phengite-quartz-carbonate-chlorite alteration; with 1 cm qtz phenocrysts)																
Sample name	Qtz	Kfspar	Ab	Phg	Cham	Clin	Cal	Ank	Rc	Ep	Py	Total	SSR	AI	CCPI	VA
RAX08G137	36.7	0.0	50.6	7.1	0.6	0.0	0.0	4.8	0.1	0.0	0.0	100.0	0.7	7.53	26	1
RAX08G180	35.8	0.0	28.0	26.9	0.0	0.0	3.9	4.9	0.6	0.0	0.0	100.0	6.6	32.8	27.2	
RAX08G179	42.5	0.0	28.4	14.0	4.5	2.7	0.0	7.4	0.3	0.0	0.0	99.9	1.3	33.8	66	
RAX08G181	41.4	0.0	26.0	26.6	0.0	0.0	1.7	3.9	0.5	0.0	0.0	100.0	1.4	38.9	28.3	2
RAX08G164	39.5	0.0	30.6	20.1	2.2	3.0	0.0	3.1	0.2	0.0	0.0	98.6	0.2	43.5	47.5	
RAX08G182	49.4	0.0	9.2	32.5	0.0	0.0	3.9	4.5	0.5	0.0	0.0	100.0	8.6	43.6	44.5	

Qtz=quartz, Kspar=k-feldspar, Ab=albite, Phg=phengite, cham=chamosite, Clin=clinochlore
Ep=epidote, Py=pyrite, Cal=calcite, ank=ankerite, Rc=rhodochrosite
SSR=sum of squared residuals, VA = visual alteration.
1 = weak albite alteration, 2 = weak phengite-quartz-carbonate-chlorite alteration

Quartz-phyric Rhyodacite (sericite +/- carbonate alteration; without 1 cm qtz phenocrysts)																
Sample name	Qtz	Kspar	Ab	Musc	Rip	Dia	Ep	Py	Cal	Ank	Rc	Total	SSR	AI	CCPI	VA
RAX08G183	47.6	0.0	21.8	17.8	1.1	2.7	0.0	8.4	0.3	0.0	0.2	100.0	0.0	28.7	53.7	1
RAX08G174	46.9	0.0	27.9	14.1	4.9	0.0	0.0	5.9	0.1	0.0	0.2	100.0	0.3	33.1	50.3	
RAX08G160	59.6	4.4	9.0	19.1	3.2	1.5	0.0	1.3	0.1	0.0	0.2	98.3	0.2	67.1	43.8	2

Qtz=quartz, Kspar=k-feldspar, Ab=albite, Musc=muscovite, rip=ripidolite, dia=diabnite
Ep=epidote, Py=pyrite, Cal=calcite, ank=ankerite, Rc=rhodochrosite
SSR=sum of squared residuals, VA = visual alteration.
1 = unaltered quartz-phyric rhyodacite; 2 = weak quartz-sericite alteration

Table 4.5: Comparison of alteration characteristics and SWIR features of several Paleozoic VMS districts

Name of District	*Name of Deposit*	*Deposit type*	*Lithology analyzed*	*Mineral Assemblage*	*AlOH (nm)*	*FeOH (nm)*
Lundberg		VHMS (stockwork)	FW basaltic andesite	Quartz, Mg-chlorite, illite	2200	2250
	Lundberg Zone (Zn-Pb-Cu-Ag)	VHMS (stockwork)	Ore-horizon rhyodacite	Quartz, illite, minor Mg-chlorite and carbonate	2200	2250
		VHMS (stockwork)	HW rhyolite	Quartz, phengite, minor Mg-chlorite and carbonate	2218	2250
Cambrian Mt. Read Volcanics	Hellyer (Zn-Pb-Cu-Ag-Au)	VHMS (mound-style)	FW Andesite	Quartz-sericite to distal chlorite-sericite-quartz-pyrite to weak sericite-quartz-pyrite	~2200	NA
(Giftkins et al., 2005; Herrmann et al.,2001)	Roseberry (Zn-Pb-Cu-Ag-Au)	VHMS (stratiform)	Volcaniclastic sandstone (proximal)	Quartz-sericite or Mn Carbonate	<2200	NA
		VHMS (stratiform)	Volcaniclastic sandstone (distal)	Quartz-sericite or Mn Carbonate	>2200	NA
	Western Tharsis (Cu-Au)	Hybrid VHMS-high sulfidation epithermal	Felsic volcaniclastic or andesite (proximal)	Quartz, chlorite, sericite	<2200	NA
		Hybrid VHMS-high sulfidation epithermal	Felsic volcaniclastic or andesite (distal)	Sericite, chlorite	>2200	NA
		Hybrid VHMS-high sulfidation epithermal	Felsic volcanic/intrusion - diagenetic zone	feldspar, quartz, chlorite, sericite, +/- carbonate	2202-2219	NA
	Highway Reward (Cu-Au)	Hybrid VHMS-high sulfidation epithermal	Felsic volcanic/intrusion - Medial zone	chlorite, sericite	2194-2212	NA
		Hybrid VHMS-high sulfidation epithermal	Felsic volcanic/intrusion - Proximal zone	quartz, sericite, pyrite	2194-2202	NA

Table 4.5: Comparison of alteration characteristics and SWIR features of several Paleozoic VMS districts

Name of District	*Name of Deposit*	*Deposit type*	*Lithology analyzed*	*Mineral Assemblage*	*AlOH (nm)*	*FeOH (nm)*
Myra Falls (Jones et al., 2005)	Battle orebody (Cu-Zn-Pb-Ag-Au)	VHMS (stratiform)	HW horizon rhyolite	Quartz, paragonite-muscovite, pyrite, minor Mg chlorite, and carbonate	2198	2241
	HW orebody (Cu-Zn-Pb-Ag-Au)	VHMS (stratiform)	HW horizon rhyolite	Quartz, muscovite, pyrite, minor Mg-chlorite, and carbonate	2201	2246
		VHMS (stratiform)	FW Price Andesite	Quartz, muscovite, Mg Chlorite, pyrite, and carbonate	2200	2246
	Regional sample	VHMS (stratiform)	HW horizon regional rhyolite	Quartz, muscovite-phengite, pyrite, minor Mg chlorite and carbonate	2206	2247
		VHMS (stratiform)	FW regional Price Andesite	Fe-chlorite, epidote, muscovite-phengite, minor carbonate, sericite, quartz	2204	2246

Chapter 5: Conclusions

Seven distinct volcanic units are recognized within the Lundberg Zone: the lower basaltic andesite (LHF), upper basaltic andesite and andesite (SHF), lower sedimentary sequence (BRF), rhyodacite (BRF), upper sedimentary sequence (BRF), quartz-phyric rhyodacite (BRF), and the structurally capping rhyolite (LSS). In the Lundberg Zone, the lower basaltic andesite (LHF) comprises pillow basalt, chert, and mafic tuff. Individual pillows/tubes range from 0.3 to 1 m in diameter and are defined by black, chloritic, fine-grained pillow rinds. The chert unit is thinly bedded and locally displays ball and pillow contacts indicating that it was formed by siliciclastic sedimentation and later silicification. The mafic tuff is a medium-grained feldspathic unit which contains abundant scoriaceous basalt clasts. Conformably overlying the lower basaltic andesite is the upper basaltic andesite (SHF). The upper basaltic andesite forms the footwall to the Lucky Strike orebody and hosts the Lundberg and Engine House polymetallic stockworks. It consists of feldspar and clinopyroxene porphyritic basaltic andesite that displays both hyaloclastite and scoriaceous texture locally. Within the intense stockwork zones, the basaltic andesite displays in situ breccia textures. Although visually indistinct, the andesite flows within the mid- to upper portions of the upper basaltic andesite are notably fractionated. Distinct breaks in volcanism occurred within the upper basaltic andesite, marked by a thick volcanosedimentary unit referred to as the 'lower sedimentary sequence'. The lower sedimentary unit comprises two horizons of rhyodacitic breccias and turbidites separated by a thick siltstone unit. Massive sulfide clasts are observed locally. Conformably overlying the upper basaltic andesite is the rhyodacite unit (BRF). It forms massive and autoclastic flows which are flanked by debris and pyroclastic flow deposits of the upper sedimentary sequence and overlain directly by a barite cap. The upper sedimentary sequence forms the main ore horizon in the Buchans mining camp and massive sulfide clasts are found throughout this unit. Structurally overlying the upper sedimentary sequence across a sequence of diabase sills is the rhyolite unit (LSS). This unit consists of QFP rhyolite which is locally autobrecciated and feldspar-rich tuff.

The Engine House Zone occurs within a similar sequence of volcanic and sedimentary rocks and is interpreted to reflect a lateral facies change of the Lundberg Zone stratigraphy. Additional exploration for stockwork mineralization should thus be targeted within basaltic andesite to andesite units of the SHF and on horizons containing massive and transported sulfides within intercalated BRF (i.e., both upper and lower sedimentary sequence). This newly discovered relationship opens up the SHF to additional exploration.

The whole-rock geochemistry of the volcanic rocks was investigated to establish a predictable chemostratigraphy for mineral exploration. Winchester and Floyd (1977) discrimination diagrams were used to distinguish the primary lithology of the altered units. The large geochemical gap between mafic and felsic lithologies indicates that the entire suite of rocks is bimodal and likely formed by partial melting (i.e., the mafic rocks from the mantle and the felsic rocks from an unknown mafic crust). All lithologies fall into one of three distinct geochemical groups: basaltic andesite (SHF), rhyodacite (BRF), and rhyolite (LSS). The upper basaltic andesite, andesite, sedimentary sequences, rhyodacite, and rhyolite units all have calc-alkalic signatures with enriched LREE, Nb, Zr, Eu, and Ti anomalies, and flat HREE profiles. The andesite unit has slightly higher incompatible and compatible REE concentrations than the upper basaltic andesite indicating fractionation. Rhyodacite tuff and clasts of the lower and upper sedimentary sequence were determined to have identical geochemistry to the rhyodacite autobreccia unit indicating that these units formed by pyroclastic eruption/mass flow of a rhyodacite-dome complex. The BRF rhyodacitic rocks have a clear FII, rather than transitional FI-FII affinity, which may suggest a shallower depth of partial melting or some degree of fractional crystallization compared to the LSS rhyolite. The LSS rhyolite lacks massive sulfide clasts and associated stockwork which may indicate that it is less prospective. However, distal hydrothermal alteration indicators have been found (Chapter 4). These felsic units have FII-rhyolite geochemistry. A rhyodacitic tuff unit of the Engine House Zone was analyzed. It sits in a similar structural position to the rhyolite unit in the southeast corner of the study area, but

has FII-rhyolite chemistry identical to that of the rhyodacite autobreccia and sedimentary sequences. It is therefore grouped with the Buchans River Formation.

Samples of both mafic and felsic rocks collected by Zagorevski (2008) at the Oriental and Maclean mines and Clementine prospect have identical lithogeochemistry to the samples of the Lundberg and Engine House zones. This suggests a predictable mine stratigraphy in the camp and provides an invaluable geochemical framework for future exploration.

Four different types of stockwork veins cut the upper basaltic andesite within the Lundberg Zone: (1) quartz-carbonate-barite-sulfide, (2) quartz-carbonate-sulfide, (3) massive sphalerite veins, and (4) quartz +/- sulfide +/- carbonate. The quartz-carbonate-barite-sulfide veins form in the uppermost portions of the stockwork zone and commonly have bladed mineral morphologies. However, barite is the only mineral which displays its primary crystal form; both carbonate and quartz replace blades of barite forming apparent epithermal texture. Quartz-carbonate-sulfide and massive sphalerite veins form in similar positions beneath the barite-rich zone and form the majority of the mineralization. Below the base metal-rich veins are small quartz +/- carbonate veins with little sulfide.

The footwall alteration within the upper basaltic andesite forms a pipe-like feeder zone comprised of three main zones: intense quartz-sericite or 'siliceous core zone', strong to intense quartz-chlorite-sericite, and moderate quartz-chlorite-sericite. The moderate quartz-chlorite-sericite alteration forms distal to mineralization. The strong to intense quartz-chlorite-sericite zone forms inside of the moderately altered envelope. Alteration intensity increases towards the most highly mineralized regions, but decreases towards the hangingwall. The intense quartz-sericite zone forms a thick (up to 40 m) altered horizon mostly overlying the main stockwork mineralization. The siliceous core zone replaces the quartz-chlorite-sericite zone in the center of the stockwork and is most proximal to massive sulfide mineralization. The rhyolite unit, which structurally overlies the Lundberg Zone, is altered to phengite-quartz-carbonate-chlorite indicating a distal hydrothermal

assemblage. Alteration intensity increases towards the core of the deposit within this structurally-emplaced unit, suggesting it may not be that far travelled. Alteration geochemistry of these assemblages revealed typical chloritization, sericitation, and silicification trends: mass gains of SiO_2, MgO, Fe_2O_3, Al_2O_3, and significant loss of Na_2O and CaO. The hanging-wall alteration immediately surrounding the Lucky Strike deposit consists of weak sericite and carbonate.

The first attempt at using shortwave infrared spectrometry in the camp successfully differentiated the above alteration assemblages. Within the altered footwall volcanics, the abundance of chlorite and illite could be estimated in most units; however, rocks in the hanging-wall had little chlorite. Within the altered hanging-wall the dominant sericite mineral was determined to be phengite rather than illite which occurs mainly in the footwall. This key feature provides an excellent fingerprint around the Lundberg Zone and may be used as an exploration tool. SiO_2 had a dramatic effect on the spectra, reducing the slope from 1400 to 2200 nm.

5.1 Interpretation of Volcanic Stratigraphy and Textures

Only preliminary reconstructions of the Buchans mining camp have been attempted due to correlation problems and lack of controls at depth. The volcanic reconstruction of the camp has been difficult because of the 'bewilderingly complex' structure and its effect on stratigraphy (Calon and Green, 1987). Seismic reflection surveys (i.e., Thurlow et al., 1992) were utilized to determine the deeper structure of the Buchans Group; however, the results of the surveys suggested that some of the previously correlated units were in fact uncorrelatable. Additional stratigraphic complexities were revealed in recent mapping (Zagorevski, 2008, 2009, 2010). The Airport Thrust observed immediately east of Buchans does not repeat LHF tuffs, as previously proposed (Thurlow and Swanson, 1987), but represents an entirely separate Seal Pond Formation in the Mary March Brook area east of Buchans (e.g., Figure 2.1: Zagorevski and Rogers, 2008). It consists of tholeiitic quartz +/- feldspar porphyritic felsic volcanic rocks with significant amounts of interlayered tholeiitc pillow

basalt and quartz porphyritic pyroclastic rocks, which are completely different from the calc-alkaline rocks of the Buchans Group (Strong, 1984).

The hyaloclastite and pillow basalts of the LHF and SHF at the base of the Lundberg Zone are interpreted to have formed in a submarine arc setting. The sedimentary lens that is interstratified with SHF reflects development of bimodal mafic-rhyodacitic volcanism with contemporaneous massive sulfide formation. The lower sedimentary sequence is conformably overlain by basaltic andesite with polymetallic stockwork veins, possibly formed in a shallow submarine environment. The overlying BRF siltstone, rhyodacite tuff, and polymictic breccia (up to 60 m thick) represent deposition in a variably active volcanic and sedimentary basin, possibly at the flank or within a felsic caldera-like setting (Henley and Thornley, 1981; Figure 5.1). This model suggests that the Lundberg Zone formed in an environment characterized by abundant explosive eruption of SHF basalt, resurgent BRF domes, and associated hydrothermal activity and massive sulfide deposition. The high proportion of felsic pyroclastic rocks older than the SHF within the LHF may also support a caldera setting and shallow environment (Kirkham and Thurlow, 1987). However, the extent of the LHF east of Buchans may not be as great as previously thought and a mafic caldera may be more likely. A more generalized representation of the paleoenvironment, generated from this study is shown in Figure 5.2.

The abundance of mafic breccia with characteristic hyaloclastite texture in the footwall (SHF and LHF) of the Lucky Strike deposit clearly demonstrates the development of a submarine volcanic complex. Perlitic fractures that cut trachytic texture indicates hydration of basaltic glass and occur throughout massive and hyaloclastite facies. Quench fragmentation of the pillowed basalt more than likely occurred by interaction with cold seawater directly on the seafloor.

The lower sedimentary sequence of the Ski Hill Formation, which is characterized by bimodal volcanism in its upper portions where it is interfingered with the Buchans River Formation, formed as a resedimented volcaniclastic deposit during basin development. The wide clast distribution and clast morphology (subrounded) reflects extensive transport rather than preservation

of texturally unmodified juvenile clasts (cf. McPhie, 1993). The presence of massive, poorly sorted beds with sharp basal contacts indicate sediment gravity flow, or more specifically debris flow, over a highly variable volcanic and sedimentary substrate deposited in a basin/channel, as previously suggested for other horizons (Binney, 1987). The presence of normal grading within some sandstone beds suggests local deposition from low-density turbidity currents supported by fluid turbulence (Binney, 1987). The clast distribution (i.e., 80% felsic, 10% mafic, 9% sedimentary, 1% sulfide) indicates a felsic bimodal source with contemporaneous massive sulfide formation.

Massive siltstone beds overlie the sulfide-poor sediment gravity flows within the lower sedimentary sequence. This is interpreted to reflect rapid change in the depositional style and background sedimentation in a low energy environment or break in high-volume effusive volcanic activity. Binney (1987) observed similar siltstone along the same horizon within the Maclean extension area and concluded that its association with sandstone indicates deposition from turbidity currents. In the Lundberg Zone, the position of the siltstone between underlying mass flow deposits and overlying turbidity current and mass flow deposits suggests that the siltstone likely was deposited from distal turbidites. This model may be supported by the distribution of transported breccias (Thurlow and Swanson, 1981); however, the incomplete tectonic reconstruction makes such interpretations difficult (Calon and Green, 1987). Near the stratigraphic top of the siltstone unit are rare interstratified monomictic rhyodacite breccias characterized by highly angular clasts and reverse grading, possibly representing intermittent resedimented syneruptive breccias from a growing rhyodacite volcanic edifice. The highly angular clasts (up to 8 cm) in a fine-grained matrix indicate that debris flow was the sediment transport mechanism. Thus, the eroding volcanic edifice may have been located at the margin of a fault-bounded siltstone basin (cf. Binney, 1987).

Immediately overlying the siltstone is another rhyodacitic polymictic breccia package, but with common interstratified sandstone and siltstone (10%). The internal normal grading and/or planar lamination forms T_{ab} divisions of the Bouma sequence indicating derivation from low density

turbidity currents. This is consistent with building up of a rhyodacitic volcanic edifice and gravity flows from the steepened edifice.

The base of the Buchans River Formation (i.e., upper sedimentary sequence) is locally marked by rhyodacite breccia. It forms autoclastic to massive flow facies and provides volcaniclastic debris for the overlying sandstone/siltstone, rhyodacite tuff, and rhyodacite breccia. The brecciated texture is interpreted to reflect slumping of semiconsolidated sediments. Rhyodacitic tuff, which forms 4.5m thick beds underlying the polymictic breccia, is crystal-rich (70%), contains fine ash (>20%) and lithic fragments (<10%) typical of a pyroclastic flow. The polymictic breccia correlates with the Lucky Strike ore horizon and is characterized by small 1 cm massive sulfide clasts (Binney, 1987). A unique feature of H-3344 (westernmost hole) is the presence of rhyodacite clasts with crustiform massive pyrite overgrowths, observed nowhere else in the Lundberg and Engine House zones, suggesting an additional source of hydrothermal activity and clast formation.

The thrust emplaced LSS rhyolite consists of interstratified crystal-rich tuff, suggesting pyroclastic activity and relatively shallow water depth.

5.2 Comparison to Other VHMS Environments

The tectonic history of Western Tasmania is strikingly similar to that proposed by Zagorevski et al. (2009) for the Annieopsquotch Accretionary Tract. In Western Tasmania, intra-oceanic arcs develop outboard of a thinned passive continental margin and were later accreted by roll-back of an east-directed slab (e.g., Crawford and Berry, 1992). A subduction zone flip subsequently occurred and formation of the Mt. Read continental arc commenced (e.g., Crawford and Berry, 1992). The Mount Read Volcanics host a wide range of mineral deposits ranging from VMS to high sulphidation epithermal (e.g., Large, 1992). In Tasmania, these types of deposits are associated with synvolcanic stratabound Au-rich deposits (e.g., Henty and South Hercules) which are characterized by low sulfide content and intense silicification (Large et al., 2001b). In the Buchans

Camp, only one stratabound Au showing (e.g., The Halfway Mountains) has been discovered, which may indicate that larger deposits remain to be found.

The Paleozoic Myra Falls district forms part of the Sicker Group within the Wrangellia arc terrane (Jones et al., 2005). This group of arc rocks form a strikingly similar package to the Buchans camp stratigraphy. The Price Formation forms the stratigraphic base of the Sicker Group and consists of clinopyroxene-feldspar porphyritic basaltic andesite and andesite massive flows and breccias which are intercalated with thick successions of agglomerate, lapilli tuff, mafic sandstone, and tuffaceous siltstone (Jones et al., 2005). The overlying Myra Formation consists of several lithostratigraphic units. The basal unit consists of rhyolitic volcaniclastic rocks which host replacement massive sulfides. The hanging-wall to these deposits (HW and Battle orebodies) consists of massive and brecciated basaltic andesite. Overlying the basaltic andesite is a mafic volcaniclastic unit with interbedded argillite, and lesser felsic volcanic rocks (Jones et al., 2005). Above this volcaniclastic unit is a second ore horizon (Lynx-Myra-Price horizon) which is interpreted to have formed directly on the seafloor rather than by replacement like the underlying HW and Battle orebodies (Jones et al., 2005). The entire sequence is overlain by the Thelwood Formation which consists of a thick succession of mudstone and lesser volcaniclastic rocks.

Although the host rocks of the Myra Falls are seemingly similar to Buchans, the metallogeny of these deposits is quite distinct. The Myra Falls camp has historically produced 21 Mt of ore at an average grade of 6 % Zn, 1.6% Cu, 0.6 % Pb, 66 g/t Ag, and 2.2 g/t Au and contains reserves in excess of 7.7 Mt at an average grade of 6.6 % Zn, 1.3 % Cu, 0.4 % Pb, 36.4 g/t Ag, and1.3 g/t Au (Jones et al., 2006). The Buchans Camp is enriched in Zn, Pb, Cu, and Ag (14.5% zinc, 7.6% lead, 1.3% copper, 126 g/t Ag) compared to Myra Falls, but has slightly lower gold content (1.37 g/t Au). The difference in metal content between Buchans, Myra Falls, and a few other VHMS deposits around the world is depicted in Figure 1.7. The lack of Pb at Myra Falls most likely reflects a bimodal mafic setting (cf. Piercey, 2007). The abundance of precious metals likely reflects a shallow water depth of formation, zone refinement, and/or input from magmatic volatiles.

5.3 Future Research

Extensive drilling has been concentrated in the immediate Lucky Strike area and along the two main "ore" channels of the camp; however, very limited drilling has been attempted outside of these areas. The complex structure and stratigraphy of the camp will continue to hinder exploration and should be the primary focus of new investigations. In particular, new drilling aimed at testing the proposed stratigraphy beyond Lucky Strike would help to constrain the paleoenvironment and the continuity of possible ore-hosting stratigraphic units. A more extensive study of the ore mineralogy and possibly fluid inclusions, would help to clarify the depositional environment and the possible role of boiling and/or direct magmatic contributions to the ore fluids. If a transitional VMS-epithermal environment can be demonstrated, exploration beyond the traditional mining camp should target atypical VMS (e.g., precious metal-rich or additional stockwork-type polymetallic mineralization) and possible shallow submarine epithermal deposits.

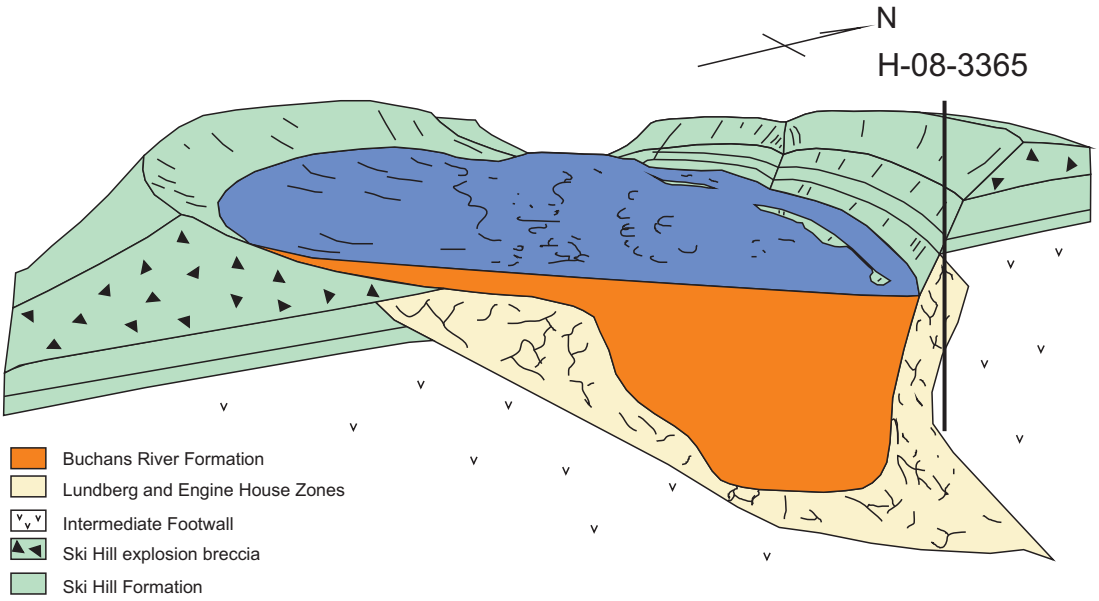

Figure 5.1: Skill Hill Formation Caldera Model representing the local conditions surrounding the Lucky Strike deposit and underlying stockwork zones (Henley and Thornley, 1981). However, this model implies excision of the Ski Hill Formation which is unobserved. Instead, a rhyodacitic tuff of the Buchans River Formation is observed directly beneath the orebody (e.g., Kowalik et al., 1981, Jambor, 1987). Although a local caldera cannot account for the observations at Lucky Strike, Thurlow and Swanson (1987) suggest that a larger scale caldera may exist. The location of drill hole 3365 demonstrates the relative position of the study area in such a model.

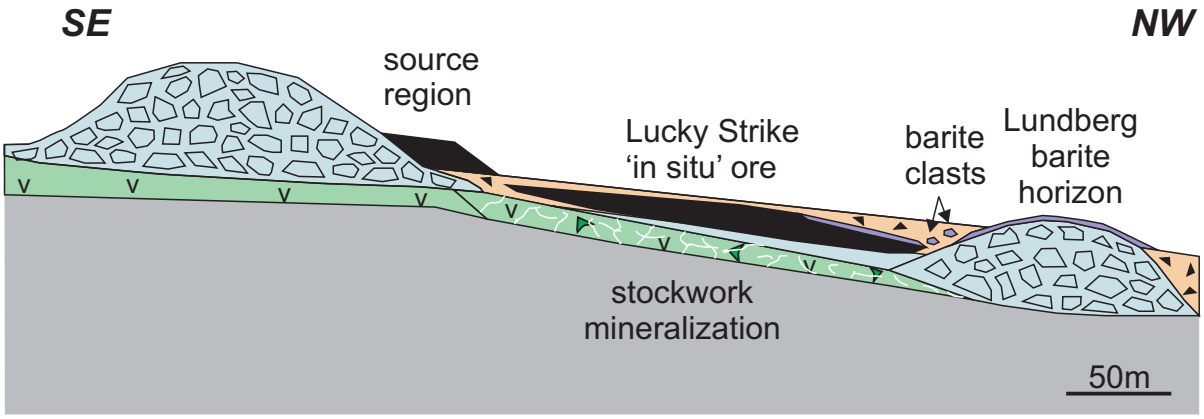

Figure 5.2: Schematic diagram of the depositional environment of the Lundberg and Engine House zones. The entire sequence dips to the northwest; the same direction as the plunge of the Maclean Channel. The Lucky strike massive sulfide deposit is envisaged as forming by limited transport of a sulfide mound. The Lundberg and Engine House stockwork mineralization is most intense directly underneath the Lucky Strike orebody and is interpreted as being in situ. However, the majority of stockwork mineralization lies to the east of the Lucky Strike orebody.

References

Barbour, D.M., Desnoyers, D.W., Graves, R.M., Kieley, J.W., King, B.M., McKenzie, C.B., Poole, J.C., Thurlow, J.G., Balch, S., MacNeil, J., 1990: Assessment report on geological, geochemical, geophysical, trenching and diamond drilling exploration for the Victoria Lake project for 1989 submission for the Anglo-Newfoundland Development Company Limited charter, Reid lots 227-228, 231-233 and 247, fee simple grants volume 1, folios 43, 61 and 110 and volume 2 folios 23 and 29 and for crown lease lots A, B, E, J and N to R in the Buchans, Red Indian Lake, Valentine Lake, Jacks Pond and Daniels Pond areas, central Newfoundland, 5 reports<BR< td>. Newfoundland and Labrador Geological Survey, Assessment File NFLD/1970, 1990, pages 1-1356.

Barrett, T.J., Maclean, W.H., 1994: Mass changes in hydrothermal alteration zones associated with VMS deposits of the Noranda area. Exploration and Mining Geology, v. 3, no. 2, pages 131-160.

Barton, P.B., Jr., Bethke, P.M., 1987: Chalcopyrite disease in sphalerite: Pathology and epidemiology. American Mineralogist, v. 72, pages 451-467.

Binney, W.P., 1987: A sedimentological investigation of the Maclean channel transported sulfide ores. *In* Buchans Geology, Newfoundland, ed. R.V. Kirkham; Geological Survey of Canada, Paper 86-24, pages 107-147, Report 8.

Bouma, A.H., 1962: Sedimentology of some Flysch Deposits: A Graphic Approach to Facies Interpretation. Elsevier, Amsterdam, 168 pages.

Buchanan, L.J., 1981: Precious metal deposits associated with volcanic environments in the southwest. *In* Relations of tectonics to ore deposits in the southern cordillera; Arizona Geological Society Digest, v. 14, pages 237-262.

Cabanis, B., Lecolle, M., 1989: Le diagramme La/10-Y/15-Nb/8; un outil pour la discrimination des series volcaniques et la mise en evidence des processus de melange et/ou de contamination crustale. The La/10-Y/15-Nb/8 diagram; a tool for distinguishing volcanic series and discovering crustal mixing and/or contamination. Comptes Rendus de l'Academie des Sciences, Serie 2, Mecanique, Physique, Chimie, Sciences de l'Univers, Sciences de la Terre, v.309, no.20; pages 2023-2029.

Calhoun, T.A., Hutchinson, R.W., 1981: Determination of flow direction and source of fragmental sulfides, Clementine deposit, Buchans, Newfoundland. *In* The Buchans Orebodies: Fifty Years of Geology and Mining, ed. E.A Swanson, D.F. Strong, and J.G Thurlow; The Geological Association of Canada, Special Paper 22, pages 187-204, technical paper 8.

Calon, T.J., & Green, F.K., 1987: Preliminary results of detailed structural analysis at Buchans. *In* Buchans Geology, Newfoundland, ed. R.V. Kirkham; Geological Survey of Canada, Paper 86-24, pages. 273-288, Report 17.

Compston, W., 2000. Interpretations of SHRIMP and isotope dilution zircon ages for the geological time-scale; I, The Early Ordovician and Late Cambrian. Mineralogical Magazine, v. 64, no. 1, pages 43-57.

Crawford, A.J., Berry, R.F., 1992: Tectonic implications of Late Proterozoic – Early Paleozoic igneous rock associations in western Tasmania. Tectonophysics, v. 214, pages 37-56.

Crerar, D.A., Barnes, H.L., 1976: Ore Solution Geochemistry V. Solubilities of Chalcopyrite and Chalcocite Assemblages in Hydrothermal Solution at 200° to 350°C. Economic Geology, v. 71, pages 772-794.

Davenport, P.H., Honarvar, P., Hogan, A., Kilfoil, G., King, J.P., Liverman, D.G.E., Kerr, A., and Evans, D.T.W., 1996: Digital geosciences atlas of the Buchans-Robert's Arm belt, Newfoundland: Newfoundland Department of Mines and Energy, Geological Survey Lissenberg Open File NFLD/2611, CD-ROM.

Drummond, S.E., Ohmoto, H., 1985: Chemical evolution and mineral deposition in a boiling hydrothermal systems. Economic Geology, v. 80, pages 126-147.

Dunning, G.R. and Chorlton, L.B., 1985: The Annieopsquotch ophiolite belt of Southwest Newfoundland; geology and tectonic significance. Geological Society of America Bulletin, v. 96, no 11, pages 1466-1476.

Gibson, H.L., Morton, R.L. and Hudak, G.J., 1999: Submarine volcanic processes, deposits and environments favorable for the location of volcanic-associated massive sulphide deposits. *In* Volcanic-Associated Massive Sulphide Deposits: Processes and Examples in Modern and Ancient Settings, ed. C.T. Barrie and M.D. Hannington. Reviews in Economic Geology, v. 8, p. 13-51.

Hannington, M.D., Scott, S.D., 1988: Mineralogy and geochemistry of a hydrothermal silica-sulfide-sulfate spire in the caldera of Axial seamount, Juan de Fuca Ridge. Canadian Mineralogist, v. 26, pages 603-625.

Hart, T.R., Gibson, H.L., Lesher, C.M., 2004: Trace element geochemistry and petrogenesis of felsic volcanic rocks associated with volcanogenic massive Cu-Zn-Pb sulfide deposits. Economic Geology, v. 99; pages 1003-1013.

Hauff, P.L., 2001: Alteration mineralogy of Alberta kimberlite: PIMA^{TM} Infrared spectroscopic analysis. EUB Special Report 12.

Haymon, R.M., Kastner, M., 1981: Hot Spring Deposits on the East Pacific Rise at 21°N: preliminary description of mineralogy and genesis. Earth and Planetary Letters, v. 53, pages 363-381.

Henley, R.W., Thornley, P., 1981: Low grade metamorphism and the geothermal environment of massive sulfide ore formation, Buchans, Newfoundland. *In* The Buchans Orebodies: Fifty Years of Geology and Mining, ed. E.A Swanson, D.F. Strong, and J.G

Thurlow; The Geological Association of Canada, Special Paper 22, pages 205-228, technical paper 9.

Herrmann, W., Berry, R.F., 2002: MINSQ – a least squares spreadsheet method for calculating mineral proportions from whole rock major element analyses. Geochemistry: Exploration, Environment, Analysis, v. 2, 361-368.

Herrmann, W., Blake, M., Doyle, M., Huston, D., Kamprad, J., Merry, N., Pontual, S., 2001: Shortwavelength infrared (SWIR) spectral analysis of hydrothermal alteration zones associated with base metal sulfide deposits at Rosebery and Western Tharsis, Tasmania, and Highway-Reward, Queensland. Economic Geology, v. 96, pages 939-955.

Herzig, P.M., Hannington, M.D., 1995: Polymetallic massive sulfides at the modern seafloor: A review. Ore Geology Reviews, v. 10, pages 95-115.

Hocking, M.W.A., Hannington, M.D., Percival, J.B., Stoffers, P., Schwarz-Schampera, U., de Ronde, C.E.J., 2010: Clay alteration of volcaniclastic material in a submarine geothermal system, Bay of Plenty, New Zealand. Journal of Volcanology and Geothermal Research, v. 191, no. 3-4, pages 180-192.

Ishikawa, Y., Sawaguchi, T., Iwaya, S., and Horiuchi, M., 1976: Delineation of prospecting targets for Kuroko deposits based on modes of volcanism of underlying dacite and alteration halos. Mining Geology, v. 26, pages 105–117 (in Japanese with English abs.).

Jambor, J.L., 1987: Geology and origin of orebodies in the Lucky strike area. *In* Buchans Geology, Newfoundland, ed. R.V. Kirkham; Geological Survey of Canada, Paper 86-24, pages 75-106, Report 7.

Jenner, G.A., 2000: Geochemical signatures for volcanic sequences in the Buchans-Robert's Arm belt, Notre Dame Subzone, Dunnage Zone, central Newfoundland:Implications for tectonic setting stratigraphy and metallogeny. Unpublished report for Billiton Exploration Canada, Buchans River Limited and Celtic Minerals.

Jenner, G.A., 2002: Assessment report on geochemical exploration for 2001 submission for fee simple grants volume 1 folios 61-62 and for second year supplementary, fourth year supplementary, fifth year, sixth year supplementary, seventh year and ninth year supplementary assessment for licence 4805 on claim 16398, licence 4823 on claims 16431-16432, licence 4867 on claims 16397, 16400-16401, 16424-16426 and 17688, licence 4868 on claim block 6648, and licences 5576M, 5649M, 5668M, 6003M, 7420M, 8295M, 8312M and 8444M on claims in the Buchans area, central Newfoundland. Newfoundland and Labrador Geological Survey, Assessment File 12A/1008, page 131.

Jones, S., Gemmell, J.B., Davidson, G.J., 2006: Petrographic, geochemical, and fluid inclusion evidence for the origin of siliceous cap rocks above volcanic-hosted massive sulfide deposits at Myra Falls, Vancouver Island, British Columbia, Canada. Economic Geology, v. 101, pages 555-584.

Jones, S., Herrmann, W., Gemmell, J.B., 2005: Short Wavelength infrared spectral characteristics of the HW horizon: Implications for exploration in the Myra Falls volcanic-hosted massive sulfide camp, Vancouver island, British Columbia, Canada. Economic Geology, v. 100, pages 273-294.

Kerrich, R.,Wyman D.A., 1997: Review of developments in trace-element fingerprinting of geodynamic setting and their implications for mineral exploration. Australian Journal of Earth Sciences, v. 44, pages 465-487.

Kirkham, R.V., & Thurlow J.G., 1987: Evaluation of a resurgent caldera and aspects of ore deposition and deformation at Buchans. *In* Buchans Geology, Newfoundland, ed. R.V. Kirkham; Geological Survey of Canada, Paper 86-24, pages 177-194, Report 10.

Kowalik, J., Rye, R., Sawkins, F.J., 1981: Stable isotope study of the Buchans polymetallic sulfide deposits. *In* The Buchans Orebodies: Fifty Years of Geology and Mining, ed. E.A Swanson, D.F. Strong, and J.G Thurlow; The Geological Association of Canada, Special Paper 22, pages 229-254, technical paper 10.

Large, R.R., 1992: Australian volcanic-hosted massive sulfide deposits: features, styles, and genetic models. Economic Geology, v. 87, pages 471-510.

Large, R.R., Gemmell, J.B., Paulick, H., Huston, D.L., 2001a: The alteration box plot: A simple approach to understanding the relationship between alteration mineralogy and lithogeochemistry associated with volcanic-hosted massive sulfide deposits. Economic Geology, v. 96, pages 957-971.

Large. R.R., McPhie, J., Gemmell, J.B., Herrmann, W., Davidson, G.J., 2001b: The spectrum of ore deposit types, volcanic environments, alteration halos, and related exploration vectors in submarine volcanic successions: some examples from Australia. Economic Geology, v. 96, pages 913-938.

Lentz, D.R., 1998: Petrogenetic evolution of felsic volcanic sequences associated with phanerozoic volcanic-hosted massive sulfide systems; the role of extensional geodynamics. Ore Geology Reviews, v. 12; pages 289-327.

Lesher, C.M., Goodwin, A.M., Campbell, I.H., Gorton, M.P., 1986: Trace-element geochemistry of ore-associated and barren, felsic metavolcanic rocks in the Superior Province, Canada. Canadian Journal of Earth Sciences, vol. 23, no 2; pages 222-237.

Lissenberg, C.J., van Staal, C.R., Bedard, J.H. and Zagorevski, A., 2005a: Geochemical constraints on the origin of the Annieopsquotch ophiolite belt, Newfoundland Appalachians. Geological Society of America Bulletin, v. 117, no. 11-12, pages 1413-1426.

Lissenberg, C.J., Zagorevski, A., McNicoll, V.J., van Staal, C.R. and Whalen, J.B., 2005b: Assembly of the Annieopsquotch accretionary tract, Newfoundland Appalachians; age and geodynamic constraints from syn-kinematic intrusions. Journal of Geology, v. 113, no. 5, pages 553-570.

Maclean, w.H., Barrett, T.J., 1993: Lithogeochemical techniques using immobile elements. Journal of Geochemical Exploration, v. 48, pages 109-133.

McPhie, J., Doyle, M., & Allen, R., 1993: Volcanic Textures: A guide to the interpretation of textures in volcanic rocks. ARC Centre of Excellence in Ore Deposits, University of Tasmania.

Newfoundland Department of National Resources, 2010. Mineral exploration statistics: Newfoundland and Labrador Exploration Statistics 1981-2010.

North American Commission on Stratigraphic Nomenclature, 2005, North American Stratigraphic Code; AAPG Bulletin, v. 89, no. 11, pages 1547-1591.

Pearce, J.A., Harris, N.B.W., Tindle, A.G., 1984: Trace element discrimination diagrams for the tectonic interpretation of granitic rocks. Journal of Petrology, v. 25, pages 956-983.

Piercey, S.J., 2007: Volcanogenic massive sulfide (VMS) deposits of the Newfoundland Appalachains: An overview of their setting, classification, grade-tonnage data and unresolved questions. *In* Current Research. Newfoundland and Labrador Department of Natural Resources, Geological Survey, report 07-1, pages 169-178.

Piercey, S.J., Paradis, S., Murphy, D.C., Mortensen, J.K., 2001: Geochemistry and paleotectonic setting of felsic volcanic rocks in the Finlayson Lake volcanic-hosted massive sulfide district, Yukon, Canada. Economic Geology, v. 96, pages 1877-1905.

Ohmoto, H., Skinner, B.J., 1983: The Kuroko and related volcanogenic massive sulfide deposits: Introduction and summary of new findings. *In* The Kuroko and Related Volcanogenic Massive Sulfide Deposits, ed. H. Ohmoto and B.J. Skinner, Economic Geology Monograph 5, pages 1-8.

Rogers, N., 2004: Red Indian Line geochemical database. Geological Survey of Canada Open File 4605.

Rogers, N., van Staal, C.R., McNicoll, V., Pollock, J. and Zagorevski, A.W., J.B., 2006: Neoproterozoic and Cambrian arc magmatism along the eastern margin of the Victoria Lake Supergroup: a remnant of Ganderian basement in central Newfoundland? Precambrian Research, v. 147, no. 3-4, pages 320-341

Rogers, N., van Staal, C.R., McNicoll, V., Theriault, R., 2003: Volcanology and tectonic setting of the Northern Bathurst Mining Camp: Part 1. Extension and rifting of the Popelogan Arc. Economic Geology Monograph 11; pages 157-179.

Shirozu, H., 1974: Clay minerals in altered wall rocks of the Kuroko-type deposits: *In* Geology of the Kuroko Deposits, ed. S. Ishihara, Mining Geology Special Issue No. 6, pages 303-310.

Simmons, S.F., Christenson, B.W., 1994: Origins of calcite in a boiling geothermal system. American Journal of Science, v. 294, pages 361-400.

Smith, I.E.M., Worthingston, T.J., Stewart, R.B., Price, R.C., Gamble, J.A., 2003: Felsic volcanism in the Kermadec Arc, SW Pacific: Crustal recycling in an oceanic setting. *In* Larter, R.D. & Leat, P.T. 2003. Intra-Oceanic Subduction Systems: Tectonic and Magmatic Processes. Geological Society, London, Special Publications 219; pages 99-118.

Strong, D.F., 1984: Rare earth elements in volcanic rocks of the Buchans area, Newfoundland. Can. J. Earth Sci. v. 21, pages 775-780.

Swinden, S.H., 1991: Paleotectonic settings of volcanogenic massive sulfide deposits in the Dunnage Zone, Newfoundland Appalachians. CIM Bulletin, v. 84, no 946, pages 59-69.

Swinden, S.H., Jenner, G.A., Kean, B F, Evans, D.T.W., 1989: Volcanic rock geochemistry as a guide for massive sulfide exploration in central Newfoundland. Report of Activities – Mineral development division, v. 89, no. 1, pages 201-219.

Swinden, H.S., Jenner, G.A. and Szybinski, Z.A., 1997: Magmatic and tectonic evolution of the Cambrian-Ordovician Laurentian margin of Iapetus; geochemical and isotopic constraints from the Notre Dame Subzone, Newfoundland. *In* The Nature of Magmatism in the Appalachian Orogen, ed. A.K. Sinha, J.B. Whalen, and J.P. Hogan; Geological Society of America Memoirs, v. 191, pages 337-365.

Thompson, A.J.B., Hauff, P.L., Robitaille, J.A., 1999: Alteration mapping in exploration; application of short-wave-infrared (SWIR) spectroscopy. SEG Newsletter, v. 39, no. 1, pages 16-27.

Thurlow, J.G., 1981: The Buchans Group: Its stratigraphic and structural setting. *In* The Buchans Orebodies: Fifty Years of Geology and Mining, ed. E.A Swanson, D.F. Strong, and J.G Thurlow; The Geological Association of Canada, Special Paper 22, pages 79-90, technical paper 2.

Thurlow, J.G., Spencer, C.P., Boerner, D.E., Reed, L.E., Wright, J.A., 1992: Geological interpretation of a high resolution reflections seismic survey at the Buchans mine, Newfoundland. Can. J. Earth Sci. v. 29, pages 2022-2037.

Thurlow, J. G., & Swanson, E.A., 1981: Geology and Ore Deposits of the Buchans Area, Central Newfoundland. *In* The Buchans Orebodies: Fifty Years of Geology and Mining, ed. E.A Swanson, D.F. Strong, and J.G Thurlow; The Geological Association of Canada, Special Paper 22, pages 113-142, technical paper 5.

Thurlow, J. G., & Swanson, E.A., 1987: Stratigraphy and structure of the Buchans Group. *In* Buchans Geology, Newfoundland, ed. R.V. Kirkham; Geological Survey of Canada, Paper 86-24, pages 35-46, Report 2.

Thurlow, J.G., Swanson, E.A., Strong, D.F., 1975: Geology and lithogeochemistry of the Buchans polymetallic sulfide deposits, Newfoundland. Economic Geology, v. 70, pages 130-144.

Urabe, T., Scott, S.D., Hattori, K., 1983: A comparison of footwall-rock alteration and geothermal systems beneath some Japanese and Canadian volcanogenic massive sulfide deposits. *In* The Kuroko and Related Volcanogenic Massive Sulfide Deposits, ed. H. Ohmoto and B.J. Skinner, Economic Geology Monograph 5, pages 345-364.

van Staal, C.R., Dewey, J.F., Mac Niocaill, C. and McKerrow, W.S., 1998: The Cambrian-Silurian tectonic evolution of the Northern Appalachians and British Caledonides; history of a complex, west and southwest Pacific-type segment of Iapetus. *In* The Past is the Key to the Present, ed. D.J. Blundell and A.C. Scott; Special Publication. Geological Society, London, Special Publications, pages 199-242.

van Staal, C.R., Whalen, J.B., McNicoll, V.J., Pehrsson, S., Lissenberg, C.J., Zagorevski, A., van Breemen, O., Jenner, G.A., 2007: The Notre Dame Arc and the Taconic Orogeny in Newfoundland. *In* 4-D Framework of Continental Crust, ed. R.D. Hatcher, Jr., M.P. Carlson, J.H. McBride and J.R. Martinez Catalan, pages. 511-552.

Waldron, J.W.F. and van Staal, C.R., 2001: Taconian Orogeny and the accretion of the Dashwoods Block; a peri-Laurentian microcontinent in the Iapetus Ocean. Geology (Boulder), v. 29, no. 9, pages 811-814.

Webster, P.C., & Barr, J.F., 2008: Technical Report on the Mineral Estimate for the Lundberg and Engine House Deposits Buchans Area Newfoundland, Canada. Mercator Geological Services Limited.

Whalen, J.B., Jenner, G.A., Longstaffe, F.J., Gariepy, C. and Fryer, B.J., 1997: Implications of granitoid geochemical and isotopic (Nd, O, Pb) data from the Cambrian-Ordovician Notre Dame Arc for the evolution of the Central Mobile Belt, Newfoundland Appalachians. *In* The Nature of Magmatism in the Appalachian Orogen, ed. A.K. Sinha, J.B. Whalen, and J.P. Hogan; Geological Society of America Memoirs, v. 191, pages 367-395.

Whitford D.J., Korsch, M.J., Porrit, P.J., Craven, S.J., 1988: Rare-earth element mobility around the volcanogenic polymetallic massive sulfide deposit at Que River, Tasmania, Australia. Chemical Geology, v. 68, pages 105-119.

Williams, H., 1988: Tectonic-stratigraphic subdivisions of central Newfoundland. Paper - Geological Survey of Canada, v. 88-1B, pages 91-98.

Winchester J.A., Floyd, P.A., 1977: Geochemical discrimination of different magma series and their differentiation products using immobile elements. Chemical Geology, v. 20, pages 325-343.

Winter, J.D., 2001: An Introduction to Igneous and Metamorphic Petrology. Pentice-Hall Inc., Upper Saddle New Jesey; pages 293-361.

Zagorevski, A., 2008: Preliminary geochemical database of the Buchans-Robert's Arm Belt, central Newfoundland: Geological Survey of Canada Open File 5986, 1 CD-ROM.

Zagorevski, A., Lissenberg, C.J., van Staal, C.R., 2009: Dynamics of accretion of arc and backarc crust to continental margins: Inferences from the Annieopsquotch accretionary tract, Newfoundland Appalachians. Tectonophysics, v. 479, no 1-2, pages 150-164.

Zagorevski, A., McNicoll, V. and van Staal, C.R., 2007a: Distinct Taconic, Salinic and Acadian deformation along the Iapetus suture zone, Newfoundland Appalachians. Canadian Journal of Earth Sciences, v. 44, pages 1567-1585.

Zagorevski, A., McNicoll, V.J., van Staal, C.R. and Rogers, N., 2007b: Tectonic history of the Buchans Group: evidence for late Taconic accretion of a peri-Laurentian arc terrane and its reimbrication during the Salinic orogeny. Geological Society of America Abstracts with Programs, v. 39, no. 1, page 51.

Zagorevski, A., Rogers, N., 2008: Stratigraphy and structural geology of the Ordovician volcano-sedimentary rocks in the Mary March Brook Area. *In* Current Research. Newfoundland and Labrador Department of Natural Resources, Geological Survey, Report 08-1, pages 101-113.

Zagorevski, A., Rogers, N., 2009: Geochemical Characteristic of the Ordovician Volcano-sedimentary Rocks in the Mary March Brook Area. *In* Current Research. Newfoundland and Labrador Department of Natural Resources, Geological Survey, Report 09-1, pages 271-288.

Zagorevski, A., Rogers, N., Haslam, R., 2010: Geology and significance of the Harry's River mafic volcanic rocks, Buchans area, Newfoundland. *In* Current Research. Newfoundland and Labrador Department of Natural Resources, Geological Survey, Report 10-1, pages 1-12.

Zagorevski, A., Rogers, N., van Staal, C.R., McNicoll, V., Lissenberg, C.J., Valverde-Vaquero, P., 2006: Lower to Middle Ordovician evolution of peri-Laurentian arc and backarc complexes in Iapetus: Constraints from the Annieopsquotch accretionary tract, central Newfoundland. Geological Society of America Bulletin, v. 118; no. 3/4; pages 324-342.

Zagorevski, A., van Staal, C.R., McNicoll, V., Rogers, N. and Valverde-Vaquero, P., 2008: Tectonic architecture of an arc-arc collision zone, Newfoundland Appalachians. *In* Formation and Applications of the Sedimentary Record in Arc Collision Zones, ed. A. Draut, P.D. Clift and D.W. Scholl; Geological Society of America Special Publications, v. 436, pages 309-334.

Appendix 3.1: Whole-rock lithogeochemistry

Analyte Symbol	Unit Symbol	Detection Limit	Analysis Method	RAX08G002	RAX08G008	RAX08G010	RAX08G011	RAX08G013	RAX08G019	RAX08G022	RAX08G024
SiO2	%	0.01	FUS-ICP-ES	74.47	69.67	50.63	54.53	70.3	57.34	51.49	72.85
Al2O3	%	0.01	FUS-ICP-ES	13.22	9.07	12.08	13.38	14.48	10.55	15.03	12.69
Fe2O3(T)	%	0.01	FUS-ICP-ES	2.39	8.66	11.67	11.01	2.83	11.56	11.39	1.89
MnO	%	0.001	FUS-ICP-ES	0.078	0.011	0.533	0.551	0.078	0.396	0.964	0.106
MgO	%	0.01	FUS-ICP-ES	0.7	0.52	9.18	9.37	1.88	9.75	12.04	4.11
CaO	%	0.01	FUS-ICP-ES	2.78	0.23	1.82	0.84	0.65	0.2	0.18	0.13
Na2O	%	0.01	FUS-ICP-ES	2.96	0.16	1.63	2.34	3.59	0.09	0.12	0.01
K2O	%	0.01	FUS-ICP-ES	2.19	2.55	0.08	0.06	2.31	0.65	1.05	2.62
TiO2	%	0.001	FUS-ICP-ES	0.178	0.362	0.466	0.517	0.195	0.409	0.485	0.203
P2O5	%	0.01	FUS-ICP-ES	0.05	0.13	0.09	0.09	0.04	0.07	0.09	0.05
LOI	%		FUS-ICP-ES	1.53	5.75	7.26	6.35	2.19	7.46	6.6	3.69
Total	%	0.01	FUS-ICP-ES	100.5	97.13	95.45	99.04	98.54	98.47	99.45	98.33
Sc	ppm	1	FUS-ICP-ES	4	14	30	30	4	23	31	5
Be	ppm	1	FUS-ICP-ES	2	< 1	< 1	< 1	2	1	1	1
V	ppm	5	FUS-ICP-ES	9	74	254	252	7	219	253	13
Cr	ppm	20	FUS-MS	80	100	80	70	< 20	60	190	90
Co	ppm	1	FUS-MS	5	13	23	20	< 1	21	29	2
Ni	ppm	20	FUS-MS	30	50	< 20	< 20	< 20	< 20	70	< 20
Cu	ppm	10	FUS-MS	20	6380	70	10	< 10	110	60	10
Zn	ppm	30	FUS-MS	30	< 30	500	330	< 30	580	680	80
Ga	ppm	1	FUS-MS	12	10	13	14	11	13	15	12
Ge	ppm	0.5	FUS-MS	1.5	0.7	< 0.5	0.5	0.8	< 0.5	0.8	< 0.5
As	ppm	5	FUS-MS	5	77	< 5	< 5	6	8	< 5	< 5
Rb	ppm	1	FUS-MS	52	53	1	< 1	69	14	23	40
Sr	ppm	2	FUS-ICP	565	14	22	33	154	9	11	52
Y	ppm	0.5	FUS-MS	17	15.9	14.3	11.3	16.1	8.7	13.3	16.4
Zr	ppm	1	FUS-MS	102	44	45	41	109	30	29	126
Nb	ppm	0.2	FUS-MS	4.7	1.6	1.2	1.2	4.7	1.1	1.1	4.5
Mo	ppm	2	FUS-MS	< 2	9	8	4	< 2	24	< 2	5
Ag	ppm	0.5	FUS-MS	5.6	21.5	< 0.5	< 0.5	< 0.5	1.4	< 0.5	0.5
In	ppm	0.1	FUS-MS	< 0.1	1.8	0.2	0.1	< 0.1	0.2	0.3	< 0.1
Sn	ppm	1	FUS-MS	< 1	< 1	< 1	< 1	< 1	< 1	< 1	< 1
Sb	ppm	0.2	FUS-MS	< 0.2	14	0.9	1.9	< 0.2	0.7	< 0.2	< 0.2
Cs	ppm	0.1	FUS-MS	0.8	1.5	0.3	0.3	1	0.4	0.8	0.9
Ba	ppm	3	FUS-ICP	1118	1162	49	107	708	254	434	6069
La	ppm	0.05	FUS-MS	31.7	11.1	7.99	8.81	29.4	3.58	8.53	29.2
Ce	ppm	0.05	FUS-MS	55.7	24	15.8	18	54.5	7.38	17.3	51.5
Pr	ppm	0.01	FUS-MS	6.17	2.52	1.64	1.83	6.16	0.78	2.27	5.71
Nd	ppm	0.05	FUS-MS	17.7	10.6	7.08	7.4	17.7	3.61	8.43	16.5
Sm	ppm	0.01	FUS-MS	3.19	2.7	1.83	1.79	3.13	1.02	1.91	2.93
Eu	ppm	0.005	FUS-MS	0.742	0.474	0.39	0.358	0.696	0.194	0.275	0.487
Gd	ppm	0.01	FUS-MS	2.6	2.69	2.14	1.93	2.53	1.23	1.99	2.35
Tb	ppm	0.01	FUS-MS	0.45	0.4	0.34	0.3	0.44	0.21	0.38	0.43
Dy	ppm	0.01	FUS-MS	2.89	2.55	2.13	1.86	2.8	1.36	2.44	2.79
Ho	ppm	0.01	FUS-MS	0.61	0.56	0.47	0.41	0.59	0.31	0.5	0.6
Er	ppm	0.01	FUS-MS	1.87	1.77	1.45	1.3	1.79	0.98	1.48	1.82
Tm	ppm	0.005	FUS-MS	0.292	0.269	0.218	0.199	0.279	0.147	0.216	0.285
Yb	ppm	0.01	FUS-MS	2.05	1.73	1.36	1.26	1.9	0.94	1.36	2.04
Lu	ppm	0.002	FUS-MS	0.332	0.263	0.195	0.185	0.308	0.142	0.198	0.346
Hf	ppm	0.1	FUS-MS	3.1	1.6	1.4	1.3	3.3	0.9	1	3.7
Ta	ppm	0.01	FUS-MS	0.41	0.08	0.06	0.06	0.43	0.05	0.03	0.38
W	ppm	0.5	FUS-MS	< 0.5	3.4	2.2	2.9	< 0.5	3.1	1.4	< 0.5
Tl	ppm	0.05	FUS-MS	0.26	0.11	< 0.05	< 0.05	0.25	0.14	0.22	0.45
Pb	ppm	5	FUS-MS	16	5	30	14	< 5	436	23	6
Bi	ppm	0.1	FUS-MS	16	92.1	6.2	1.3	< 0.1	32.9	194	4.3
Th	ppm	0.05	FUS-MS	11.5	3	2.04	2.37	12.1	1.3	2.22	10.8
U	ppm	0.01	FUS-MS	3.28	1.48	0.84	0.73	2.73	0.73	0.67	3.49

Appendix 3.1: Whole-rock lithogeochemistry

Analyte Symbol	Unit Symbol	Detection Limit	Analysis Method	RAX08G025	RAX08G027	RAX08G029	RAX08G030	RAX08G031	RAX08G036	RAX08G039	RAX08G040
SiO2	%	0.01	FUS-ICP-ES	69.19	72.47	80.21	72.87	55.96	67.25	61.1	78.1
Al2O3	%	0.01	FUS-ICP-ES	14.13	13.35	11.02	11.08	19.45	14.16	18.3	11.36
Fe2O3(T)	%	0.01	FUS-ICP-ES	3.3	1.88	1.4	1.6	3.46	3.98	4.12	2.12
MnO	%	0.001	FUS-ICP-ES	0.071	0.057	0.022	0.051	0.082	0.143	0.058	0.015
MgO	%	0.01	FUS-ICP-ES	1.84	1.41	0.4	0.6	2.26	4.69	3.49	0.71
CaO	%	0.01	FUS-ICP-ES	1.61	2.64	1.05	2.79	3.18	0.5	2.11	0.23
Na2O	%	0.01	FUS-ICP-ES	0.93	2.6	0.14	2.55	0.53	0.67	1.37	1.54
K2O	%	0.01	FUS-ICP-ES	4.56	2.11	2.15	2.2	5.93	2.58	3.24	2.61
TiO2	%	0.001	FUS-ICP-ES	0.202	0.185	0.166	0.287	0.563	0.562	0.495	0.305
P2O5	%	0.01	FUS-ICP-ES	0.04	0.04	0.05	0.06	0.14	0.2	0.13	0.06
LOI	%		FUS-ICP-ES	3.78	3.69	3.96	3.84	6.88	4.22	5	2.56
Total	%	0.01	FUS-ICP-ES	99.65	100.4	100.6	97.93	98.43	98.96	99.41	99.61
Sc	ppm	1	FUS-ICP-ES	5	4	4	7	15	17	13	9
Be	ppm	1	FUS-ICP-ES	2	2	< 1	< 1	2	1	2	1
V	ppm	5	FUS-ICP-ES	7	5	< 5	10	60	22	45	15
Cr	ppm	20	FUS-MS	50	< 20	130	< 20	40	40	< 20	70
Co	ppm	1	FUS-MS	< 1	1	< 1	1	4	7	5	2
Ni	ppm	20	FUS-MS	< 20	< 20	< 20	< 20	< 20	< 20	< 20	< 20
Cu	ppm	10	FUS-MS	10	10	< 10	< 10	10	10	< 10	80
Zn	ppm	30	FUS-MS	30	230	40	210	250	250	1380	1280
Ga	ppm	1	FUS-MS	11	11	12	8	19	15	18	12
Ge	ppm	0.5	FUS-MS	1.1	1.3	2.6	1	1	0.6	0.8	0.7
As	ppm	5	FUS-MS	< 5	7	28	98	< 5	9	< 5	35
Rb	ppm	1	FUS-MS	134	50	44	40	118	51	68	60
Sr	ppm	2	FUS-ICP	134	244	51	96	57	22	158	41
Y	ppm	0.5	FUS-MS	17.4	14.7	14.9	33.2	39.5	29	40.9	32.8
Zr	ppm	1	FUS-MS	112	110	93	156	211	99	206	135
Nb	ppm	0.2	FUS-MS	5	4.4	3.9	3.9	6.2	3.1	6	3.7
Mo	ppm	2	FUS-MS	< 2	< 2	2	< 2	< 2	7	< 2	14
Ag	ppm	0.5	FUS-MS	< 0.5	< 0.5	< 0.5	0.9	< 0.5	3.8	< 0.5	1.7
In	ppm	0.1	FUS-MS	< 0.1	< 0.1	< 0.1	< 0.1	< 0.1	< 0.1	< 0.1	< 0.1
Sn	ppm	1	FUS-MS	< 1	< 1	1	< 1	1	< 1	2	1
Sb	ppm	0.2	FUS-MS	< 0.2	< 0.2	5.9	6.9	< 0.2	< 0.2	< 0.2	< 0.2
Cs	ppm	0.1	FUS-MS	2.2	1.2	0.5	0.9	3.6	1.5	3	1.1
Ba	ppm	3	FUS-ICP	1874	779	449	817	1072	582	2322	916
La	ppm	0.05	FUS-MS	32.3	32.8	23.4	27.6	41.9	32.8	46.8	22.3
Ce	ppm	0.05	FUS-MS	57.3	56.5	40	55.5	87.4	62.3	90.3	46.7
Pr	ppm	0.01	FUS-MS	6.36	6.23	3.75	6.73	11.3	7.87	11.5	5.98
Nd	ppm	0.05	FUS-MS	18.7	18	11.2	23.4	39.5	26.8	37.9	20.3
Sm	ppm	0.01	FUS-MS	3.36	3.15	2.05	5.1	8.3	5.73	7.81	4.44
Eu	ppm	0.005	FUS-MS	0.774	0.921	0.396	1.5	1.95	0.974	1.76	1.03
Gd	ppm	0.01	FUS-MS	2.74	2.55	1.73	4.81	7.47	5.09	7.07	4.23
Tb	ppm	0.01	FUS-MS	0.48	0.43	0.31	0.82	1.28	0.92	1.25	0.82
Dy	ppm	0.01	FUS-MS	3.1	2.73	2.06	5.32	7.71	5.51	7.51	5.73
Ho	ppm	0.01	FUS-MS	0.67	0.56	0.48	1.15	1.51	1.12	1.54	1.26
Er	ppm	0.01	FUS-MS	2.01	1.67	1.65	3.63	4.45	3.39	4.62	3.94
Tm	ppm	0.005	FUS-MS	0.32	0.255	0.276	0.566	0.658	0.515	0.69	0.597
Yb	ppm	0.01	FUS-MS	2.21	1.79	1.93	3.71	4.17	3.33	4.57	3.83
Lu	ppm	0.002	FUS-MS	0.358	0.287	0.312	0.555	0.643	0.523	0.721	0.573
Hf	ppm	0.1	FUS-MS	3.6	3.4	2.5	4	6.1	3.1	6	4
Ta	ppm	0.01	FUS-MS	0.45	0.41	0.41	0.26	0.45	0.16	0.46	0.25
W	ppm	0.5	FUS-MS	< 0.5	< 0.5	0.8	< 0.5	< 0.5	0.7	< 0.5	< 0.5
Tl	ppm	0.05	FUS-MS	0.5	0.85	1.85	1.48	1.36	0.44	1.02	1.77
Pb	ppm	5	FUS-MS	7	74	10	37	7	64	24	155
Bi	ppm	0.1	FUS-MS	8.1	17	0.1	0.4	20.5	19.3	25.8	12.4
Th	ppm	0.05	FUS-MS	12.7	11.6	10	6.93	11.3	8.4	11.8	6.74
U	ppm	0.01	FUS-MS	3.37	3.9	2.36	2.38	4.01	2.67	1.45	4.02

Appendix 3.1: Whole-rock lithogeochemistry

Analyte Symbol	Unit Symbol	Detection Limit	Analysis Method	RAX08G044	RAX08G045	RAX08G050	RAX08G051	RAX08G060	RAX08G061	RAX08G062	RAX08G063
SiO2	%	0.01	FUS-ICP-ES	55.65	67.67	57.53	58.75	63.35	45.59	63.1	60.73
Al2O3	%	0.01	FUS-ICP-ES	14.34	9.98	14.28	13.15	16.86	15.62	14.12	10.82
Fe2O3(T)	%	0.01	FUS-ICP-ES	9.26	9.82	10.21	10.07	3.34	11.53	3.57	10.66
MnO	%	0.001	FUS-ICP-ES	0.581	0.079	0.398	0.446	0.069	0.173	0.122	0.357
MgO	%	0.01	FUS-ICP-ES	10.52	2.07	9.06	7	2.73	8.14	7.67	9.1
CaO	%	0.01	FUS-ICP-ES	0.43	0.27	0.42	0.37	1.13	9.23	0.16	0.31
Na2O	%	0.01	FUS-ICP-ES	0.06	0.06	0.01	< 0.01	1.59	1.91	0.12	< 0.01
K2O	%	0.01	FUS-ICP-ES	1.27	2.38	1.68	1.87	3.5	1.1	2.27	0.88
TiO2	%	0.001	FUS-ICP-ES	0.528	0.68	0.548	0.9	0.233	0.914	0.234	0.694
P2O5	%	0.01	FUS-ICP-ES	0.1	0.17	0.08	0.17	0.05	0.24	0.04	0.25
LOI	%		FUS-ICP-ES	6.26	6.41	6.28	6.04	4.29	3.39	5.65	6.46
Total	%	0.01	FUS-ICP-ES	98.99	99.58	100.5	98.77	97.14	97.83	97.06	100.2
Sc	ppm	1	FUS-ICP-ES	31	21	30	27	4	38	6	19
Be	ppm	1	FUS-ICP-ES	1	1	2	2	1	1	1	1
V	ppm	5	FUS-ICP-ES	265	236	290	290	7	338	46	156
Cr	ppm	20	FUS-MS	240	30	< 20	40	< 20	250	< 20	70
Co	ppm	1	FUS-MS	24	19	21	22	2	41	5	19
Ni	ppm	20	FUS-MS	60	20	20	< 20	< 20	120	< 20	< 20
Cu	ppm	10	FUS-MS	10	160	10	140	< 10	150	< 10	30
Zn	ppm	30	FUS-MS	250	860	310	770	30	< 30	150	390
Ga	ppm	1	FUS-MS	14	14	17	17	14	13	16	15
Ge	ppm	0.5	FUS-MS	0.6	0.5	0.8	0.6	0.7	1.2	< 0.5	0.8
As	ppm	5	FUS-MS	22	104	39	39	< 5	11	< 5	25
Rb	ppm	1	FUS-MS	30	53	37	47	87	19	41	22
Sr	ppm	2	FUS-ICP	10	9	13	11	214	280	18	16
Y	ppm	0.5	FUS-MS	13.4	16.6	15.3	25.7	16	19.9	18.4	23.4
Zr	ppm	1	FUS-MS	42	60	40	85	163	49	138	87
Nb	ppm	0.2	FUS-MS	1.4	1.9	1.4	3.2	5.7	2.6	4.9	2.8
Mo	ppm	2	FUS-MS	3	25	10	8	< 2	< 2	7	27
Ag	ppm	0.5	FUS-MS	< 0.5	1.4	< 0.5	< 0.5	< 0.5	< 0.5	< 0.5	< 0.5
In	ppm	0.1	FUS-MS	0.1	0.3	0.2	< 0.1	< 0.1	< 0.1	0.3	0.2
Sn	ppm	1	FUS-MS	< 1	< 1	< 1	< 1	14	< 1	40	< 1
Sb	ppm	0.2	FUS-MS	< 0.2	1.8	1.1	1.6	0.9	1.4	3.6	1.1
Cs	ppm	0.1	FUS-MS	0.9	1	1.1	0.9	2.3	0.5	1.1	0.4
Ba	ppm	3	FUS-ICP	409	1138	473	521	1530	847	1015	683
La	ppm	0.05	FUS-MS	9.74	9.82	5.06	19.2	30.1	15.9	33.5	11.9
Ce	ppm	0.05	FUS-MS	19.9	20.9	10.7	39.8	58.4	34.5	59.9	27.6
Pr	ppm	0.01	FUS-MS	2.45	2.63	1.5	5.15	5.11	3.71	5.49	3.47
Nd	ppm	0.05	FUS-MS	8.84	10	6.19	18	16.2	15.5	16.5	13.1
Sm	ppm	0.01	FUS-MS	2	2.38	1.55	3.92	3.26	3.96	3.07	3.09
Eu	ppm	0.005	FUS-MS	0.331	0.383	0.281	0.545	0.62	1.15	0.462	0.442
Gd	ppm	0.01	FUS-MS	1.97	2.66	1.98	3.96	2.63	3.94	2.14	3.23
Tb	ppm	0.01	FUS-MS	0.37	0.46	0.39	0.73	0.43	0.59	0.41	0.63
Dy	ppm	0.01	FUS-MS	2.39	2.92	2.63	4.67	2.72	3.49	2.68	4.26
Ho	ppm	0.01	FUS-MS	0.49	0.65	0.55	0.96	0.6	0.73	0.61	0.93
Er	ppm	0.01	FUS-MS	1.43	2.11	1.62	2.82	1.98	2.23	2.02	2.85
Tm	ppm	0.005	FUS-MS	0.203	0.324	0.237	0.409	0.316	0.329	0.332	0.436
Yb	ppm	0.01	FUS-MS	1.29	2.03	1.51	2.58	2.17	2.04	2.31	2.81
Lu	ppm	0.002	FUS-MS	0.206	0.294	0.225	0.384	0.36	0.305	0.382	0.433
Hf	ppm	0.1	FUS-MS	1.3	1.6	1.3	2.6	5.1	1.5	4.3	2.6
Ta	ppm	0.01	FUS-MS	0.05	0.09	0.06	0.13	0.5	0.15	0.44	0.15
W	ppm	0.5	FUS-MS	0.5	4.4	2.6	7.2	0.7	0.6	2	4.1
Tl	ppm	0.05	FUS-MS	0.22	1.26	0.26	0.16	0.72	0.1	0.97	0.19
Pb	ppm	5	FUS-MS	17	1340	60	72	6	< 5	< 5	66
Bi	ppm	0.1	FUS-MS	66.5	18.7	239	19.1	15.5	< 0.1	4.2	200
Th	ppm	0.05	FUS-MS	2.36	3.48	1.91	5.03	14.5	2.83	11	5.14
U	ppm	0.01	FUS-MS	0.72	1.63	0.8	1.97	2.3	0.92	5.29	2.01

Appendix 3.1: Whole-rock lithogeochemistry

Analyte Symbol	Unit Symbol	Detection Limit	Analysis Method	RAX08G064	RAX08G065	RAX08G070	RAX08G073	RAX08G075	RAX08G077	RAX08G080	RAX08G083
SiO2	%	0.01	FUS-ICP-ES	56.35	68.23	80.34	57.9	53.72	76.6	90	76.67
Al2O3	%	0.01	FUS-ICP-ES	11.41	14.08	11.01	14.15	11.6	10.5	3.51	12.35
Fe2O3(T)	%	0.01	FUS-ICP-ES	10.43	3.37	0.77	9.5	10.34	1.29	1.93	2.52
MnO	%	0.001	FUS-ICP-ES	0.796	0.076	0.017	0.399	1.053	0.066	0.008	0.015
MgO	%	0.01	FUS-ICP-ES	12.77	1.3	0.48	7.71	14.48	0.23	0.11	0.84
CaO	%	0.01	FUS-ICP-ES	0.37	2.47	0.44	0.23	0.3	2.77	0.15	0.22
Na2O	%	0.01	FUS-ICP-ES	0.06	1.1	0.12	< 0.01	< 0.01	2.6	0.18	0.13
K2O	%	0.01	FUS-ICP-ES	0.02	4.13	3.29	2.13	0.04	1.79	0.95	3.55
TiO2	%	0.001	FUS-ICP-ES	0.398	0.195	0.287	0.685	0.398	0.143	0.07	0.456
P2O5	%	0.01	FUS-ICP-ES	0.08	0.05	0.06	0.12	0.06	0.04	< 0.01	0.1
LOI	%		FUS-ICP-ES	6.69	4.73	2.72	5.97	7.34	3.51	1.62	3.66
Total	%	0.01	FUS-ICP-ES	99.37	99.74	99.53	98.78	99.31	99.54	98.53	100.5
Sc	ppm	1	FUS-ICP-ES	32	5	6	27	33	3	1	20
Be	ppm	1	FUS-ICP-ES	1	2	< 1	2	1	< 1	< 1	2
V	ppm	5	FUS-ICP-ES	242	12	< 5	305	244	6	< 5	229
Cr	ppm	20	FUS-MS	< 20	< 20	80	30	520	130	140	< 20
Co	ppm	1	FUS-MS	3	< 1	< 1	45	33	< 1	< 1	14
Ni	ppm	20	FUS-MS	< 20	< 20	< 20	30	130	< 20	< 20	< 20
Cu	ppm	10	FUS-MS	< 10	< 10	10	10	260	< 10	580	10
Zn	ppm	30	FUS-MS	110	40	260	230	560	< 30	290	< 30
Ga	ppm	1	FUS-MS	14	12	11	16	13	8	4	12
Ge	ppm	0.5	FUS-MS	< 0.5	1.6	1.2	0.6	0.6	1.4	< 0.5	0.5
As	ppm	5	FUS-MS	9	< 5	27	70	10	7	18	116
Rb	ppm	1	FUS-MS	37	127	64	49	< 1	27	16	72
Sr	ppm	2	FUS-ICP	8	97	91	14	7	78	67	20
Y	ppm	0.5	FUS-MS	17.1	17.3	27.4	16.5	10.9	14.6	1.6	8.8
Zr	ppm	1	FUS-MS	135	116	145	50	26	75	36	31
Nb	ppm	0.2	FUS-MS	4.6	4.5	3.7	1.7	1	3.7	1.3	0.7
Mo	ppm	2	FUS-MS	6	< 2	2	4	2	3	15	3
Ag	ppm	0.5	FUS-MS	< 0.5	< 0.5	33.3	0.6	< 0.5	< 0.5	< 0.5	< 0.5
In	ppm	0.1	FUS-MS	0.2	< 0.1	< 0.1	0.2	0.3	< 0.1	< 0.1	< 0.1
Sn	ppm	1	FUS-MS	< 1	< 1	1	< 1	< 1	< 1	< 1	< 1
Sb	ppm	0.2	FUS-MS	2.1	4.3	13.3	1.3	0.9	1	3.2	3.3
Cs	ppm	0.1	FUS-MS	1	2.4	1.4	0.9	0.3	0.8	0.2	1.4
Ba	ppm	3	FUS-ICP	92	1276	5704	1091	29	721	5907	1907
La	ppm	0.05	FUS-MS	30.4	36	21.4	11.8	8.97	19.9	3.07	5.47
Ce	ppm	0.05	FUS-MS	54.4	62.8	45.5	24.7	17.9	36.8	6.2	10.9
Pr	ppm	0.01	FUS-MS	4.63	5.37	4.64	3.3	2.3	3.58	0.68	1.27
Nd	ppm	0.05	FUS-MS	14.7	17.1	18.1	11.9	7.91	11.9	2.37	5.32
Sm	ppm	0.01	FUS-MS	2.88	3.35	4.42	2.67	1.7	2.28	0.51	1.32
Eu	ppm	0.005	FUS-MS	0.474	0.818	1.11	0.316	0.22	0.605	0.122	0.306
Gd	ppm	0.01	FUS-MS	2.39	2.72	4.12	2.52	1.69	2.11	0.46	1.54
Tb	ppm	0.01	FUS-MS	0.39	0.44	0.66	0.48	0.32	0.35	0.07	0.25
Dy	ppm	0.01	FUS-MS	2.46	2.69	4.25	3.08	2.02	2.19	0.33	1.54
Ho	ppm	0.01	FUS-MS	0.55	0.6	0.96	0.62	0.42	0.48	0.06	0.32
Er	ppm	0.01	FUS-MS	1.97	2.01	3.21	1.85	1.18	1.6	0.17	1.03
Tm	ppm	0.005	FUS-MS	0.327	0.32	0.506	0.275	0.167	0.258	0.03	0.164
Yb	ppm	0.01	FUS-MS	2.29	2.21	3.32	1.75	1.02	1.76	0.2	1.06
Lu	ppm	0.002	FUS-MS	0.375	0.352	0.506	0.256	0.146	0.27	0.031	0.158
Hf	ppm	0.1	FUS-MS	4.1	3.7	4.1	1.6	0.8	2.1	1	0.9
Ta	ppm	0.01	FUS-MS	0.4	0.44	0.29	0.08	0.03	0.31	0.17	0.08
W	ppm	0.5	FUS-MS	0.8	0.9	2.7	8.4	2.2	< 0.5	1.1	2.4
Tl	ppm	0.05	FUS-MS	0.78	0.86	2.24	0.29	0.13	0.65	1.38	1.52
Pb	ppm	5	FUS-MS	< 5	14	140	22	26	14	38	14
Bi	ppm	0.1	FUS-MS	94.2	0.4	3.2	109	136	0.5	16.9	2.7
Th	ppm	0.05	FUS-MS	11.9	12.3	6.89	3.22	1.77	8.71	3.27	2.02
U	ppm	0.01	FUS-MS	5.63	3.17	2.32	1.26	0.56	2.15	2.83	1.35

Appendix 3.1: Whole-rock lithogeochemistry

Analyte Symbol	Unit Symbol	Detection Limit	Analysis Method	RAX08G085	RAX08G086	RAX08G089	RAX08G092	RAX08G097	RAX08G101	RAX08G110	RAX08G112
SiO2	%	0.01	FUS-ICP-ES	51.12	71.42	50.96	59.14	54.98	39.9	60.06	73.67
Al2O3	%	0.01	FUS-ICP-ES	14.23	13.3	13.73	12.95	16.17	15.54	12.42	11.76
Fe2O3(T)	%	0.01	FUS-ICP-ES	9.58	2.05	10.45	9.24	8.66	11.82	8.42	3.46
MnO	%	0.001	FUS-ICP-ES	0.58	0.057	0.995	0.474	0.447	0.204	0.327	0.137
MgO	%	0.01	FUS-ICP-ES	15.05	1.31	14.57	8.7	9.6	8.3	8.94	3.11
CaO	%	0.01	FUS-ICP-ES	0.45	1.44	0.28	0.39	0.36	8.58	1.08	0.21
Na2O	%	0.01	FUS-ICP-ES	0.06	1.05	0.02	0.05	1.63	2.31	1.78	0.13
K2O	%	0.01	FUS-ICP-ES	0.22	4.95	0.29	1.3	1.17	0.41	0.27	2.59
TiO2	%	0.001	FUS-ICP-ES	0.653	0.18	0.534	0.689	0.645	1.026	0.486	0.331
P2O5	%	0.01	FUS-ICP-ES	0.24	0.05	0.1	0.13	0.14	0.31	0.09	0.07
LOI	%		FUS-ICP-ES	7.88	3.32	7.47	5.97	5.64	10.34	5.84	3.84
Total	%	0.01	FUS-ICP-ES	100.1	99.13	99.4	99.03	99.45	98.74	99.7	99.3
Sc	ppm	1	FUS-ICP-ES	22	4	35	25	25	35	31	10
Be	ppm	1	FUS-ICP-ES	< 1	1	1	< 1	1	2	1	< 1
V	ppm	5	FUS-ICP-ES	97	6	259	266	260	269	218	19
Cr	ppm	20	FUS-MS	20	< 20	260	20	90	610	170	< 20
Co	ppm	1	FUS-MS	13	< 1	32	18	19	48	22	4
Ni	ppm	20	FUS-MS	< 20	< 20	60	< 20	< 20	210	40	< 20
Cu	ppm	10	FUS-MS	< 10	< 10	10	< 10	< 10	50	< 10	< 10
Zn	ppm	30	FUS-MS	550	50	410	410	190	90	230	200
Ga	ppm	1	FUS-MS	16	12	15	14	16	16	12	12
Ge	ppm	0.5	FUS-MS	0.7	1.5	0.9	0.6	0.6	1.3	0.6	0.7
As	ppm	5	FUS-MS	< 5	6	< 5	42	7	24	39	63
Rb	ppm	1	FUS-MS	5	128	7	27	28	10	7	45
Sr	ppm	2	FUS-ICP	13	279	10	10	28	257	51	11
Y	ppm	0.5	FUS-MS	27.5	16.3	12.5	15.9	19.3	24.2	12.4	30.6
Zr	ppm	1	FUS-MS	89	101	34	49	47	91	37	140
Nb	ppm	0.2	FUS-MS	2.7	5	1.4	1.6	1.9	4.3	1.6	3.9
Mo	ppm	2	FUS-MS	5	< 2	2	6	< 2	< 2	4	< 2
Ag	ppm	0.5	FUS-MS	< 0.5	< 0.5	< 0.5	< 0.5	< 0.5	< 0.5	< 0.5	< 0.5
In	ppm	0.1	FUS-MS	0.2	< 0.1	< 0.1	< 0.1	0.3	< 0.1	< 0.1	0.1
Sn	ppm	1	FUS-MS	1	< 1	< 1	< 1	< 1	< 1	< 1	< 1
Sb	ppm	0.2	FUS-MS	1.4	1.2	0.6	< 0.2	0.4	2.5	< 0.2	0.6
Cs	ppm	0.1	FUS-MS	0.6	2.6	0.9	0.6	0.5	2	0.8	0.9
Ba	ppm	3	FUS-ICP	157	2856	169	576	360	145	118	956
La	ppm	0.05	FUS-MS	21.8	32	8.31	10.8	11.1	17	5.56	29.5
Ce	ppm	0.05	FUS-MS	46.4	57.1	16.4	21.8	22.4	36.8	12.7	60.6
Pr	ppm	0.01	FUS-MS	5.46	5.53	1.9	2.5	2.61	4.56	1.55	6.9
Nd	ppm	0.05	FUS-MS	19.9	16.8	7.46	9.53	10	17.6	6.41	24.8
Sm	ppm	0.01	FUS-MS	4.68	2.94	1.73	2.17	2.34	4.39	1.6	5.21
Eu	ppm	0.005	FUS-MS	0.72	0.461	0.329	0.343	0.392	1.34	0.321	0.629
Gd	ppm	0.01	FUS-MS	4.47	2.49	1.92	2.3	2.67	4.47	1.73	4.62
Tb	ppm	0.01	FUS-MS	0.73	0.41	0.32	0.4	0.47	0.71	0.31	0.78
Dy	ppm	0.01	FUS-MS	4.61	2.5	1.97	2.56	3.1	4.19	2.01	4.93
Ho	ppm	0.01	FUS-MS	1.01	0.56	0.43	0.57	0.67	0.86	0.44	1.08
Er	ppm	0.01	FUS-MS	3.21	1.78	1.35	1.77	2.07	2.5	1.36	3.47
Tm	ppm	0.005	FUS-MS	0.494	0.285	0.203	0.265	0.308	0.361	0.203	0.546
Yb	ppm	0.01	FUS-MS	3.16	1.99	1.27	1.62	1.93	2.22	1.27	3.58
Lu	ppm	0.002	FUS-MS	0.463	0.313	0.181	0.231	0.277	0.318	0.183	0.538
Hf	ppm	0.1	FUS-MS	2.6	2.9	1	1.4	1.3	2.3	1	3.8
Ta	ppm	0.01	FUS-MS	0.13	0.43	0.06	0.07	0.1	0.24	0.07	0.27
W	ppm	0.5	FUS-MS	2.3	< 0.5	1.7	1.7	2.5	0.6	1	1.3
Tl	ppm	0.05	FUS-MS	0.17	1.63	0.08	0.46	0.39	0.16	0.09	1.04
Pb	ppm	5	FUS-MS	< 5	24	40	26	< 5	7	6	7
Bi	ppm	0.1	FUS-MS	0.6	0.5	1.3	2	1	0.1	1.8	1.5
Th	ppm	0.05	FUS-MS	5.38	11.4	2.36	2.93	3.04	3.15	1.83	6.98
U	ppm	0.01	FUS-MS	2.53	3.37	0.76	1.02	1.07	0.93	0.55	3.11

Appendix 3.1: Whole-rock lithogeochemistry

Analyte Symbol	Unit Symbol	Detection Limit	Analysis Method	RAX08G117	RAX08G118	RAX08G122	RAX08G124	RAX08G129	RAX08G130	RAX08G131	RAX08G135	RAX08G137
SiO2	%	0.01	FUS-ICP-ES	65.85	75.31	74.81	75.16	67.86	57.7	70.24	56.76	75.51
Al2O3	%	0.01	FUS-ICP-ES	13.09	12.04	13.66	12.69	15.45	15.19	12.66	16.54	12.46
Fe2O3(T)	%	0.01	FUS-ICP-ES	6.34	2.89	1.73	1.99	3.13	10.39	5.64	8.61	1.68
MnO	%	0.001	FUS-ICP-ES	0.179	0.02	0.053	0.059	0.024	0.635	0.143	0.371	0.039
MgO	%	0.01	FUS-ICP-ES	5.12	0.54	0.62	0.71	3.85	7.16	2.04	6.02	0.4
CaO	%	0.01	FUS-ICP-ES	0.33	0.28	0.67	1.01	0.54	0.48	0.5	0.39	1.25
Na2O	%	0.01	FUS-ICP-ES	0.09	0.1	5.08	3.74	0.29	3.33	2.26	2.46	5.75
K2O	%	0.01	FUS-ICP-ES	2.62	3.45	2.08	2.06	1.21	0.32	1.94	1.74	0.17
TiO2	%	0.001	FUS-ICP-ES	0.597	0.367	0.183	0.207	0.262	0.615	0.508	0.648	0.272
P2O5	%	0.01	FUS-ICP-ES	0.13	0.1	0.05	0.05	< 0.01	0.11	0.19	0.14	0.06
LOI	%		FUS-ICP-ES	5.4	3.62	0.99	2.2	6.55	4.81	3.58	4.58	1.59
Total	%	0.01	FUS-ICP-ES	99.76	98.72	99.92	99.89	99.17	100.8	99.71	98.26	99.18
Sc	ppm	1	FUS-ICP-ES	27	13	4	4	7	32	17	31	7
Be	ppm	1	FUS-ICP-ES	< 1	< 1	1	1	1	1	1	1	< 1
V	ppm	5	FUS-ICP-ES	265	51	9	16	13	291	39	299	26
Cr	ppm	20	FUS-MS	< 20	70	100	< 20	< 20	100	< 20	70	160
Co	ppm	1	FUS-MS	15	6	< 1	1	4	28	10	41	2
Ni	ppm	20	FUS-MS	< 20	< 20	< 20	< 20	< 20	40	< 20	40	< 20
Cu	ppm	10	FUS-MS	30	20	< 10	< 10	< 10	690	50	40	< 10
Zn	ppm	30	FUS-MS	360	40	30	70	150	530	90	370	40
Ga	ppm	1	FUS-MS	14	13	10	12	15	15	14	17	9
Ge	ppm	0.5	FUS-MS	0.6	0.6	1.2	1.7	0.9	0.8	0.6	0.7	0.9
As	ppm	5	FUS-MS	86	179	< 5	7	153	16	70	97	< 5
Rb	ppm	1	FUS-MS	55	67	46	58	25	7	37	33	4
Sr	ppm	2	FUS-ICP	7	26	184	197	249	90	76	57	143
Y	ppm	0.5	FUS-MS	9.3	14.6	17.9	18.1	16.7	13.9	22.6	15.1	12.4
Zr	ppm	1	FUS-MS	40	60	114	108	152	44	79	50	120
Nb	ppm	0.2	FUS-MS	1.2	2	4.8	3.9	5.5	1.7	2.5	1.9	5.4
Mo	ppm	2	FUS-MS	24	6	< 2	< 2	5	< 2	11	< 2	3
Ag	ppm	0.5	FUS-MS	< 0.5	< 0.5	< 0.5	< 0.5	2.4	0.5	< 0.5	< 0.5	< 0.5
In	ppm	0.1	FUS-MS	< 0.1	< 0.1	< 0.1	< 0.1	< 0.1	0.2	0.1	0.1	< 0.1
Sn	ppm	1	FUS-MS	< 1	< 1	< 1	1	< 1	< 1	< 1	< 1	1
Sb	ppm	0.2	FUS-MS	0.3	1.5	6.3	2.6	11.2	1.9	1.6	2.6	1.9
Cs	ppm	0.1	FUS-MS	0.8	1.2	0.5	0.8	1	0.3	0.7	0.9	0.1
Ba	ppm	3	FUS-ICP	1001	1202	1170	811	8433	246	681	767	85
La	ppm	0.05	FUS-MS	5.17	16.7	35.1	30.1	33	13.9	24.7	15.5	17.3
Ce	ppm	0.05	FUS-MS	10.5	32.3	62.2	49.7	60.3	28	48	30.1	32
Pr	ppm	0.01	FUS-MS	1.45	3.56	5.37	4.66	6.75	3.54	6.16	3.68	3.28
Nd	ppm	0.05	FUS-MS	6.25	12.6	16.9	15.2	19.2	12.5	21	13.3	10.9
Sm	ppm	0.01	FUS-MS	1.61	2.79	3.32	2.93	3.51	2.8	4.61	2.92	2.18
Eu	ppm	0.005	FUS-MS	0.198	0.499	0.834	0.659	0.867	0.711	0.612	0.729	0.533
Gd	ppm	0.01	FUS-MS	1.73	2.44	2.76	2.56	2.88	2.51	4.12	2.74	1.99
Tb	ppm	0.01	FUS-MS	0.31	0.38	0.44	0.41	0.52	0.44	0.74	0.42	0.31
Dy	ppm	0.01	FUS-MS	1.75	2.41	2.69	2.59	3.27	2.69	4.48	2.57	1.91
Ho	ppm	0.01	FUS-MS	0.35	0.53	0.6	0.57	0.64	0.54	0.89	0.56	0.41
Er	ppm	0.01	FUS-MS	1.12	1.69	2	1.91	1.9	1.57	2.7	1.73	1.35
Tm	ppm	0.005	FUS-MS	0.173	0.264	0.324	0.312	0.297	0.232	0.397	0.26	0.215
Yb	ppm	0.01	FUS-MS	1.24	1.75	2.22	2.13	1.96	1.49	2.62	1.65	1.46
Lu	ppm	0.002	FUS-MS	0.223	0.267	0.354	0.355	0.3	0.221	0.396	0.236	0.229
Hf	ppm	0.1	FUS-MS	1.1	1.7	3.6	3	4.5	1.4	2.5	1.4	3.2
Ta	ppm	0.01	FUS-MS	0.08	0.1	0.45	0.42	0.48	0.07	0.13	0.11	0.51
W	ppm	0.5	FUS-MS	2.6	1.1	1	0.9	2.4	2.1	4.8	1.5	< 0.5
Tl	ppm	0.05	FUS-MS	0.66	1.35	0.5	1.26	9.95	0.36	0.31	1.61	0.09
Pb	ppm	5	FUS-MS	80	15	18	22	36	129	16	15	< 5
Bi	ppm	0.1	FUS-MS	1.2	2.7	23.7	0.7	< 0.1	205	338	2.2	< 0.1
Th	ppm	0.05	FUS-MS	2.42	4.42	12.2	10.2	13.5	3.12	6.02	3.28	6.15
U	ppm	0.01	FUS-MS	1.17	1.47	3.51	3.1	11.3	0.96	2.11	1.14	1.52

Appendix 3.1: Whole-rock lithogeochemistry

Analyte Symbol	Unit Symbol	Detection Limit	Analysis Method	RAX08G139	RAX08G140	RAX08G141	RAX08G142	RAX08G144	RAX08G146	RAX08G148	RAX08G151
SiO2	%	0.01	FUS-ICP-ES	78.61	82.53	55.7	62.22	71.52	70.91	55.54	59.17
Al2O3	%	0.01	FUS-ICP-ES	10.34	7.94	17.92	13.89	13.64	11.62	15.37	13.38
Fe2O3(T)	%	0.01	FUS-ICP-ES	2.73	2.48	9.98	6.88	2.76	5.76	8.06	8.82
MnO	%	0.001	FUS-ICP-ES	0.024	0.016	0.412	0.328	0.05	0.022	0.445	0.44
MgO	%	0.01	FUS-ICP-ES	0.45	0.34	3.7	7.86	1.29	0.84	10.51	8.32
CaO	%	0.01	FUS-ICP-ES	0.19	0.24	0.35	0.36	1.22	0.24	0.27	0.27
Na2O	%	0.01	FUS-ICP-ES	0.11	1.12	3.14	0.06	1.45	0.09	0.08	0.08
K2O	%	0.01	FUS-ICP-ES	3.05	1.87	2.2	2.01	4.08	3.71	1.81	1.55
TiO2	%	0.001	FUS-ICP-ES	0.376	0.209	0.733	0.582	0.234	0.42	0.606	0.544
P2O5	%	0.01	FUS-ICP-ES	0.08	0.05	0.12	0.22	0.06	0.09	0.13	0.11
LOI	%		FUS-ICP-ES	2.94	2.2	4.9	5.46	3.15	4.84	6.8	5.74
Total	%	0.01	FUS-ICP-ES	98.89	98.98	99.16	99.88	99.45	98.54	99.64	98.43
Sc	ppm	1	FUS-ICP-ES	11	6	31	19	6	22	34	26
Be	ppm	1	FUS-ICP-ES	< 1	< 1	2	< 1	1	1	1	1
V	ppm	5	FUS-ICP-ES	48	18	344	74	21	209	250	243
Cr	ppm	20	FUS-MS	< 20	110	40	60	< 20	150	70	80
Co	ppm	1	FUS-MS	4	3	24	7	2	21	23	23
Ni	ppm	20	FUS-MS	< 20	< 20	< 20	< 20	< 20	30	< 20	< 20
Cu	ppm	10	FUS-MS	220	< 10	< 10	< 10	< 10	20	< 10	< 10
Zn	ppm	30	FUS-MS	4130	40	160	590	50	40	270	410
Ga	ppm	1	FUS-MS	11	8	17	15	13	13	18	16
Ge	ppm	0.5	FUS-MS	0.7	0.5	< 0.5	0.5	1.3	< 0.5	< 0.5	0.7
As	ppm	5	FUS-MS	141	27	8	26	7	134	30	14
Rb	ppm	1	FUS-MS	59	40	43	42	118	85	40	36
Sr	ppm	2	FUS-ICP	16	27	55	9	139	22	17	13
Y	ppm	0.5	FUS-MS	25.5	15.5	17.3	20.7	17.4	9.8	16.4	14.6
Zr	ppm	1	FUS-MS	110	88	52	81	122	36	53	41
Nb	ppm	0.2	FUS-MS	3	2.7	1.2	3.1	4.7	1.4	1.7	1.7
Mo	ppm	2	FUS-MS	7	11	< 2	7	< 2	8	3	3
Ag	ppm	0.5	FUS-MS	0.5	< 0.5	< 0.5	< 0.5	< 0.5	< 0.5	< 0.5	< 0.5
In	ppm	0.1	FUS-MS	0.2	< 0.1	< 0.1	0.1	< 0.1	0.1	0.1	0.1
Sn	ppm	1	FUS-MS	< 1	< 1	< 1	< 1	< 1	< 1	< 1	< 1
Sb	ppm	0.2	FUS-MS	1.8	0.6	< 0.2	1.1	1.5	1.3	< 0.2	0.2
Cs	ppm	0.1	FUS-MS	0.8	0.6	1	1.4	2	1.2	1.3	1.7
Ba	ppm	3	FUS-ICP	1431	862	711	471	783	1450	764	432
La	ppm	0.05	FUS-MS	21.8	7.59	14.7	22.5	30.9	7.46	17	8.71
Ce	ppm	0.05	FUS-MS	44.2	16.4	27.1	44.9	57.2	14.6	35.3	17.5
Pr	ppm	0.01	FUS-MS	4.99	1.91	3.08	5.42	5.46	1.62	3.91	2.04
Nd	ppm	0.05	FUS-MS	18.8	7.4	12.1	19.3	16.5	6.17	14	8.05
Sm	ppm	0.01	FUS-MS	4.22	1.75	2.9	3.97	3.1	1.43	3.12	1.95
Eu	ppm	0.005	FUS-MS	0.827	0.218	0.881	0.512	0.608	0.252	0.4	0.317
Gd	ppm	0.01	FUS-MS	4.07	1.81	3.07	3.5	2.48	1.45	2.8	2
Tb	ppm	0.01	FUS-MS	0.67	0.33	0.49	0.56	0.47	0.28	0.49	0.39
Dy	ppm	0.01	FUS-MS	4.2	2.31	2.97	3.48	3.05	1.87	3.05	2.53
Ho	ppm	0.01	FUS-MS	0.91	0.55	0.62	0.76	0.64	0.4	0.62	0.52
Er	ppm	0.01	FUS-MS	2.81	1.89	1.95	2.45	1.98	1.23	1.85	1.59
Tm	ppm	0.005	FUS-MS	0.427	0.304	0.296	0.381	0.332	0.187	0.279	0.236
Yb	ppm	0.01	FUS-MS	2.73	2.04	1.9	2.46	2.32	1.2	1.79	1.47
Lu	ppm	0.002	FUS-MS	0.41	0.329	0.289	0.377	0.365	0.184	0.256	0.218
Hf	ppm	0.1	FUS-MS	2.8	2.3	1.4	2.3	3.3	1	1.5	1.1
Ta	ppm	0.01	FUS-MS	0.19	0.2	0.09	0.13	0.38	0.06	0.07	0.07
W	ppm	0.5	FUS-MS	1.9	1.1	3.2	3.9	0.9	2.3	2.4	1.7
Tl	ppm	0.05	FUS-MS	1.81	1.01	0.75	0.82	4.79	1.39	0.8	0.63
Pb	ppm	5	FUS-MS	477	8	< 5	13	20	24	< 5	27
Bi	ppm	0.1	FUS-MS	3	2	< 0.1	2.5	0.3	7.5	1.3	0.7
Th	ppm	0.05	FUS-MS	4.84	4.45	3.09	5.76	11.4	2.49	3.8	2.71
U	ppm	0.01	FUS-MS	1.99	1.57	1.06	1.88	3.29	0.94	1.73	0.91

Appendix 3.1: Whole-rock lithogeochemistry

Analyte Symbol	Unit Symbol	Detection Limit	Analysis Method	RAX08G153	RAX08G155	RAX08G156	RAX08G157	RAX08G159	RAX08G160	RAX08G164	RAX08G165
SiO2	%	0.01	FUS-ICP-ES	58.71	71.27	56.61	82.73	53.69	79.43	72.49	81.58
Al2O3	%	0.01	FUS-ICP-ES	19.19	10.61	14.26	9.44	13.45	10.13	13.06	9.89
Fe2O3(T)	%	0.01	FUS-ICP-ES	2.98	5.21	9.49	1.24	11.18	1.91	2.87	1.8
MnO	%	0.001	FUS-ICP-ES	0.061	0.197	0.569	0.032	0.689	0.038	0.106	0.012
MgO	%	0.01	FUS-ICP-ES	2.33	4.24	10.19	0.17	11.35	0.62	1.71	0.32
CaO	%	0.01	FUS-ICP-ES	2.54	0.26	0.36	0.78	0.27	0.35	0.76	0.18
Na2O	%	0.01	FUS-ICP-ES	1.41	< 0.01	0.87	3.75	0.31	1.04	3.5	0.17
K2O	%	0.01	FUS-ICP-ES	3.64	2.03	0.98	1.37	0.51	2.21	1.57	2.77
TiO2	%	0.001	FUS-ICP-ES	0.524	0.495	0.584	0.128	0.498	0.287	0.332	0.321
P2O5	%	0.01	FUS-ICP-ES	0.12	0.16	0.12	0.04	0.11	0.08	0.08	0.08
LOI	%		FUS-ICP-ES	5.81	4.01	5.82	0.82	6.65	2.34	2.36	2.63
Total	%	0.01	FUS-ICP-ES	97.31	98.46	99.85	100.5	98.72	98.44	98.83	99.76
Sc	ppm	1	FUS-ICP-ES	15	16	27	3	29	8	10	9
Be	ppm	1	FUS-ICP-ES	2	1	1	< 1	1	< 1	1	< 1
V	ppm	5	FUS-ICP-ES	49	82	278	< 5	259	20	56	20
Cr	ppm	20	FUS-MS	40	< 20	70	< 20	210	120	< 20	< 20
Co	ppm	1	FUS-MS	4	9	18	< 1	22	2	4	3
Ni	ppm	20	FUS-MS	< 20	< 20	< 20	< 20	40	< 20	< 20	< 20
Cu	ppm	10	FUS-MS	10	< 10	20	< 10	< 10	60	20	20
Zn	ppm	30	FUS-MS	1230	270	240	40	430	1570	230	1190
Ga	ppm	1	FUS-MS	19	12	16	7	14	11	13	12
Ge	ppm	0.5	FUS-MS	0.8	0.5	0.8	1	0.7	0.7	0.9	1
As	ppm	5	FUS-MS	< 5	48	6	< 5	5	45	12	79
Rb	ppm	1	FUS-MS	77	43	23	19	12	41	40	56
Sr	ppm	2	FUS-ICP	161	12	14	123	11	38	83	23
Y	ppm	0.5	FUS-MS	40.5	21.3	13	11.8	10.7	23.4	13.3	27.3
Zr	ppm	1	FUS-MS	224	87	45	78	38	134	138	128
Nb	ppm	0.2	FUS-MS	6.7	2.9	1.8	3.2	1.2	3.6	5.9	2.9
Mo	ppm	2	FUS-MS	< 2	18	4	< 2	5	3	< 2	5
Ag	ppm	0.5	FUS-MS	< 0.5	< 0.5	< 0.5	< 0.5	< 0.5	< 0.5	< 0.5	< 0.5
In	ppm	0.1	FUS-MS	< 0.1	< 0.1	0.2	< 0.1	0.2	< 0.1	< 0.1	0.2
Sn	ppm	1	FUS-MS	1	< 1	< 1	< 1	< 1	< 1	4	1
Sb	ppm	0.2	FUS-MS	2.4	1.3	1.1	4.4	6.3	2	1.8	2.9
Cs	ppm	0.1	FUS-MS	2.8	0.9	0.4	0.2	0.4	0.7	0.7	0.9
Ba	ppm	3	FUS-ICP	2745	1164	280	915	175	754	403	788
La	ppm	0.05	FUS-MS	47.6	17.6	10.5	17.9	8.18	20.5	17.8	25.4
Ce	ppm	0.05	FUS-MS	94.7	38.7	21.5	32.8	16	42.1	35	50
Pr	ppm	0.01	FUS-MS	11.9	4.97	2.8	2.9	1.63	4.7	3.62	5.58
Nd	ppm	0.05	FUS-MS	38.4	16.9	9.83	9.64	6.61	17.1	11.6	21.8
Sm	ppm	0.01	FUS-MS	7.78	3.57	2.16	1.98	1.59	3.76	2.33	5.02
Eu	ppm	0.005	FUS-MS	1.82	0.428	0.366	0.438	0.271	0.791	0.575	1.05
Gd	ppm	0.01	FUS-MS	7.15	3.39	2.09	1.71	1.66	3.65	2	4.75
Tb	ppm	0.01	FUS-MS	1.33	0.61	0.38	0.27	0.26	0.71	0.38	0.71
Dy	ppm	0.01	FUS-MS	8.22	4	2.36	1.74	1.66	4.41	2.45	4.36
Ho	ppm	0.01	FUS-MS	1.6	0.85	0.49	0.4	0.38	0.88	0.5	0.95
Er	ppm	0.01	FUS-MS	4.59	2.62	1.44	1.37	1.19	2.62	1.51	3.13
Tm	ppm	0.005	FUS-MS	0.662	0.399	0.218	0.226	0.18	0.4	0.248	0.484
Yb	ppm	0.01	FUS-MS	4.05	2.64	1.39	1.58	1.14	2.53	1.68	3.11
Lu	ppm	0.002	FUS-MS	0.579	0.401	0.209	0.257	0.174	0.375	0.258	0.474
Hf	ppm	0.1	FUS-MS	6.6	2.7	1.4	2.4	1.2	3.5	3.6	3.2
Ta	ppm	0.01	FUS-MS	0.54	0.17	0.08	0.31	0.1	0.27	0.49	0.23
W	ppm	0.5	FUS-MS	0.9	2.9	2.5	1.2	2.9	1.9	1.8	2.2
Tl	ppm	0.05	FUS-MS	0.74	0.22	0.16	0.25	0.11	0.95	0.65	1.67
Pb	ppm	5	FUS-MS	35	15	6	8	15	514	10	43
Bi	ppm	0.1	FUS-MS	< 0.1	127	10.9	1.7	7.5	0.5	1	1.2
Th	ppm	0.05	FUS-MS	13.2	6.04	2.86	8.37	2.22	5.24	6.03	5.96
U	ppm	0.01	FUS-MS	2.53	2.26	0.77	2.15	0.74	1.82	1.34	2.17

Appendix 3.2: Duplicate whole-rock lithogeochemical analyses

Analyte Symbol	Unit Symbol	Detection Limit	Analysis Method	RAX08G129 Orig	RAX08G129 Split	RAX08G131 Orig	RAX08G131 Dup	RAX08G137 Orig	RAX08G137 Dup
SiO2	%	0.01	FUS-ICP-ES	67.86	67.74	69.49	71	75.88	75.13
Al2O3	%	0.01	FUS-ICP-ES	15.45	15.28	12.51	12.82	12.52	12.4
Fe2O3(T)	%	0.01	FUS-ICP-ES	3.13	3.15	5.57	5.71	1.7	1.66
MnO	%	0.001	FUS-ICP-ES	0.024	0.024	0.142	0.144	0.04	0.038
MgO	%	0.01	FUS-ICP-ES	3.85	3.9	2.03	2.06	0.41	0.39
CaO	%	0.01	FUS-ICP-ES	0.54	0.56	0.49	0.5	1.28	1.22
Na2O	%	0.01	FUS-ICP-ES	0.29	0.29	2.24	2.29	5.77	5.74
K2O	%	0.01	FUS-ICP-ES	1.21	1.12	1.88	1.99	0.19	0.15
TiO2	%	0.001	FUS-ICP-ES	0.262	0.261	0.502	0.514	0.278	0.266
P2O5	%	0.01	FUS-ICP-ES	< 0.01	< 0.01	0.19	0.19	0.07	0.06
LOI	%		FUS-ICP-ES	6.55	6.42	3.58	3.58	1.59	1.59
Total	%	0.01	FUS-ICP-ES	99.17	98.75	98.63	100.8	99.72	98.64
Sc	ppm	1	FUS-ICP-ES	7	6	17	17	7	7
Be	ppm	1	FUS-ICP-ES	1	1	1	1	1	< 1
V	ppm	5	FUS-ICP-ES	13	12	40	38	28	25
Sr	ppm	2	FUS-ICP-ES	249	246	75	77	143	143
Ba	ppm	3	FUS-ICP-ES	8433	8298	671	691	86	85
Cr	ppm	20	FUS-MS	< 20	< 20	< 20	< 20	160	160
Co	ppm	1	FUS-MS	4	4	9	10	2	1
Ni	ppm	20	FUS-MS	< 20	< 20	< 20	< 20	< 20	< 20
Cu	ppm	10	FUS-MS	< 10	< 10	50	60	< 10	< 10
Zn	ppm	30	FUS-MS	150	190	90	90	40	40
Ga	ppm	1	FUS-MS	15	15	14	14	9	9
Ge	ppm	0.5	FUS-MS	0.9	0.7	0.5	0.7	1	0.9
As	ppm	5	FUS-MS	153	113	65	74	< 5	< 5
Rb	ppm	1	FUS-MS	25	23	36	37	4	4
Y	ppm	0.5	FUS-MS	16.7	16.8	22.4	22.9	12.6	12.2
Zr	ppm	1	FUS-MS	152	153	78	80	119	120
Nb	ppm	0.2	FUS-MS	5.5	5.4	2.5	2.6	5.6	5.3
Mo	ppm	2	FUS-MS	5	5	10	11	3	3
Ag	ppm	0.5	FUS-MS	2.4	0.9	< 0.5	< 0.5	< 0.5	< 0.5
In	ppm	0.1	FUS-MS	< 0.1	< 0.1	0.1	0.1	< 0.1	< 0.1
Sn	ppm	1	FUS-MS	< 1	< 1	< 1	< 1	1	1
Sb	ppm	0.2	FUS-MS	11.2	8.2	1.5	1.7	1.5	2.3
Cs	ppm	0.1	FUS-MS	1	0.9	0.7	0.7	0.1	0.1
La	ppm	0.05	FUS-MS	33	32.6	24.5	24.9	17.3	17.2
Ce	ppm	0.05	FUS-MS	60.3	59.1	47.3	48.6	32.3	31.8
Pr	ppm	0.01	FUS-MS	6.75	6.63	6.09	6.23	3.28	3.28
Nd	ppm	0.05	FUS-MS	19.2	19.1	20.8	21.2	11	10.8
Sm	ppm	0.01	FUS-MS	3.51	3.49	4.53	4.69	2.18	2.19
Eu	ppm	0.005	FUS-MS	0.867	0.809	0.612	0.612	0.529	0.537
Gd	ppm	0.01	FUS-MS	2.88	2.98	4.06	4.18	2.02	1.95
Tb	ppm	0.01	FUS-MS	0.52	0.53	0.73	0.75	0.31	0.31
Dy	ppm	0.01	FUS-MS	3.27	3.25	4.43	4.53	1.91	1.91
Ho	ppm	0.01	FUS-MS	0.64	0.64	0.88	0.9	0.42	0.41
Er	ppm	0.01	FUS-MS	1.9	1.87	2.66	2.74	1.36	1.34
Tm	ppm	0.005	FUS-MS	0.297	0.292	0.39	0.405	0.217	0.214
Yb	ppm	0.01	FUS-MS	1.96	1.94	2.58	2.66	1.47	1.44
Lu	ppm	0.002	FUS-MS	0.3	0.297	0.389	0.402	0.23	0.228
Hf	ppm	0.1	FUS-MS	4.5	4.6	2.5	2.5	3.2	3.1
Ta	ppm	0.01	FUS-MS	0.48	0.46	0.12	0.13	0.53	0.5
W	ppm	0.5	FUS-MS	2.4	2.2	4.6	5	0.7	< 0.5
Tl	ppm	0.05	FUS-MS	9.95	6.3	0.3	0.31	0.09	0.08
Pb	ppm	5	FUS-MS	36	26	14	17	< 5	< 5
Bi	ppm	0.1	FUS-MS	< 0.1	< 0.1	325	351	0.3	< 0.1
Th	ppm	0.05	FUS-MS	13.5	13.5	5.9	6.13	6.17	6.13
U	ppm	0.01	FUS-MS	11.3	11.1	2.06	2.15	1.51	1.53

Appendix 3.2: Duplicate whole-rock lithogeochemical analyses

Analyte Symbol	Unit Symbol	Detection Limit	Analysis Method	RAX08G174 Orig	RAX08G174 Split	RAX08G183 Orig	RAX08G183 Dup	RAX08G195 Orig	RAX08G195 Split
SiO2	%	0.01	FUS-ICP-ES	74.47	75.44	72.91	72.82	51.1	50.54
Al2O3	%	0.01	FUS-ICP-ES	11.37	11.47	11.57	11.58	15.66	15.52
Fe2O3(T)	%	0.01	FUS-ICP-ES	3.23	3.27	3.11	3.1	10.51	10.54
MnO	%	0.001	FUS-ICP-ES	0.064	0.064	0.131	0.131	0.652	0.648
MgO	%	0.01	FUS-ICP-ES	1.26	1.25	0.86	0.89	11.98	11.89
CaO	%	0.01	FUS-ICP-ES	1.48	1.46	2.2	2.2	0.47	0.47
Na2O	%	0.01	FUS-ICP-ES	3.32	3.35	2.43	2.46	0.12	0.1
K2O	%	0.01	FUS-ICP-ES	1.12	1.23	0.96	1.02	1.36	1.33
TiO2	%	0.001	FUS-ICP-ES	0.224	0.217	0.227	0.231	0.566	0.554
P2O5	%	0.01	FUS-ICP-ES	0.04	0.04	0.05	0.05	0.11	0.1
LOI	%		FUS-ICP-ES	2.5	2.7	4.79	4.79	7.57	7.61
Total	%	0.01	FUS-ICP-ES	99.08	100.5	99.25	99.28	100.1	99.29
Sc	ppm	1	FUS-ICP-ES	11	10	11	11	31	30
Be	ppm	1	FUS-ICP-ES	< 1	< 1	< 1	< 1	1	1
V	ppm	5	FUS-ICP-ES	13	7	9	12	304	299
Sr	ppm	2	FUS-ICP-ES	< 20	89	107	106	13	12
Ba	ppm	3	FUS-ICP-ES	4	371	370	367	419	414
Cr	ppm	20	FUS-MS	< 20	< 20	< 20	< 20	< 20	< 20
Co	ppm	1	FUS-MS	40	4	1	1	20	19
Ni	ppm	20	FUS-MS	60	< 20	< 20	< 20	< 20	< 20
Cu	ppm	10	FUS-MS	12	40	20	< 10	< 10	< 10
Zn	ppm	30	FUS-MS	0.6	60	70	50	410	280
Ga	ppm	1	FUS-MS	< 5	12	12	12	19	18
Ge	ppm	0.5	FUS-MS	28	0.7	1.3	1.2	0.8	0.7
As	ppm	5	FUS-MS	87	6	10	11	9	10
Rb	ppm	1	FUS-MS	30.4	28	26	26	29	29
Y	ppm	0.5	FUS-MS	122	29.9	31.1	31.1	15.5	15
Zr	ppm	1	FUS-MS	3.8	120	123	123	42	43
Nb	ppm	0.2	FUS-MS	5	3.7	3.7	3.6	1.5	1.5
Mo	ppm	2	FUS-MS	< 0.5	5	< 2	< 2	< 2	2
Ag	ppm	0.5	FUS-MS	< 0.1	< 0.5	< 0.5	< 0.5	< 0.5	< 0.5
In	ppm	0.1	FUS-MS	< 1	0.3	0.1	< 0.1	0.2	0.2
Sn	ppm	1	FUS-MS	0.8	< 1	2	1	< 1	< 1
Sb	ppm	0.2	FUS-MS	0.4	0.7	2.6	1.7	0.9	0.3
Cs	ppm	0.1	FUS-MS	372	0.4	0.5	0.5	1.1	1
La	ppm	0.05	FUS-MS	19.5	19.4	20	19.8	9.62	9.08
Ce	ppm	0.05	FUS-MS	40.1	40.4	39	38.7	19.2	18.3
Pr	ppm	0.01	FUS-MS	4.45	4.64	4.39	4.41	2.16	2.05
Nd	ppm	0.05	FUS-MS	17.3	17.8	17.1	17.6	8.37	8.02
Sm	ppm	0.01	FUS-MS	4.02	4.04	4.23	4.26	1.98	1.94
Eu	ppm	0.005	FUS-MS	0.773	0.807	0.96	0.941	0.295	0.278
Gd	ppm	0.01	FUS-MS	4	4.16	4.68	4.67	2.12	2.07
Tb	ppm	0.01	FUS-MS	0.82	0.83	0.77	0.78	0.42	0.42
Dy	ppm	0.01	FUS-MS	5.31	5.36	4.82	4.97	2.73	2.68
Ho	ppm	0.01	FUS-MS	1.09	1.09	1.05	1.07	0.53	0.52
Er	ppm	0.01	FUS-MS	3.37	3.32	3.54	3.55	1.57	1.55
Tm	ppm	0.005	FUS-MS	0.539	0.531	0.566	0.581	0.248	0.242
Yb	ppm	0.01	FUS-MS	3.5	3.54	3.7	3.79	1.59	1.53
Lu	ppm	0.002	FUS-MS	0.526	0.542	0.57	0.572	0.229	0.226
Hf	ppm	0.1	FUS-MS	3.4	3.5	3.5	3.5	1.1	1.2
Ta	ppm	0.01	FUS-MS	0.26	0.27	0.28	0.27	0.05	0.05
W	ppm	0.5	FUS-MS	0.6	1.2	1.1	0.9	2.4	2
Tl	ppm	0.05	FUS-MS	0.36	0.4	2.71	0.35	0.51	0.43
Pb	ppm	5	FUS-MS	6	10	10	7	11	7
Bi	ppm	0.1	FUS-MS	0.3	0.5	0.2	0.2	1.3	1
Th	ppm	0.05	FUS-MS	5.25	5.24	5.28	5.3	2.58	2.44
U	ppm	0.01	FUS-MS	1.62	1.62	1.63	1.65	0.79	0.76

Appendix 4.1: Summary of alteration mineralogy determined by SWIR

Sample No.	Drill Hole	Depth (m)	UTM (NAD83 - Zn 21N)*		Quartz	Illite	Chlorite	Phengite	Lithology
			Easting	Northing					
RAX08G001	H3393	40.0	509846	5408083			○	●	Rhy
RAX08G002	H3393	53.2	509846	5408083			○	●	Rhy
RAX08G003	H3393	69.0	509846	5408083				●	Rhy
RAX08G004	H3393	80.8	509846	5408083				●	Rhy
RAX08G005	H3393	87.0	509846	5408083		◒	◒		Rhy
RAX08G006	H3393	90.1	509846	5408083		◒	●		slts
RAX08G007	H3393	123.7	509846	5408083	●	●			bslt
RAX08G008	H3393	125.3	509846	5408083	●	●			bslt
RAX08G009	H3393	171.0	509846	5408083		◒	●		bslt
RAX08G010	H3393	214.5	509846	5408083			●		bslt
RAX08G011	H3393	226.5	509846	5408083			●		bslt
RAX08G012	H3393	241.5	509846	5408083			●		bslt
RAX08G013	H3396	7.8	509754	5407998				●	Rhy
RAX08G014	H3396	41.0	509754	5407998				●	Rhy
RAX08G015	H3396	57.2	509754	5407998			○	●	Rhy
RAX08G016	H3396	85.1	509754	5407998		○	●		bslt
RAX08G017	H3396	93.4	509754	5407998		○	●		bslt
RAX08G018	H3396	105.3	509754	5407998		◒	●		bslt
RAX08G019	H3396	150.9	509754	5407998			●		bslt
RAX08G020	H3396	176.2	509754	5407998			●		bslt
RAX08G021	H3396	194.6	509754	5407998			●		cgl
RAX08G022	H3396	210.4	509754	5407998			●		bslt
RAX08G023	H3396	222.6	509754	5407998					bslt
RAX08G024	H3396	66.2	509754	5407998		●	○		bslt
RAX08G025	H3388	14.6	509650	5408087			○	●	Rhy
RAX08G026	H3388	64.7	509650	5408087		●			Rhy
RAX08G027	H3388	161.6	509650	5408087					Rhy
RAX08G028	H3388	172.8	509650	5408087				●	Rhy
RAX08G029	H3388	177.5	509650	5408087		●			Rhy
RAX08G030	H3388	201.6	509650	5408087	●	●			Rhyd clast
RAX08G031	H3388	203.5	509650	5408087					bslt
RAX08G032	H3388	218.4	509650	5408087			●		poly bx
RAX08G033	H3388	230.0	509650	5408087					bslt
RAX08G034	H3388	237.7	509650	5408087		◒	●		int. Dyke
RAX08G035	H3388	239.0	509650	5408087		●	○		bslt
RAX08G036	H3388	250.4	509650	5408087		◒	◒		bslt
RAX08G037	H3388	120.9	509650	5408087					diabase
RAX08G038	H3372	23.1	510056	5408001		◒	◒		ss bx
RAX08G039	H3372	30.4	510056	5408001					bslt
RAX08G040	H3372	36.5	510056	5408001	●	●			bslt
RAX08G041	H3372	45.8	510056	5408001			●		bslt
RAX08G042	H3372	93.8	510056	5408001		○	●		bslt
RAX08G043	H3372	104.7	510056	5408001			●		bslt
RAX08G044	H3372	124.1	510056	5408001			●		bslt
RAX08G045	H3365	27.5	510149	5408006	●	●			bslt

Appendix 4.1: Summary of alteration mineralogy determined by SWIR

Sample No.	Drill Hole	Depth (m)	UTM (NAD83 - Zn 21N)*		Quartz	Illite	Chlorite	Phengite	Lithology
			Easting	Northing					
RAX08G046	H3365	51.1	510149	5408006			●		bslt
RAX08G047	H3365	81.4	510149	5408006			●		bslt
RAX08G048	H3365	100.0	510149	5408006					vein
RAX08G049	H3365	105.5	510149	5408006					vein
RAX08G050	H3365	118.9	510149	5408006		○	●		bslt
RAX08G051	H3365	136.2	510149	5408006		○	●		bslt
RAX08G052	H3365	64.0	510149	5408006					vein
RAX08G053	H3365	77.2	510149	5408006			●		bslt
RAX08G054	H3365	77.7	510149	5408006					vein
RAX08G055	H3365	99.5	510149	5408006					vein
RAX08G056	H3365	100.5	510149	5408006		○	●		bslt
RAX08G057	H3365	113.3	510149	5408006			●		bslt
RAX08G058	H3365	144.7	510149	5408006		○	●		bslt
RAX08G059	H3395	5.7	509668	5407999	◒	●	○		Rhy
RAX08G060	H3395	43.7	509668	5407999					Rhy tuff
RAX08G061	H3395	63.5	509668	5407999			●		diabase
RAX08G062	H3395	74.4	509668	5407999		●	○		Rhyd
RAX08G063	H3395	171.1	509668	5407999		○	●		bslt
RAX08G064	H3395	228.6	509668	5407999			●		bslt
RAX08G065	H3378	38.6	509501	5408037		●	○		Rhy
RAX08G066	H3378	78.2	509501	5408037		●			Rhy
RAX08G067	H3378	113.0	509501	5408037					Rhy
RAX08G068	H3378	183.4	509501	5408037			●		diabase
RAX08G069	H3378	213.1	509501	5408037					barite
RAX08G070	H3378	217.6	509501	5408037	●	●			Rhyd
RAX08G071	H3378	234.2	509501	5408037		○	●		bslt
RAX08G072	H3378	253.0	509501	5408037	●	●			bslt
RAX08G073	H3378	254.0	509501	5408037			●		bslt
RAX08G074	H3378	313.1	509501	5408037		◒	●		bslt
RAX08G075	H3378	331.2	509501	5408037			●		bslt
RAX08G076	H3386	6.2	509651	5407919	◒	●			Rhy
RAX08G077	H3386	21.2	509651	5407919		●	○		Rhy
RAX08G078	H3386	45.7	509651	5407919			●	◒	ss bx
RAX08G079	H3386	52.8	509651	5407919			●		diabase
RAX08G080	H3386	66.5	509651	5407919		●			Rhyd
RAX08G081	H3386	71.0	509651	5407919			●		diabase
RAX08G082	H3386	115.8	509651	5407919	●	●			Rhyd
RAX08G083	H3386	119.0	509651	5407919	●	●			Rhyd
RAX08G084	H3386	135.5	509651	5407919			●		bslt
RAX08G085	H3386	149.4	509651	5407919			●		bslt
RAX08G086	H3341	25.3	509847	5408055				●	Rhy
RAX08G087	H3341	77.7	509847	5408055		●			Rhy
RAX08G088	H3341	91.4	509847	5408055					bslt
RAX08G089	H3341	129.5	509847	5408055			●		bslt
RAX08G090	H3341	86.1	509847	5408055		●	●		Rhyd

Appendix 4.1: Summary of alteration mineralogy determined by SWIR

Sample No.	Drill Hole	Depth (m)	UTM (NAD83 - Zn 21N)*		Quartz	Illite	Chlorite	Phengite	Lithology
			Easting	Northing					
RAX08G091	H3341	130.8	509847	5408055		●	●		bslt
RAX08G092	H3341	144.8	509847	5408055		◪	●		bslt
RAX08G093	H3341	150.6	509847	5408055		◪	●		bslt
RAX08G094	H3341	168.1	509847	5408055					bslt
RAX08G095	H3341	182.6	509847	5408055		○	●		bslt
RAX08G096	H3341	183.2	509847	5408055			●		vein
RAX08G097	H3341	286.2	509847	5408055		○	●		bslt
RAX08G098	H3341	466.6	509847	5408055		○	●		bslt
RAX08G099	H3341	514.9	509847	5408055		○	●		pillow rim
RAX08G100	H3341	524.6	509847	5408055					carbonate
RAX08G101	H3341	537.8	509847	5408055					bslt
RAX08G102	H3341	539.8	509847	5408055		●	○		chert
RAX08G103	H3341	558.7	509847	5408055		○	●		ss/ms
RAX08G104	H3341	565.4	509847	5408055					vein
RAX08G105	H3341	580.8	509847	5408055	●	●			chert
RAX08G106	H3341	622.7	509847	5408055		○	●		bslt
RAX08G107	H3341	650.7	509847	5408055		○	●		bslt
RAX08G108	H3341	657.0	509847	5408055		●	○		ss
RAX08G109	H3398	21.5	510051	5407855					vein
RAX08G110	H3398	109.0	510051	5407855			●		bslt
RAX08G111	H3398	132.5	510051	5407855			●		diabase
RAX08G112	H3362	19.0	510040	5407694		●	○		Rhyd clast
RAX08G113	H3362	29.2	510040	5407694		●	○		Rhyd bx
RAX08G114	H3362	66.0	510040	5407694	●	●	○		ss
RAX08G115	H3362	70.1	510040	5407694	◪	●	○		slts
RAX08G116	H3362	85.0	510040	5407694	●	●			Rhyd bx
RAX08G117	H3384	33.5	510039	5407760		◪	●		bslt
RAX08G118	H3384	55.5	510039	5407760	●	●			Rhyd
RAX08G119	H3384	65.5	510039	5407760		●	○		slts
RAX08G120	H3384	96.1	510039	5407760		●	○		Rhyd bx
RAX08G121	H3362	20.3	509390	5407903		◪	●		Rhy tuff
RAX08G122	H3344	109.9	509390	5407903				●	Rhy
RAX08G123	H3344	139.1	509390	5407903	●		○	●	Rhy bx
RAX08G124	H3344	141.4	509390	5407903				●	Rhy
RAX08G125	H3344	154.1	509390	5407903		◪	◪		Rhyd bx
RAX08G126	H3344	167.0	509390	5407903		●	◪		Rhy tuff
RAX08G127	H3344	171.8	509390	5407903		○	●		Rhyd bx
RAX08G128	H3344	193.1	509390	5407903	●	◪	●		ss bx
RAX08G129	H3344	179.5	509390	5407903	●	●	○		Rhyd
RAX08G130	H3344	224.9	509390	5407903			●		bslt
RAX08G131	H3344	243.5	509390	5407903		●	◪		Rhyd
RAX08G132	H3344	210.0	509390	5407903		◪	●		Rhyd bx
RAX08G133	H3344	267.0	509390	5407903					bslt
RAX08G134	H3344	283.0	509390	5407903		○	●		bslt
RAX08G135	H3344	284.4	509390	5407903		○	●		bslt

Appendix 4.1: Summary of alteration mineralogy determined by SWIR

Sample No.	Drill Hole	Depth (m)	UTM (NAD83 - Zn 21N)*		Quartz	Illite	Chlorite	Phengite	Lithology
			Easting	Northing					
RAX08G136	H3344	429.5	509390	5407903		●	○		bslt
RAX08G137	H3408	24.7	509750	5407680		●	○		Rhy
RAX08G138	H3408	123.1	509750	5407680			●		diabase
RAX08G139	H3408	136	509750	5407680	●	●			Rhyd
RAX08G140	H3408	159	509750	5407680	●	●			Rhyd
RAX08G141	H3408	168.8	509750	5407680		○	●		bslt
RAX08G142	H3405	27.4	510152	5407798		○	●		bslt
RAX08G143	H3405	56.7	510152	5407798		○	●		bslt
RAX08G144	H3381	17.3	509738	5407918				●	Rhy
RAX08G145	H3381	59.0	509738	5407918			●		diabase
RAX08G146	H3381	81.0	509738	5407918	●	●			Rhyd
RAX08G147	H3381	122.9	509738	5407918	●	●			bslt
RAX08G148	H3381	129.2	509738	5407918		●	○		bslt
RAX08G149	H3401	26.4	510103	5407798			●		calcite
RAX08G150	H3401	22.9	510103	5407798			●		bslt
RAX08G151	H3401	92.7	510103	5407798		◒	◒		bslt
RAX08G152	H3369	26.1	510007	5407978		◒	◒		Rhy bx
RAX08G153	H3369	39.6	510007	5407978		●			Rhy tuff
RAX08G154	H3369	43.8	510007	5407978		●			ss bx
RAX08G155	H3369	58.7	510007	5407978		◒	●		bslt
RAX08G156	H3369	97.8	510007	5407978			●		bslt
RAX08G157	H3376	15.9	509949	5408000			○	●	Rhy
RAX08G158	H3376	47.0	509949	5408000		●			ss bx
RAX08G159	H3376	108.6	509949	5408000					bslt
RAX08G160	H3368	21.3	510002	5407547		◒	◒		Rhy
RAX08G161	H3368	61.3	510002	5407547		●	○		ss
RAX08G162	H3368	79.0	510002	5407547	◒	●			ms
RAX08G163	H3368	92.6	510002	5407547	●	●			Rhyd
RAX08G164	H3368	104.3	510002	5407547	●	●			Rhyd
RAX08G165	H3368	106.0	510002	5407547	◒	●			Rhyd
RAX08G166	H3368	117.6	510002	5407547				●	basalt
RAX08G167	H3371	12.4	510064	5407597		●	○		Rhy tuff
RAX08G168	H3371	30.6	510064	5407597		○	●		Turb
RAX08G169	H3371	46.7	510064	5407597					diabase
RAX08G170	H3371	76.6	510064	5407597	●	●			Rhyd
RAX08G171	H3371	85.6	510064	5407597		●	○		Rhy
RAX08G172	H3371	118.5	510064	5407597		●	○		ms/ss
RAX08G173	H3366	16.2	509952	5407605		○	●		Rhy
RAX08G174	H3366	27.5	509952	5407605		○	●		Rhy
RAX08G175	H3366	28.5	509952	5407605		●	○		ms
RAX08G176	H3366	93.6	509952	5407605					diabase
RAX08G177	H3366	95.1	509952	5407605		●			Rhyd
RAX08G178	H3366	103.0	509952	5407605		●	○		Rhyd
RAX08G179	H3404	12.9	509959	5407488		●	◒		Rhyd
RAX08G180	H3404	81.7	509959	5407488		●	○		Rhyd

Appendix 4.1: Summary of alteration mineralogy determined by SWIR

Sample No.	Drill Hole	Depth (m)	UTM (NAD83 - Zn 21N)*		Quartz	Illite	Chlorite	Phengite	Lithology
			Easting	Northing					
RAX08G181	H3404	89.9	509959	5407488		●			Rhyd
RAX08G182	H3404	102.6	509959	5407488		●			Rhy
RAX08G183	H3404	117.6	509959	5407488		●	○		Rhy
RAX08G184	H3374	43.4			●	●			Rhy
RAX08G185	H3374	28.7			●	●			bslt
RAX08G186	H3397	92.0	510109	5407938					bslt
RAX08G187	H3397	104.2	510109	5407938		◒	●		bslt
RAX08G188	H3397	131.8	510109	5407938		○	●		bslt
RAX08G189	HG24404	Box 19†					●		bslt
RAX08G190	HG24404	Box 34†				◒	●		int. dyke
RAX08G191	H3382	31.9	509550	5408090		●	○		Rhy
RAX08G192	H3382	168.7	509550	5408090					diabase
RAX08G193	H3382	275.1	509550	5408090	●	●			bslt
RAX08G194	H3382	305.7	509550	5408090					vein
RAX08G195	H3382	331.9	509550	5408090		○	●		bslt
RAX08G196	H3406	26.5	509561	5408010					Rhy
RAX08G197	H3406	34.6	509561	5408010		●			Rhy
RAX08G198	H3406	156.0	509561	5408010					diabase
RAX08G199	H3406	195.1	509561	5408010	●	●			bslt
RAX08G200	H3406	265.0	509561	5408010			●		bslt

*H3341 and H3344 are in NAD27

†Depth tags and blocks are unreliable

Appendix 4.2: SWIR wavelength positions

Sample name	H_2O + OH feature (nm)	Interlayer H_2O feature (nm)	AlOH feature (nm)	FeOH feature (nm)	MgOH feature (nm)
RAX08G001	1413	1912	2223	-	2346
RAX08G002	1414	1911	2222.5	2251	2344.5
RAX08G003	1415	1909	2223.5	-	2345
RAX08G004	1411	1908	2209	2252	2348
RAX08G005	1413	1908	2209	2248	2347
RAX08G006	1408	1915	2204	2253	2348
RAX08G007	1411	1908	2203	-	2347
RAX08G008	1411	1908	2205.5	-	2348
RAX08G009	1409	1909.5	2207	2249	2347
RAX08G010	1403	1910	-	2253	2340
RAX08G011	1401	-	-	2253.5	2340
RAX08G012	1400	-	-	2252	2339
RAX08G013	1413	1907	2220	-	2350
RAX08G014	1413.5	1909	2212	-	2352
RAX08G015	1412	1910	2217	2248	2348
RAX08G016	1408	1908	2209	2249	2342
RAX08G017	1407	1910	2213	2248	2344
RAX08G018	1406	1910	2215	2249	2343
RAX08G019	1401	1911	-	2251	2340
RAX08G020	1395	1911	-	2250	2338
RAX08G021	1399	-	2204	2250.5	2337
RAX08G022	1401	1907	-	2252	2342
RAX08G023	1403	1910	-	2252	2339.5
RAX08G024	1410	1908	-	2248.5	2350
RAX08G025	1412	1908	2021	-	2350
RAX08G026	1412.5	1909	2012	-	2350
RAX08G028	1414	1906	2220	-	2350
RAX08G029	1412	1908	2205	-	2350
RAX08G030	1414	1909	2209	-	2350
RAX08G032	1402	1909	-	2249	2339
RAX08G033	1409	1906	2210	2251	2346
RAX08G034	1410	1909	2209	2249	2349
RAX08G035	1410	1910	2211	2246	2344
RAX08G036	1410	1907	2207	2247	2349
RAX08G038	1409	1909	2204	2252	2347
RAX08G039	-	-	-	-	-
RAX08G040	1412	1907	2212	-	2349
RAX08G041	1393	1908	-	2248	2333
RAX08G042	1407	1912	2210	2250	2346
RAX08G043	1405	1912	-	2252	2344
RAX08G044	1404	1907	-	2250	2341
RAX08G045	1411	1908	2208	-	2347
RAX08G046	1403	-	-	2252	2340
RAX08G047	1401	-	-	2251	2341
RAX08G050	1407	-	-	-	-
RAX08G051	1407	-	2211	2250	2244

Appendix 4.2: SWIR wavelength positions

Sample name	H_2O + OH feature (nm)	Interlayer H_2O feature (nm)	AlOH feature (nm)	FeOH feature (nm)	MgOH feature (nm)
RAX08G053	1402	-	-	2253	2241
RAX08G056	1409	1909	2208	2248	2347
RAX08G057	1402	1910	-	2252	2343
RAX08G058	1405	1911	-	2252	2343
RAX08G059	1412	1907	2210	-	2353
RAX08G061	1399	1911	-	2254	2343
RAX08G062	1410	1907	2203	2250	2343
RAX08G063	1404	1910	-	2250	2346
RAX08G064	1397	1908	-	2253	2337
RAX08G065	1413	1910	2220	-	2346
RAX08G066	1411	1909	2203	-	2349
RAX08G068	-	-	-	-	-
RAX08G069	-	-	-	-	-
RAX08G070	1411	1908	2205	-	2349
RAX08G071	1409	1908	2209	2248	2345
RAX08G072	1411	1908	2208	-	2347
RAX08G073	1403	-	-	2251	2341
RAX08G074	1406	-	-	2250	-
RAX08G075	1396	-	-	-	-
RAX08G076	1411	1907	2201	-	-
RAX08G077	1414	1909	2207	-	2350
RAX08G078	1412	-	-	-	2350
RAX08G079	1404	-	-	2259	2341
RAX08G080	1411	1912	2201	-	2350
RAX08G081	1400	1914	-	2252	2337
RAX08G082	1411	1908	2207	-	2350
RAX08G083	1411	1909	2206	-	2351
RAX08G084	1399	-	-	2250	2339
RAX08G085	1399	-	-	2251	2341
RAX08G086	1414	1909	2222.5	-	2345
RAX08G087	1411	1909	2209	-	2351
RAX08G089	1399	1907	-	2251	2341
RAX08G090	1409	1909	2215	2250	2344.5
RAX08G091	1411	-	2208	-	-
RAX08G092	1407	1910	2210	2250	2342
RAX08G093	1407	-	2207	2250.5	2347
RAX08G095	1407	-	-	2253	2342
RAX08G096	1403	-	-	2252.5	2342
RAX08G097	1405	1909	-	2252	2344
RAX08G098	1399	1912	-	2253	2343
RAX08G099	1405	1909	-	2254	2340
RAX08G102	1411.5	1905	2215	-	2350
RAX08G103	1405	1910	-	2253	2340
RAX08G105	1411	1911	2200	-	2345
RAX08G106	1403	-	-	2251	2346.5
RAX08G107	1403	1912	-	2256	2340

Appendix 4.2: SWIR wavelength positions

Sample name	H_2O + OH feature (nm)	Interlayer H_2O feature (nm)	AlOH feature (nm)	FeOH feature (nm)	MgOH feature (nm)
RAX08G108	1410	1905	2206	-	2349
RAX08G109	1405	1930	-	-	2338
RAX08G110	1400	-	-	-	2340
RAX08G111	1401	-	-	2252	2340
RAX08G112	1411	1909	2206	2247.5	2349
RAX08G113	1409	1907	2205	2250	2347
RAX08G114	1410.5	1910	2202	-	2348
RAX08G115	1411	1911	2204.5	-	2348
RAX08G116	1411	1909	2203.5	-	2350
RAX08G117	1909	1905	-	2250	2346
RAX08G118	1411	1908	2203	-	2344
RAX08G119	1411	1907	2203	2250	2344
RAX08G120	1411	1908.5	2209	2248	2347
RAX08G121	1409	1910	2205	2248	2345
RAX08G122	1412.5	1913	-	-	-
RAX08G123	1412	1908	-	-	-
RAX08G124	1413	1907	2217.5	-	2351
RAX08G125	1407	1910	-	2251	2346
RAX08G126	1409	1908	2208	2250	2342
RAX08G127	1404	1909	-	2249	2342
RAX08G128	1408	1912	2203	2250	2341
RAX08G129	1406	1907	2196	-	2345
RAX08G130	1404	1910	-	2253.5	2345
RAX08G131	1410	1908.5	2204	-	2346
RAX08G132	1408.5	1908	2206	2252	2245
RAX08G133	1407	-	-	-	-
RAX08G134	1406.5	1909	2211	2251.5	2343
RAX08G135	1405	1907	-	2253.5	2344
RAX08G136	1411	1905	2203	-	2350
RAX08G137	1409	1908	2193	2260	2346
RAX08G138	-	-	-	-	-
RAX08G139	1411	1907	2201	-	2347
RAX08G140	1412	1912	2206	-	2348
RAX08G141	1407	1911	-	2254	2350
RAX08G142	1407	1910	2210	2251	2345
RAX08G143	1405	1912	-	2252	2339
RAX08G144	1415	1909	2221	-	2347
RAX08G145	-	-	-	-	-
RAX08G146	1412	1907	2211	-	2348.5
RAX08G147	1411	1907	2206	-	2348.5
RAX08G148	1409	1909	2205	2247.5	2345.5
RAX08G149	1395	-	-	2250	2341
RAX08G150	1405	1910	-	2250.5	2344
RAX08G151	1409	1907	2206	2251	2346
RAX08G152	1411	-	2208	2253	2347
RAX08G153	1412	1909	2207	-	2349

Appendix 4.2: SWIR wavelength positions

Sample name	H_2O + OH feature (nm)	Interlayer H_2O feature (nm)	AlOH feature (nm)	FeOH feature (nm)	MgOH feature (nm)
RAX08G154	1411	1909.5	2206	-	2350
RAX08G155	1407	1911	2209	2250	2346
RAX08G156	1403	1910	-	2253	2342
RAX08G157	1414	1918	2215	-	-
RAX08G158	1412	1909	2207	-	2351
RAX08G159	1411	1914	2207	2251	2344
RAX08G161	1411	1910	2200	-	2349
RAX08G162	1411	1907	2196	-	2349
RAX08G163	1411	1909	2205	-	2350
RAX08G164	1411	1909	2201	-	2346
RAX08G165	1410	1905	2200	-	2347
RAX08G166	1409	1909	2193	2255	2344
RAX08G167	1410	1909	2197	2256	2349
RAX08G168	1410	1909	-	2252	2349
RAX08G169	-	-	-	-	-
RAX08G170	1411	1911	2203	-	2346
RAX08G171	1408	1907	2196	-	2343.5
RAX08G172	1414	1922	2214	-	2351.5
RAX08G173	1409	1918	2205	2257.5	2345
RAX08G174	1408	1911	2207	2256	2343
RAX08G175	1411	1909	2205	-	2346
RAX08G176	1411	-	-	-	-
RAX08G177	1411	1909	2205	-	2346
RAX08G178	1410	1912	2207	2251	2342
RAX08G179	1407	1911	2192	2257	2341
RAX08G180	1411	1909	2202	2247.5	2347
RAX08G181	1412	1911	2207	-	2347.5
RAX08G182	1409	1907	2196	-	2347
RAX08G183	1409	1908	2190	2259	2350
RAX08G184	1411	1909	2202	-	2350
RAX08G185	1411	1908	2207.5	-	2350
RAX08G187	1407	1910	2209	2251	2348
RAX08G188	1405	-	-	2252.5	2345
RAX08G189	1404	-	-	2254	2342
RAX08G190	1410	1907	2205	2252	2347
RAX08G191	1415	1911	2224	-	2340
RAX08G192	-	-	-	-	-
RAX08G193	1412	1909	2209	-	2247
RAX08G195	1405	1909	-	2252	2346
RAX08G196	1413	1909	2219	-	2349
RAX08G197	1415	1910	2225	-	2346
RAX08G198	-	-	-	-	-
RAX08G199	1412	1905	2206	-	2349
RAX08G200	1403	-	-	2251.5	2337

Appendix 4.3: Mass balance calculations of major oxides and trace elements of the Lundberg and Engine House zones

Sample Name	RAX08G002	RAX08G010	RAX08G011	RAX08G013	RAX08G019	RAX08G022	RAX08G024	RAX08G025	RAX08G027	RAX08G029
SiO2 (%)	8.421	45.033	29.499	-1.285	65.135	56.809	-8.898	-4.384	0.295	23.512
Al2O3 (%)	1.115	-4.554	2.815	1.484	4.367	14.580	-2.179	0.722	0.175	-0.152
Fe2O3(T) (%)	0.941	0.785	5.181	1.230	12.341	12.796	-0.020	1.629	0.218	-0.014
MnO (%)	0.034	-0.182	0.627	0.029	0.612	1.841	0.043	0.019	0.006	-0.026
MgO (%)	0.162	-2.406	10.879	1.346	16.793	22.320	3.099	1.253	0.841	-0.130
CaO (%)	2.437	-7.380	-6.444	0.010	-7.291	-7.320	-0.552	0.969	2.066	0.617
Na2O (%)	-1.772	-5.034	-1.758	-1.325	-5.073	-5.003	-5.071	-4.133	-2.385	-4.908
K2O (%)	0.368	3.053	-0.410	0.336	0.828	1.719	0.290	2.561	0.107	0.555
TiO2 (%)	0.016	-0.402	-0.133	0.021	-0.070	0.119	0.001	0.023	0.009	0.020
P2O5 (%)	0.006	-0.020	-0.066	-0.008	-0.058	-0.011	-0.005	-0.009	-0.009	0.011
Sc (ppm)	0.471	-14.175	11.174	0.183	13.317	31.848	0.524	1.089	0.145	0.903
Be (ppm)	1.235	-	-	1.092	1.423	1.494	-0.095	1.036	1.073	-
V (ppm)	1.059	-291.905	-18.229	-1.679	52.490	139.790	2.762	-1.875	-3.818	-
Cr (ppm)	-10.588	111.268	76.609	-	94.550	373.571	-18.571	-49.107	-	59.355
Co (ppm)	-	-10.059	1.732	-	14.740	33.130	-	-	-	-
Ni (ppm)	-	46.659	-	-	-	124.966	-	-	-	-
Cu (ppm)	-	8761.070	-112.479	-	97.337	-0.602	-	-	-	-
Zn (ppm)	3.529	-	412.070	-	1103.813	1356.059	42.381	0.536	208.364	19.032
Ga (ppm)	3.412	-2.698	4.302	1.505	9.933	15.077	0.857	1.196	1.400	4.710
Ge (ppm)	0.476	0.975	0.748	-0.363	-	1.691	-	-0.080	0.147	1.987
As (ppm)	-	107.275	-	-	16.347	-	-	-	-	-
Rb (ppm)	12.118	62.139	-	26.165	16.907	36.917	-9.810	90.393	5.818	7.935
Sr (ppm)	447.471	-176.495	-146.661	-22.936	-177.610	-172.748	-136.952	-47.607	68.873	-121.484
Y (ppm)	1.100	2.922	-2.335	-1.061	-1.453	8.883	-3.062	-0.189	-2.665	0.365
Zr (ppm)	0.000	0.000	0.000	0.000	0.000	0.000	0.000	0.000	0.000	0.000
Nb (ppm)	0.453	0.429	-0.006	0.116	0.448	0.525	-0.729	0.289	-0.240	-0.019
Mo (ppm)	-	11.919	5.360	-	48.420	-	-	-	-	-
In (ppm)	-	2.508	0.150	-	0.409	0.634	-	-	-	-
Sb (ppm)	-	19.385	2.721	-	1.310	-	-	-	-	0.932
Cs (ppm)	0.394	1.860	0.219	0.546	0.587	1.461	0.314	1.739	0.744	0.113
Ba (ppm)	79.529	1096.037	-362.862	-429.523	-3.833	394.546	4321.000	737.464	-362.673	-619.613
La (ppm)	0.329	-0.536	-2.828	-4.351	-8.685	2.031	-8.681	-2.223	-1.107	-6.416
Ce (ppm)	0.053	1.416	-5.108	-5.200	-16.940	4.549	-15.605	-3.877	-3.645	-13.168
Pr (ppm)	1.526	-0.393	-1.168	1.073	-2.310	0.894	-0.204	1.104	1.087	-0.773
Nd (ppm)	2.882	-1.352	-5.056	1.612	-8.744	1.699	-1.971	2.134	1.755	-3.171
Sm (ppm)	0.245	0.072	-1.014	-0.046	-1.606	0.347	-0.669	0.100	-0.055	-0.807
Eu (ppm)	-0.005	-0.402	-0.527	-0.106	-0.666	-0.481	-0.393	-0.046	0.120	-0.349
Gd (ppm)	0.146	0.135	-0.727	-0.114	-1.100	0.593	-0.634	0.029	-0.117	-0.639
Tb (ppm)	0.063	0.003	-0.105	0.020	-0.125	0.249	-0.051	0.049	0.006	-0.060
Dy (ppm)	0.540	0.061	-0.711	0.238	-0.713	1.666	-0.166	0.465	0.139	-0.165
Ho (ppm)	0.082	0.032	-0.135	0.017	-0.115	0.309	-0.057	0.082	-0.020	-0.012
Er (ppm)	0.090	0.251	-0.271	-0.128	-0.213	0.913	-0.353	0.046	-0.269	0.023
Tm (ppm)	0.002	0.049	-0.028	-0.032	-0.026	0.131	-0.066	0.002	-0.060	0.014
Yb (ppm)	0.071	0.230	-0.296	-0.233	-0.259	0.695	-0.374	0.029	-0.365	0.146
Lu (ppm)	0.017	0.030	-0.059	-0.032	-0.046	0.083	-0.041	0.010	-0.057	0.028
Hf (ppm)	-0.135	0.429	0.144	-0.149	0.039	0.314	-0.252	0.064	-0.076	-0.535
Ta (ppm)	0.008	1.111	1.090	0.000	1.102	1.063	-0.106	0.008	-0.025	0.053
W (ppm)	-	4.517	4.116	-	6.114	2.739	-	-	-	-0.019
Tl (ppm)	-0.209	0.023	-	-0.239	0.156	0.335	-0.093	0.009	0.381	1.768
Pb (ppm)	-0.118	-8.834	5.132	-	875.093	32.817	-12.571	-10.875	58.691	-5.742
Bi (ppm)	-5.818	128.312	1.944	-	67.226	410.076	-19.810	-15.455	-6.082	-23.577
Th (ppm)	0.653	0.120	-0.517	0.455	-1.404	0.633	-2.429	0.727	-0.178	0.058
U (ppm)	0.156	0.160	-0.811	-0.655	-0.410	-0.486	-0.352	-0.080	0.532	-0.617

Appendix 4.3: Mass balance calculations of major oxides and trace elements of the Lundberg and Engine House zones

Sample Name	RAX08G030	RAX08G031	RAX08G039	RAX08G040	RAX08G044	RAX08G045	RAX08G050	RAX08G060	RAX08G062	RAX08G065
SiO2 (%)	1.206	-31.301	-26.247	19.141	29.193	17.106	36.135	-30.504	-22.684	-7.756
Al2O3 (%)	-2.065	1.341	0.802	0.048	3.740	-6.994	4.694	-1.868	-1.996	0.177
Fe2O3(T) (%)	-0.749	0.240	0.820	0.128	2.235	-1.247	4.367	0.606	1.219	1.582
MnO (%)	0.003	0.013	-0.005	-0.032	0.651	-0.116	0.413	-0.005	0.048	0.022
MgO (%)	0.399	1.504	2.508	0.627	12.224	-1.015	10.754	1.289	5.716	0.658
CaO (%)	1.389	0.936	0.159	-1.216	-7.072	-7.424	-7.056	0.120	-0.538	1.757
Na2O (%)	-3.568	-5.796	-5.129	-4.363	-5.169	-5.196	-5.242	-3.968	-4.981	-3.999
K2O (%)	1.261	3.515	1.522	2.103	1.354	1.932	2.075	0.368	-0.205	1.979
TiO2 (%)	-0.044	0.090	0.047	0.024	-0.135	-0.211	-0.066	-0.020	0.010	0.009
P2O5 (%)	0.002	0.047	0.042	0.012	-0.055	-0.027	-0.078	-0.015	-0.017	-0.001
Sc (ppm)	-1.176	3.045	1.760	2.333	11.565	-12.225	12.295	-1.202	0.957	0.914
Be (ppm)	-	1.526	1.563	1.193	0.840	0.402	2.445	-0.301	-0.174	0.966
V (ppm)	2.321	37.782	27.170	9.889	-8.226	-153.887	49.425	-4.104	29.000	2.793
Cr (ppm)	-	30.521	-	83.481	322.236	2.600	-	-	-	-
Co (ppm)	-41.968	-39.948	-39.092	-40.615	6.859	-8.758	4.013	-	-	-
Ni (ppm)	-	-	-	-	64.571	-2.567	7.650	-	-	-
Cu (ppm)	-	7.630	-	95.407	-112.835	36.037	-112.105	-	-	-
Zn (ppm)	194.731	168.758	1056.544	1504.519	283.561	797.313	393.755	-9.018	93.913	9.310
Ga (ppm)	-4.744	1.498	1.068	1.311	3.803	-2.327	9.423	-0.209	3.217	1.793
Ge (ppm)	1.032	0.763	0.625	0.835	0.876	0.511	1.226	-0.710	-	0.372
As (ppm)	101.141	-	-	41.741	32.110	106.253	59.768	-	-	-
Rb (ppm)	26.282	75.038	38.146	56.556	32.086	42.448	45.003	14.847	-12.130	78.810
Sr (ppm)	-137.923	-193.507	-113.515	-188.104	-181.405	-186.805	-176.078	-34.331	-169.130	-88.672
Y (ppm)	-2.736	-6.860	-5.034	2.117	0.328	-2.270	4.217	-6.710	-2.700	-0.898
Zr (ppm)	0.000	0.000	0.000	0.000	0.000	0.000	0.000	0.000	0.000	0.000
Nb (ppm)	-0.975	-0.269	-0.311	-0.587	0.243	0.141	0.346	-0.813	-0.752	-0.378
Mo (ppm)	-	-	-	16.696	3.759	24.922	14.705	-	-	-
In (ppm)	-	-	-	-	0.146	0.307	0.307	-	-	-
Sb (ppm)	6.621	-	-	-	-	1.719	1.566	-5.671	-3.326	-2.074
Cs (ppm)	0.739	2.557	2.155	1.122	1.084	0.792	1.456	1.109	0.409	1.859
Ba (ppm)	318.186	292.972	1289.767	567.415	74.105	639.817	202.033	-99.939	-331.522	84.000
La (ppm)	-3.515	-0.029	4.577	-5.405	-1.784	-5.967	-8.246	-14.048	-7.426	0.279
Ce (ppm)	-7.721	1.689	5.574	-9.306	-2.975	-10.667	-15.622	-21.356	-12.717	-0.483
Pr (ppm)	-0.854	0.822	1.188	-0.668	-0.328	-1.217	-1.605	-1.796	-0.835	-0.093
Nd (ppm)	-7.850	-1.860	-2.379	-7.790	-3.218	-5.903	-6.634	-5.570	-3.270	-0.095
Sm (ppm)	-1.137	-0.067	-0.296	-1.105	-0.771	-1.258	-1.315	-1.040	-0.784	-0.028
Eu (ppm)	-0.052	-0.112	-0.224	-0.372	-0.579	-0.671	-0.631	-0.400	-0.452	-0.030
Gd (ppm)	-1.036	-0.300	-0.474	-0.955	-0.738	-0.895	-0.579	-0.921	-0.992	-0.087
Tb (ppm)	-0.114	0.017	0.017	0.018	-0.014	-0.084	0.044	-0.139	-0.101	-0.008
Dy (ppm)	-0.109	0.283	0.269	1.234	-0.004	-0.509	0.538	-0.788	-0.476	-0.046
Ho (ppm)	-0.013	-0.048	0.004	0.303	-0.033	-0.084	0.095	-0.180	-0.096	-0.010
Er (ppm)	0.246	-0.105	0.111	1.199	-0.128	-0.059	0.268	-0.615	-0.331	-0.025
Tm (ppm)	0.004	-0.078	-0.041	0.132	-0.030	0.005	0.037	-0.103	-0.050	-0.010
Yb (ppm)	0.129	-0.518	-0.128	0.868	-0.297	-0.106	0.134	-0.702	-0.312	-0.048
Lu (ppm)	-0.037	-0.119	-0.047	0.073	-0.035	-0.036	0.009	-0.102	-0.038	-0.008
Hf (ppm)	-0.172	0.355	0.389	0.470	0.097	-0.165	0.192	-0.033	-0.048	0.036
Ta (ppm)	-0.832	-0.757	-0.740	-0.802	1.073	1.092	1.092	-0.100	-0.087	-0.018
W (ppm)	-	-	-	-	0.510	4.275	3.765	-0.510	0.652	-0.116
Tl (ppm)	1.417	0.928	0.687	2.001	0.191	1.157	0.268	0.004	0.301	0.345
Pb (ppm)	26.186	-6.659	6.757	172.852	9.012	1353.233	76.150	-13.804	-	-4.241
Bi (ppm)	0.413	15.642	20.164	14.788	97.058	19.105	366.268	-12.860	-20.230	-23.307
Th (ppm)	-1.248	0.222	0.822	-0.362	-0.616	-0.505	-1.133	-2.059	-3.113	-0.112
U (ppm)	0.356	0.960	-0.967	2.694	-0.851	-0.237	-0.676	-1.901	0.860	-0.395

Appendix 4.3: Mass balance calculations of major oxides and trace elements of the Lundberg and Engine House zones

Sample Name	RAX08G070	RAX08G073	RAX08G075	RAX08G077	RAX08G083	RAX08G086	RAX08G089	RAX08G092	RAX08G097	RAX08G110
SiO2 (%)	15.205	18.955	74.625	41.622	99.579	5.803	39.848	21.955	19.678	47.475
Al2O3 (%)	-1.275	0.158	10.159	2.300	7.231	1.352	7.564	-0.989	3.900	3.387
Fe2O3(T) (%)	-1.545	0.367	13.099	0.231	-6.297	0.584	7.561	0.279	0.015	2.670
MnO (%)	-0.031	0.292	2.286	0.047	-0.167	0.011	1.597	0.396	0.386	0.345
MgO (%)	0.313	6.322	31.009	-0.270	-1.469	0.859	23.139	7.754	9.391	11.681
CaO (%)	-1.001	-7.418	-6.993	3.540	-7.265	0.955	-7.195	-7.212	-7.230	-5.911
Na2O (%)	-6.067	-5.251	-5.245	-1.128	-5.000	-3.895	-5.221	-5.194	-3.131	-2.308
K2O (%)	2.643	2.111	-0.406	0.641	6.520	3.507	0.023	1.126	1.026	-0.053
TiO2 (%)	-0.021	-0.066	0.032	0.034	-0.004	0.020	0.057	-0.044	-0.065	-0.101
P2O5 (%)	0.007	-0.054	-0.060	0.011	-0.003	0.006	-0.021	-0.038	-0.018	-0.052
Sc (ppm)	-1.738	-0.578	44.124	0.560	5.868	0.515	29.423	-2.404	-1.074	17.679
Be (ppm)	-	1.832	1.738	-	3.335	0.129	1.183	-	0.684	1.037
V (ppm)	-	-21.070	180.277	0.120	57.829	-2.228	71.962	-62.229	-55.894	-33.827
Cr (ppm)	88.828	8.730	1197.950	97.600	-	-	440.715	-3.030	89.333	253.599
Co (ppm)	-	27.000	49.634	-	-0.486	-	29.524	-5.652	-3.389	8.279
Ni (ppm)	-	13.780	283.500	-	-	-	85.176	-	-	43.270
Cu (ppm)	11.103	-115.170	485.570	-	-107.656	-	-109.401	-	-	-
Zn (ppm)	266.690	200.660	1238.988	-	-	26.436	657.886	431.598	166.489	299.734
Ga (ppm)	-0.786	2.986	14.020	2.160	7.099	3.545	10.414	0.884	4.238	3.251
Ge (ppm)	1.332	0.736	1.415	0.928	0.989	0.493	1.623	0.751	0.783	0.994
As (ppm)	29.979	85.820	23.577	-	229.381	-	-	52.543	9.130	64.614
Rb (ppm)	56.062	48.374	-	-4.960	130.674	98.475	0.921	22.078	24.819	-0.103
Sr (ppm)	-135.959	-178.836	-179.496	-65.440	-156.452	130.911	-177.971	-183.490	-159.481	-111.505
Y (ppm)	-6.577	0.999	6.469	4.292	-1.829	0.498	3.307	0.661	5.942	1.314
Zr (ppm)	0.000	0.000	0.000	0.000	0.000	0.000	0.000	0.000	0.000	0.000
Nb (ppm)	-0.892	0.284	0.558	0.824	-0.416	0.844	0.724	0.202	0.678	0.851
Mo (ppm)	2.221	4.284	4.095	-	5.312	-	2.986	6.886	-	6.007
In (ppm)	-	0.245	0.707	-	-	-	-	-	0.391	-
Sb (ppm)	14.268	1.474	2.002	-4.780	6.405	-4.946	0.962	-	0.402	-
Cs (ppm)	1.364	0.873	0.477	0.716	2.538	2.435	1.393	0.521	0.422	1.095
Ba (ppm)	5808.407	814.726	-454.467	-74.080	3248.099	2053.604	-218.143	197.748	-53.308	-327.343
La (ppm)	-8.239	-1.533	5.149	-4.852	-5.184	1.019	-1.018	-2.489	-1.523	-6.788
Ce (ppm)	-14.479	-1.738	10.183	-6.264	-10.466	2.250	-2.452	-4.748	-2.805	-10.979
Pr (ppm)	-2.648	0.142	1.519	0.072	-1.393	0.872	-0.478	-0.776	-0.500	-1.336
Nd (ppm)	-11.903	-1.531	2.529	1.188	-5.600	2.062	-2.670	-4.198	-3.077	-5.500
Sm (ppm)	-1.492	-0.417	0.318	0.146	-1.080	-0.002	-0.571	-0.975	-0.638	-1.039
Eu (ppm)	-0.368	-0.675	-0.543	0.086	-0.457	-0.314	-0.469	-0.633	-0.551	-0.530
Gd (ppm)	-1.425	-0.523	0.372	0.447	-0.568	0.050	-0.151	-0.736	-0.131	-0.747
Tb (ppm)	-0.227	0.034	0.200	0.092	-0.060	0.023	0.023	-0.054	0.059	-0.040
Dy (ppm)	-0.881	0.284	1.271	0.639	-0.447	0.132	0.060	-0.289	0.551	-0.162
Ho (ppm)	-0.134	0.012	0.242	0.130	-0.115	0.032	0.027	-0.035	0.126	-0.019
Er (ppm)	0.064	0.053	0.567	0.432	-0.178	0.009	0.219	-0.001	0.485	0.038
Tm (ppm)	-0.018	0.011	0.068	0.068	-0.002	-0.002	0.040	0.006	0.076	0.010
Yb (ppm)	-0.014	-0.035	0.225	0.455	-0.084	0.026	0.110	-0.153	0.337	-0.076
Lu (ppm)	-0.048	-0.022	0.008	0.056	-0.024	-0.001	-0.010	-0.047	0.025	-0.033
Hf (ppm)	0.252	0.162	0.086	-0.408	-0.020	-0.327	0.003	-0.049	-0.104	-0.143
Ta (ppm)	-0.778	1.098	1.071	0.021	1.158	0.035	1.108	1.088	1.130	1.116
W (ppm)	2.998	10.078	4.967	-	4.526	-	2.845	1.907	3.041	1.437
Tl (ppm)	2.377	0.226	0.177	0.488	2.876	1.340	0.014	0.445	0.379	0.019
Pb (ppm)	143.448	11.172	45.500	3.280	11.884	9.089	56.318	16.727	-	-5.859
Bi (ppm)	3.553	133.634	320.646	-22.940	5.339	-23.136	2.344	2.502	1.304	2.982
Th (ppm)	-0.750	-0.112	0.113	1.039	-0.066	0.667	0.195	-0.395	-0.095	-1.028
U (ppm)	0.476	-0.357	-0.582	-0.242	0.768	0.294	-0.532	-0.626	-0.506	-0.991

Appendix 4.3: Mass balance calculations of major oxides and trace elements of the Lundberg and Engine House zones

Sample Name	RAX08G112	RAX08G117	RAX08G118	RAX08G122	RAX08G124	RAX08G129	RAX08G130	RAX08G135	RAX08G137	RAX08G139
SiO2 (%)	10.721	48.885	28.363	0.000	4.526	-23.915	28.357	17.558	-3.076	41.056
Al2O3 (%)	0.024	2.870	-2.806	0.000	-0.265	-2.073	3.972	3.088	-1.823	1.634
Fe2O3(T) (%)	1.579	-1.564	-7.682	0.000	0.371	0.618	3.195	-0.724	-0.134	1.596
MnO (%)	0.108	0.077	-0.167	0.000	0.009	-0.035	0.688	0.258	-0.016	-0.015
MgO (%)	3.357	4.716	-2.902	0.000	0.129	2.268	6.845	4.251	-0.240	0.439
CaO (%)	-1.249	-7.194	-7.150	0.000	0.396	-0.265	-7.031	-7.222	0.518	-1.212
Na2O (%)	-6.051	-5.119	-2.108	0.000	-1.132	-4.863	-0.618	-2.241	0.382	-6.039
K2O (%)	1.969	3.515	2.848	0.000	0.094	-1.173	-0.054	1.633	-1.919	3.454
TiO2 (%)	0.041	0.009	-0.470	0.000	0.036	0.014	-0.049	-0.112	0.075	0.210
P2O5 (%)	0.021	-0.002	-0.055	0.000	0.003	-	-0.048	-0.029	0.007	0.057
Sc (ppm)	3.100	7.698	-15.243	0.000	0.222	1.250	10.902	4.326	2.650	7.700
Be (ppm)	-	-	-	0.000	0.056	-0.250	0.773	0.606	-	-
V (ppm)	13.850	11.113	-184.560	0.000	7.889	0.750	10.416	-28.426	15.700	62.255
Cr (ppm)	-	-	55.577	0.000	-	-	111.268	57.770	52.000	-
Co (ppm)	-38.400	-5.183	-20.770	-	-	-	10.839	22.096	-	-37.145
Ni (ppm)	-	-	-	-	-	-	32.727	26.040	-	-
Cu (ppm)	-	-81.455	-9.367	-	-	-	833.865	-78.390	-	322.000
Zn (ppm)	208.000	470.380	-38.103	0.000	43.889	82.500	657.066	372.300	8.000	6022.818
Ga (ppm)	0.800	4.825	-1.233	0.000	2.667	1.250	4.268	4.212	-1.450	3.100
Ge (ppm)	0.805	0.920	0.664	0.000	0.594	-0.525	1.115	0.858	-0.345	1.025
As (ppm)	72.450	131.795	198.093	-	-	-	22.291	118.922	-	206.373
Rb (ppm)	36.750	72.588	54.327	0.000	15.222	-27.250	-1.948	28.758	-42.200	71.355
Sr (ppm)	-224.350	-185.273	-342.727	0.000	23.944	2.750	-70.614	-126.118	-48.150	-213.582
Y (ppm)	-1.810	-4.978	-4.003	0.000	1.206	-5.375	0.135	-0.717	-6.120	0.323
Zr (ppm)	0.000	0.000	0.000	0.000	0.000	0.000	0.000	0.000	0.000	0.000
Nb (ppm)	-0.515	0.039	0.213	0.000	-0.683	-0.675	0.568	0.529	0.330	-0.609
Mo (ppm)	-	36.160	5.760	-	-	-	-	-	-	10.245
In (ppm)	0.115	-	-	-	-	-	0.279	0.123	-	0.293
Sb (ppm)	0.190	0.340	1.550	0.000	-3.556	2.100	2.527	3.068	-4.495	2.135
Cs (ppm)	0.845	0.996	0.570	0.000	0.344	0.250	0.188	0.873	-0.405	0.981
Ba (ppm)	574.400	1011.193	760.433	0.000	-313.944	5154.750	-180.117	417.502	-1089.250	1569.464
La (ppm)	1.925	-8.077	1.181	0.000	-3.328	-10.350	3.365	3.003	-18.665	-0.093
Ce (ppm)	4.690	-15.929	0.985	0.000	-9.739	-16.975	6.989	4.883	-31.800	-0.307
Pr (ppm)	0.135	-1.682	-0.335	0.000	-0.451	-0.308	1.028	0.608	-2.254	-0.496
Nd (ppm)	-3.480	-6.542	-3.566	0.000	-0.856	-2.500	1.295	0.186	-6.545	-4.484
Sm (ppm)	-0.409	-1.223	-0.912	0.000	-0.227	-0.688	0.211	-0.110	-1.249	-0.223
Eu (ppm)	-0.877	-0.759	-0.606	0.000	-0.138	-0.184	-0.071	-0.168	-0.328	-0.390
Gd (ppm)	-0.687	-0.962	-1.261	0.000	-0.058	-0.600	-0.116	-0.254	-0.870	-0.043
Tb (ppm)	-0.063	-0.079	-0.174	0.000	-0.007	-0.050	0.059	-0.039	-0.146	0.021
Dy (ppm)	0.069	-0.810	-1.116	0.000	0.044	-0.238	0.256	-0.341	-0.876	0.547
Ho (ppm)	0.042	-0.212	-0.223	0.000	0.002	-0.120	0.004	-0.061	-0.211	0.132
Er (ppm)	0.491	-0.499	-0.512	0.000	0.016	-0.575	-0.028	-0.094	-0.718	0.613
Tm (ppm)	0.048	-0.061	-0.057	0.000	0.005	-0.101	-0.003	-0.007	-0.120	0.045
Yb (ppm)	0.417	-0.280	-0.453	0.000	0.028	-0.750	-0.104	-0.157	-0.833	0.296
Lu (ppm)	0.009	0.006	-0.072	0.000	0.021	-0.129	-0.028	-0.047	-0.136	-0.010
Hf (ppm)	0.070	-0.114	-0.119	0.000	-0.433	-0.225	0.150	-0.084	-0.560	-0.202
Ta (ppm)	-0.790	1.123	1.111	0.000	-0.007	-0.090	1.098	1.135	0.035	-0.822
W (ppm)	1.495	3.765	0.947	0.000	-0.050	0.800	2.706	1.619	-	2.781
Tl (ppm)	1.086	0.881	1.254	0.000	0.830	6.963	0.372	1.844	-0.415	2.539
Pb (ppm)	-3.950	106.800	-3.500	0.000	5.222	9.000	163.920	2.590	-	686.155
Bi (ppm)	1.725	1.839	2.988	0.000	-22.961	-	285.602	2.697	-	4.391
Th (ppm)	-0.373	-0.351	0.381	0.000	-1.433	-2.075	0.287	-0.039	-6.358	-1.316
U (ppm)	1.477	-0.109	0.329	0.000	-0.238	4.965	-0.565	-0.504	-2.066	0.813

Appendix 4.3: Mass balance calculations of major oxides and trace elements of the Lundberg and Engine House zones

Sample Name	RAX08G141	RAX08G144	RAX08G146	RAX08G148	RAX08G151	RAX08G153	RAX08G156	RAX08G157	RAX08G159	RAX08G160
SiO2 (%)	13.632	-7.980	68.714	12.208	36.436	-31.802	25.085	46.103	34.580	21.435
Al2O3 (%)	3.935	-0.914	2.596	0.587	2.815	0.293	2.235	0.137	4.507	-1.329
Fe2O3(T) (%)	0.485	0.849	-1.472	-1.958	1.907	-0.258	1.647	0.082	6.755	-0.105
MnO (%)	0.289	-0.006	-0.160	0.318	0.461	-0.006	0.578	-0.006	0.914	-0.004
MgO (%)	1.232	0.585	-1.700	9.026	9.309	1.455	10.751	-0.372	15.179	0.525
CaO (%)	-7.287	0.470	-7.291	-7.388	-7.296	0.336	-7.210	0.470	-7.264	-1.069
Na2O (%)	-1.555	-3.725	-5.104	-5.164	-5.137	-5.187	-4.072	0.401	-4.757	-4.950
K2O (%)	2.093	1.732	5.817	1.593	1.817	1.606	0.835	-0.078	0.323	1.645
TiO2 (%)	-0.042	0.036	-0.191	-0.205	-0.093	0.037	-0.110	0.004	-0.103	0.005
P2O5 (%)	-0.060	0.006	-0.048	-0.051	-0.037	0.026	-0.038	0.008	-0.024	0.036
Sc (ppm)	2.864	1.607	3.781	5.645	5.193	2.381	3.100	0.385	13.102	1.212
Be (ppm)	1.738	-0.066	1.083	0.537	0.875	1.438	0.742	-	0.993	-
V (ppm)	10.523	10.623	-39.119	-105.849	-31.685	27.219	-16.302	-	22.808	16.030
Cr (ppm)	19.104	-	227.367	52.912	91.560	28.750	67.306	-	310.713	144.179
Co (ppm)	0.122	-	7.588	-1.568	6.218	-40.125	-3.650	-	7.319	-40.597
Ni (ppm)	-	-	28.083	-	-	-	-	-	41.526	-
Cu (ppm)	-	-	-93.374	-	-	7.188	-100.186	-	-	72.090
Zn (ppm)	107.295	16.721	-13.209	230.963	531.680	862.063	245.613	28.462	612.338	1864.343
Ga (ppm)	3.410	2.148	5.506	4.189	7.292	0.656	5.166	0.231	5.954	0.216
Ge (ppm)	-	0.015	-	-	1.047	0.575	1.090	0.262	1.129	0.841
As (ppm)	9.431	-	228.172	34.698	20.932	-	8.173	-	8.066	54.067
Rb (ppm)	38.990	64.262	133.036	34.564	42.124	40.344	19.631	-18.231	7.658	34.261
Sr (ppm)	-131.163	-54.115	-158.539	-176.338	-176.563	-121.281	-176.929	-4.231	-178.255	-191.343
Y (ppm)	1.164	-1.641	-2.543	-0.262	2.599	-7.891	-1.521	-0.654	-1.969	-8.885
Zr (ppm)	0.000	0.000	0.000	0.000	0.000	0.000	0.000	0.000	0.000	0.000
Nb (ppm)	-0.385	-0.408	0.584	0.166	0.742	-0.184	0.652	-0.123	0.136	-0.675
Mo (ppm)	-	-	13.002	2.850	3.865	-	4.829	-	7.446	3.604
In (ppm)	-	-	0.170	0.116	0.150	-	0.272	-	0.323	-
Sb (ppm)	-	-4.898	2.094	-	0.179	1.225	1.378	0.131	10.043	1.903
Cs (ppm)	0.949	1.369	1.813	1.274	2.312	1.823	0.315	-0.208	0.415	0.651
Ba (ppm)	315.320	-438.344	1946.188	360.805	123.053	1447.969	-141.418	167.308	-240.537	380.925
La (ppm)	1.329	-6.226	-3.297	3.662	-2.977	2.213	-1.697	-8.938	-2.804	-7.369
Ce (ppm)	-0.073	-8.751	-7.159	8.808	-5.855	3.066	-2.732	-14.262	-6.209	-14.417
Pr (ppm)	-0.273	-0.268	-1.146	0.618	-0.854	0.753	-0.090	-1.132	-1.275	-2.153
Nd (ppm)	-1.856	-1.482	-5.614	0.072	-4.084	-4.400	-2.729	-2.811	-5.457	-11.454
Sm (ppm)	-0.271	-0.423	-1.255	-0.081	-0.775	-0.808	-0.748	-0.426	-1.125	-1.882
Eu (ppm)	-0.023	-0.266	-0.633	-0.599	-0.588	-0.292	-0.563	-0.194	-0.625	-0.650
Gd (ppm)	0.006	-0.443	-1.144	-0.375	-0.623	-0.861	-0.766	-0.261	-0.935	-1.615
Tb (ppm)	0.024	-0.001	-0.077	0.013	0.029	-0.004	-0.036	-0.045	-0.135	-0.107
Dy (ppm)	0.009	0.160	-0.308	0.036	0.291	0.308	-0.277	-0.147	-0.814	-0.301
Ho (ppm)	-0.017	-0.002	-0.067	-0.031	0.029	-0.050	-0.081	-0.015	-0.135	-0.143
Er (ppm)	0.084	-0.150	-0.121	-0.075	0.162	-0.201	-0.253	0.002	-0.295	-0.352
Tm (ppm)	0.023	-0.014	-0.008	-0.003	0.027	-0.104	-0.029	0.006	-0.036	-0.099
Yb (ppm)	0.060	-0.052	-0.137	-0.110	0.018	-0.789	-0.287	0.089	-0.341	-0.660
Lu (ppm)	0.005	-0.013	-0.023	-0.040	-0.010	-0.194	-0.051	0.022	-0.055	-0.159
Hf (ppm)	-0.150	-0.516	-0.097	-0.065	-0.155	0.444	0.107	-0.092	0.136	-0.095
Ta (ppm)	1.106	-0.095	1.102	1.081	1.105	-0.712	1.109	0.003	1.161	-0.776
W (ppm)	3.552	-0.159	3.696	2.556	2.322	-	3.186	0.754	4.458	2.283
Tl (ppm)	0.754	3.976	2.237	0.795	0.812	0.422	0.088	-0.135	0.047	1.031
Pb (ppm)	-	0.689	25.067	-	24.568	13.156	-7.627	-6.308	8.397	605.567
Bi (ppm)	-	-23.420	12.771	1.504	1.047	-	14.848	-21.215	12.099	0.601
Th (ppm)	-0.417	-1.548	0.180	0.335	-0.008	1.088	-0.164	0.033	-0.479	-2.104
U (ppm)	-0.652	-0.436	-0.301	0.099	-0.541	-0.282	-0.853	-0.368	-0.708	0.087

Appendix 4.3: Mass balance calculations of major oxides and trace elements of the Lundberg and Engine House zones

Sample Name	RAX08G164	RAX08G165	RAX08G166	RAX08G170	RAX08G171	RAX08G174	RAX08G177	RAX08G179	RAX08G180	RAX08G181
SiO2 (%)	-14.927	28.612	-9.784	15.349	-6.666	24.276	25.233	-11.237	-23.927	-16.463
Al2O3 (%)	-2.871	-1.060	-2.331	-0.894	-0.134	1.505	3.760	-3.614	-2.896	-2.874
Fe2O3(T) (%)	0.641	-0.136	0.185	0.637	0.277	1.863	0.370	2.144	-0.488	-0.399
MnO (%)	0.035	-0.035	0.009	-0.034	-0.014	0.034	0.009	0.063	0.016	-0.008
MgO (%)	0.793	0.183	0.608	0.317	0.533	1.443	1.404	1.188	-0.255	-0.205
CaO (%)	-0.042	-1.264	2.218	-1.250	0.863	0.463	0.775	0.951	1.559	0.709
Na2O (%)	-2.189	-5.986	-5.538	-6.017	-1.903	-1.819	-3.389	-2.497	-2.676	-2.664
K2O (%)	-0.783	2.474	0.894	2.690	-0.114	0.468	2.415	-1.742	-0.180	-0.079
TiO2 (%)	0.091	0.064	0.034	0.078	0.097	-0.044	-0.068	0.041	0.055	0.054
P2O5 (%)	0.016	0.041	0.050	0.031	0.045	-0.007	0.008	0.003	0.016	-0.002
Sc (ppm)	4.261	2.920	4.480	4.160	3.985	6.116	-0.214	2.234	1.846	0.783
Be (ppm)	-0.174	-	1.840	-	0.953	-	-	-0.109	-0.269	-0.203
V (ppm)	37.261	17.156	6.720	13.695	9.148	9.156	13.831	18.609	19.500	20.497
Cr (ppm)	-	-	-	-	-	-	-	-	-	-76.084
Co (ppm)	-	-39.227	-40.240	-39.574	-41.095	-37.721	-40.271	-	-	-
Ni (ppm)	-	-	27.600	-	-	-	-	-	-	-
Cu (ppm)	-	25.156	-	11.418	-	52.787	13.644	-	-	-
Zn (ppm)	160.000	1474.797	33.200	3928.780	35.160	57.180	59.864	121.406	-8.077	9.860
Ga (ppm)	0.739	2.094	-1.040	1.844	-0.615	2.836	2.008	0.688	0.231	-0.434
Ge (ppm)	-0.457	1.258	1.104	0.685	0.762	0.792	2.319	-0.398	-0.469	-0.403
As (ppm)	-	99.367	11.040	95.915	105.746	-	-	-	-	-
Rb (ppm)	-12.957	55.438	42.040	51.227	2.148	21.951	72.322	-38.875	-2.885	1.035
Sr (ppm)	-115.435	-208.070	-156.040	-213.021	-93.148	-122.189	-82.822	-106.516	-92.654	-105.874
Y (ppm)	-6.913	-2.662	-8.112	-4.343	-0.227	3.118	-4.664	-7.658	-6.646	-8.334
Zr (ppm)	0.000	0.000	0.000	0.000	0.000	0.000	0.000	0.000	0.000	0.000
Nb (ppm)	0.074	-1.352	1.256	-0.547	-0.046	0.015	4.551	0.277	1.631	1.020
Mo (ppm)	-	6.289	-	7.993	-	6.598	-	-	-	-
In (ppm)	-	0.252	-	0.343	-	-	-	-	-	-
Sb (ppm)	-4.813	3.148	0.696	2.012	1.977	0.556	1.274	-5.766	-5.715	-5.981
Cs (ppm)	0.078	0.942	0.730	0.495	0.286	0.338	0.902	-0.055	0.304	-0.022
Ba (ppm)	-837.087	466.156	38.040	893.170	111.379	-34.082	173.576	-1073.813	-755.654	-758.643
La (ppm)	-20.396	-0.052	-1.548	-1.970	-0.467	-6.266	1.974	-26.345	-18.731	-21.787
Ce (ppm)	-33.287	-2.109	-3.360	-4.368	2.830	-12.081	-1.009	-44.477	-31.654	-36.929
Pr (ppm)	-2.380	-0.781	-0.928	-1.017	0.069	-1.927	0.073	-3.473	-1.723	-2.333
Nd (ppm)	-7.317	-4.580	-7.620	-7.450	-3.039	-9.170	-3.347	-10.345	-4.477	-6.217
Sm (ppm)	-1.395	-0.086	-1.230	-0.862	0.097	-1.095	-0.615	-1.904	-1.055	-1.407
Eu (ppm)	-0.359	-0.279	-0.413	-0.613	0.029	-0.580	-0.424	-0.440	-0.347	-0.432
Gd (ppm)	-1.108	-0.025	-1.216	-0.942	-0.027	-0.721	-0.679	-1.317	-0.787	-1.038
Tb (ppm)	-0.126	-0.067	-0.077	0.011	0.164	0.122	-0.005	-0.155	-0.104	-0.161
Dy (ppm)	-0.666	-0.116	-0.144	0.669	1.373	1.407	-0.006	-0.811	-0.768	-1.048
Ho (ppm)	-0.187	-0.005	-0.105	0.056	0.172	0.238	-0.054	-0.235	-0.205	-0.257
Er (ppm)	-0.753	0.437	-0.216	0.211	0.606	0.947	0.129	-0.878	-0.758	-0.964
Tm (ppm)	-0.119	0.029	-0.061	-0.014	0.067	0.131	-0.014	-0.138	-0.130	-0.158
Yb (ppm)	-0.832	0.212	-0.333	-0.035	0.558	0.919	0.284	-0.964	-0.795	-1.024
Lu (ppm)	-0.141	-0.014	-0.100	-0.057	0.021	0.084	0.131	-0.155	-0.106	-0.141
Hf (ppm)	-0.626	-0.275	-0.068	-0.189	-0.108	0.187	0.475	-0.661	-0.604	-0.650
Ta (ppm)	-0.045	-0.811	-0.640	-0.837	-0.805	-0.757	-0.391	-0.014	0.069	0.060
W (ppm)	0.487	2.767	0.644	17.699	0.572	0.792	-	-0.377	-	-
Tl (ppm)	0.037	1.991	1.049	2.117	1.938	0.365	0.995	-0.322	-0.193	-0.245
Pb (ppm)	-9.739	42.086	-0.960	38.241	10.864	-4.082	-3.814	-	-14.346	-
Bi (ppm)	-22.874	1.509	0.460	3.882	0.286	0.396	-	-23.611	-	-
Th (ppm)	-7.219	-0.903	0.303	-1.435	-1.188	-1.472	2.515	-6.821	-6.515	-6.636
U (ppm)	-2.403	0.629	0.485	0.549	1.063	0.038	0.997	-2.130	-2.019	-2.091

Appendix 4.3: Mass balance calculations of major oxides and trace elements of the Lundberg and Engine House zones

Sample Name	RAX08G182	RAX08G183	RAX08G186	RAX08G189	RAX08G191	RAX08G195	RAX08G197	RAX08G200
SiO2 (%)	-12.862	21.370	27.354	81.845	-12.582	22.552	-5.320	124.701
Al2O3 (%)	-2.522	1.658	2.133	5.710	-1.708	5.666	-0.162	9.995
Fe2O3(T) (%)	-0.058	1.658	0.034	10.635	1.058	4.060	1.902	7.563
MnO (%)	0.042	0.121	0.515	0.865	0.015	0.755	0.043	0.651
MgO (%)	-0.156	0.932	8.277	17.800	0.645	14.355	1.337	18.858
CaO (%)	1.897	1.390	-7.100	-7.240	0.515	-7.014	1.166	-7.327
Na2O (%)	-4.438	-3.006	-1.992	-5.126	-3.940	-5.082	-4.031	-5.244
K2O (%)	-0.062	0.286	0.326	0.222	1.972	1.485	2.288	1.845
TiO2 (%)	0.065	-0.040	-0.138	-0.127	-0.010	-0.080	0.008	0.032
P2O5 (%)	-0.008	0.005	-0.014	-0.070	-0.005	-0.040	0.000	-0.068
Sc (ppm)	1.911	5.998	2.300	29.809	0.453	11.565	0.035	43.611
Be (ppm)	-0.156	-	0.713	-	-0.109	0.840	0.009	2.045
V (ppm)	22.244	6.398	-36.528	62.561	-0.984	48.695	0.080	162.030
Cr (ppm)	-	-	11.928	913.343	-	-	-	1197.950
Co (ppm)	-	-41.691	-1.518	46.266	-	1.020	-	38.460
Ni (ppm)	-	-	-	195.929	-	-	-	296.826
Cu (ppm)	-	-	-	-83.644	-	-	-	-47.473
Zn (ppm)	37.556	56.537	331.789	1254.144	5.625	517.085	10.354	664.941
Ga (ppm)	0.133	2.707	3.359	9.641	1.578	11.101	2.106	15.353
Ge (ppm)	0.320	1.702	0.933	1.314	-0.042	1.168	0.515	1.599
As (ppm)	-	14.398	22.654	85.382	-	13.136	-	66.630
Rb (ppm)	1.289	19.033	6.957	8.004	62.656	30.626	92.212	41.604
Sr (ppm)	-118.978	-98.252	-160.020	-185.054	28.859	-177.026	77.292	-169.348
Y (ppm)	-7.007	3.708	0.226	-1.278	-3.116	3.393	-2.061	6.623
Zr (ppm)	0.000	0.000	0.000	0.000	0.000	0.000	0.000	0.000
Nb (ppm)	1.618	-0.157	0.465	0.827	-0.258	0.389	-0.058	0.865
Mo (ppm)	-	-	-	5.948	-	-	-	12.706
In (ppm)	-	-	-	-	-	0.292	-	-
Sb (ppm)	15.824	2.380	1.079	1.850	-5.053	1.194	2.174	4.411
Cs (ppm)	0.429	0.464	0.303	0.865	1.103	1.375	3.636	1.103
Ba (ppm)	-737.644	-42.000	-179.027	-260.126	441.141	88.700	1080.743	1054.969
La (ppm)	-20.660	-5.952	0.791	-2.799	-0.633	-1.959	0.311	-2.381
Ce (ppm)	-35.516	-14.082	0.496	-3.559	-1.370	-3.997	0.147	-2.969
Pr (ppm)	-2.144	-2.041	-0.226	-0.730	0.401	-0.751	-0.023	-0.812
Nd (ppm)	-5.584	-9.224	-2.261	-3.860	-0.156	-3.904	0.351	-3.434
Sm (ppm)	-1.099	-0.850	-0.478	-0.866	-0.212	-0.800	-0.001	-0.358
Eu (ppm)	-0.284	-0.355	-0.409	-0.447	-0.134	-0.631	-0.083	-0.246
Gd (ppm)	-0.792	0.126	-0.415	-0.920	-0.391	-0.519	-0.127	0.012
Tb (ppm)	-0.111	0.048	0.032	-0.029	-0.004	0.059	-0.026	0.192
Dy (ppm)	-0.798	0.801	0.013	-0.296	0.018	0.493	-0.138	1.385
Ho (ppm)	-0.195	0.187	-0.055	-0.157	-0.066	0.026	-0.055	0.238
Er (ppm)	-0.801	1.147	-0.163	-0.420	-0.397	0.076	-0.194	0.583
Tm (ppm)	-0.137	0.170	-0.016	-0.048	-0.071	0.036	-0.027	0.076
Yb (ppm)	-0.844	1.195	-0.234	-0.407	-0.448	0.141	-0.192	0.379
Lu (ppm)	-0.107	0.137	-0.047	-0.086	-0.065	-0.002	-0.033	0.053
Hf (ppm)	-0.644	0.281	-0.068	-0.049	-0.483	-0.195	0.032	0.066
Ta (ppm)	0.082	-0.733	1.093	1.088	-0.049	1.073	-0.006	1.080
W (ppm)	-	1.309	2.445	3.064	-0.466	3.283	0.312	5.643
Tl (ppm)	-0.196	1.893	0.216	0.155	0.952	0.614	0.438	0.296
Pb (ppm)	-13.778	-0.220	28.176	170.289	-6.422	0.255	20.336	37.504
Bi (ppm)	-	0.262	1.199	4.816	-23.522	1.897	5.153	349.143
Th (ppm)	-6.373	-1.476	-0.329	-0.798	-1.245	-0.294	-0.094	0.258
U (ppm)	-1.821	0.047	-0.703	-0.851	-0.624	-0.749	-0.282	-0.196